Investigation on propagation and radiation for body-centric applications

Qiang Zhang

Sorbonne Université

Ecole doctorale Informatique, Télécommunications et Electronique (Paris)

Laboratoire d'Electronique et Electromagnétisme (L2E)

Etude de la propagation et du rayonnement pour des applications au voisinage du corps humain

Investigation on propagation and radiation for body-centric applications

Par **Qiang Zhang**

Thèse de doctorat en Informatique, Télécommunication et Electronique

Dirigée par Aziz Benlarbi-Delaï

Présentée et soutenue publiquement le 4 décembre 2019

Devant un jury composé de :

M. Aziz Benlarbi-Delaï	Professeur, Sorbonne Université	Directeur de thèse
Mme. Claire Migliaccio	Professeur, Université Nice Sophia Antipolis	Rapporteuse
M. Alain Sibille	Professeur, Télécom Paris	Rapporteur
M. Ala Sharaiha	Professeur, Université de Rennes 1	Examinateur
M. Philippe De Doncker	Professeur, Université Libre de Bruxelles	Examinateur
Mme. Hélène Roussel	Professeur, Sorbonne Université	Examinatrice
M. Julien Sarrazin	MCF HDR, Sorbonne Université	Encadrant
M. Massimiliano Casaletti	MCF HDR, Sorbonne Université	Encadrant

Abstract

In the past decade, the aging of population and the increase in medical costs have brought a lot of innovations in the medical domain. One of them is the use of wireless sensors that are located in, on, or around the human body to remotely monitor patient's physiological signs in real-time via Body Area Network (BAN). Due to the nature of the transmitted data, high data security is one of the most essential requirements in the system. Accordingly, the first objective of this thesis is to improve the communication security between on-body sensors at the physical layer with a novel transmission mechanism that uses human skin as a transmission medium and confines the surface-wave signal inside the skin. As the similar quasi-static human body communication method considered in the BAN standard operates at very low frequencies (centered at 21 MHz), this greatly limits the transmission bandwidth, therefore the data rates. To tackle such issues, the potential of using higher frequencies for the skin-confined communication is investigated in detail for the first time. A planar lossy multilayer human body model, made of skin, fat, muscle tissues, is established for numerical analysis, using complex frequency dependent dielectric property for each tissue. Transverse resonance method (TRM) is used to analyze existing modes within the human body model. Confinement capabilities as well as propagation losses are investigated for frequencies up to 60 GHz. Since the tissue thickness varies with location and person, three skin thicknesses, typically 0.5 mm, 1 mm, and 1.5 mm, are considered and compared. This study concludes with a discussion of the skin-confined propagation mode excitation by a horizontal on-body dipole. It should be noted that the developed TRM-based dispersion analysis code is the core work of this thesis and is used throughout all the main analysis in this thesis.

Another innovation in the medical domain can be referred to the non-contact sensor-less remote medical monitoring using Doppler radar, which

has become a promising way to further improve patient comfort and treatment efficiency. Leaky-wave antennas are good candidatures for such applications due to their directive radiation pattern, ease of fabrication, and especially the frequency-depending beam scanning properties. A fast scanning is desired in order to cover a large angular range with a given operation frequency bandwidth. Therefore, a highly-dispersive guiding structure is classically required for the leaky-wave antennas. Consequently, in the second part of this thesis, an original TRM-procedure-based design is proposed to increase the frequency dispersion of the guiding structure to some extent. The approach uses a grounded dielectric slab covered by a metasurface composed of a lattice of square patches. Using this enhanced dispersion, a periodic leaky-wave antenna is designed and simulated in the 60 GHz band and compared to more conventional ones in terms of angular scanning. A coplanar-fed surface-wave launcher is further designed to efficiently excite the scanning-enhanced leaky-wave antenna.

Keywords: skin-confined propagation, dispersion analysis, body area network (BAN), human body communication (HBC), multilayered human body model, transverse resonance method (TRM), 60 GHz, leaky-wave antenna (LWA), scanning range enhancement, surface-wave launcher

Résumé en français

Au cours de la dernière décennie, le vieillissement de la population et la hausse des coûts des soins médicaux ont engendré de nombreuses innovations dans le domaine de santé. L'une d'elles consiste à utiliser des capteurs sans fil autour du corps humain pour surveiller les signaux vitaux du patient à distance et en temps réel via des réseaux corporels de type BAN (Body Area Network en anglais). En raison de la nature des données transmises, une sécurité élevée est l'une des exigences les plus essentielles du système. En conséquence, le premier objectif de cette thèse est d'améliorer la sécurité des communications entre les capteurs sur le corps humain au niveau de la couche physique, grâce à un nouveau mécanisme de transmission utilisant la peau comme support de propagation de l'onde électromagnétique. Les méthodes classiques de communication utilisant le corps humain envisagées dans le standard 802.15.6 dédié aux BANs fonctionnent à très basse fréquence (centrée à 21 MHz), cela limite considérablement la largeur de bande de transmission, donc les débits de données. Afin de résoudre ces problèmes, l'utilisation de fréquences plus élevées pour la communication confinée dans la peau est étudiée en détail pour la première fois. Un modèle de corps humain planaire et multicouche, constitué de peau, de graisse et de muscle, est établi pour l'analyse numérique, à l'aide des permittivités complexes dépendantes de la fréquence pour chaque tissu. La méthode de résonance transverse (transverse resonance method en anglais ou TRM) est utilisée pour analyser les modes existants dans le modèle du corps humain. Les capacités de confinement ainsi que les pertes de propagation sont étudiées pour des fréquences jusqu'à 60 GHz. Sachant que l'épaisseur des tissus varie avec l'emplacement et la personne, trois épaisseurs de peau, typiquement 0.5 mm, 1 mm et 1.5 mm, sont considérées et comparées dans l'analyse. Cette étude se termine par une discussion sur l'excitation de la propagation confinée dans la peau par un dipôle horizontal placé sur le corps humain. Il convient de noter

que l'élaboration d'un code d'analyse de la dispersion basé sur la méthode TRM constitue l'essentiel du travail de cette thèse et est également utilisé pour le second objectif de cette thèse.

Une autre innovation dans le domaine médical concerne la surveillance sans contact et sans capteur utilisant des techniques radars de type Doppler. Cette approche est un moyen prometteur afin d'améliorer encore plus le confort du patient et l'efficacité des traitements. Les antennes à ondes de fuite sont de bonnes candidatures pour ces applications grâce à leurs caractéristiques avantageuses telles que le rayonnement directif, la simplicité de fabrication, et en particulier le balayage du faisceau en fonction de la fréquence. Un balayage rapide est souhaité afin de couvrir une large plage angulaire avec une bande de fréquence limitée. Par conséquent, une structure guidante hautement dispersive est typiquement requise pour ce type d'antenne. Pour améliorer la dispersion des guides d'ondes en technologie imprimée, différentes stratégies peuvent être envisagées. Par exemple, les substrats à haute permittivité peuvent être utilisés. Cependant, les substrats planaires disponibles à faibles pertes sont limités en termes de valeurs de permittivité diélectrique. Une autre méthode consiste à densifier artificiellement le substrat en utilisant des métasurfaces. Ainsi, dans la deuxième partie de cette thèse, une procédure originale de conception basée sur le code TRM développé dans la première partie de la thèse est proposée pour augmenter dans une certaine mesure la dispersion de la structure guidante. L'approche utilise un substrat diélectrique métallisé en face arrière et de l'autre côté recouvert d'une métasurface composée d'un réseau de patchs. En utilisant cette dispersion améliorée, une antenne périodique à ondes de fuite est conçue et simulée dans la bande des 60 GHz et comparée en termes de balayage angulaire à des antennes à ondes de fuite plus classiques. Un excitateur d'ondes de surface alimenté par une ligne de transmission coplanaire est en outre conçu pour alimenter efficacement l'antenne à ondes de fuite à balayage amélioré. Des prototypes ont été fabriqués à l'aide d'une graveuse laser et des mesures de diagramme de rayonnement ont été réalisées pour des essais expérimentaux.

Mots clés: propagation, analyse dispersive, réseau corporel, communication sur le corps humain, modèle de corps humain multicouches, méthode de résonance transverse, 60 GHz, antenne à ondes de fuite, amélioration du balayage angulaire, excitateur d'ondes de surface

Contents

Abstract **1**

Résumé en français **3**

1 Context and Objectives **8**
1.1 Body Area Network (BAN) 8
1.1.1 Introduction 8
1.1.2 Advantages 12
1.1.3 Classification of BAN 14
1.2 On-Body Sensor Applications 16
1.3 In-Body Sensor Applications 19
1.4 Non-Sensor Applications 21
1.5 Requirements 24
1.6 Frequency Regulations for BAN 28
1.7 Dedicated BAN Standard (IEEE 802.15.6) 30
1.8 Compatible BAN Standards 31
1.8.1 IEEE 802.15.1 standard (Bluetooth) 32
1.8.2 IEEE 802.15.4 standard (Zigbee) 33
1.8.3 IEEE 802.11 standard (Wi-Fi) 33
1.9 BAN On-body Antennas 34
1.10 Motivation and Objectives 37
1.10.1 Skin-confined on-body propagation analysis 37
1.10.2 Enhanced angular-scanning leaky-wave antenna design for Doppler radar detection 44
1.11 Thesis Outline 47

2 Skin-Confined On-Body Propagation Analysis **49**
2.1 Introduction 49

2.2 On-Body Propagation Channel Modeling Methods 50
2.3 Propagation Modes 52
2.4 Human Body Modeling 54
2.5 Total Reflection and Critical Angle : Skin-Confined Propagation Mechanism 56
2.6 Transverse Resonance Method 65
2.7 Transverse Impedance of Different Propagation Modes 68
2.8 Skin-Confined Propagation Calculation 70
2.9 Human Tissue Thickness 73
2.9.1 Skin thickness measurement methods 74
2.9.2 Measured tissue thicknesses 76
2.10 Analysis of Skin-Confined Propagation 77
2.10.1 Dispersion and attenuation curves 79
2.10.2 Confinement 84
2.10.3 Electromagnetic fields distribution 86
2.10.4 Fat thickness influence on the propagation 97
2.10.5 Surface impedance 98
2.11 Discussion for the Surface-Wave Excitation 100

3 Enhanced Scanning Range Leaky-Wave Antenna Design 107
3.1 Introduction of leaky-wave antennas 107
3.2 Advantages 109
3.3 Fast-Wave and Slow-Wave 110
3.4 Different Types of Leaky-Wave Antenna 112
3.4.1 Uniform leaky-wave antenna 112
3.4.2 Periodic leaky-wave antenna 114
3.5 Applications of Leaky-Wave Antenna 117
3.5.1 Cooperative smart cars system 117
3.5.2 Real-time spectrum analyzer 118
3.5.3 5G signal direction of arrival estimation 119
3.5.4 Non-contact medical monitoring 120
3.6 Scanning Range of Leaky-Wave Antennas in Current Literature 121
3.7 Method to Enhance the Scanning Range 123
3.8 Classical GDS Periodic Leaky-Wave Antenna 124
3.8.1 GDS dispersion calculation for different substrates . . . 124
3.8.2 Scanning range of GDS periodic leaky-wave antennas with different substrates 127
3.9 Metasurface-based Enhanced-Dispersion Waveguide 133

3.9.1 Design methodology 133
3.9.2 Metasurface calculations 136
3.9.3 Simulations of the metasurface-based GDS waveguide . 140
3.10 Leaky-Wave Antenna Based on New Designed Waveguide . . . 145
3.11 Launcher 150
3.11.1 Launcher design 150
3.11.2 Simulations of launcher 152
3.11.3 Simulations of leaky-wave antenna with launcher . . . 154
3.11.4 Simulations of leaky-wave antenna with launcher and connector 157
3.12 Test of Fabrication 161
3.13 Discussions 163

Conclusion and Perspective **165**

Bibliography **167**

Chapter 1

Context and Objectives

1.1 Body Area Network (BAN)

1.1.1 Introduction

In the past decade, communication systems in the vicinity of the human body have attracted an increasing attention from wireless communication researchers. Firstly interpreted as "Body Sensor Network (BSN)" in 2006 [1], the IEEE Task Group 6 (TG6) has established an international standard for Body Area Network (BAN), the IEEE 802.15.6, for the purpose of providing a short-range, extremely low-power, highly reliable, data rates up to 10 Mbps wireless communications in, on, or around the human body [2].

A wide range of applications can be found in BAN. One of the areas of greatest interest is the healthcare and medical domain [3]. As predicted by United Nations in [4], the worldwide population over age 65 will double in 2030, from 495 million in 2009 to 974 million. The relative size of the aging population is expected to reach more than 9% in 2020. It will reach almost 17% by 2050 [5]. In developed countries, this increase is particularly pronounced. The aging population accelerates the prevalence of chronic diseases, such as cardiovascular diseases, hypertension, and diabetes, which have become a major threat to human health and result in massive medical care issues [3, 6]. Early detections and preventions are required to address such disease problems. Currently, the scarce medical ressources cannot support the great volume of demands while the medical costs have been continuously growing [7]. The healthcare systems are suffering from severe challenges. These trends highlight the need to find more efficient, innovative,

and affordable solutions to face the incoming problems in the healthcare and medical domain. One solution leads thus to the remote medical monitoring using miniaturized and low-powered sensors.

Traditionally, nurses and doctors in clinical settings perform care through regular ward visits and monitoring vital signs through wired medical machines connected to patients. Nurses visit patients every few hours to track changes in patient's health status in order to early recognize the clinical deterioration. The medical devices can also be compact and portable on patient's body. Figure 1.1 shows a conventional medical monitoring equipment for electrocardiography (ECG) recording – Holter monitor [8] – a portable device for monitoring electrical activities in the human cardiovascular system for about 24 - 48 hours. The system consists of 3 to 8 electrode sensors attached to patient's chest, which continuously measure patient's cardiac electrical signals and transmit them through cables to a central recorder mounted on the patient's belt. Doctors then use these recorded data to diagnose the patient's cardiovascular system.

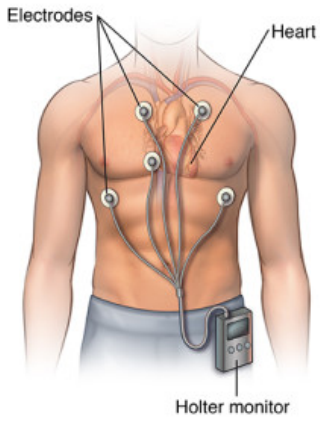

Figure 1.1: Holter Monitor for electrocardiography recording [9]

It should be noted that, to observe occasional cardiac arrhythmia (irregular heartbeat), since it is difficult to identify in a relative short period of time, an extended recording time is required. However, the cables attached to patients constraint their activities, and sometimes make them feel uncomfortable. Moreover, for patients with more transient cardiac symptoms, a

duration of at least one month is necessary for the observation, while typical Holter device provides only a 24 - 48 hours lifespan battery. The frequent device replacement can cause inconvenience to patients.

The above problematics lead to the emergence of the BAN, a wireless network consisting of numerous sensor/actuator nodes placed on or implanted within the human body. Sensors collect diverse human vital signs such as heart rate, blood pressure, glucose level, body temperature etc., and if necessary, also the surrounding environment features [7, 10]. The collected data can be directly communicated between nodes as a standalone ad-hoc network [11, 12] or be routed together to a data hub. The data hub could be a personal digital assistant (PDA) or simply a smartphone. In turn, through the data hub, the gathered information is transmitted to an analysis center or emergency services over a cellular network or Internet (with an intermediate gateway)(figure 1.2). Doctors and physicians can access these real-time data to make therapy decisions regarding a patient's treatment options and in turn the patients can be alerted by SMS or alarm of the feedback information [7]. In addtion, the data hub and sensors can form a local loop for self-analysis. In some emergency situations (e.g., high level of sugar in blood is detected), an immediate auto-medication (e.g., insulin injection) could be directly triggered by the actuators [6, 12].

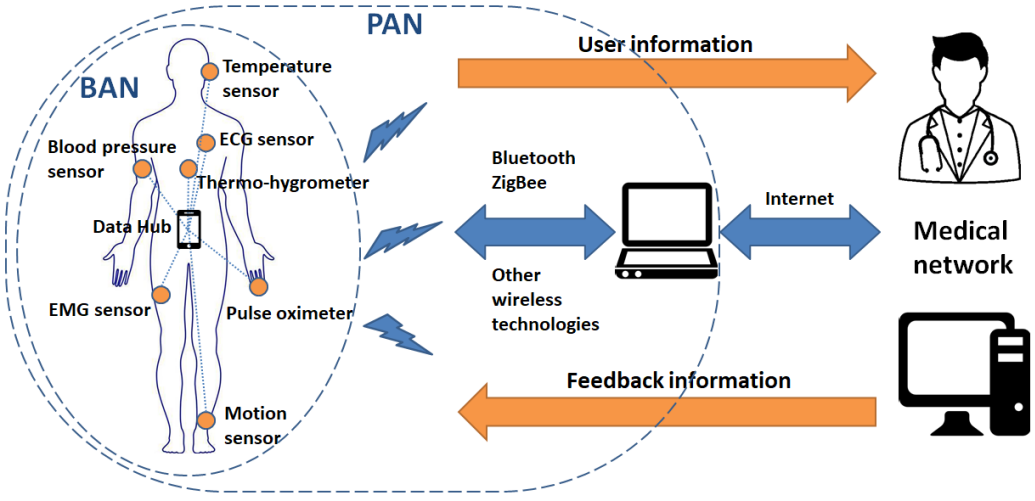

Figure 1.2: BAN healthcare application

As shown in figure 1.2, a simple star network is sufficient for BAN. However, in some cases it may be desiralbe to support multi-hop communication to achieve a connection between devices that are occluded by the body. BAN's coverage is within three meters from the human body [13]. Communication between the human body and external devices within ten meters is ensured with Bluetooth (IEEE 802.15.1), ZigBee (IEEE 802.15.4), or other similar wireless technologies often available at the central node. For ease of use, the network should be scalable and tolerate dynamic insertion and de-insertion of nodes [14].

Typical examples of BAN in the medical domain include early detection, prevention and monitoring of diseases, intelligent emergency care management systems, intensive care unit systems, post-operative rehabilitation, elderly assistance at home or in retirement room, and assisted living applications for disabled people [15].

Nowadays, with the the advance of integrated circuit technology, the miniaturization of electronic sensors (e.g., 7 nm CMOS technology) [16–18] and the standardization of ultra-low-power wireless technology [2, 3, 19], the BAN remote monitoring system can finally be realized, which has unleashed a revolution in our daily life. A number of recent projects have focused on BAN medical implementation. In the project of [20], the hardware and software architecture of the BAN for ambulatory health status monitoring (heart activity and body motion) was discussed. An investigation in healthcare delivery by combining wearable sensors and implantable sensors was given in [21]. A BAN hearthcare architecture for both indoor and outdoor scenarios was proposed in [22] to enhance patient mobility. In [23], the BAN is used as a way to improve remote functional rehabilitation of patients at home. Other studies on the BAN heathcare system can be found, such as HealthGear for detection of patient's sleep apnea events [24], BlueCode for emergency medical care [25–27], SMART for patient physiological signal monitoring in waiting area of emergency room [28], MobiHealth for a medical sensor network based on mobile phone communicaiton technologies GPRS/UMTS [29], etc.

Indeed, many other non-medical applications can also benefit from BAN, including domotic, sports, military, entertainment etc [7]. The TG6 has issued a call for BAN applications in 2008, for which a detailed summary can be found in [30]. Some non-medical examples of BAN applications are given in table 1.1.

Aiding professional and amateur sport training
Assessing soldier fatigue and battle readiness
Soldier enhanced security system
Video/audio streaming
Data/image/video file transfer
Remote control of entertainment devices
Body motion capture, gesture recognition, position
Forgotten things monitor
Emotion detection
Interactive gaming
Social networking

Table 1.1: Some examples of non-medical applications for BAN [30]

1.1.2 Advantages

BAN has enabled remote continuous wireless monitoring in a small range around the human body, which can find many advantages and benefits in the healthcare domain. The remote healthcare allows medical professionals to provide treatment to patients and to achieve real-time monitoring of the patient's health situation in a different location. This system can be of great benefit for patients who live far away from urban medical centers or who have limited mobility as well as the ones suffering from chronic disease that need long-term home care. On the basis of the traditional wearable sensors, the additional wireless implanted sensors can provide an extensive range of patient's bio-information, which can be crucial for a quick and efficient reaction when emergency happens. The main advantages of BAN will be discussed as following.

First, with the advancement and miniaturization of microelectronics, tiny wireless biosensors can be manufactured for wearable patient monitoring system at low cost, which greatly reduces hospital budgets for combersome medical equipment and thereby indirectly reduces the medical costs for patients [31]. With these portable sensor devices, patient's vital signs can be remotely monitored everywhere and anytime, which means patients no longer need to be hospitalized, which can further reduce their medical expense and in the same time reduce the hospital workload. People can track their health without having to frequently visit the doctors [32]. Wireless devices do not restrict patient activities, making them more mobile, convenient and com-

fortable [3, 7, 33, 34]. In addition, the small size and wireless nature of the device make the system unobtrusive. This is in stark contrast to the traditional wired-connection monitoring systems which can be problematic and awkward when worn by a person [33]. Moreover, for elderly people who prefer to live alone, a long-term remote monitoring (in terms of sudden falls, cardiac arrests etc.) can provide them with a better independent life [35].

Moreover, traditional nurse-care struggles to provide continuous monitoring due to human physical limitations, especially for long-term trend analysis (e.g., overnight monitoring), in addition to the shortage of skilled staffs and overload, which reduce the quality of healthcare [6]. The emergence of remote wireless medical monitoring has significantly solved these problems. Due to the miniaturization and low power of the sensors, the devices have longer lifespan to ensure long-term uninterrupted healthcare service without intervention (e.g., battery replacement). 24-hour monitoring allows doctors to grasp more complete pathological information from patients, especially those with transient and random symptoms, which improves treatment performance and efficiency. When an abnormality is detected, the system can immediately alert the doctor, achieving a faster and more effective feedback procedure in the doctor-patient activities. Rapid identification of emergencies such as heart attack or sudden fall is sufficient to save a patient's life. The monitoring data can be upload to the hospital's center server. Doctors and patients can review the data everywhere and anytime, providing better management and administration of the healthcare information while maintaining good data security and confidentiality.

Furthermore, since the range of BAN is within three meters, in an environment where a large number of patients wearing or be implanted many sensor and actuator nodes (e.g., nursing or retirement homes), this can reduce the radio interference between different users using BAN system because wireless communication is only confined around each user. Also, this reduces the complexity of controlling multiple nodes on a same person, as the command can be directed to the central control node in the corresponding personal BAN [36].

Therefore, BAN provides a very effective, innovative solution to the medical/healthcare area.

1.1.3 Classification of BAN

A node in a BAN is defined as an independent device with communication capabilities. The nodes can be classified according to the operating location related to the human body [7]:

1. Implanted node – node placed inside the human body. The node may be implanted in close contact with the skin or sometimes even in the deeper body tissues (e.g., glucose sensor implants, cochlear implants) [33] or locate inside the gastrointestinal system (e.g., gastrointestinal endoscope capsule).

2. Body surface node – node placed on the human body or less than 2 centimeters away from it [13] (e.g., smart watches, hearing aids, wearable body temperature sensors).

3. External node – node not in contact with the human body. It can be a few centimeters to 5 meters away from the body [13], i.e., indoor communication range. This type of node could be an analysis system or a router to an external network.

These different node implementations make the BAN experience different kinds of wireless propagation scenarios, which increases the complexity and difficulty of designing such networks. The typical communication scenarios in BAN are defined as shown in figure 1.3:

1. In-body to on/off-body – communication between an implant node and a body surface node or an external node.

   In this scenario, at least one implanted node is involved, i.e., the propagation channel includes the human body as a communication medium. The human body is composed of lossy tissues, and hence in this scenario, the attenuation at the same frequency might be higher than in the other cases. Moreover, since surgery may be required to replace the battery, the power consumption of the implants should be ultra-low to ensure long-term operation and avoid device replacements. In addition, the implanted device should be very tiny and biocompatible, which impose stringent requirements on the size, form, and materials of the antenna.

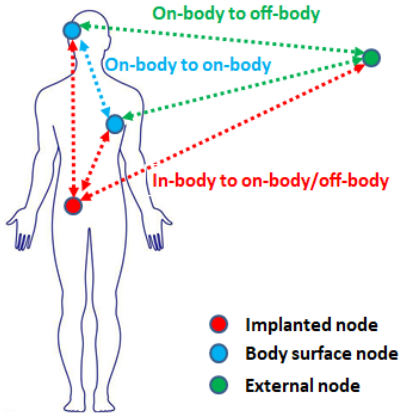

Figure 1.3: BAN communication scenarios

2. On-body to on-body – intercommunication within body surface nodes.

   The on-body to on-body communication strongly experiences the body surface within the communication channel, and so has a higher attenuation than in free space. Therefore, in order to establish a reliable link, the analysis of the human body propagation channel becomes very important for such communications. Different methods can be used to characterize the propagation channel and will be illustrated in chapter 2. Because of the dynamic feature of the human body, the shadowing from the body movement should be taken into consideration for the channel analysis. Moreover, due to the confidentiality and safety issues, the propagating wave should surround the body surface and be confined along it without excessively radiating outward or toward the body.

3. On-body to off-body – communication between body surface node and external node.

   For this scenario, the main channel is the free space. The communication is usually ensured by PAN technology, such as Bluetooth or ZigBee. Cellular network can also be used, especially in outdoor environments. However, regarding the human safety reasons for electromagnetic exposure, the transmit power should be strictly constrained and regulated. As for the antenna, contrary to the on-body to on-body scenario, the

radiation should be outward from the human body and the radiation toward or along the human body should be minimized.

1.2 On-Body Sensor Applications

BAN provides a large number of applications in the medical area. These applications can be categorized according to the location of the bio-sensor relative to the human body. Table 1.2 summarizes some of the available on-body sensor measurements in the medical and healthcare domains.

Electroencephalography (EEG), electrical activities of brain
Electrocardiography (ECG), electrical activities of heart, i.e., heart rate
Electromyography (EMG), electrical activities of muscle
Temperature
Respiration monitor
Pulse oximetery (oxygen saturation)
Blood pressure monitor
PH monitor
Glucose sensor (wearable)
Movement / fall detection

Table 1.2: Examples of on-body sensor measurement [30]

In the following subsections, we give some detailed examples of on-body sensor applications in the medical domain as well as a non-medical application for infantry training in the military domain.

Flexible microfluidic circuit for ECG and EEG measurement

As mentioned before, with the development of electronic miniaturization, it has become possible to centralize different electronic components in small electronic devices. Figure 1.4 shows a flexible patch-shaped sensor from the works in [37] that can be adhered to the human body and continuously monitors patient's ECG and EEG parameters.

In order to increase the flexibility of the device, a microfluidic technology is used instead of using a traditional hard planar substrate. This means

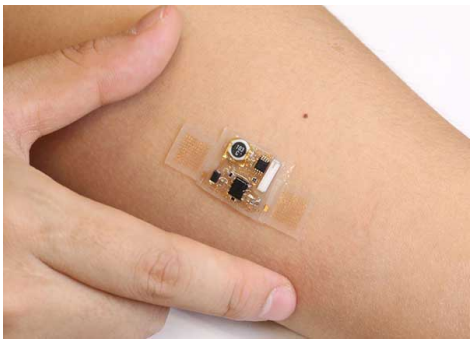

Figure 1.4: Flexible circuit for ECG and EEG monitoring [37]

a dielectric fluid – a high-molecular-weight silicone oligomer (Sylgard 184, without curing agent) – is applied to support the components of the device. The circuit is wirelessly powered and the transmitted data signal can be caught and displayed on a smartphone. The experimental tests have demonstrated that the device has the same performance as commercial ECG and EEG monitoring sensors. Due to the softness of the device, it is more adaptable to the soft, textured, curvilinear, and time-dynamic surfaces of the skin. This type of sensor is used to give patients more comfort.

Glucowise^{TM} – non-invasive glucose monitoring device

Glucowise^{TM} is a biomedical application under developement in [38]. It is a non-invasive glucose sensor that could accurately determine blood glucose level in seconds. Compared to traditional blood sampling methods, the sensor does not need to pierce the patient's skin, providing a 100% painless approach for glucose analysis.

To measure glucose levels, the device is gently squeezed onto the section between the thumb and forefinger (see figure 1.5) or the earlobe. The glucose concentration is obtained by transmitting a low power signal at around 65 GHz across these parts and analyzing the received signal by the sensor on the opposite side of the transmitter. The 65 GHz frequency is chosen to have a small enough wavelength to provide sufficient resolution of the blood region. The chosen body areas should be thin enough for the signal to pass through and have an adequate blood supply in the capillaries. The collected information is sent to smartphone via Bluetooth communication, where an

application allows the user to read the analyzed glucose levels.

Figure 1.5: Glucowise^{TM} - non-invasive medical device for glucose level detection [38]

Virtual reality simulator for military team training

With the aim of improving military infantry training, a multi-soldier virtual reality (VR) simulation system integrated with BAN is proposed in [39]. The simulator immerses soldiers in complex virtual battlefields extracted from real-world situations (e.g., a rescue mission in enemy camps) and trains them to improve their adaptability to fast changing battlefield and their teamwork ability. Compared with the traditional training, soldier in the VR system is not exposed to the risks of real situations. In addition, this resolves the space limitation issues of training, thereby enhancing the confidentiality.

In the proposition, the VR simulator is deployed in a 5 m^2 space and can support up to six soldiers. Soldiers in the simulator are equipped with a head mounted display, a voice communication headset, an omnidirectional treadmill, a simulated rifle and numerous inertial sensor nodes (e.g., accelerometers, gyroscopes) connected in a BAN at 2.4 GHz (figure 1.6). The worn sensors continuously track soldier's movements and postures, and then send the collected data to a sink node. The centralized information is analyzed to model soldiers into a virtual environment with real-time and high-performance solutions. Soldiers accomplish the mission in cooperation with the others. After the simulation, soldiers can review their action details in the virtual mission rehearsals and other various digital record data to make improvements and overcome shortcomings in action.

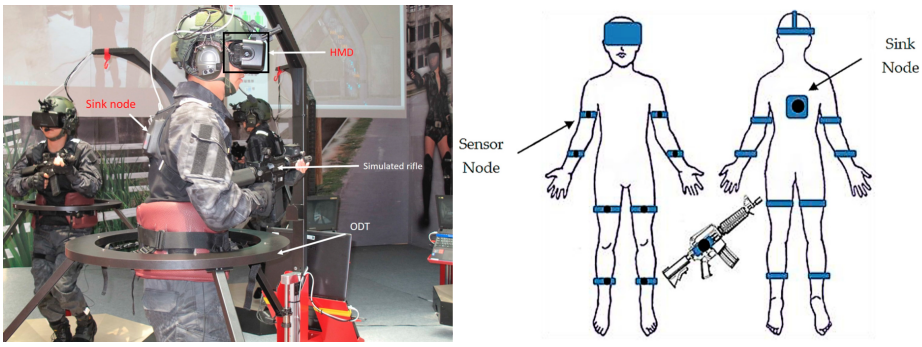

Figure 1.6: Virtual reality soldier simulator [39]

1.3 In-Body Sensor Applications

Table 1.3 shows some of the in-body BAN sensor measurements in the medical area as well as some examples of actuators in table 1.4 because they are often implanted in the human body. Then, an example of an In-body sensor application – wireless capsule endoscopy – is presented in detail.

Glucose sensor (implant)
Cardiac arrhythmia monitor/recorder
Brain liquid pressure sensor
Endoscope capsule (gastrointestinal)

Table 1.3: Examples of in-body sensor measurement [30]

Insulin pump
Implanted drug delivery
Deep brain stimulator
Cortical stimulator
Visual/audio neuro-stimulator
Cardiac pacemaker
Defibrillator

Table 1.4: Examples of medical actuators [30]

Wireless capsule endoscopy

Figure 1.7 shows a medical in-body sensor application – wireless endoscopy. The gastrointestinal tract within the human body is inevitably a complex environment that is difficult to access for medical diagnosis (e.g., bleeding, infection, tumor...) and treatment [40]. This tract is part of the human digestive system that extends from the mouth to the anus. Conventional endoscopic approach (figure 1.7(a)) employs a flexible tube with light and a camera at its end to obtain visual (image or video) of the gastrointestinal environment and locate pathological sections. However, due to the rigidity and large dimension of the tube, patients suffer from a lot of pain and discomfort during the operation, which makes them unwilling to undergo an examination. Moreover, conventional endoscopy has difficulty to access the small intestine.

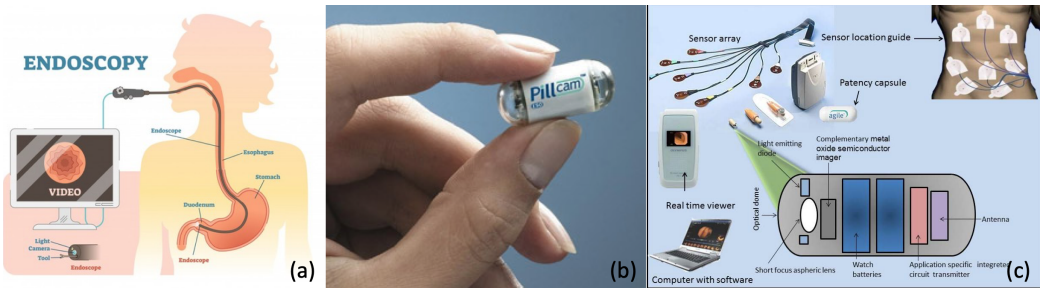

Figure 1.7: Wireless endoscopy application: (a) conventional endoscopy (b) wireless endoscopy capsule (c) wireless endoscopy operation [41–43]

In the past few decades, the invented wireless endoscopic technology [40, 44] has helped patients achieve more comfortable and complete endoscopy. Patients only need to swallow a pill-sized capsule (figure 1.7(b)) that integrates a miniaturized wireless camera, an illumination system, and a transmission module. The capsule continuously communicates with an external recorder worn on patient's belt. Camera vision can be observed in real-time through a viewing device as shown in figure 1.7(c). Doctors and physicians then analyze the recorded data in their computer. Some sensors may be attached to the patient's body in order to accurately determine the location and position of the capsule, and thus the lesion in the patient's digestive tract. In some models, the sensor module can equally provide feedback information

to the capsule to direct it into the area of interest.

1.4 Non-Sensor Applications

Nowadays, most methods of measuring respiration and heart rates involve direct physical contacts with the patient [45, 46]. Although they have wireless connectivity to the external analysis systems, the affixed sensors on the human body can still suffer from the limitation of battery life, especially for long-term monitoring. And in some cases, the battery reaching its end of charge may also result in inaccurate measurements of vital signs [47].

Moreover, contact-based monitoring is not always feasible for certain special situations, such as burn patients or newborns [48]. It may be difficult to find adequate areas to attach the probes to burn patients. And the newborns in need of intensive care often suffer form skin damage due to the use of electrode contacts, adhesive tape and other probes to measure vital signs. In some cases, the use of these physical measurement devices can cause physical scars in newborns.

Using non-contact approach to measure patients' vital signs will allow for non-invasive continuous monitoring of the patient without risking further injury to patients. The external non-contact measurement device can be continuously powered, thus it is not affected by the battery lifespan problem as the portable devices. In addition, the non-contact feature can give patients more comfort thus improve their quality of life.

In the following part, we will present some current non-sensor applications in both medical and non-medical areas.

Doppler radar for heartbeat and respiration rate detection

Recently, Doppler radar has become of increased interest for indoor applications. In particular, human vital sign monitoring radar systems are rapidly evolving for breathing and heartbeat rate detection – the most common vital signs measured in hospital settings [49–51]. Besides, such systems can also be used for sleep studies [52] and even for non-medical applications such as searching for victims (in the ruins, under the snow etc) [53]. The radar system provides patients with non-contact and continuous vital signs

monitoring, giving them more comfort and lower medical cost. Additionally, the non-contact nature of such system eliminates the need for nurses to install sensors on patients, meanwhile allowing doctors to get faster and more accurate patient information, which increases healthcare efficiency in emergencies.

The principle of using Doppler radar for heartbeat and respiration detection was first proposed in the 1970s [52, 54]. In fact, when the radar target is the chest wall of a person as shown in figure 1.8, the reflected signal contains chest displacement information caused by heartbeat and breathing. The displacement returns a phase-modulated signal to the radar, in which the heartbeat and breath rate can be extracted by applying techniques such as filtering, DC (Direct Current) removal, autocorrelation, DFT (Discrete Fourier Transform) and peak finding.

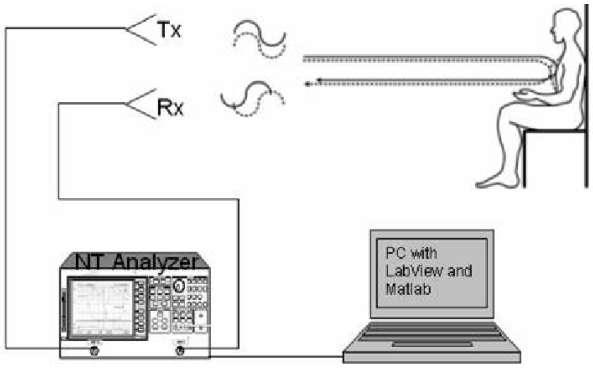

Figure 1.8: Doppler radar for heart rate detection [55]

In [48], the proposed 2.4 GHz continuous-wave Doppler system shows that the performance of measurement at a distance of 50 cm can be guaranteed at a transmitter output power of -12.5 dBm (0.05 mW), refered to a commercial piezoelectric heart rate detection sensor (83.7% measurements have a accuracy within 1 beat/min and 93% within 5 beats/min). When the output power is increased to 16.25 dBm (42 mW), the distance can be extended to 2 m (91.8% accuracy compared to the reference). Works in [55] also shows the possibility of detecting the heartbeat activity (e.g., heart rate, heart rate variability) at 16 GHz at different power levels within a distance of one meter between the person and the radars. In [56], a 60 GHz Doppler radar is used to estimate physiological data of the human body and demon-

strates the capability to accurately detect respiration and heartbeat rates, despite the intermodulation effects between them.

Google Soli™ - touchless interaction sensing device for human band motion detection

Google Soli™ [57] is a new touchless sensing technology for human hand motion detection (figure 1.9). The objective is to provide users with the possibility of non-contact device control through a simple set of hand gestures and motions.

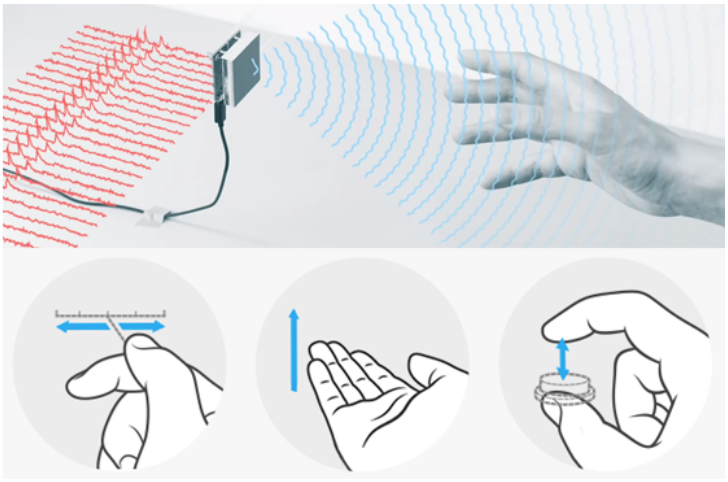

Figure 1.9: Google Soli [57]

Equipped with a 60 GHz miniature radar, Soli™ emits electromagnetic waves in a broad beam. The reflected signal from the hand within the beam is collected by an in-built sensor. The parameters of the received signal such as energy level, time delay, and frequency shift are analyzed and converted to the hand's size, shape, orientation, distance, and velocity. These features can be virtually interpreted as user actions on physical tools, e.g., slider, dial, or button as shown in figure 1.9. Using this technology, users can remotely command their connected objects (e.g., projected screen, computer, lights...) without having to make real contact with them.

For subtle motion detection, Soli™ is based on a mathematical analysis of the time variations of the received signal. Therefore, the equipment

does not require large bandwidth and high spatial resolution like the conventional video detection systems to recognize small image changes, which greatly reduces the complexity and size of the sensor.

1.5 Requirements

The numerous application possibilities of BAN have led to various system requirements. These requirements are not independent of each other, and in some cases, one may limit another. For example, high data rate typically needs higher emission power, but in turn restricts the battery life. Therefore, compromises and appropriate choice should be made between them based on application target.

Table 1.5 shows some of the typical measurement parameters and their technical requirements in medical applications. It can be noted that due to the strong heterogeneity of the measurements, the data rate ranges from a few Kb/s to several Mb/s. Thus, certain degree of flexibility in terms of throughput data rate is needed in BAN systems. In general, it can be seen that the application data rate is not high. However, since different types of vital signs may be measured simultaneously, the aggregate data rate can easily reach several Mb/s, which is higher than the data rate of

Application	**Target data rate**	**Desired battery lifetime**
Deep brain stimulation	1 Mb/s	> 3 years
Hearing aid	200 Kb/s	> 40 hours
Capsule endoscope	1 Mb/s	> 24 hours
Drug dosage	< 1 Kb/s	> 24 hours
ECG (6 leads)	72 Kb/s	> 1 week
ECG (12 leads)	288 Kb/s	> 1 week
EEG	86.4 Kb/s	> 1 week
EMG	320 Kb/s	> 1 week
Temperature	< 1 Kb/s	> 1 week
Glucose monitoring	1.6 Kb/s	> 1 week
Oxygen	< 1 Kb/s	> 1 week
Respiration rate	< 10 Kb/s	> 1 week
Audio	1 Mb/s	> 24 hours
Video	< 10 Mb/s	> 12 hours

Table 1.5: Technical requirements for different medical sensors [6, 10, 31]

most existing low-power wireless networks [31]. Since the sensor nodes can communicate between each other, the communication link typically needs to be bidirectional (but not necessarily symmetric, e.g., the throughput level between the normal node and the coordinator).

In the following subsections, we will discuss in detail some of the most important requirements in BAN, such as device portability, power consumption, QoS (Quality of Service) in terms of reliability and latency, data safety and security.

Device portability and power consumption

As shown in table 1.5, many medical sensors should maintain a battery life of at least one week. In some cases such as chronic diseases analysis, the continuous monitoring needs even longer operating time up to months and years [31]. These devices are not expected to have frequent battery changes, especially for implanted nodes for which replacing battery may require undergoing surgery. However, high battery capacity results in large battery sizes, which in turn heavily affects the patient's daily life or even body functions.

On the other hand, since the BAN devices are equipped either on or implanted inside the human body, the various operation nodes including antenna and battery should be tiny and lightweight, so that they can be worn and provide more comfort for patients. In addition, wearing these devices sometimes make patients feel embarrassed, so the miniaturization of the device is important to make the monitoring unobtrusive. However, as mentioned previously, the size limitation leads to very limited energy storage.

To address the conflict between device size and operating duration, ultra-low power consumption is a fundamental necessity for BAN. In a sensor node, the power supply provides energy for the sensing components, the transmission components, and the microprocessors or microcontrollers. For the transmission components, a minimum transmit power should also be considered to ensure the reliability of the transmission. It is likely that the wireless communicaiton is the most power consuming feature in BAN systems [31,58]. Good compromises should be made between the device size, weight, power consumption, and transmission reliability in BAN systems. Efficient data transmission mechanisms and power management need to be proposed in the PHY (Physical) and MAC (Medium Access Control) layers. For example, to save energy, the MAC layer can turn off the radio when there is no need to send or receive data.

Furthermore, although the initial installation is set up in the hospital, the remote monitoring outside or at home needs to be performed without intervention of medical staffs. In order to facilitate the use of BAN devices for patients, the system should have self-configuration and self-maintaining capabilities [12, 59, 60].

QoS (reliability, latency)

Since the information transmitted in BAN is typically physiological signs for patient's therapy, reliable and accurate operation during data collection and transmission is critical to BAN applications. Erroneous readings can lead to wrong medical diagnosis and decisions on critical issues related to physiology [61]. Thus, BAN has more stringent requirement on reliablility than other wireless networks. BAN designers should target reliable communication techniques to ensure uninterrupted communication and optimal throughput [33]. Moreover, some medical applications that provide high priority alert message cannot tolerate long response times. In [62], with the implementation of a rapid response system (RRS), a 50% reduction in cardiac arrest rates and unexpected death in surgical patients was confirmed. Therefore, real-time transmission with high performance is required in BAN [15].

Reliability and latency depend respectively on packet loss probability and packet transmission delay. These are affected by the Bit Error Rate (BER) in the transmission channel at the PHY layer level (e.g., channel loss, interference etc) and the MAC layer transmission procedures (e.g., channel access technique, packet size selection, retransmission procedure, etc.). So the design of PHY and MAC layers plays a very important role in the BAN system [36]. Adaptive choice of modulation and coding technique at the PHY layer can reduce the BER and increase probability of successful packet transmission, thereby reducing the latency. Typically, enhanced coding need more redundant bits, which means more power consumption. The compromise should be made between the reliability and the power consumption.

It should be noted that since the human body can be considered as a high-loss dielectric, the BAN channel should be accurately analyzed to infer the level of loss in different scenarios (e.g., link through/on/over the human body, shadowing, movement fading, etc.), thereby estimating the energy level at the reception. This is directly related to the SNR thus the BER. In addition, since BAN should coexist and operate with other devices in similar frequency bands (different BANs or other networks), the radio interference

level from other devices should also be considered at the reception level. If the interference and noise floor are high, the node needs to transmit at a higher power level to ensure a reliabe link [36]. Optimized transmission protocol and low power emission of the BAN device can reduce its interference to surrounding BAN users and other wireless systems.

Due to the diversity of applications in BAN, the QoS framework should be flexible so that it can be dynamically configured to meet application requirements without unduly reducing system performance [6].

Safety

In BAN, there is another major factor affecting the power consumption settings – human safety under radio exposure. The human body exposed to electromagnetic fields will absorb the radiation energy, which may consequently lead to tissue temperature rise. It should be noted that a prolonged temperature rise within the human tissues may result in tissue damage and blood flow reduction in certain sensitive organs [7]. As the operating environment of BAN is in the vicinity or inside the human body, the radiation power of these devices should be within a safe level to protect the human tissues.

The absorption effect of the human body varies with both the human tissue characteristics and the frequency of the applied field. Exposure to low-frequency electromagnetic fields normally results in negligible energy absorption and no measurable temperature rise in the body. However, exposure to electromagnetic fields at frequencies above about 100 kHz can lead to significant absorption of energy and temperature increases.

Hence, there is a need to apply specifications to the emission power of devices in BAN, which is the SAR (Specific Absorption Rate) – the power absorbed per mass of the human tissues measured in W/kg. It is usually averaged either over the whole body, or over a small sample volume (typically 1 g or 10 g of tissue). Typically, SAR in near field of the antenna depends mainly on the magnetic field while in far field it depends essentially on the electric field [13]. Different regions of the world have different SAR regulations, e.g., for local exposure (head), the SAR value in USA is limited at 1.6W/kg in 1 g [63] and in Europe 2W/kg in 10 g [64]. These specifications consequently limit the transmit power of the devices, which is less than 1.6 mW in USA and less than 20 mW in Europe [3].

Security

Because in medical domain, the transmitted information is typically patient's health parameters that they do not want to share, the data security becomes a top priority in the BAN applications. When data are transmitted over a wireless channel, such as the on-body to off-body communication, they are susceptible to eavesdropping, identity threats, medical information misuse and medical fraud [34, 35]. According to [65], a deadly dose of insulin can be injected by maliciously hacking the patient's insulin pump. Also, a pacemaker can be hacked to deliver deadly electrical shock to cause cardiac arrest. In these cases, it is critical to have strict laws and regulations to ensure patient's security and protect the data privacy. All the wireless medical sensors must meet such requirements and ensure data integrity and authentication. Due to the power limitation in BAN, typical security mechanisms proposed for other communication networks cannot be used in BAN. For this reason, more resource efficient and lightweight security protocols are required for such communication standards [7, 65].

Since BAN has a very large number of applicaitons, both medical and non-medical, multi-level security is required so that each application can choose the level that best suits its needs. For example camera pill may not require a strong encryption and authentication process. However, pacemakers may need a strong authentication process [14].

1.6 Frequency Regulations for BAN

For BAN, there are different requirements for frequencies due to different operating environment, such as in/on body or air channels. The available frequencies for BAN radio in different countries are regulated by the local communication authorities. Since some BAN devices are expected to be globally portable, such as hearing aids, it is desirable to allocate worldwidely the frequencies [6]. The TG6 has formed and operated a Regulatory Subcommittee that has been investigating and collecting information on the available frequencies in [66]. Figure 1.10 shows some of the potential frequencies for BAN and the corresponding regions [3, 19, 67].

The Medical Implant Communications Service (MICS) band is a licensed band created in 1999 by the U.S. Federal Communications Commission (FCC) for implant communication. For this specification, most countries have the

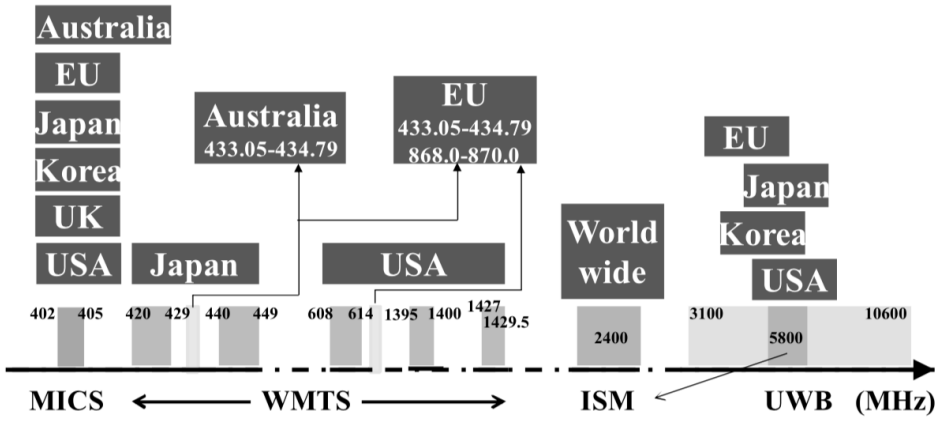

Figure 1.10: BAN frequency bands allocation [3]

same band range of 401 - 406 MHz, which has better capability to penetrate the human tissues than higher frequencies [7]. In USA, the MICS is superseded in 2009 by another specification Medical Device Radiocommunications Service (MedRadio), and in 2011, the band range of MedRadio was further expended to various narrow bands in 400 - 500 MHz [68].

The Wireless Medical Telemetry Services (WMTS) is a licensed band for remote monitoring of a patient's health, such as the on-body to off-body communication scenario mentioned in section 1.1.3. For example, a wireless cardiac monitors that can be used to monitor a patient after surgery can use the WMTS standard. Similar to the MedRadio band, only authorized healthcare providers are eligible to operate the WMTS device and that only within a healthcare facility. Furthermore, the use of WMTS has not been internationally recognized, thus many devices cannot be marketed or used freely in countries outside the USA. Due to the relatively narrow bandwidth (hundreds of kHz [7]) of the signal channel, neither MICS nor WMTS supports high data rate applications [3].

Contrarily, the Industrial, Scientific and Medical (ISM) band can support high data rate applications and is available worldwide. However, many wireless systems including Wi-Fi, Bluetooth, and ZigBee operate in the ISM band (2.4 GHz), thus this band has a high probability to face interferences.

In addition, a 21 MHz-centred Human Body Communication (HBC) band is defined in the BAN standard [2] for communication using the human body

as a transmission channel.

1.7 Dedicated BAN Standard (IEEE 802.15.6)

There are already some commercial short-range communication standards available, such as Bluetooth, ZigBee. However, these standards apply to general purpose sensor network applications, so they are not optimum for medical applications [36].

The IEEE 802.15.6 standard [2], established by the TG6 in February 2012, defines the PHY and MAC layers optimized for short-range transmissions in, on, or around the human body. Its purpose is to support low complexity, low cost, ultra-low power, and highly reliable wireless communications for use near or inside the human body (but not limited to humans) to meet a variety of both medical and non-medical applications.

It has been agreed that it is difficult to use a single PHY layer to meet all the requirements for BAN. Therefore, TG6 has proposed three different alternatives, namely Narrow Band (NB) PHY, Ultra Wide Band (UWB) PHY, and Human Body Communication (HBC) PHY. The NB PHY is centered at different frequencies and uses one of the following narrow bands: 402 - 405 MHz (MICS), 420 - 450 MHz, 863 - 870 MHz, 902 - 928 MHz, 950 - 956 MHz, 2360 - 2400 MHz, and 2400 - 2483.5 MHz (2.5 GHz ISM). The UWB PHY uses 3200 - 4700 MHz and 6200 – 10200 MHz for applications requiring high data rate up to 10 Mbps or more, with a bandwidth about 500 MHz [69]. The HBC PHY is centered at 21 MHz and is an innovative approach that uses the human body as a transmission medium to transfer healthcare data. Most of the energy will be confined to the human body surface with little energy radiated into the surrounding environment [70]. This provides great energy efficiency, high data security, and low interference. The maximum data rate of the HBC can reach up to 1.3125 Mb/s as specified in the BAN standard [2]. More details of the HBC will be discussed in the section 1.10.1. For each of the above communication approaches, the IEEE 802.15.6 standard defines the type of the data packet organization, the modulation scheme, the symbol and data rate, etc.

In terms of emission power, for NB PHY, when operating in a low power low duty cycle mode, at the center frequency of 403.65 MHz, a transmitter should be capable of transmitting at most -40 dBm (0.1 μW) effective isotropic radiated power (EIRP) (subclause 8.3 of ETSI EN 301 839-

1). When operating in the normal mode in the 402 MHz to 405 MHz frequency band, a transmitter shall be capable of transmitting at most -16 dBm (25 μW) EIRP. When operating in all other frequency bands of NB PHY, a transmitter shall be capable of transmitting at -10 dBm (0.1 mW) EIRP and the maximum radiated transmission power should be less than 0 dBm (1 mW) [7]. As for UWB applications, the power spectrum density (PSD) is limited by FCC in USA and ETSI (European Telecommunications Standards Institute) in Europe at -41.3 dBm/MHz (75 nW/MHz) in order to reduce the interference to other wireless systems operating in the same spectrum [71,72]. For the HBC PHY, since only the electrodes are currently specified in the standard to excit the human surface propagation, the electric field strength produced by an HBC electrode radiating in free space, measured at 30 m, should not exceed 30 μW/m [2].

The receiver sensitivity level is also specified in the BAN standard [2]. For the NB PHY, a -95 dBm level at the receiver input is proven to be capable of ensuring a 75.9 Kb/s data rate transmission for the 402-405 MHz MICS band, and a -92 dBm level can ensure a 121.4 Kb/s data rate for the 2400 - 2483.5 MHz ISM band. For the UWB PHY, a -91 dBm level at the receiver can achieve a 394.8 Kb/s data rate. As for the HBC PHY, with the same noise configuration as the NB PHY, a -97.35 dBm level at the input of the receiver can realize a 164.1 Kb/s data rate.

There is only one single MAC layer for all the PHY layers to control channel access, which means the MAC layer is flexible and combine different access techniques. In order to ensure high level security, the standard defines three security levels in the MAC layer: level 0 - unsecured communication, level 1 - authentication only, and level 2 - both authentication and encryption so that each application can choose its security level according to its requirement.

1.8 Compatible BAN Standards

As mentioned in section 1.1.1, BAN is an ultra short-range network (within three meters from the human body). In order to extend its communication range to achieve a communication with external nodes such as gateways or control units, or between different BAN users, it should incorporate other networks such as Bluetooth (IEEE 802.15.1), ZigBee (IEEE 802.15.4), Wi-Fi (IEEE 802.11), or even mobile cellular network. Standardization of these

technologies enables interoperability and a seamless user experience [6]. In this section, we will detail some of the existing BAN-compatible wireless technologies.

1.8.1 IEEE 802.15.1 standard (Bluetooth)

Bluetooth [73] or the IEEE 802.15.1 standard, commonly referred to as PAN (Personal Area Network), is designed as a short-range and high-security wireless communication standard. A typical connection of Bluetooth is Piconet, which is established by a master device with up to seven other slave devices. Devices in a Piconet can synchronize and simultaneously communicate with each other through the master node.

Due to the limited number of devices in the Piconet, the physical size of Bluetooth network is relatively small. Although the basic Bluetooth protocol does not support relaying, the network can be extended with Scatternet technique. A Scatternet is a combination of several different Piconets, where a Piconet node (master or slave) can choose to participate as a slave into another Piconet [15,33]. This technique enhances Bluetooth's scalability and extends its the coverage, which is very useful for the medical applications of BAN in large care centers.

Bluetooth devices operate in the 2.4 GHz ISM band. The entire bandwidth of Bluetooth is divided into 79 subchannels of 1 MHz. Using the frequency-hopping spread spectrum method [74], the interference, jamming and interception can be significantly reduced. Typically, Bluetooth covers from 1 to 100 m (the latest Bluetooth version 5.0 can reach a range of approximately 300 m) with transmission power ranging from 0 dBm to 20 dBm and data rate up to 3 Mb/s [33].

It is worth noting that a divided version of Bluetooth - Bluetooth Low Power (Bluetooth LP) - was first mentioned in [75] in 2004 and released into Bluetooth 4.0 in 2010, specifically for medical and fitness applications. Compared to the classic Bluetooth technique, Bluetooth LP delivers considerably lower power consumption and a slightly reduced data rate (up to 2 Mb/s) while maintaining similar coverage. In addition, the latency term in this release has also been significantly improved. These features are more suitable for the on-body to off-body communication in medical BAN applications, especially for critical vital signs monitoring and emergency alarming.

1.8.2 IEEE 802.15.4 standard (Zigbee)

ZigBee or IEEE 802.15.4 standard, is another PAN ad-hoc network specification particularly designed for small wireless medical sensors and home automation that require low data rate, long battery life, and secure networking [33]. The most significant advantage of ZigBee is its low power consumption.

ZigBee is highly optimized for low duty cycle operation of sensing devices (i.e., the sensor can turn off the radio most of the time). This is in contrast to Bluetooth, in which a slave device needs to keep synchronization with the master device, resulting in longer radio-on time and hence much higher average power consumption [6].

A ZigBee network basically consists of three parts: coordinator, router and end device. The coordinator is the most powerful part of ZigBee, which initially starts the communication system, bridges with other networks, and manages security functions. In medical applications, the end devices are the sensor nodes that collect vital data from the human body. The collected information is communicated between the end devices through the routers. In most cases, the end devices are in sleep mode. They are only woken up when data collection or transmission is required. The mechanism allows the system to consume less power therefore have a long operating lifespan (expanding battery life for years) [76].

ZigBee devices operate in the following frequency bands: 868 MHz (Europe), 915 MHz (Americas and Australia), and 2.4 GHz (Worldwide ISM). Because ZigBee is an ultra-low power network, it is more susceptible to interference from other existing wireless networks, especially in the crowded 2.4 GHz band with Bluetooth and Wi-Fi. Moreover, its low transmit power, typically between -25 dBm and 0 dBm [77], limits its data rate (250 Kb/s maximum) as well as its coverage (10 - 100 m). It may not be suitable for real-time and large-scale BAN applications. However, it is suitable for personal use, such as assisted living, health monitoring, sports, etc [15].

1.8.3 IEEE 802.11 standard (Wi-Fi)

Wi-Fi or IEEE 802.11 standard is known as Wireless Local Area Network (WLAN) and its range is larger than PAN. Generally Wi-Fi technology operates in ISM bands 2.4 and 5 GHz with a coverage of 100 meters. Wi-Fi allows users to transfer data at broadband speed (up to 1 Gb/s) when connected to

an access point or in ad hoc mode. It is ideal for large data transmissions, providing high-speed wireless connectivity and allowing video conferencing, voice calls and video streaming. It is very convenient because it is integrated into all smart phones, tablets, and laptops. The disadvantage of Wi-Fi is its high energy consumption. The transmit power is typically between 15 dBm and 20 dBm [15, 77].

1.9 BAN On-body Antennas

To date, most medical sensors used are wearable and mounted on the human body. The key component to ensure wireless communication of these sensors is the antenna. BAN antenna design should consider many specifications, such as size, efficiency, gain, etc. In general, it is complicated to provide high gain and high efficiency in a conventional antenna with a limited volume [78]. Moreover, large bandwidth is usually needed for high data rate requirement [79], which is also limited by the size of the antenna. Furthermore, the impact of human body on the antenna should be taken into account in the design procedure. Various on-body antennas have been designed in recent research works (figure 1.11). Table 1.6 gives some of the dimensions and gains for different on-body antennas.

In recent literature, many researchers have focused their antenna design on wearable textile antennas because of their good flexibility and comfortable integration with the garments. Textile antennas are printed antennas that typically use flexible commercial tissue (e.g., denim, coton woven fabric, fleece etc.) as the substrate material rather than conventional hard dielectric sheets. Electrotexile (e.g., ShieldIt^{TM} super) is commonly used for the conductive part of the antennas due to its great flexibility. The textiles have more insertion loss, but their flexibility simplifies the integration of antenna with the clothes [85]. Although they are less effiient, their gain is sufficient to establish appropriate short range and high data rate communications for BAN [85]. In recent research, various designs of textile-based antennas for body-centric communication were studied in different frequency bands (e.g., 800 MHz, 2.45 GHz, 60 GHz, etc).

Patch antennas are typically chosen for on-body to off-body communication because their main radiation is perpendicular to the human body surface. In addition, their ground plane minimizes radiation toward the human body, making the body's impact on antenna characteristics almost negligi-

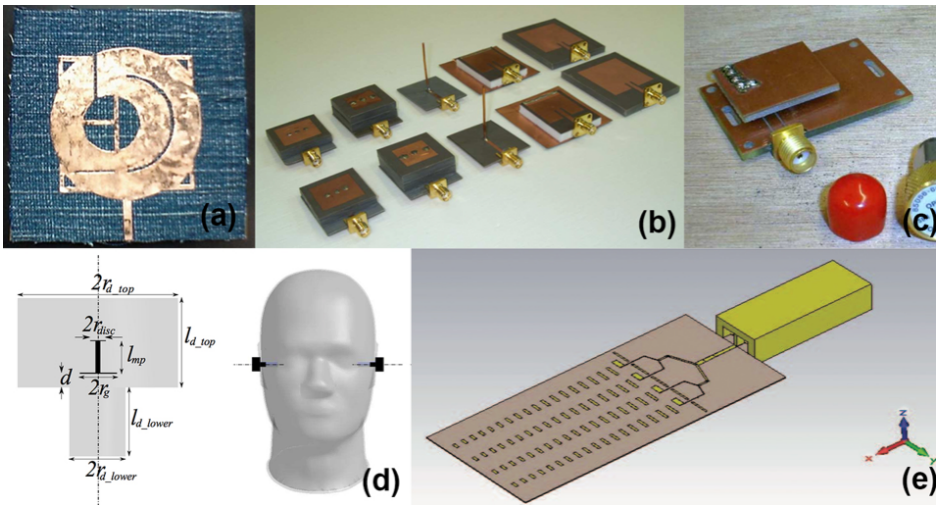

Figure 1.11: On-body antennas for BAN (a) Blue jean textile antenna [80] (b) Patch antennas [81] (c) PIFA [82] (d) Monopole embedded in dielectric element [83] (e) Printed Yagi antenna [84]

ble [85–88]. The bandwidth of a patch antenna is proportionally dependent on the thickness between the patch element and the ground plane. Therefore, the thickness of the substrate affects the antenna's bandwidth as well as its size and flexibility. In order to give users better comfort, the antennas should be made as small and thin as possible. If the patch antenna is reduced to a sticker thickness (several hundred micrometers), its operating bandwidth drastically decreases. If antennas without ground plane such as plannar monopole antennas are used, the matching bandwidth widens but the human body effect becomes important and should be considered into the design [89, 90].

Some methods for increasing the bandwidth of patch antenna, such as corner truncation or slotting technique, are introduced in [80, 86] for BAN. A method of minimizing radiation perpendicular to the human body surfaceand increasing the tangential pattern by feeding the patch in a higher mode is proposed in [81]. This allows patch antennas to realize equally on-body to on-body communication. EBG (Electromagnetic Band-Gap) material can be used as high impedance surface between the on-body antenna and the body to further reduce radiation to the human body for safety reasons [91].

Antenna type	Frequency (GHz)	Thickness (mm)	Surface (mm^2)	On-body gain (dBi)
Double substrate layers UWB Loop antenna [79]	3.1 - 5.1	15	25 × 24	5
Higher Mode Microstrip Patch Antenna (HMMPA-5) [81]	2.45	5.75	37 × 30	1.2
Funtamental mode fed Microstrip Patch Antenna (MPA-F) [81]	2.45	5	60 × 50	6.2
Into-the-ear (ITE) monopole embedded in dielectric using HBC [83]	2.45	19.5	10 (radius)	-47.2 (S21)
Into-the-channel (ITC) monopole embedded in dielectric using HBC [83]	2.45	11	3.5 (radius)	-91.7 (S21)
Printed Yagi antenna [84]	60	0.127	32.6 × 15	17
Coton woven textile-based patch-array antenna [85]	60	0.44	20 × 5.15	8
Blue jeans textile antenna [86]	5.2	1.1	44 × 44	5.91
Aperture-coupled multilayer textile patch antenna [87]	2.45	3.71	61.6 × 49	8
Flexibale foam-based textile patch antenna [88]	2.45	3.94	50 × 46	6.99
UWB Monopole [89]	3.1 - 10.6	1.6	32 × 22	≈ 1.5
Dual-band coplanar patch antenna on EBG (Electromagnetic Band-Gap) material [91]	2.45 / 5.8	4.48	120 × 120	6.4 / 7.6
End-fire textile-based Yagi antenna [92]	60	0.2	26 × 8	11.9

Table 1.6: Dimension and gain for different on-body antennas

Other types of on-body antennas are also reported in the literature. Monopoles are often used for on-body to on-body communication and the on-body channel analysis in low microwave bands. A monopole antenna embedded in a dielectric component can reduce significantly its size [83]. Printed Yagi array antennas, including textile-based [92] and conventional dielectric substrate based [84], can also be used for on-body to on-body communication at higher frequency bands such as millimeter waves. Yagi array antenna could have low thickness, high directivity, and large bandwidth [84]. Since

the main radiation beam is tangential to the body surface, the coupling between body-worn devices is maximized, giving a relative high gain and low pass loss in the communication. It should be noted that since such antennas are very directive, they are sensitive to body movements, where beam tilt could cause dramatic drops in QoS.

1.10 Motivation and Objectives

1.10.1 Skin-confined on-body propagation analysis

For long-term and continuous medical monitoring, it is desirable to use sticker-type sensors placed on the human body to enhance patient comfort. However, the complexity of the communication environment near the human body makes it difficult to establish wireless on-body communications in this configuration. Effects such as body-antenna interactions, high pass loss, human motion shadowing effects, should be carefully taken into account.

Interaction body-antenna

The human body is an extremely challenging environment for the operation of wireless communications systems, which behaves as a lossy medium at microwaves and millimeter waves. As sensors are worn close to the human body, the antenna used for data transmission is typically sensitive to antenna-body interaction effects, including near-field coupling, radiation pattern distortion, and shifts in input impedance, which may degrade their efficiency and reduce the reliability of transmission [85,93–95]. These effects vary between different antennas, ground plane dimensions, and separation distances from the human body. Some body-antenna interaction studies can be found in the current literature [89, 92, 96]. For example, in [92], a textile-based Yagi antenna was designed for on-body to on-body communications. The measured antenna efficiency dropped from 78% in free space to 48% on the skin-equivalent phantom. Since people change continuously their types of physical activities, the antenna performance is further influenced by the human body movement (e.g., shadowing, small-scale fading, etc.) [11].

Therefore, it is very important that the antenna characteristics are not disturbed by the human body. As a consequence, a human body model should be considered during the antenna design procedures. Antennas for

BAN should be specifically designed to operate in a body-centric environment and handle the issues resulting therein, such as propagation through and around the body. A good body-centric channel propagation analysis and a great comprehension of the electromagnetic field distributions in close proximity of the human body are very important for antenna design in BAN.

In order to illustrate the effect of body-antenna interaction, we performed some simulations with CST microwave studio® to depict the human body influence on a coplanar monopole antenna at 2.4 GHz and 60 GHz, with or without the human body model (a planar multilayer structure composed with skin, fat, and muscle tissues, of thicknesses 1 mm, 13 mm, and 6 mm, respectively) as shown in figure 1.12. The human body model is further discussed in chapter 2. In the simulations, the monopole antenna touches the skin to mimic, for instance, a sticker that can be confortably worn by a patient, and the dimensions of the monopoles are shown in table 1.7. In addition, complex dielectric constants of human tissues are considered in the simulations [97].

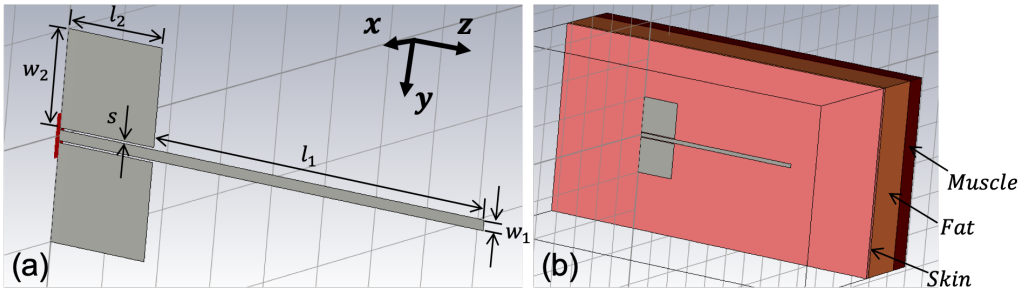

Figure 1.12: Coplanar monopole antenna at 2.4 GHz (a) in free space model and (b) with lossy human body model

Frequency (GHz)	l_1 (mm)	w_1 (mm)	l_2 (mm)	w_2 (mm)	s (mm)
2.4	35	1	10	9.3	0.2
60	1.32	0.04	0.5	0.47	0.01

Table 1.7: Dimensions of the monopole antennas

As shown in figure 1.13, at 2.4 GHz, the maximum gain of the monopole antenna attached to the human body model drops significantly from 2.07 dB

to -11.4 dB compared to the monopole antenna in free space, and the far field form changes completely. Moreover, the maximum gain direction in the simulation is toward the human body. Due to the dielectric loss of the human tissues, great changes in input impedance and S11 reflection parameters were also observed in the simulations (figure 1.14).

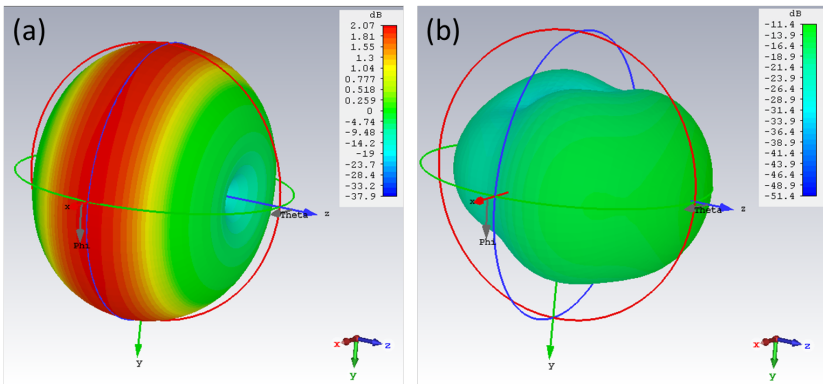

Figure 1.13: Far field of the coplanar monopole antenna (a) in free space and (b) with lossy body model at 2.4 GHz

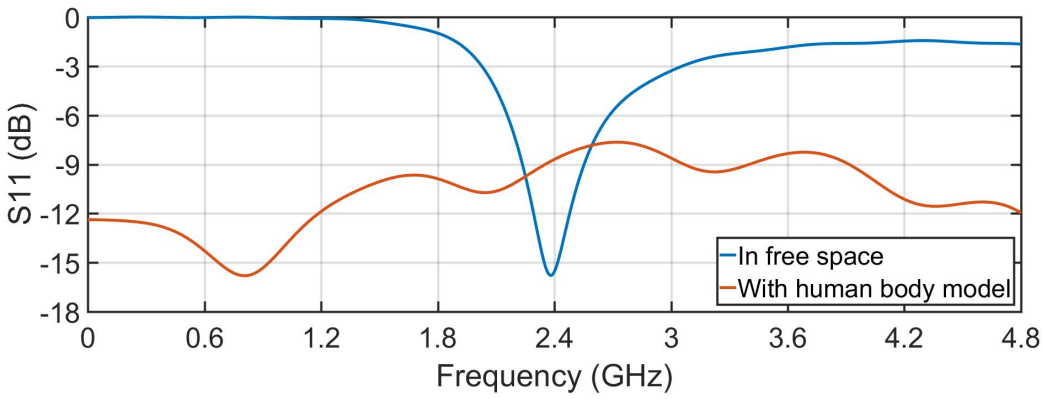

Figure 1.14: S11 parameters of the coplanar monopole antenna in free space and with lossy body model at 2.4 GHz

Since the wavelength of 60 GHz is much smaller than 2.4 GHz, the radiation of the 60 GHz antenna is more sensitive to the distance between the

antenna and the human body. Therefore, with the 60 GHz monopole design, different distances between the antenna and the human body model were considered, from 10 mm to 1 mm, in the simulations. Distortion of radiation pattern at different distances was observed as shown in figure 1.15. When the monopole approaches the human body, the maximum gain increases due to the reflection of the body surface and is found toward the outside of the human body in various directions according to the distance between the antenna and the human body. As the antenna touches the human body, there is no longer reflection from the body surface and most of the radiated energy is absorbed by the human body, so the maximum gain in this case drops dramatically. Consequently, similar to the 2.4 GHz antenna simulation results, changes in the input impedance and shifts of the S11 parameters was observed, as shown in figure 1.16. Additional simulations at other frequencies such as 8 GHz and 28 GHz, showed similar results and demonstrate that the body effect is a factor that cannot be ignored in the on-body antenna design for BAN.

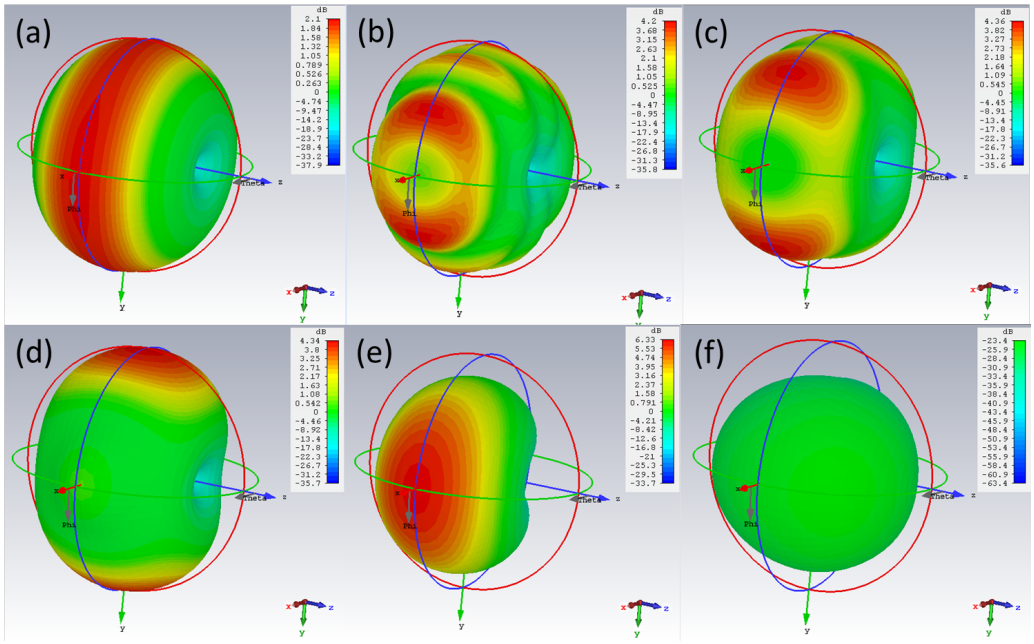

Figure 1.15: Far field at 60 GHz of the coplanar monopole antenna (a) In free space (b) 10 mm (c) 5 mm (d) 3 mm (e) 1 mm (f) 0 mm from lossy body model

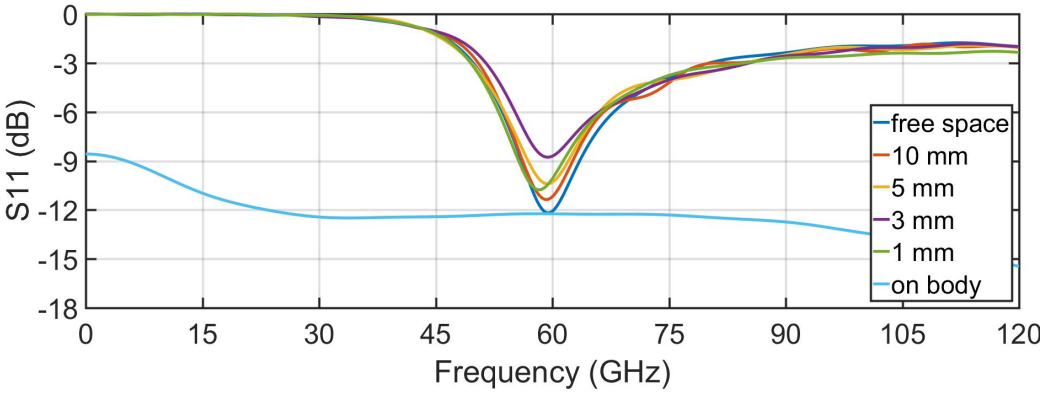

Figure 1.16: S11 parameters of the coplanar monopole antenna in different distances from the human body model at 60 GHz

Indeed, as described in section 1.9, the body-antenna interaction can be eliminated by adding a ground plane between them, but at the expense of reducing the antenna operation bandwidth. Therefore, it is very important to investigate the on-body propagation to understand how these electromagnetic fields induced in the human body adversely affect the antenna characteristics, so that the near-body antenna can be better designed. From another point of view, as we have seen, when an ungrounded sticker-type antenna is placed in direct contact with the human body, its radiation-to-air performance drops drastically, and most of the energy is absorbed by the body. In this case, it could be great to directly use the human body as a communication support for such antennas (rather launchers in this case), instead of radiating the signal into the air. Thus, an on-body propagation analysis can be very helpful in understanding how to excite an appropriate propagating wave into the human body.

Characterization of on-body propagation

The human body is considered to be a promising innovative transmission channel for BAN in HBC (Human Body Communication), which means that the body becomes an integral component of the wireless system. HBC typically uses low frequencies from a few hundreds hertz to hundreds of kilohertz [70]. There is no need to use antennas to radiate the signal into the air. Instead, electrodes are necessary. In HBC, the body surface-confined

transmission restricts the off-body detection, thereby increasing the system security. In addition, with less energy leakage into air, the transmission is more power-efficient and the interference between BAN users is considerably reduced.

There are usually two principal methods in the current literature to implement the HBC: capacitive coupling and galvanic coupling [70] (see figure 1.17). The transmitter and receiver are composed with two electrodes to induce electrical signals into the human body.

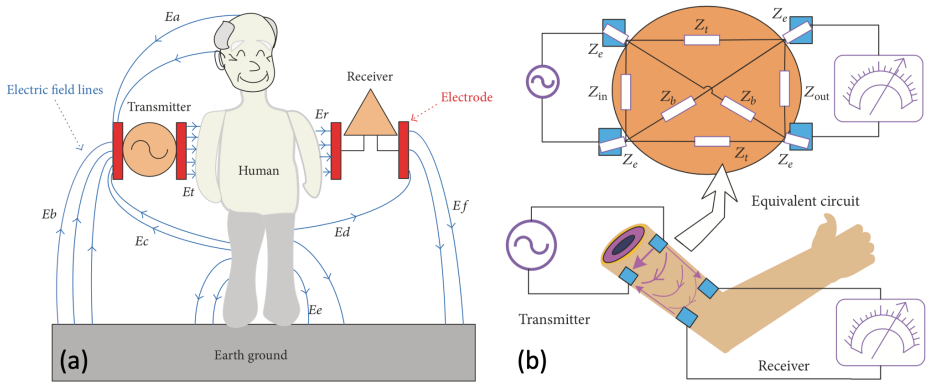

Figure 1.17: HBC transmission models (a) capacitive coupling (b) galvanic coupling [70]

For the capacitive coupling method, first proposed by Zimmerman, the induced electrical signal is controlled by electrical potential [98]. In both transmitter and receiver, one signal electrode is attached to the human skin while the other ground electrode floats in the air. The electrode excitaiton induces electric fields, which is the basis of the signal transmission mechanism [98] (figure 1.17(a)). In particular, the electrodes attached to the skin create a forward path through the human body (E_t and E_r in figure 1.17(a)) while the floating electrodes are coupled to the ground through the air and form a return path (E_b and E_f in figure 1.17(a)), thus closing the communication loop. The ground plane plays a very important role in guiding the return electrical field path, so that the ground plane is a necessary condition for this modeling. Because of the presence of an external path through the ground, the detected signal is unstable and highly influenced by the surrounding environment, which may result in communication disruption in certain

situations (e.g., user standing on insulated media) [98]. In this implementation, the electrical field is perpendicular to the human body surface and leak away from the body.

For the galvanic coupling method [99], the electrical signal is controlled by current flow. Compared to the capacitive coupling, no ground plane is needed in the modeling. In the transmitter and receiver, both electrodes are directly attached to the human skin. The couple of electrodes of the transmitter generate a primary alternative ionic current flow through their different electrical potentials (figure 1.17(b)). A small secondary current flow is induced into the conductive human body. A potential difference is then induced between the two electrodes of the receiver. In this configuration, the electrical fields are parallel and well confined to the human body surface, so this coupling is less sensitive to the surrounding environment. In the current literature, on-body communications using galvanic technique have been experimented and showed a coverage ranging from 10 cm (transmit power: -3 dBm, data rate: 255 Kb/s, modulation: BPSK [100]) to 40 cm (transmit power: -21 dBm, data rate: 0.9 Kb/s, modulation: PWM [101]).

Since the galvanic coupling method is based on the current flow in the ionic fluid of human tissues, very low frequencies (typically less than 1 MHz) are required for such mechanism [70]. As for the capacitive coupling method, in order to avoid the human body radiating as an antenna ($\lambda/2$ dipole around 1 m), the operation frequencies also need to be configured low (usually less than 150 MHz). Consequently, the transmission mechanism is in the quasi-static domain and is analyzed with equivalent electronic circuit models. However, the low frequency limits the operation bandwidth, which further limits the transmission data rate. For example, in the work of [3], measurements of in-body channel in the 13.5 MHz ISM band are realized to reliably transmit one bit to signal an emergency condition. Moreover, the traditional HBCs, especially the capacitive coupling implementation, are not well confined to the human body, so the signal may be easily detected, leading to secure issues [102]. Therefore, it is necessary to investigate whether on-body communications can be achieved at higher frequencies to realize higher data rate, more reliable, and more secure wireless communications. Moreover, wide bandwidth enables using Impulse Radio (IR) schemes such as On-Off-Keying (OOK) modulations (considered in the IEEE 802.15.6 standard), which exhibit low-duty cycle and therefore consume very little.

To date, propagation at few GHz between on-body sensors have been mostly studied as a space wave interacting with human tissues using either

Sommerfeld integral-based theory [103, 104] for flat part of the human body, or creeping wave formulation [105, 106] for curved parts. The confinement of on-body surface-waves inside the human skin has not been paid much interest. One can cite the work in [107], where authors used Transverse Resonance Method (TRM) to determinate the wave propagation in the multilayered human tissues, but no physical insights have been given and the studied band covered only up to 11.5 GHz.

Thesis objective I

From the two previous points of view, in order to better understand the electromagnetic interaction between the human body and the nearby antennas, and to check whether the human body can be used as a transmisison media at high frequencies between the on-body sensors, the on-body propagation is analytically studied up to 60 GHz in this thesis. As the human body can be considered as a multilayer structure composed of different tissues, and the outer skin tissue has a much higher permitivity than air and its surrounding fat tissue [97], our idea is to use human skin as a transmission media like a fiber optic cable, unlike the traditional static HBC mechanism. Therefore, our first objective in this thesis is to establish an appropriate human body model to analyze the propagation of surface-waves confined in the human skin, such as dispersion, attenuation, propagation modes, electromagnetic field distribution, surface impedance, etc, to determine whether this skin-confined propagation mechanism can be used for on-body communication at high frequencies, as well as how the surface-wave may be confined in the human skin, in order to provide more secure wireless communications than the traditional HBC.

1.10.2 Enhanced angular-scanning leaky-wave antenna design for Doppler radar detection

The first objective of this thesis led to a dispersive analysis that will also be used to address the second objective described in the following sub-sections.

Need of enhanced scanning capability radars for non-sensor medical monitoring

Although medical on-body sensors are becoming more and more seamless for patients, it can still be a discomfort in some situations as mentioned in section 1.4 (e.g., skin troubles for long-term monitoring, burn patient, etc). Placing on-body sensors on patients is also a costly and time-consuming task in hospitals. Therefore, whenever possible, sensor-less non-contact monitoring is an attractive technique. Several prototypes that use radars for breathing and heart rate detection as well as elderly fall detection are presented in current literature, such as under-bed sensor monitoring [108], where ultra-sensitive accelerometers are used to capture the vibrations upon the bed caused by a subject's heart rate, respiration and body movement. However, this is difficult to monitor for people standing in the room or even sitting on the bed. Other camera-based technique is also presented in [109] by measuring changes in face color of a person due to heart beat, but the accuracy and reliability of this approach need to be improved, and in any case will lead to acceptability issues for the people to be monitored.

Another promising method for the breathing and heart rate detection is to use Doppler radar mentioned in section 1.4. Because the accuracy of a sensor can deteriorate rapidly with distance when in a noisy or cluttered environment, highly directive antennas are required for the radars [49]. In addition, the beam-steering function can help the system to find the correct direction of the target person, thereby avoiding the environment noise relative to an omnidirectional antenna [48].

Leaky-wave antenna is a good candidate for Doppler medical radar because it has high directivity / high gain and its direction of radiation changes according to the operating frequency, leading to beam-steering capabilities with no need to physically move the antennas. In addition, compared to the phased arrays, this beam-steering technique is much simpler and less expensive. The beam scanning feature of leaky-wave antennas is very suitable for Doppler radar because they have a monochromatic operation.

Benefits of the 60 GHz band

In the current literature, different frequencies are used for Doppler radar to detect breathing and heartbeat rates. In [110], three different carrier frequencies of 5.8 GHz, 24 GHz, and 35 GHz are applied to the Doppler system. The

results show that higher frequencies can achieve higher breathing and heartbeat rates detection accuracy. Therefore, in [111], a 60 GHz Doppler radar is designed to detect weak heartbeat signals. Throughout the world, approximately 5 to 7 GHz bandwidth is available in the 60 GHz millimeter-wave band [69]. The propagation pathloss is higher than the microwave bands, which confines the detection range of a radar using this band. However, the range is still sufficient for indoor applications. In addition, the short-range operation at 60 GHz can reduces interference to surrounding devices and provides more secure communication [112, 113]. This allows a larger number of users to be collocated in a certain area. The radio wavelength at 60 GHz in free space is 5 mm. Thus the use of 60 GHz can make the antenna small and directive, and improve the sensitivity of the Doppler radar to detect the body movements, which provides higher detection resolutions.

In terms of human safety, the penetration level of electromagnetic waves into the human body is quantified by a parameter called skin depth δ (corresponding to the power density of $1/e^2$ or 13.5% of that at the surface) [114]. When the human body is exposed to electromagnetic radiation, the electromagnetic waves decrease exponentially from the outer surface of the human tissue (skin). Therefore, the coupled electric current mainly flows within a certain depth of the surface of the human body. At 60 GHz, the skin depth of the human body is about 0.5 mm [114,115], which means that the internal organs of the human body are not affected by the radiation at 60 GHz.

The unlicensed 57 - 64 GHz band has been identified as a highly promising solution for future BAN [85]. As shown in figure 1.18, FCC has authorized the use of 57 - 64 GHz unlicensed band. In Europe, ETSI adopted a larger band from 57 to 66 GHz. Moreover, the 59 - 66 GHz band is available in Japan. There is a 5 GHz world wide available unlicensed band around 60 GHz [116]. To date, 60 GHz band is typically used for the exploitation of WiGig (IEEE 802.11ad) and high data rate wireless multimedia networks (IEEE 802.15.3d) [116], to offer multiple gigabits per second ultra-high data rate in short-range. However, some works have demonstrated its high potential in estimating heartbeat rate in a non-contact manner [56]. With respect to non-contact heartbeat detection performed at lower frequencies, millimeter-waves provide a stronger Doppler response and are therefore promising in terms of reliability and accuracy. Although the Ka-band has been proven to have good performance [117], the 60 GHz has a 7 GHz license-free bandwidth and, thanks to its large frequency scanning potential, offers unique degrees of freedom for large beam-scanning.

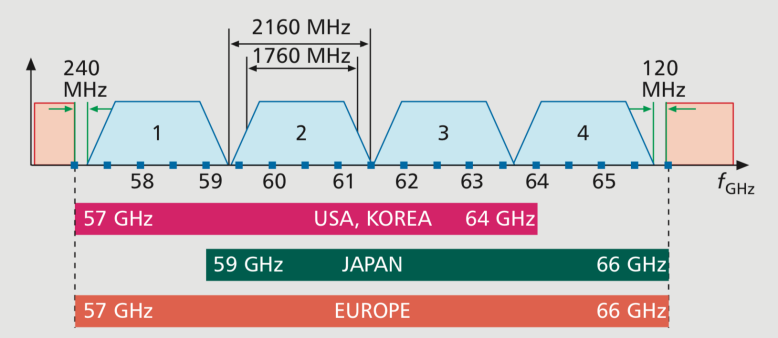

Figure 1.18: Globe unlicensed bands around 60 GHz and channelization of 802.15.3c [116]

Thesis objective II

For the above reasons, the second objective of this thesis focuses on the design of a leaky-wave antenna for 60 GHz Doppler radar detection. Since the direction of the beam is frequency controlled, it is important for a given frequency range specification to cover the whole area to be monitored. To do so, a metasurface is designed based on a dispersion analysis to enhance the angular-scanning capability of the leaky-wave antennas.

1.11 Thesis Outline

The core-work of this PhD dissertation is the dispersive analysis of multilayer structures, which leads to two contributions, as shown in figure 1.19, namely, a skin-confined propagation analysis, and the design of fast-scanning leaky-wave antennas.

The dispersion analysis uses the classical Transverse Resonance Method (TRM) that is presented in chapter 2 along with the study of the wave propagation properties within the human skin. The topology of the multilayer geometry that is used to model the human tissues is introduced using complex frequency dependent dielectric properties. Confinement capabilities as well as propagation losses are investigated for frequency up to 60 GHz, considering three different skin thicknesses, typically 0.5 mm, 1 mm, and 1.5 mm. The effects of the inner fat and muscle tissues on the propagation is also examined. Finally, a horizontal on-body dipole is simulated in the full-wave

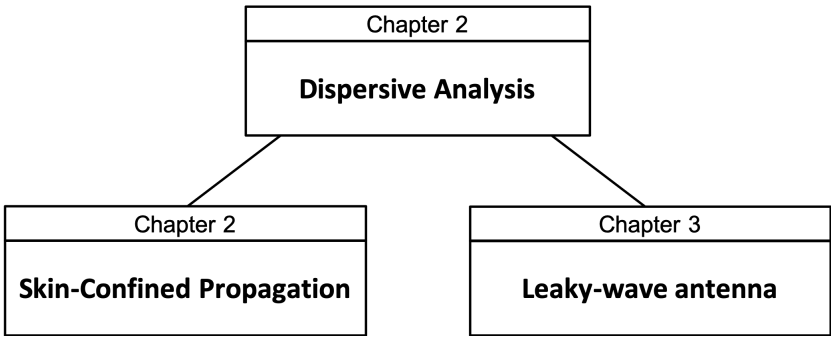

Figure 1.19: Thesis outline

simulation to assess the possibility to excite the skin-confined propagation mode.

The second objective related to the leaky-wave antenna is presented in the second part of this thesis in chapter 3. A state of the art on the leaky-wave antennas is introduced, and the original approach to design enhanced-scanning leaky-wave antennas by using metasurface is then detailed. The performance of the leaky-wave antennas with and without metasurface are compared in full-wave simulations. A coplanar-fed surface-wave launcher is further designed to efficiently excite the scanning-enhanced leaky-wave antenna.

Chapter 2

Skin-Confined On-Body Propagation Analysis

2.1 Introduction

As illustrated in section 1.10.1, in the frequency band centered at 21 MHz, the human body is considered to be the transmission channel for human body communication (HBC) in the BAN standard. Capacitive coupling and galvanic coupling methods are commonly considered as transmission mechanisms. HBCs restrict the off-body detection, which increases system security. In addition, signal collisions between BAN users can be greatly eliminated due to less energy leakage into the air, providing more reliable and efficient communication. However, the HBC proposed in BAN standard exhibits low data rates (1.3 Mb/s) [2], and robust electrode design is still an open issue.

At higher frequency bands for on-body communication scenarios, creeping waves have been studied in recent researches [105, 106, 118] and have demonstrated that such waves propagate along the body surface between sensor nodes. However, while higher frequencies allow for larger bandwidth and thus higher data rates, it also increases power consumption. Nevertheless, UWB combined with on-off-keying (OOK) modulations (considered in 802.15.6 standard) can significantly reduce the energy consumption by achieving a low duty cycle of the transceiver [119]. Creeping waves enable on-body communication even when body shadowing occurs, but do not ensure strong confinement around the body, especially at lower frequencies, e.g., 400 - 800 MHz or 2.45 GHz. Therefore, this chapter investigates the

possibility of establishing on-body communications within the human skin in order to ensure a high level of security.

Whatever the communication mechanism, it is essential to characterize the propagation channel to assess the performance of the wireless network. Good channel characterizations help optimize communication design by minimizing emission power while maintaining reliable throughput, enhancing power efficiency and battery life. Since the BAN is in close proximity to the human body, a human body model should be considered in the modeling of the entire channel to take into account the influence of the human body on the propagation. A good understanding of the field distribution of the on-body propagation is also important for antennas designed on the human body since the interaction of the human-antenna depends on the propagation on the human body.

2.2 On-Body Propagation Channel Modeling Methods

There are basically three methods for characterizing the on-body propagation channels: measurements, numerical simulations, and analytical calculations.

Measurements can be used to characterize the path loss of specific models and scenarios, using real people [96, 120–122] or experimental phantoms [81, 123, 124]. The phantoms are artificial models that simulate the electromagnetic properties of biological tissues, which is also used for dosimetry and body-antenna interaction analysis [125, 126]. The statistical formula of the channel model can be deduced from the measurement results. In most of researches, such as the channel modeling subgroup of TG6 [13], the semi-empirical Friis formula expressed in dB is used for path loss description as a function of the distance d, taking into account the shadowing effects from the human body produced by body movement and posture:

$$PL(d) = PL_0 + 10n \log_{10}\left(\frac{d}{d_0}\right) + S \tag{2-1}$$

where PL_0 is the path loss for the reference distance d_0, n the path loss exponent depending on the propagation environment (e.g., in free space, n is equal to 2), and S the shadowing statistical coefficient, which is typically a zero-mean Gaussian variable. The coefficients in the formula vary with

different locations according to the human body, the separation distance between the antenna and the human body, the different person's body shapes, etc. The statistical approach can also model dynamic scenarios when people are in movement [127]. However, the Friis formula is a general expression, which is regardless of the mode of propagation. Because communications are performed around actual human bodies, measurement-based methods may be limited by human safety concerns [6]. Moreover, the measurements are usually based on one or a few persons. The lack of sampling makes it difficult to generalize accurate human body channel estimation. Also, the dynamic environment due to the body movements further complicates the validation of the models. Typically, the empirical measurements are expensive, time consuming and difficult to repeat [128].

The on-body propagation can also be studied by full-wave numerical simulations with complete human body models and usually with FDTD (Finite Difference Time Domain) simulator or commercial softwares [96, 128–130]. However, when the frequency becomes higher, the relatively small wavelength compared to the human body model requires a finer mesh solution, and the complexity of human tissues structure results in a very large computational problem (e.g., long simulation time, memory consuming, etc). Therefore, a simpler model that considers the human tissues as a flat multilayer geometry was applied in [131], which was capable of determining discrete propagation modes that can be supported by such a structure. Flat geometries have been shown to be valid enough in the case of on-body communications using Norton theory for instance [132]. At high operating frequencies such as 60 GHz channel, the curvature radius of some human body parties (e.g. arms or legs) becomes large compared to the wavelength. Therefore, a local flat approximation (optical approximation) can be quite accurate. However, both statistical measurements and the numerical simulations lack a clear explanation for the physics of the propagation mechanism.

The theoretical analysis of on-body propagation is to solve the funtamental electromagnetic equations (e.g., Maxwell's equations, wave equations, dyadic Green's function, etc.) of the propagation for specific models configurated with boudary value problems or to use transverse resonance method (TRM) [107, 133–135]. This provides a more detailed description of the human body channel, such as propagation modes, electromagnetic field distribution etc. Compared to numerical simulations, the calculation time can be significantly reduced if some analytical formulas can be established. As mentioned in the section 1.10.1, propagation between on-body sensors have

been mostly studied using either Sommerfeld integral-based theory for flat part of the human body, or creeping wave formulation for curved parts. The confinement of on-body surface-waves inside the human skin has not been paid much interest.

In our work, we will propose a semi-analytical channel modeling method for skin-confined on-body propagation up to 60 GHz. This method will not use large computational power and outlines a simple and accurate assessment of the human body propagation channel.

2.3 Propagation Modes

In a given waveguide with specified boundary value configurations, many propagation modes can exist that satisfy the wave equations. Existing modes may depend on the geometry of the guide, the characteristics of the composed guiding material, and the frequency. Basically, the propagation modes can be classified into the following three types:

- Transverse ElectroMagnetic (TEM) modes, where neither electric nor magnetic field exists in the direction of propagation, i.e., the electromagnetic fields are contained in a local plane (usually referred as equiphase plane), which is always normal to the direction of propagation;
- Transverse Electric (TE) modes, where the electric field at each point is only in the transverse direction of the guide. No electric field is in the direction of propagation;
- Transverse Magnetic (TM) modes, similar to the TE modes, but only the magnetic field is in the transverse direction of the guide and no magnetic field is in the direction of propagation.

Assume a general planar lossless waveguide with a 2D lateral section as shown in figure 2.1. The dimension along the z-axis is considered infinite and the direction of propagation is only supposed to be along the positive z-axis. Thus, only the wave having a propagation factor $e^{-j\beta z}$ is taken into account here (β being the propagation constant).

In order to simplify the model and calculation, the dimension in the y-axis is also considered infinite and no field variation is considered in the y

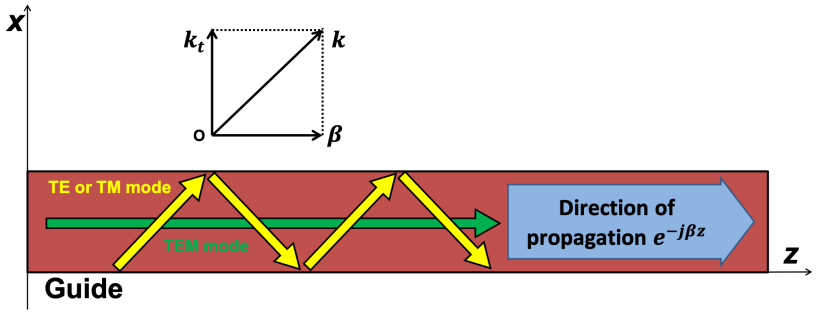

Figure 2.1: General planar lossless wave guide and the different propagation modes

direction ($\partial/\partial y$=0). The intrinsic wavenumber of a propagating wave k in a lossless media is determined as

$$k = \omega\sqrt{\varepsilon\mu} \tag{2-2}$$

where ω represents the angular frequency, ε and μ the permittivity and permeability of the medium, respectively. Thus, as indicated by the arrows in figure 2.1, the intrinsic wave vector $\boldsymbol{k}$ of a propagating wave can be decomposed into a component $\boldsymbol{k_t}$ in the transverse direction (in our case just along the x-axis since no variation is supposed in the y-axis direction) and the component $\boldsymbol{\beta}$ in the direction of propagation (z-axis) with the following formula for their wavenumber:

$$k^2 = \beta^2 + k_t^2 \tag{2-3}$$

For the TEM mode, as shown by the green arrow in figure 2.1, the wave vector $\boldsymbol{k}$ is aligned to the mode propagation direction (z-axis), thus the transverse component $\boldsymbol{k_t}$ is zero [136] and the propagation constant β is equal to the intrinsic wavenumber k. For the TE and TM modes, the wave bounces between the top and the bottom boundaries of the guide (yellow arrows in figure 2.1), creating a transversely stationary wave inside the guide. The wave vector $\boldsymbol{k}$ is not directed along the propagation direction, so the two components $\boldsymbol{\beta}$ and $\boldsymbol{k_t}$ are both non-zero elements.

For a given frequency, the transverse component of a propagating mode is a fixed spatial function of the cross-sectional geometry of the guide. Since the wavenumber is a known quantity (2-2), if we know k_t, we can easily

determine the propagation constant of the guide. In section 2.6, a technique called Transverse Resonance Method (TRM) will be introduced to estimate the k_t quantity.

It should be noted that, in the case where dielectric loss is present, the dielectric constant ε becomes complex (see the following section 2.4).

2.4 Human Body Modeling

The human body is partially conductive and consists of tissues of different dielectric constants, thicknesses, and thus characteristic impedance. The human body for on-body communications can be modeled as a planar multilayered structure composed of skin, fat, and muscle from the outer layer to the inner layer (figure 2.2). This is a classic approximate human body model used in several papers such as [107].

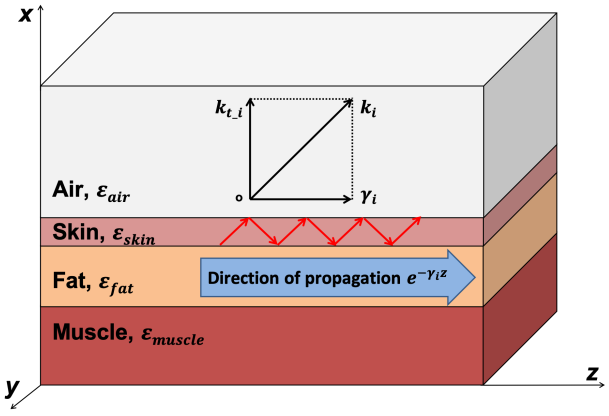

Figure 2.2: Multilayered human body modeling

In order to take into account the dielectric loss, the tissues are characterized by a complex permittivity

$$\varepsilon = \varepsilon_0 \varepsilon_r = \varepsilon_0 (\varepsilon_r^{'} - j\varepsilon_r^{''}) \tag{2-4}$$

where ε_0 is the vacuum permittivity (8.854×10^{-12} F/m), and ε_r is the complex relative body tissue permittivity. If we refer to the source-free Maxwell-Ampere equation

$$\nabla \times \boldsymbol{H} = j\omega\varepsilon \boldsymbol{E} \tag{2-5}$$

and use the complex permittivity form

$$\begin{aligned} \nabla \times \boldsymbol{H} &= j\omega\varepsilon\boldsymbol{E} \\ &= j\omega\varepsilon_0(\varepsilon_r^{'} - j\varepsilon_r^{''})\boldsymbol{E} \\ &= j\omega\varepsilon_0\varepsilon_r^{'}\boldsymbol{E} + \omega\varepsilon_0\varepsilon_r^{''}\boldsymbol{E} \\ &= j\omega\varepsilon_0\varepsilon_r^{'}\boldsymbol{E} + \sigma\boldsymbol{E} \end{aligned} \tag{2-6}$$

where $\sigma = \omega\varepsilon_0\varepsilon_r^{''}$ is the effective conductivity (S/m) at a considered angular frequency ω and the "$\sigma\mathbf{E}$" component is the effective current density (A/m^2) which causes dissipated power of the propagating waves. When a person is exposed to alternating fields, the effective conductivities σ of human tissues exhibit very high values, resulting in a relatively high current density, thereby producing a tissue heating effect. This is the main mechanism for the selective heating of human tissue in tumor therapy [137, 138]. At the same time, the tissue heating consumes considerable energy, especially when the frequency gets high, which is the main cause of propagation loss in human tissues (also known as dielectric loss). The complex relative permittivity values for skin, fat, muscle, and other human tissues can be found in [97], with frequencies ranging from 10 Hz up to 100 GHz. The value of the complex permittivity of human tissue depends on the frequency.

The dielectric loss can also be expressed in form of electric loss tangent at the given frequency

$$\tan\delta = \frac{\sigma}{\omega\varepsilon_0\varepsilon_r^{'}} = \frac{\varepsilon_r^{''}}{\varepsilon_r^{'}} \tag{2-7}$$

The $\tan\delta$ is usually commercially used in the classification of materials, i.e., if $\tan\delta \ll 1$, the material is seen as a dielectric (insulator); Contrarily, if $\tan\delta \gg 1$, the material is considered as a conductor.

As the permittivity is complex, the intrinsic wavenumber in a human tissue becomes also complex, as well as its transverse and guiding-direction components. Since the relative permeability of human tissue is equal to one, the complex intrinsic wavenumber of each layer k_i, at a given frequency, is now determined as

$$k_i = j\omega\sqrt{\varepsilon_i(\omega)\mu_0} \tag{2-8}$$

where ω and μ_0 represent the angular frequency and the vacuum permeability (12.57×10^{-7} H/m) respectively, and $\varepsilon_i(\omega)$ is the frequency-dependent complex permittivity of the tissue "i" (i.e. skin, fat, muscle) or air. The

relation in (2-3) consequently becomes

$$k_i^2 = \gamma_i^2 + k_{t\_i}^2 \tag{2-9}$$

where γ_i and k_{t_i} are respectively the corresponding complex transverse and propagation components of the layer "i".

In this case, the propagation constant component $j\beta$ in the propagation convention should be replaced by the complex form $\gamma = \alpha + j\beta$ (figure 2.2), where the additional α represents the attenuation constant.

2.5 Total Reflection and Critical Angle : Skin-Confined Propagation Mechanism

Before stepping into the analysis of the propagation along the human body model, it is interesting to introduce the mechanism of the skin-confined on-body propagation.

For two lossless media with the same permeability μ, there is an oblique angle θ_c with respect to the normal of the interface between the two media, called the critical angle, which allows total reflection when a plane wave arrives on the interface with an incident angle equal to or greater than θ_c. This effect occurs only when the wave propagates from a denser media 1 to a less dense media 2, i.e., $\varepsilon_1 > \varepsilon_2$.

As shown in figure 2.3, assuming a TE polarized wave (i.e., the electric field is only in the y-axis direction) propagates from the media 1 to the media 2 with an oblique incident angle θ_i. The angles θ_i, θ_r, and θ_t are respectively the incident, reflected, and transmitted wave angles relative to the normal of the interface. These three angles follow the Snell's law of refraction

$$\theta_r = \theta_i \tag{2-10}$$

$$\beta_1 \sin\theta_i = \beta_2 \sin\theta_t \tag{2-11}$$

where β_1 and β_2 are the intrinsic wavenumbers of the two lossless media

$$\beta_i = \omega\sqrt{\mu_i\varepsilon_i} \quad (i = 1, 2) \tag{2-12}$$

The critical angle is given in [139] as

$$\theta_c = \sin^{-1}\left(\sqrt{\frac{\mu_2\varepsilon_2}{\mu_1\varepsilon_1}}\right) \tag{2-13}$$

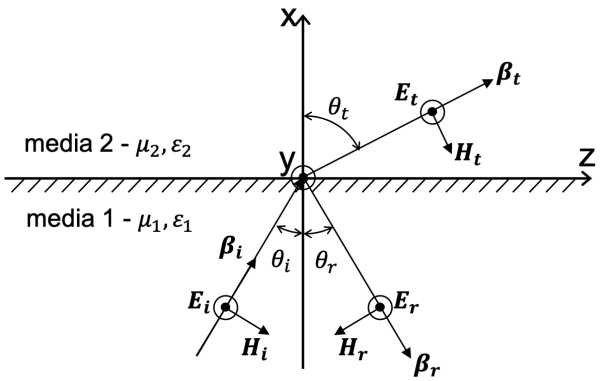

Figure 2.3: TE polarized mode projected at an oblique angle on an interface between two lossless media ($\varepsilon_1 > \varepsilon_2$)

We can see from (2-11) that when $\theta_i = \theta_c$, the transmission angle θ_t is

$$\theta_t = \sin^{-1}\left(\frac{\beta_1}{\beta_2}\sin\theta_i\right) = \sin^{-1}\left(\sqrt{\frac{\mu_1\varepsilon_1}{\mu_2\varepsilon_2}}\sqrt{\frac{\mu_2\varepsilon_2}{\mu_1\varepsilon_1}}\right) = \sin^{-1}(1) = 90^\circ \quad (2\text{-}14)$$

which means the transmitted wave propagates along the interface between the two media.

The electromagnetic fields of the incident, reflected, transmitted waves can be expressed as

$$\boldsymbol{E_i} = \hat{a}_y E_i e^{-j\boldsymbol{\beta}_i\cdot\mathbf{r}} = \hat{a}_y E_0 e^{-j\beta_1(x\cos\theta_i + z\sin\theta_i)} \quad (2\text{-}15)$$

$$\begin{aligned}\boldsymbol{H_i} &= (-\hat{a}_x\sin\theta_i + \hat{a}_z\cos\theta_i)\, H_i e^{-j\boldsymbol{\beta}_i\cdot\mathbf{r}} \\ &= (-\hat{a}_x\sin\theta_i + \hat{a}_z\cos\theta_i)\,\frac{E_0}{\eta_1} e^{-j\beta_1(x\cos\theta_i + z\sin\theta_i)} \quad (2\text{-}16)\end{aligned}$$

$$\boldsymbol{E_r} = \hat{a}_y E_r e^{-j\boldsymbol{\beta}_r\cdot\mathbf{r}} = \hat{a}_y \Gamma E_0 e^{-j\beta_1(-x\cos\theta_r + z\sin\theta_r)} \quad (2\text{-}17)$$

$$\begin{aligned}\boldsymbol{H_r} &= (-\hat{a}_x\sin\theta_r - \hat{a}_z\cos\theta_r)\, H_r e^{-j\boldsymbol{\beta}_r\cdot\mathbf{r}} \\ &= (-\hat{a}_x\sin\theta_r - \hat{a}_z\cos\theta_r)\,\frac{\Gamma E_0}{\eta_1} e^{-j\beta_1(-x\cos\theta_r + z\sin\theta_r)} \quad (2\text{-}18)\end{aligned}$$

$$\boldsymbol{E_t} = \hat{a}_y E_t e^{-j\boldsymbol{\beta}_t\cdot\mathbf{r}} = \hat{a}_y T E_0 e^{-j\beta_2(x\cos\theta_t + z\sin\theta_t)} \quad (2\text{-}19)$$

$$\begin{aligned}\boldsymbol{H_t} &= (-\hat{a}_x\sin\theta_t + \hat{a}_z\cos\theta_t)\, H_t e^{-j\boldsymbol{\beta}_t\cdot\mathbf{r}} \\ &= (-\hat{a}_x\sin\theta_t + \hat{a}_z\cos\theta_t)\,\frac{T E_0}{\eta_2} e^{-j\beta_2(x\cos\theta_t + z\sin\theta_t)} \quad (2\text{-}20)\end{aligned}$$

where η_1 and η_2 are the wave impedances of the media 1 and media 2, Γ and T are the reflection coefficient and the transmission coefficient respectively and are given in [139] as

$$\Gamma = \frac{\sqrt{\frac{\mu_2}{\varepsilon_2}}\cos\theta_i - \sqrt{\frac{\mu_1}{\varepsilon_1}}\cos\theta_t}{\sqrt{\frac{\mu_2}{\varepsilon_2}}\cos\theta_i + \sqrt{\frac{\mu_1}{\varepsilon_1}}\cos\theta_t} \tag{2-21}$$

$$T = \frac{2\sqrt{\frac{\mu_2}{\varepsilon_2}}\cos\theta_i}{\sqrt{\frac{\mu_2}{\varepsilon_2}}\cos\theta_i + \sqrt{\frac{\mu_1}{\varepsilon_1}}\cos\theta_t} \tag{2-22}$$

When $\theta_i = \theta_c$, since $\theta_t = 90°$, $\cos\theta_t$ in (2-21) and (2-22) is equal to zero, therefore the reflection and transmission coefficients reduce to

$$\Gamma = 1 \tag{2-23}$$

$$T = 2 \tag{2-24}$$

and the transmitted fields of (2-19) and (2-20) then reduce to

$$\boldsymbol{E_t} = \hat{a}_y 2E_0 e^{-j\beta_2 z} \tag{2-25}$$

$$\boldsymbol{H_t} = -\hat{a}_x \frac{2E_0}{\eta_2} e^{-j\beta_2 z} \tag{2-26}$$

It is apparent that the transmitted wave travels parallel to the interface along the positive z-axis direction and there is no variation in the transverse x-axis direction, creating a uniform plane surface-wave in the z-axis direction (figure 2.4 (a)). Therefore, even if the transmission coefficient in (2-24) is equal to 2, as the power flow direction of the transmitted fields is parallel to the interface, there is no transfer of real power across the interface in the normal direction with respective to the boundary [139].

When $\theta_i > \theta_c$, from the equation (2-14) of Snell's law of refraction, we can see that

$$\sin\theta_t|_{\theta_i > \theta_c} > 1 \tag{2-27}$$

which has no physically realizable angle θ_t (θ_t is a complex angle). In order to interpret this case, let us analyze again the transmitted electric field $\mathbf{E}_t$

in equation (2-19)

$$\begin{aligned}\boldsymbol{E_t}|_{\theta_i>\theta_c} &= \hat{a}_y T E_0 e^{-j\beta_2(x\cos\theta_t + z\sin\theta_t)} \\ &= \hat{a}_y T E_0 e^{-j\beta_2\left(x\sqrt{1-\sin^2\theta_t} + z\sin\theta_t\right)} \\ &= \hat{a}_y T E_0 e^{-j\beta_2 x\sqrt{1-\sin^2\theta_t}} e^{-j\beta_2 z\sin\theta_t}\end{aligned} \tag{2-28}$$

As in the case $\theta_i > \theta_c$, we have $\sin\theta_t > 1$ (equation (2-27)) and the $\sqrt{1-\sin^2\theta_t}$ component in (2-28) can be written as [139]

$$\sqrt{1-\sin^2\theta_t} = -j\sqrt{\sin^2\theta_t - 1} \tag{2-29}$$

and equation (2-28) reduces to

$$\begin{aligned}\boldsymbol{E_t}|_{\theta_i>\theta_c} &= \hat{a}_y T E_0 e^{-\beta_2 x\sqrt{\sin^2\theta_t - 1}} e^{-j\beta_2 z\sin\theta_t} \\ &= \hat{a}_y E_{eff} e^{-\alpha_{eff}x} e^{-j\beta_{eff}z}\end{aligned} \tag{2-30}$$

where

$$\alpha_{eff} = \beta_2\sqrt{\sin^2\theta_t - 1} \tag{2-31}$$

$$\beta_{eff} = \beta_2\sin\theta_t \tag{2-32}$$

Similarly, we obtained a transmitted wave that travels parallel to the surface between the two media with equi-phase planes parallel to the x-axis (figure 2.4 (b)). In addition, the wave exponentially decays in the positive x-axis direction (perpendicular to the interface) with the equi-amplitude planes parallel to the z-axis. The transmitted wave is tightly bound to the surface and forms a nonuniform surface-wave. It is important to note that at a given frequency and two given media, in the case of $\theta_i > \theta_c$, the larger the angle of incidence θ_i, the greater the value of the effective attenuation constant α_{eff} normal to the surface, which means the wave is more tightly confined to the surface.

The above analysis procedure can be repeated for the TM polarized propagation. However, the critical angle is not a function of polarization [139], the TM propagation mode has the same effect as the TE mode according to the critical angle. The critical angle is commonly used to design may practical instruments and transmission lines such as grounded dielectric slab waveguide, fiber optic cables etc.

Nevertheless, the human tissues are lossy media. As mentioned in section 2.4, to consider the dielectric loss in the previous analysis, we can simply

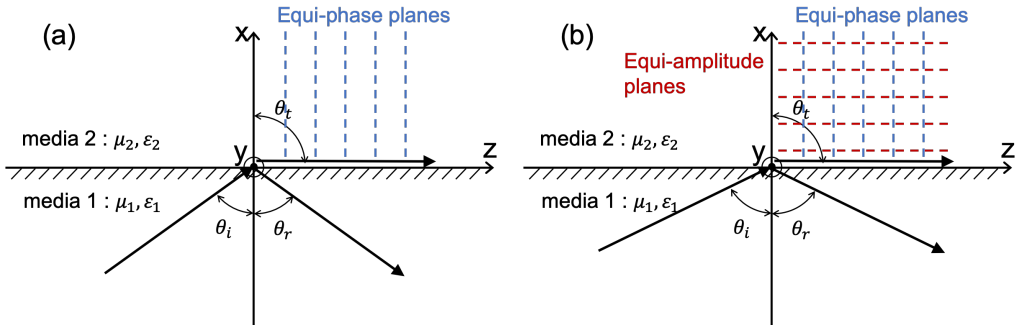

Figure 2.4: Equi-phase and equi-amplitude plane for (a) critical ($\theta_i = \theta_c$) and (b) above critical ($\theta_i > \theta_c$) incident angles

replace the lossless propagation constant component $j\beta$ by the lossy form $k = \alpha + j\beta$ and the Snell's law of refraction in equation (2-11) changes into

$$k_1 \sin\theta_i = k_2 \sin\theta_t \tag{2-33}$$

Let us assume that the wave travels from the skin layer to the air layer (figure 2.5(a)). Since the propagation modes (TE or TM) obey to the same principles in terms of critical angle, the transmitted electric field from skin to air can be expressed as

$$\boldsymbol{E_{t\_(skin/air)}} = \boldsymbol{E_{air}} e^{-k_{air}(x\cos\theta_t + z\sin\theta_t)} = \boldsymbol{E_{air}} e^{-j\beta_{air}(x\cos\theta_t + z\sin\theta_t)} \tag{2-34}$$

where, from equation (2-33)

$$\sin\theta_t = \frac{k_{skin}}{k_{air}} \sin\theta_i = \frac{\alpha_{skin} + j\beta_{skin}}{j\beta_{air}} \sin\theta_i \tag{2-35}$$

thereby

$$\cos\theta_t = \sqrt{1 - \sin^2\theta_t} = \sqrt{1 - \left(\frac{\alpha_{skin} + j\beta_{skin}}{j\beta_{air}} \sin\theta_i\right)^2} \tag{2-36}$$

It is obvious that $\sin\theta_t$ and $\cos\theta_t$ are now complex values.

In the case of $\theta_i > \theta_c$, similarly to (2-29), $\cos\theta_t$ can be written as

$$\cos\theta_t = \sqrt{1 - \sin^2\theta_t} = -j\sqrt{\left(\frac{\alpha_{skin} + j\beta_{skin}}{j\beta_{air}} \sin\theta_i\right)^2 - 1} \tag{2-37}$$

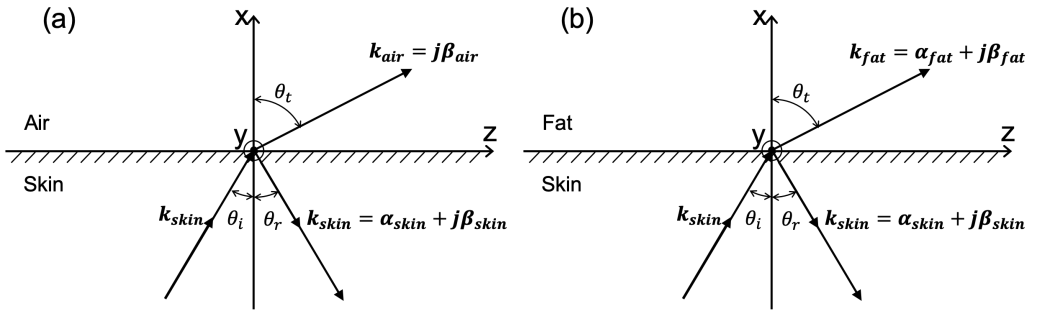

Figure 2.5: Obliquely projected wave (a) from skin to air (b) from skin to fat

Assuming the complex form of $\cos\theta_t$

$$\cos\theta_t = \rho e^{j\zeta} = \rho\left(\cos\zeta + j\sin\zeta\right) \tag{2-38}$$

equation (2-34) can be written as

$$\begin{aligned}
\boldsymbol{E_{t_(skin/air)}} &= \boldsymbol{E_{air}} e^{-j\beta_{air}\left(x\rho(\cos\zeta + j\sin\zeta) + z\frac{\alpha_{skin}+j\beta_{skin}}{j\beta_{air}}\sin\theta_i\right)} \\
&= \boldsymbol{E_{air}} e^{-j\beta_{air}x\rho(\cos\zeta+j\sin\zeta) - z(\alpha_{skin}+j\beta_{skin})\sin\theta_i} \\
&= \boldsymbol{E_{air}} e^{-j\beta_{air}x\rho\cos\zeta + \beta_{air}x\rho\sin\zeta - z\alpha_{skin}\sin\theta_i - j\beta_{skin}z\sin\theta_i} \\
&= \boldsymbol{E_{air}} e^{-(-\beta_{air}x\rho\sin\zeta + z\alpha_{skin}\sin\theta_i)} e^{-j(\beta_{air}x\rho\cos\zeta + \beta_{skin}z\sin\theta_i)} \\
&= \boldsymbol{E_{air}} e^{-\left(\alpha_{x_eff}x + \alpha_{z_eff}z\right)} e^{-j\left(\beta_{x_eff}x + \beta_{z_eff}z\right)}
\end{aligned} \tag{2-39}$$

where

$$\begin{aligned}
\alpha_{x_eff} &= -\beta_{air}\rho\sin\zeta \\
\alpha_{z_eff} &= \alpha_{skin}\sin\theta_i \\
\beta_{x_eff} &= \beta_{air}\rho\cos\zeta \\
\beta_{z_eff} &= \beta_{skin}\sin\theta_i
\end{aligned} \tag{2-40}$$

It is apparent that the transmitted wave is a non uniform plane wave and the effective attenuation and propagation constants are in the x-z plan and depend on the incident angle.

For the case where the wave travels from the skin layer to the fat layer (figure 2.5(b)), we can use the previous procedure again by changing k_{air} in

equation (2-34) to $k_{fat} = \alpha_{fat} + \beta_{fat}$. The transmitted electric field can be written in the same final form as equation (2-39)

$$\boldsymbol{E_{t\_(skin/fat)}} = \boldsymbol{E_{fat}} e^{-\left(\alpha_{x\_eff} x + \alpha_{z\_eff} z\right)} e^{-j\left(\beta_{x\_eff} x + \beta_{z\_eff} z\right)} \tag{2-41}$$

where

$$\begin{aligned} \alpha_{x\_eff} &= \alpha_{fat}\rho\cos\zeta - \beta_{fat}\rho\sin\zeta \\ \alpha_{z\_eff} &= \alpha_{skin}\sin\theta_i \\ \beta_{x\_eff} &= \alpha_{fat}\rho\sin\zeta + \beta_{fat}\rho\cos\zeta \\ \beta_{z\_eff} &= \beta_{skin}\sin\theta_i \end{aligned} \tag{2-42}$$

Compared to (2-40), in the x-axis direction, α_{x_eff} and β_{x_eff} both have one more term due to the dielectric loss in the fat layer. Using the formulas (2-39), (2-40), (2-41), and (2-42), the reflection and the transmission behavior of the lossy media interface such as the skin/air and the skin/fat interfaces can be analyzed.

Since the real part of skin's relative complex permittivity is greater than fat and air ($\mathrm{Re}(\varepsilon_{skin}) > \mathrm{Re}(\varepsilon_{fat}) > 1$) [97], the critical angle of the skin/fat interface $\theta_{c(skin/fat)}$ is greater than the skin/air interface $\theta_{c(skin/air)}$. If the oblique incident wave angle at the two interfaces in the skin layer is greater than the critical angle $\theta_{c(skin/fat)}$, the propagating wave will be completely reflected back to the skin and form nonuniform surface-waves at the outer layers of the two interfaces. If the wave propagating in the skin meet certain phase, amplitude, and boundary conditions, the skin can act as a waveguide similar to a fiber optic cable, which confines and guides the waves along the human body surface. The propagating waves bounce back and forth between the skin/air and the skin/fat interfaces inside the skin (red arrows in figure 2.2), thereby forms a standing wave in the transverse direction, while in the outer layers (air and fat), the wave forms an exponential transverse decay away from the surfaces. This is the main mechanism of the skin-confined on-body propagation.

In the total reflection condition ($\theta_i > \theta_c$), with dielectric losses added in the media (skin and fat layers), the direction of propagation of the transmitted wave (vector β_t) are no longer parallel to the surface (z-axis), but is inclined at an angle θ_β into the skin (i.e., θ_t greater than 90°) (figure 2.6). In addition, the direction of decay of the transmitted wave (vector α_t) are as well no longer along the surface normal (x-axis). The decay direction has an

angle θ_α relative to the normal of the x-axis, which represents the attenuation of the bound wave outward from the surface and the attenuation in the direction of the propagation.

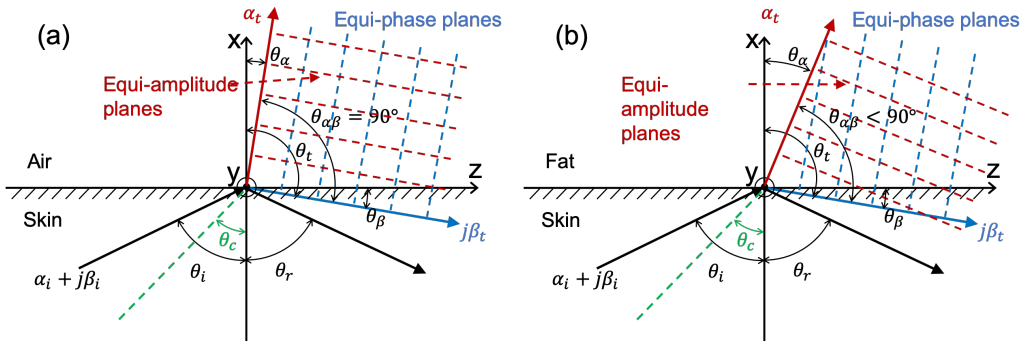

Figure 2.6: Oblique wave projected with an incident angle greater than the critical angle (a) from skin (lossy) to air (lossless) (b) from skin (lossy) to fat (lossy)

Tables 2.1 and 2.2 show the transmitted wave characteristics at 1 GHz and 10 GHz for the total reflection at the skin/air and skin/fat interfaces. The wave is obliquely projected from the skin layer and the angle of incidence is greater than the critical angle ($\theta_i > \theta_c$). The critical angles θ_c here were calculated without considering the tissue dielectric loss, i.e., 8.99° and 10.30° for the 1 GHz and 10 GHz skin/air interface, 21.39° and 22.55° for the skin/fat interface respectively. However, we have observed that the addition of the dielectric loss would reduce the critical angle. The attenuation constant value α_t and its direction angle θ_α relative to the surface normal (x-axis), the propagation constant value β_t and its direction angle θ_β relative to the surface (z-axis), as indicated in figure 2.6, are shown in the tables 2.1 and 2.2 for skin/air and skin/fat interfaces, respectively.

In table 2.1 for the skin/air interface, since the air is a lossless media, we found as expected that the direction of the attenuation constant α_t is always orthogonal to the direction of the propagation constant β_t and θ_α is always equal to θ_β. As the angle of incidence θ_i increases, α_t becomes exhibits a greater value and the direction is closer to the normal of the surface, thus the attenuation from the outward direction of the surface increases and the surface-waves are more tightly bound to the interface. However, the attenu-

θ_i Incident angle from skin	α_t transmitted wave attenuation constant [Np/m]	θ_α relative to x-axis	β_t transmitted wave propagation constant [rad/m]	θ_β relative to z-axis
1 GHz (relative permittivities $\varepsilon_{skin} = 40.94 - 16.17j$, $\varepsilon_{air} = 1$)				
20°	42.91	11.96°	47.75	11.96°
40°	86.98	11.08°	89.47	11.08°
60°	118.64	10.94°	120.48	10.94°
80°	135.38	10.90°	136.99	10.90°
10 GHz (relative permittivities: $\varepsilon_{skin} = 31.29 - 14.40j$, $\varepsilon_{air} = 1$)				
20°	368.37	14.15°	423.82	14.15°
40°	763.80	12.80°	792.03	12.80°
60°	1045.40	12.60°	1066.20	12.60°
80°	1194.00	12.54°	1212.20	12.54°

Table 2.1: Surface-wave on skin/air interface at 1 GHz and 10 GHz

θ_i Incident angle from skin	α_t transmitted wave attenuation constant [Np/m]	θ_α relative to x-axis	β_t transmitted wave propagation constant [rad/m]	θ_β relative to z-axis
1 GHz (relative permittivities: $\varepsilon_{skin} = 40.94 - 16.17j$, $\varepsilon_{fat} = 5.45 - 0.96j$)				
40°	74.91	12.89°	89.47	11.08°
60°	110.08	11.80°	120.46	10.89°
80°	127.93	11.55°	136.97	10.85°
10 GHz (relative permittivities: $\varepsilon_{skin} = 31.29 - 14.40j$, $\varepsilon_{fat} = 4.60 - 1.05j$)				
40°	650.91	15.07°	791.10	12.50°
60°	965.78	13.66°	1065.30	12.37°
80°	1124.80	13.33°	1211.40	12.36°

Table 2.2: Surface-wave on skin/fat interface at 1 GHz and 10 GHz

ation in the direction of propagation also increases as the angle of incidence increases. As for the propagation constant, the direction of propagation is closer to the surface as the angle of incidence increases and the propagation constant value β_t become closer to the intrinsic skin wavenumber. In addition, as the propagation constant along the surface become greater, the surface-wave becomes slower (phase velocity). When we shift the frequency from 1 GHz to 10 GHz, for a given angle of incidence, θ_α or θ_β does not change greatly (about 2° of difference). However, the attenuation and propagation constants increase massively, resulting in higher surface confinement and higher propagation decay along the surface, as well as slower phase velocities.

As for the skin/fat interface (table 2.2), we observed the same phenomenon as the skin/air surface-wave. The wave confinement is however weaker, which is due to the higher relative permittiviy of the fat compared to the air. It should be noted that the directions of α_t and β_t are no longer orthogonal in this case compared to the surface-wave at the skin/air interface (less than 90°).

Therefore, it can be seen from this section that when the incident wave in the skin layer satisfies the condition $\theta_i > \theta_{c(skin/fat)}$, the human skin is able to act as a dielectric-type waveguide. The confined propagating waves bounce between the skin/air and the skin/fat interfaces inside the skin, forming transverse standing waves while propagating along the skin layer. In the outer air and fat layers, the waves have an exponential decay away from these two interfaces, which avoids signal detection from nearby locations around the user, enhancing the data transmission security. It is also observed that the transverse decay in the fat layer is weaker than in the air layer, so the muscle next to the fat may affect the propagation depending on the thickness of the fat at different location in the human body. It has also been found that when losses are considered in the tissues, the transmitted surface-waves in the air and fat layers have propagation constant β_t that are directed back to the skin, rather than parallel to interface in the lossless case. This gives a first insight of the skin-confined surface-wave form and behaviors around the skin. Nevertheless, for a propagation mode to exist within the skin layer, a fixed incident angle is required to satisfy the equi-phase situations inside the "skin-guide" and the boundary conditions. The TRM will therefore be applied to propagation mode calculations to further investigate the skin-confined propagation in the following sections.

2.6 Transverse Resonance Method

The transverse resonance method (TRM) is commonly used to determine the propagation constant of waveguides, such as rectangular waveguide, dielectric slab guide etc, as well as traveling wave antennas.

Typically, the characteristics of a propagating wave in a waveguide are analyzed by solving homogeneous Maxwell's equations with a specified boundary configuration. The complete electromagnetic wave description inside the guide provides us a clear physical insight into the nature of the guiding structure. Although this method is powerful, the calculation work is enormous

when the guide becomes complex (e.g., a multilayer structure that causes a large number of simultaneously necessary boundary conditions), and this can be done only in a separable framework. If we are more interested in the propagation constant (such as the case of traveling wave antennas) or the dielectric losses in propagation, the TRM is a simpler and more straightforward manner to achieve the goal.

The transverse resonance procedure is based on the fact that in a waveguide, the fields form standing waves in the transverse direction of the guide [136]. Using the separation of variables, only the non-homogeneous transverse direction is analyzed with a standard equivalent transmission line. Guided-wave modes are represented by the resonant solutions of the transmission line.

To introduce this approach, let us assume the previous human body model (figure 2.7), whose cross section is defined in the xz-plane. Our purpose is to determine the different propagation modes that can exist inside this model. Again, to simplify the calculation, we initially consider the dimensions along y-axis and z-axis (direction of propagation) are of infinite length. In addition, the air and muscle layers are also supposed infinite in the positive x-axis direction and the negative x-axis direction, respectively. As mentioned in

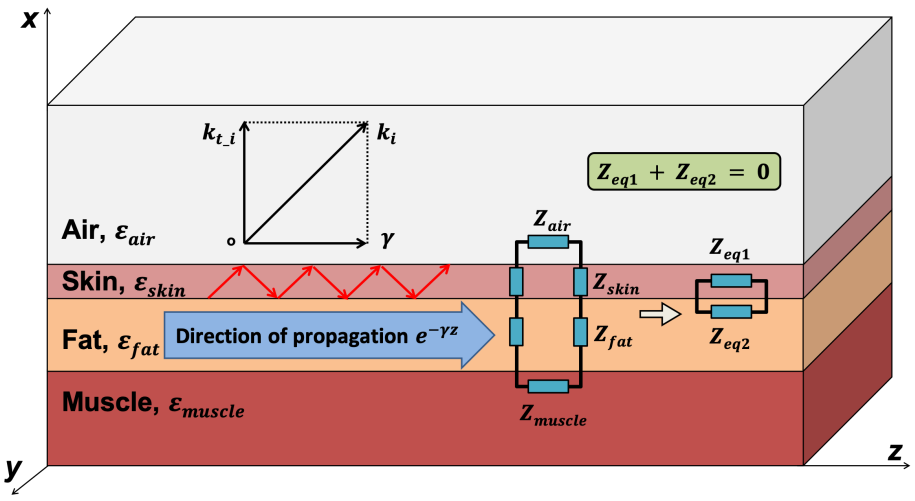

Figure 2.7: Transverse resonance method for the human body modeling

section 2.5, the propagating waves are confined in the skin layer, bouncing back and forth between the upper (skin/air) and lower (skin/fat) interfaces, thereby forming a standing wave in the transverse direction (x-axis). In the outer layers (air and fat), the waves form an exponential transverse decay away from the surfaces.

The cross section is thus modeled as a connection of two transmission lines (one for the skin layer and the other for the fat layer), as well as two loads representing the infinite air and muscle media, with the respective characteristic wave impedances Z_{air}, Z_{skin}, Z_{fat}, and Z_{muscle} (figure 2.7). One condition of a such resonant transmission line is that, at any point of the line, the sum of the input impedances seen looking to either side must be zero. Let us consider the observed point is at the interface between the skin layer and the fat layer. The characteristic input impedances at the observed point seen looking toward the upper side Z_{eq1} and toward the lower side Z_{eq2} can be calculated with transmission line theory as

$$\begin{aligned} Z_{eq1} &= Z_{skin}\frac{Z_{air} + Z_{skin}\tanh\left(k_{t\_skin}d_{skin}\right)}{Z_{skin} + Z_{air}\tanh\left(k_{t\_skin}d_{skin}\right)} \\ Z_{eq2} &= Z_{fat}\frac{Z_{muscle} + Z_{fat}\tanh\left(k_{t\_fat}d_{fat}\right)}{Z_{fat} + Z_{muscle}\tanh\left(k_{t\_fat}d_{fat}\right)} \end{aligned} \tag{2-43}$$

where k_{t_skin} and k_{t_fat} represent the transverse propagation component of the skin and fat layers respectively, d_{skin} and d_{fat} the thicknesses of the skin and fat layers respectively. Therefore, to satisfy the transverse resonance condition, we should verify

$$Z_{eq1} + Z_{eq2} = 0 \tag{2-44}$$

This condition follows from the boundary conditions that require continuous tangential components of the electromagnetic fields at the boundary interfaces between different layers [139].

In addition, to satisfy the boundary condition, the propagation component γ must be identical in all the layers. So we can deduce the transverse wavenumber k_{t_i} of each layer "i" using the relation (2-9) with the same γ and the corresponding complex intrinsic wavenumber k_i. It will be illustrated in the following section 2.7 that the characteristic impedance of the transverse transmission line of i-layer is also a function of the transverse wavenumber k_{t_i}. Consequently, γ becomes the only complex unknown in the transverse resonance equation and is found numerically.

It should be noted that, although the muscle layer has a greater real part of permittivity than skin [97], the muscle layer is considered infinite in the transverse direction. Therefore, the propagating waves will not be confined in the muscle layer but mostly confined in the skin.

2.7 Transverse Impedance of Different Propagation Modes

The wave impedance of a waveguide depends on the propagation mode. Considering a general source-free lossless waveguide as defined in figure 2.1, and a time-harmonic $e^{j\omega t}$ condition, Maxwell's equations can be written as

$$\nabla \times \boldsymbol{E} = -j\omega\mu\boldsymbol{H} \tag{2-45}$$

$$\nabla \times \boldsymbol{H} = j\omega\varepsilon\boldsymbol{E} \tag{2-46}$$

With the $e^{-j\beta z}$ propagation dependence along the z-axis, the scalar x-, y-, and z-components of (2-45) and (2-46) can be reduced into the following forms:

$$\frac{\partial E_z}{\partial y} + j\beta E_y = -j\omega\mu H_x \tag{2-47}$$

$$-j\beta E_x - \frac{\partial E_z}{\partial x} = -j\omega\mu H_y \tag{2-48}$$

$$\frac{\partial E_y}{\partial x} - \frac{\partial E_x}{\partial y} = -j\omega\mu H_z \tag{2-49}$$

$$\frac{\partial H_z}{\partial y} + j\beta H_y = j\omega\varepsilon E_x \tag{2-50}$$

$$-j\beta H_x - \frac{\partial Hz}{\partial x} = j\omega\varepsilon E_y \tag{2-51}$$

$$\frac{\partial Hy}{\partial x} - \frac{\partial Hx}{\partial y} = j\omega\varepsilon E_z \tag{2-52}$$

The impedance along the direction of propagation (z-axis) are defined as

$$Z = E_x/H_y \tag{2-53}$$

or

$$Z = -E_y/H_x \tag{2-54}$$

For each propagation mode, the definition is different for the six above equations from (2-47) to (2-52). For the TEM mode, we have $E_z = 0$ and $H_z = 0$. For the TE mode, we have $E_z = 0$ and $H_z \neq 0$. And finally for the TM mode, the condition $E_z \neq 0$ and $H_z = 0$ should be satisfied.

Therefore, the expressions to obtain the wave impedance Z depend on the nature of the considered mode. For example, assuming $E_z = 0$ and $H_z = 0$, we can deduce the impedance for the TEM mode from the equation 2-48 using the formula 2-53:

$$Z_{TEM} = \frac{\omega\mu}{\beta} \tag{2-55}$$

Assuming $E_z = 0$ and $H_z \neq 0$, we can also deduce the impedance for TE mode from the equation 2-48:

$$Z_{TE} = \frac{\omega\mu}{\beta} \tag{2-56}$$

The impedance formulas are the same for TEM and TE modes. Assuming $E_z \neq 0$ and $H_z = 0$, we can deduce the impedance for the TM mode from the equation 2-50:

$$Z_{TM} = \frac{\beta}{\omega\varepsilon} \tag{2-57}$$

For the transverse resonance technique, the transverse wavenumbers k_{t_i} are considered, and thus the wave impedances used as the characteristic impedances of the transmission lines are determined by using k_{t_i} instead of β in equations (2-55) to (2-57).

It is to be noted that the transverse component of the z-directional TEM mode is zero ($\beta = k$), so the transverse impedance for the TEM modes is infinite. However, the TEM mode does not satisfy the boundary conditions of the human body model [139].

For the impedance of the TE and TM modes, we can deduce the following formulas in the lossless case:

$$Z_{t\_lossless\_TE} = \frac{\omega\mu}{k_{t\_i}} \tag{2-58}$$

$$Z_{t\_lossless\_TM} = \frac{k_{t\_i}}{\omega\varepsilon} \tag{2-59}$$

In the lossy case, according to [136, 139], the transverse characteristic wave impedances become

$$Z_{t\_lossy\_TE} = \frac{j\omega\mu}{k_{t\_i}} \tag{2-60}$$

$$Z_{t\_lossy\_TM} = \frac{k_{t\_i}}{j\omega\varepsilon} \tag{2-61}$$

2.8 Skin-Confined Propagation Calculation

In this section, the calculation of the skin-confined propagation is divided into two parts based on the propagation mode (TE or TM).

As illustrated in section 2.6, the propagation component γ should be identical in all the layers to satisfy the boundary conditions, thus the transverse component k_{t_i} in each layer can be calculated with the equation (2-9) as

$$k_{t\_i} = \pm\sqrt{k_i^2 - \gamma^2} \tag{2-62}$$

The sign of k_{t_i} in each layer should be carefully chosen to satisfy the transverse standing wave condition in the skin layer and the exponential transverse decay condition in the layers closely around the skin. In our case, according to the choice of the propagation and transverse conventions $e^{-\gamma z}$ and $e^{-k_{t\_i}x}$, and also the intrinsic wavenumber in (2-8), the signs of k_{t_i} in (2-62) should be chosen positive in all the layers.

TE mode

Since the dielectric loss is considered in the calculations, the transverse impedance of TE mode is deduced from (2-60). Therefore, using (2-60) and (2-62), the impedance associated with each layer of the human body model can be deduced as shown in figure 2.8. Since the skin/fat surface is selected as the reference surface, the TRM equation in (2-44) can be expressed as

$$Z_{skin}\frac{Z_{air} + Z_{skin}\tanh\left(k_{t\_skin}d_{skin}\right)}{Z_{skin} + Z_{air}\tanh\left(k_{t\_skin}d_{skin}\right)} + Z_{fat}\frac{Z_{muscle} + Z_{fat}\tanh\left(k_{t\_fat}d_{fat}\right)}{Z_{fat} + Z_{muscle}\tanh\left(k_{t\_fat}d_{fat}\right)} = 0 \tag{2-63}$$

Since all the impedance expressions in figure 2.8 have the same angular frequency ω dependence, this term can be canceled out when replacing the impedance variables (i.e., $Z_{air}, Z_{skin}, Z_{fat}, Z_{muscle}$) in (2-63) into their ana-

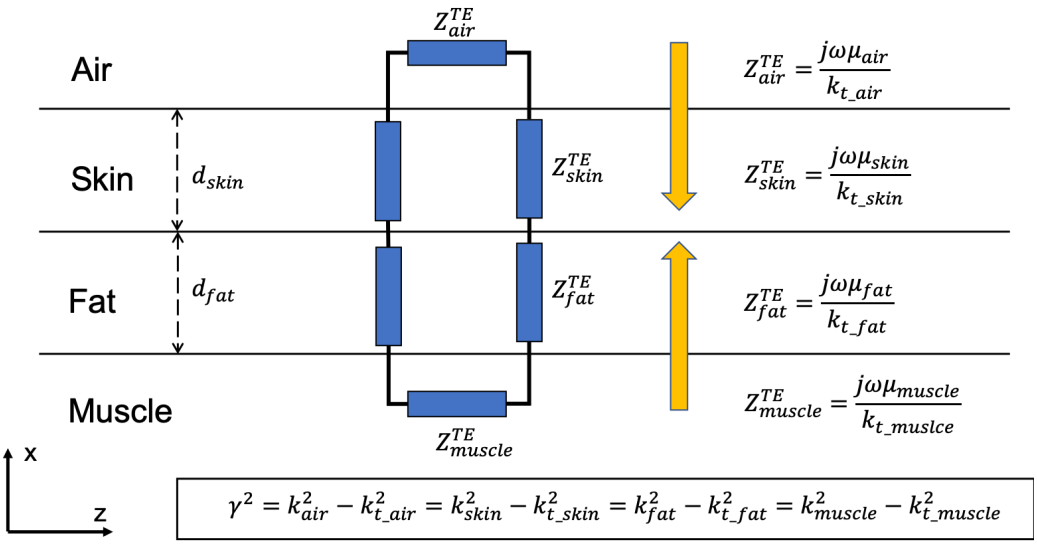

Figure 2.8: Equivalent TRM transmission line for a TE mode propagation in the human body model

lytical expressions in figure 2.8, which reduces to

$$\frac{\mu_{skin}}{k_{t\_skin}} \frac{\frac{\mu_{air}}{k_{t\_air}} + \frac{\mu_{skin}}{k_{t\_skin}} \tanh\left(k_{t\_skin} d_{skin}\right)}{\frac{\mu_{skin}}{k_{t\_skin}} + \frac{\mu_{air}}{k_{t\_air}} \tanh\left(k_{t\_skin} d_{skin}\right)} + \frac{\mu_{fat}}{k_{t\_fat}} \frac{\frac{\mu_{muscle}}{k_{t\_muscle}} + \frac{\mu_{fat}}{k_{t\_fat}} \tanh\left(k_{t\_fat} d_{fat}\right)}{\frac{\mu_{fat}}{k_{t\_fat}} + \frac{\mu_{muscle}}{k_{t\_muscle}} \tanh\left(k_{t\_fat} d_{fat}\right)} = 0 \quad (2\text{-}64)$$

where μ_{air}, μ_{skin}, μ_{fat}, μ_{muscle} are equal to the vacuum permeability μ_0, and d_{skin}, d_{fat} are the thicknesses of the skin and fat layers respectively.

Applying (2-62) to (2-64), this complex TRM equation therefore has only one complex unknown γ, and the roots of this equation will be the solutions of the propagation component γ for the propagating modes. Note that complex roots of a complex function can be found numerically in Matlab by means of the "cxroot" function [140], which uses a Fletcher's version of the Levenberg-Maquardt algorithm to find the complex root of a complex function. So a visual inspection of the complex equation (2-64) is often required to give an initial guess point (i.e., for the first considered frequency of a given mode).

For example, figure 2.9 shows the logarithmic values of the complex equation (2-64) in function of complex $\gamma = \alpha + j\beta$ (α ranging from -200 to 200, β

ranging from 0 to 500), for the 1 mm-thickness skin and 13 mm-thickness fat human body model at 5 GHz. Using the "cxroot" function and a sufficient number of guess points in the complex plane, the two zeros ($\gamma = 47 + 255j$ and $\gamma^{'} = 167 + 61j$) of the dispersion equation represented in figure 2.9 can be successfully identified by our Matlab code. It should be noted that the zeros of the real propagation modes (slow-waves further presented in chapter 3) require satisfying the condition $\beta > Im(k_{fat})$, thus only one TE mode ($\gamma = 47+255j$) exists at 5 GHz for the 1 mm-skin human body model. As the range of α extends in the positive direction, an infinite number of phantom modes like $\gamma^{'}$ appear, whose imaginary value β smaller than $Im(k_{fat})$ and its real part α is very large. Such modes are improper and do not propagate and can be easily eliminated from our Matlab code.

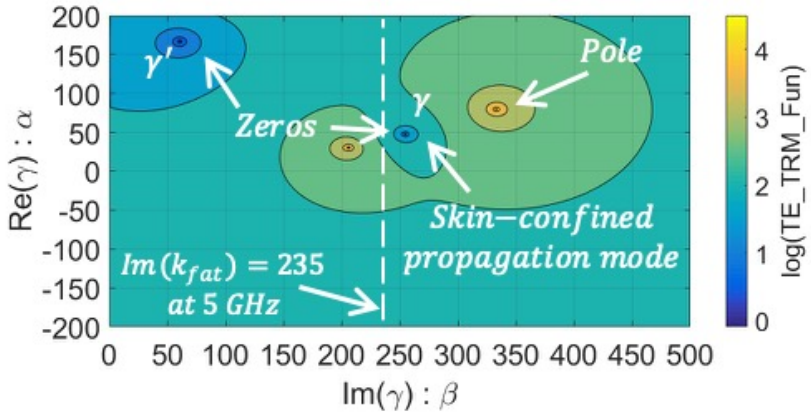

Figure 2.9: TE mode TRM function logarithmic values at 5 GHz in function of γ (skin thickness 1 mm and fat thickness 13 mm)

TM mode

For TM modes, the only difference from the previous TE mode calculation is the definition of the transverse impedance equation, as shown in figure 2.10. Using the TRM equation (2-63) and the definition of the TM mode transverse impedance (2-61), the dispersion equation for TM mode can be

written as

$$\frac{k_{t\_skin}}{\varepsilon_{skin}} \frac{\frac{k_{t\_air}}{\varepsilon_{air}} + \frac{k_{t\_skin}}{\varepsilon_{skin}} \tanh\left(k_{t\_skin} d_{skin}\right)}{\frac{k_{t\_skin}}{\varepsilon_{skin}} + \frac{k_{t\_air}}{\varepsilon_{air}} \tanh\left(k_{t\_skin} d_{skin}\right)} + \frac{k_{t\_fat}}{\varepsilon_{fat}} \frac{\frac{k_{t\_muscle}}{\varepsilon_{muscle}} + \frac{k_{t\_fat}}{\varepsilon_{fat}} \tanh\left(k_{t\_fat} d_{fat}\right)}{\frac{k_{t\_fat}}{\varepsilon_{fat}} + \frac{k_{t\_muscle}}{\varepsilon_{muscle}} \tanh\left(k_{t\_fat} d_{fat}\right)} = 0 \quad (2\text{-}65)$$

where ε_{air}, ε_{skin}, ε_{fat}, ε_{muscle} are products of the vacuum permittivity ε_0 and the relative permittivity of the human tissues found in [97].

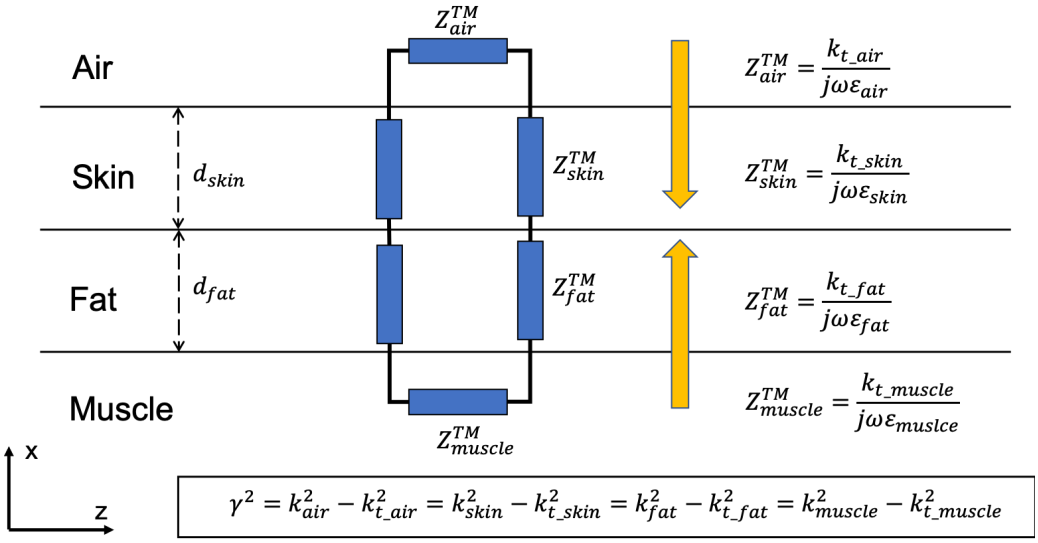

Figure 2.10: Equivalent TRM transmission line for a TM mode propagation in the human body model

2.9 Human Tissue Thickness

As discussed in the previous section 2.8, the skin and fat thicknesses play an important role in the dispersion equation, thus affecting the propagation behavior. In this section, we describe the human tissue topology and provide a brief survey of the medical measurements of human tissue thicknesses in order to obtain the relevant inputs for the TRM-based skin-confined propagation model.

Human skin consists of three basic layers: the epidermis, the dermis, and the hypodermis (figure 2.11). The epidermis is much thinner than the dermis and can be ignored in some cases. The hypodermis, also known as subcutaneous tissue or fat, is located beneath the dermis and is composed of many types of cells, such as fibroblasts, fat cells, and leukocytes. Furthermore, muscle can be found under the fat tissue layer [141].

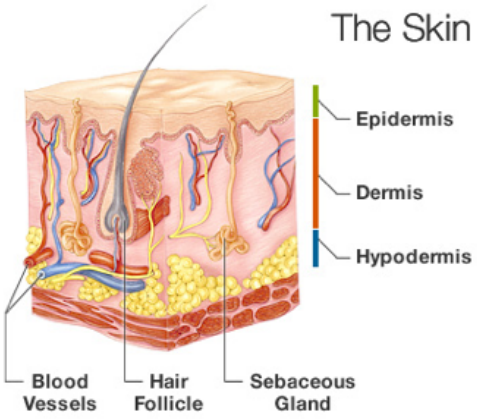

Figure 2.11: Human body skin structure [142]

The dielectric proprieties of body tissues depend on frequency [97]. They have important loss characteristics at high frequencies (microwave or millimeter-wave). In addition, their thicknesses varies with the human sex, age, and the tissue location. Accurately considering the tissue thickness in the TRM equation is very important for accurate and reliable channel characterization of the on-body propagation in practice. To date, accurate human body tissue thickness has not been found in the literature relative to the human body channel characterization and the on-body antenna design. Therefore, a bibliographic study in the medical literature was performed in our work to provide a meaningful human body modeling for the TRM analysis.

2.9.1 Skin thickness measurement methods

As illustrated in figure 2.12, different skin thickness measurement methods were reported in the medical literature. In the following subsections, we

present three typical methods: the radiological method, the Harpenden skinfold caliper method, and the ultra sound method.

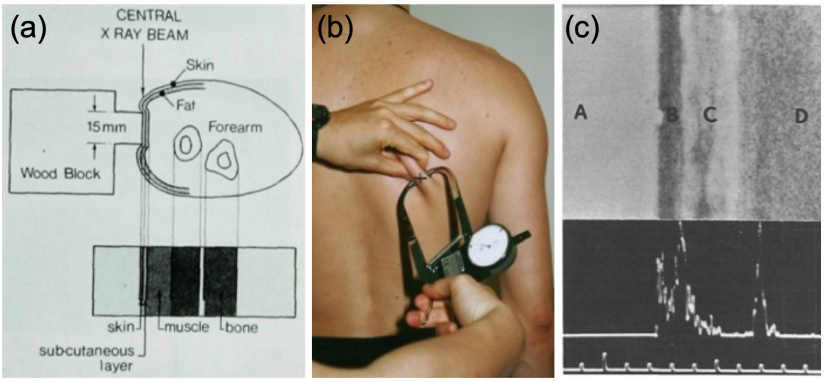

Figure 2.12: Skin thickness measurement methods: (a) radiological method [143], (b) Harpenden skinfold caliper method [144] (c) ultrasound method (A – lucite block, B – skin, C – fat, D – muscle) [145]

Radiological method

The principle of the radiological method is schematically shown in figure 2.12(a). This is the most accurate method available to date. As shown in the figure, a beam of X-rays is projected onto a part of the human body (here the forearm). The forearm tissues absorb a certain amount of X-rays. The absorption depends on the particular density and composition of each tissue. The X-rays that pass through are captured by a detector behind the forearm. When the skin surface of the forearm is flattened against a wood block, the homogeneous brighter area produced by the skin on the radiograph can be well recognized and can be easily measured.

Harpenden skinfold caliper method

As shown in figure 2.12(b), the Harpenden skinfold caliper is a precision instrument designed for measurement of skinfold thickness. In the measurement procedure, the skinfold is firmly grasped and pulled away from the human body. Then the caliper is placed perpendicular to the fold and

the pressure-based instrument dial shows automatically the accurate skinfold thickness value.

This method is an unconventional manner, because after the fold measurement, the thickness of the skin should be estimated by a specific software to exclude the thickness of the fat in the fold. The use of this instrument has been well established and documented over the past 40 years.

Ultrasound method

This method (figure 2.12(c)) uses the ultrasonic echo technique to determine the thickness of human skin. High-resolution pulsed ultrasound has been used to determine the geometry of eyes and the diagnosis of choroidal tumors for many years. The geometry is determined by measuring the total transit time of the high frequency sound pulses that are beamed into the eye and reflected at the tissue interfaces that encounters a high acoustical impedance gradient. If the tissue acoustical velocity is known, the measured times can be related to the distance between the interfaces of different tissues. For example, the speed of sound in human skin can be referred to 1580 m/s, which was determined by Daly and Wheeler in the 1970's [146].

2.9.2 Measured tissue thicknesses

The results of the arm skin thickness for the different measurement methods are given in table 2.3, which shows that the skin thickness varies around 1 mm. It should be noted that according to [141], the skin thickness is very thin in the facial section, for example 0.12 mm, while in the palm area, the skin thickness can be very thick, for example 5 mm.

Skin thickness (mm)	Method
0.90 – 1.30	X-ray technique [143]
0.82 – 1.19	X-ray technique [145]
0.75 – 1.16	Ultra sound technique [145]
0.81 – 1.11	- [147]
0.93 – 1.15	Caliper technique [148]
0.91 – 1.04	X-ray technique [148]
1.10 – 1.30	X-ray technique (Black 1969) [148]
0.6	- [141]

Table 2.3: Measurement of arm skin thickness by different methods

Other tissue thicknesses were discovered during our bibliographic research in the medical literature, but results were very different according to the human part that was considered, unfortunately not mentioned. Very few articles mention the thickness of fat and muscle. In fact, depending on the condition of the person (e.g., age, sex, weight, tissue location etc), the thickness of these two tissues varies very widely. In [141], the fat thickness of the belly section is given as 30 mm. In [149], the fat thickness of the buttocks is 32 mm and the muscle thickness is 58 mm. It can be estimated that for the tiny part of the human body, such as the forearm, the fat thickness could be thinner.

Therefore, in our analysis, as the propagation is confined in the skin, we will consider three different skin thicknesses to study its effect on the propagation.

2.10 Analysis of Skin-Confined Propagation

The most important propagation features of the human body channel are the dispersion and attenuation in the direction of propagation, which can be easily deduced from our TRM codes. To validate our TRM calculations, numerical simulations were performed using CST Microwave Studio® for selected frequencies. A similar planar multilayer human body structure was established in the simulation and a waveguide port was set to excite the propagation modes into the model, as shown in figure 2.13.

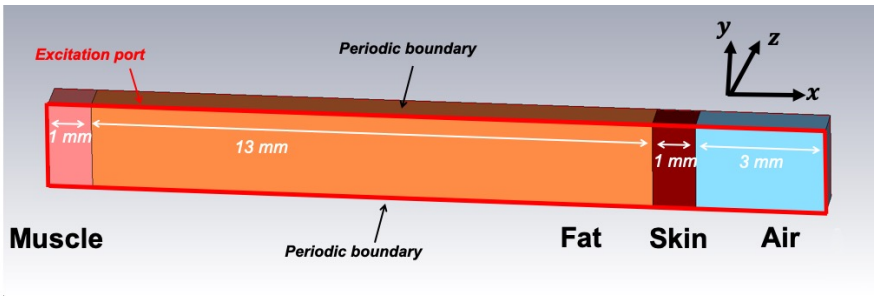

Figure 2.13: Multilayer human body model in CST

In this demonstration model, the skin thickness is configured to be 1 mm and the fat is 13 mm. Periodic boundary conditions were applied on the two

xz-surfaces to simulate the infinite y-axis dimension. The other boundaries were set as absorbent conditions (PML), which can practically simulate the semi-infinite dimension feature of the air and muscle layers. The muscle thickness was chosen as 1 mm to reduce the undesirable modes found in CST and the air thickness was chosen as 3 mm.

It should be noted that the heights of the muscle and air layers should be large enough so that the absorbent condition does not disturb the modes under investigation exhibiting an exponential decay within these layers. However, a large height will result in large number of ghost modes exhibiting standing wave behaviors at the waveguide port within these layers because the simulated model is still a closed structure in the x-axis directions (even with PMLs). It becomes then cumbersome to find out the modes of interest, especially when dielectric losses are considered in the simulation at high operating frequencies, and the computation time increases as a large number of modes need to be calculated. In addition, the mesh number also affects the accuracy of the port mode calculations. When the simulation is performed at high frequencies, the number of mesh cells is greatly increased and the computational calculation load becomes quite huge, which takes a lot of time. By using the CST port mode calculation in the frequency domain, the propagation modes at the excitation port can be calculated, but only one frequency is available to be analyzed per simulation run. The advantages of the TRM calculations in the analysis are thus revealed.

Nevertheless, good agreement was observed between the CST simulation results and our TRM code. For example, for the 1 mm-thickness skin and 13 mm-thickness fat model in lossless case at 60 GHz, the propagation constants of the TE and TM modes calculated in CST are 3026 rad/m (figure 2.14) and 2624 rad/m, respectively. In our TRM calculations, we obtained 3041 rad/m and 2612 rad/m for the respective modes, which confirms the validity of the developed code.

In the following subsections, we will present analysis results of the skin-confined on-body propagation from our TRM calculations, such as dispersion and attenuation along the direction of the propagation, propagation confinement, and surface impedance. With the obtained dispersion/attenuation features from TRM, electromagnetic field distribution and power distribution are also calculated by solving the classical Maxwell's equations by means of the auxiliary vector potentials. The effects of the muscle layer on the propagation are also analyzed in our work.

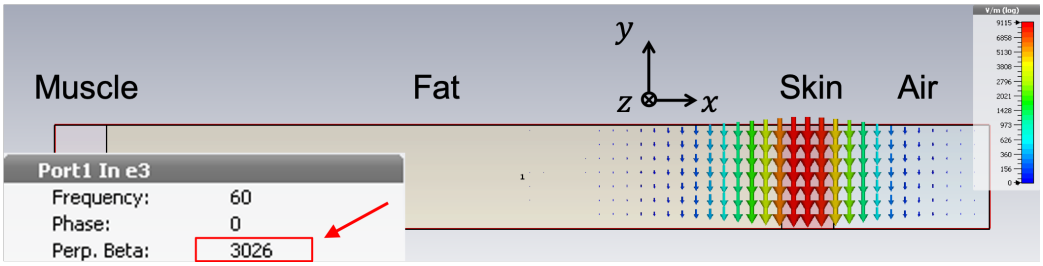

Figure 2.14: Calculated TE mode in the CST port mode calculation at 60 GHz and the electric field distribution of the excitation for the 1 mm-thickness skin and 13 mm-thickness fat human body model

2.10.1 Dispersion and attenuation curves

Dispersion (rad/m) and attenuation (dB/cm) for modes propagating up to 60 GHz are calculated and results are shown in figure 2.15(a) for a 0.5 mm-thick skin and a 13 mm-thick fat layer. The first mode is a TE mode, starting propagating at about 8 GHz, which is confined within the skin layer. The propagation constant β increases with the frequency, resulting in the increase of the ratio β/k_{skin}, which means that the wave's angle of incidence in the skin layer θ_i (as mentioned in section 2.5) becomes larger. In addition, since the propagation constant β is greater that the intrinsic fat wavenumber k_{fat}, from the definition of the critical angle (2-13), it can be verified that this skin-confined TE mode propagation has always an angle of incidence in the skin layer θ_i greater than the critical angle of the skin/fat interface. It is apparent that the skin layer guides like a "fiber optic cable" the fundamental TE mode.

In addition, another TM solution is found ("TM_Zenneck_Skin/Fat" in figure 2.15), which has a propagation constant very close, but smaller to the intrinsic fat wavenumber k_{fat}. It represents the so-called Zenneck surface-waves at the fat/skin (or fat/muscle) interface. A Zenneck surface-wave is a wave propagating along a surface between two different media, which is characterized by a phase velocity greater than that of the light and an attenuation along the direction of propagation [150]. Furthermore, the wave is decayed away from the surface. However, in [150], it is indicated that the radial Zenneck wave is not a major contribution to the total field of

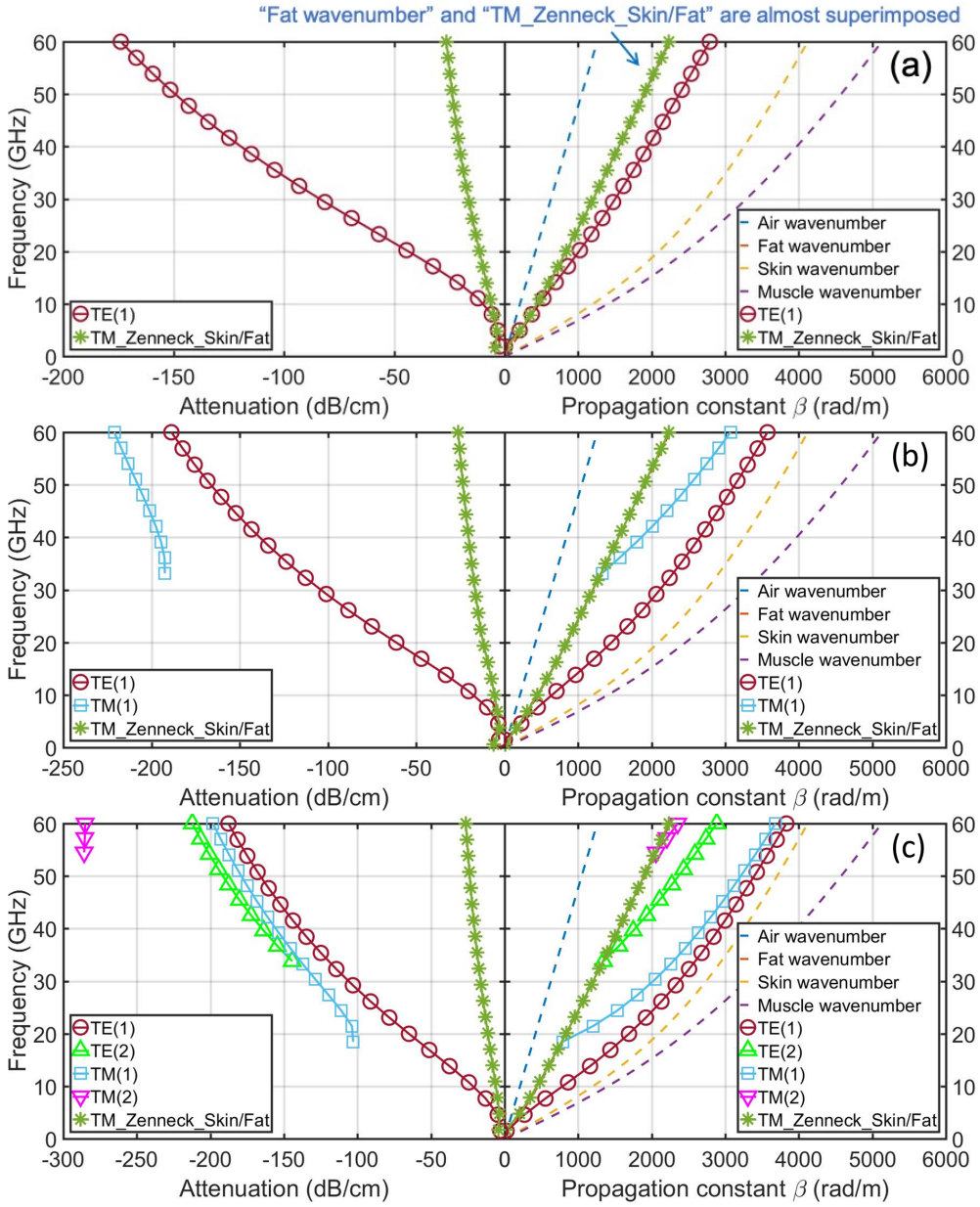

Figure 2.15: Propagation and attenuation constants in the direction of propagation for three different skin thicknesses ((a) 0.5 mm, (b)1 mm, (c)1.5 mm) (fat thickness is 13 mm)

a vertical electric dipole over a homogeneous conducting earth. It is also mentioned that the Zenneck wave is generally difficult to be excited with a finite-size source because it has a rather slow decay with height above the earth's surface [151]. From our analysis, this Zenneck mode has relatively low attenuation in the direction of propagation. As indicated in [131], the vertical component of the electric field (relative to our TM Zenneck mode) with respect to the human body surface is much less attenuated than the horizontal component (relative to our skin-confined TE mode), which confirms our observation. Nevertheless, as shown in section 2.10.3 below, although the Zenneck solution contributes to describe the total field distribution, they are too loosely bounded to the interface to be used for on-body communications.

It should be noted that another TM Zenneck solution was also found at lower frequencies, which has a propagation constant close but smaller to the intrinsic air wavenumber k_{air}, noted here "TM_Zenneck_Skin/Air". This Zenneck mode has an upper cut-off frequency and disappears from about 2 GHz. Since the figures in 2.15 have a large frequency range of up to 60 GHz, this Zenneck mode is not represented in the figures. More details will be discussed in the following of this section.

Figures 2.15(b) and 2.15(c) show the same results when the skin thickness is increased to 1 mm and 1.5 mm respectively. The same Zenneck surface-wave solutions are naturally found. As expected, the fundamental TE mode has a cut-off frequency that decreases when skin thickness increases. Moreover, as the frequency increases, higher order propagation modes appear successively. The cut-off frequencies of the different confined TE and TM modes are shown in table 2.4. In the three analyzed models, the first TM mode is only found with the 1 mm-thick and the 1.5 mm-thick skin models, and the second TE mode only with the 1.5 mm-thick skin model after the first TM mode.

Skin thickness	TE(1)	TM(1)	TE(2)	TM(2)
0.5 mm	8 GHz	-	-	-
1 mm	4 GHz	33 GHz	-	-
1.5 mm	3 GHz	18 GHz	34 GHz	54 GHz

Table 2.4: Cut-off frequencies of different propagation modes for the three different skin thickness models

The attenuation of each mode along the direction of propagation is given in terms of dB/cm on the left side of the figures 2.15. Only the fundamental

TE mode exhibits reasonable attenuation for frequencies below 8 GHz, which may be suitable for on-body ranging transmission. Table 2.5 shows the detailed attenuation of the fundamental TE mode of the three analyzed models at different frequencies in the range of 3 - 10 GHz. As the frequency increases, its attenuation becomes significantly larger. Higher order propagation modes always have greater attenuation.

Frequency	0.5 mm skin	1 mm skin	1.5 mm skin
3 GHz	-	-	-2.8 dB/cm
4 GHz	-	-3.1 dB/cm	-3.8 dB/cm
5 GHz	-	-4.1 dB/cm	-5.5 dB/cm
6 GHz	-	-5.8 dB/cm	-7.9 dB/cm
7 GHz	-	-8.1 dB/cm	-10.8 dB/cm
8 GHz	-5.8 dB/cm	-10.9 dB/cm	-14.0 dB/cm
9 GHz	-7.4 dB/cm	-14.1 dB/cm	-17.6 dB/cm
10 GHz	-9.4 dB/cm	-17.7 dB/cm	-21.4 dB/cm

Table 2.5: Attenuation of the fundamental TE mode in the frequency range of 3 - 10 GHz for the three different skin thickness models

Figure 2.16 shows the attenuation with respect to frequency of the TE fundamental mode for six different skin thicknesses, ranging from 0.5 to 3 mm (the fat thickness is kept as 13 mm). It can be seen that, at a given frequency, the thinnest skin model exhibit the lowest attenuation. However, as shown in tables 2.4 and 2.5, thinner skin also has a higher starting cut-off frequency, which in turn limits the operating frequency range of the thinnest skin model.

As for the "TM_Zenneck_Skin/Air" mode mentioned at the beginning of this section which is found only at low frequencies, figure 2.17 shows the dispersion and attenuation along the direction of propagation for the 1 mm-thickness skin model. In this model, the "TM_Zenneck_Skin/Air" mode is only found below 1.7 GHz and has ultra low attenuation along the direction of propagation. This kind of Zenneck mode and its corresponding cut-off phenomenon was also observed in the work of [131], which indicated that this Zenneck surface-wave at the interface between air and human body has no low-frequency cut-off but a high-frequency cut-off due to the shift of the surface impedance from inductive to capacitive when the frequency gets higher.

Let us analyze the surface impedance seen by an incident plane wave from the air layer and normal to the skin/air interface, using the transmission line based model of figures 2.8 and 2.10 (equivalent to normal incidence), for

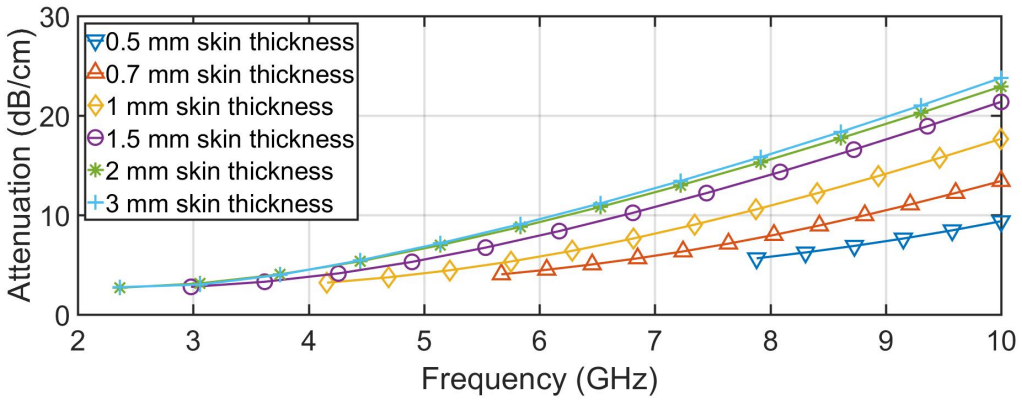

Figure 2.16: Attenuation of the TE fundamental mode for different skin thickness models (0.5 - 3 mm) up to 10 GHz (fat thickness is 13 mm)

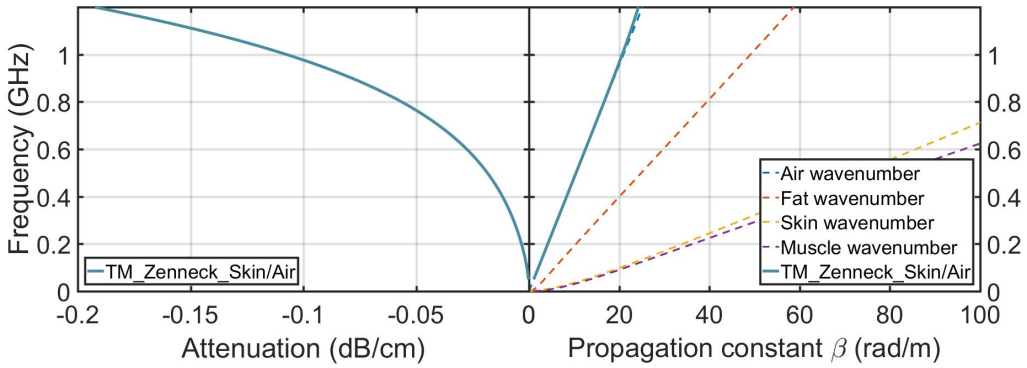

Figure 2.17: Propagation and attenuation constants in the direction of propagation of the TM_Zenneck_Skin/Air mode for the 1 mm-thickness skin and 13 mm-thickness fat human body model

the 1 mm-thickness skin and 13 mm-thickness fat human body model. The characteristic wave impedance of each tissue layer in lossy case is calculated as [139]

$$Z_{surface\_lossy} = \frac{j\omega\mu}{k_i} \tag{2-66}$$

where k_i is the intrinsic wavenumber of each layer "i" expressed in equation

(2-8). Figure 2.18 shows the complex surface impedance (resistance and reactance values) obtained at the skin/air interface as well as the fat/muscle interface for comparison. It can be seen that the reactance of the surface impedance at the air/skin interface changes from a positive value to a negative value at 1.6 GHz, shifting the surface impedance from inductive to capacitive. This is the same frequency at which the 'TM_Zenneck_Air/Skin" mode described above is no longer to be found, which may explain why this Zenneck mode disappears at this frequency. As for the fat/muscle interface, we can see that the surface impedance is always inductive below 60 GHz, which is the reason why we can always find the "TM_Zenneck" mode at all the frequencies in this range.

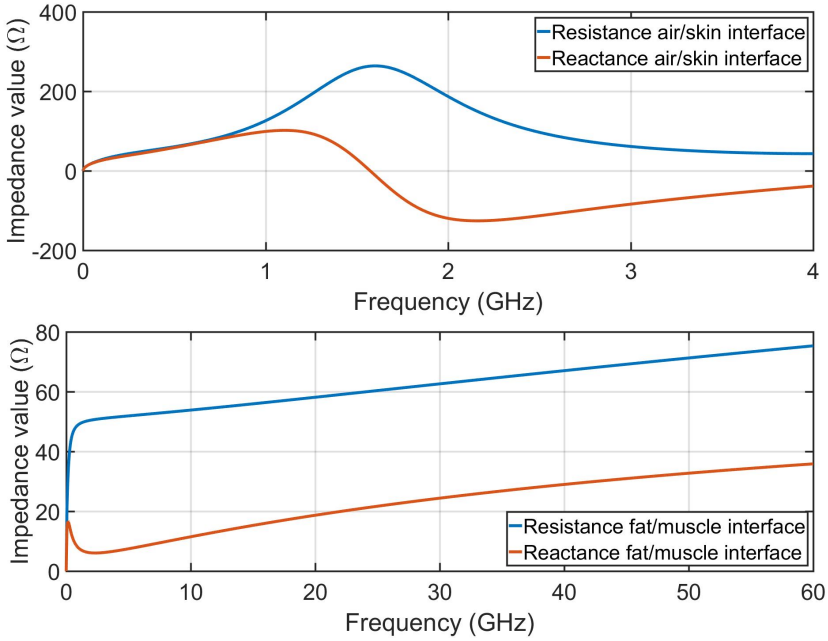

Figure 2.18: Normal incidence surface impedance seen at the air/skin surface and the fat/muscle surface toward the human body for the 1 mm-thickness skin and 13 mm-thickness fat model

2.10.2 Confinement

All solutions but Zenneck ones have a propagation constant β ranging between the fat wavenumber k_{fat} and the skin wavenumber k_{skin}, and represent

consequently slow waves confined within the skin. However, it is to be noted that since $\mathrm{Re}(\varepsilon_{muscle}) > \mathrm{Re}(\varepsilon_{skin})$, a slow wave that propagates within the skin would also propagate within the muscle. However, the surface-wave launcher is likely to be located at the skin/air interface. So if the transverse attenuation within the fat is large enough, the amount of the slow wave energy guided within the muscle layer shall be small. To quantify this assumption, the transverse attenuation within the fat layer is given in figure 2.19 for the fundamental TE mode. It can be observed that the attenuation is always greater than 5 dB/cm in the 4 - 10 GHz range of interest. Thus, depending on the fat thickness, the slow wave will not leak much into the muscle tissue.

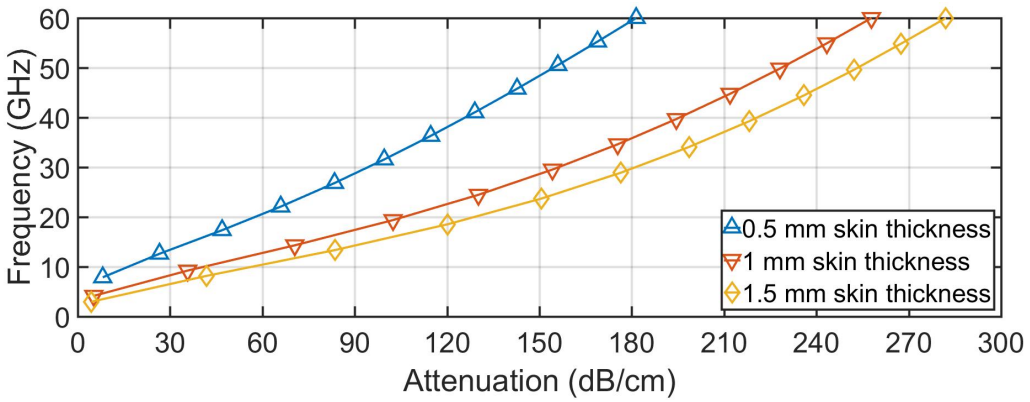

Figure 2.19: Transverse attenuation in fat layer of TE fundamental mode for different skin thickness models (0.5 mm, 1 mm, 1.5 mm) up to 10 GHz (fat thickness is 13 mm)

To investigate the confinement of the slow wave within the skin with respect to the field decay in the air, figure 2.20 shows the transverse attenuation constant in the air for the fundamental TE mode. In the frequency ranging below 10 GHz, the field decays away by about 15 dB/cm and up to 70 dB/cm as the frequency increases. Such an attenuation ensures that on-body slow wave propagation is confined enough in order to avoid any eavesdropper to intercept the communication. It is also observed that this attenuation is more than twice as high as the attenuation along the direction of propagation.

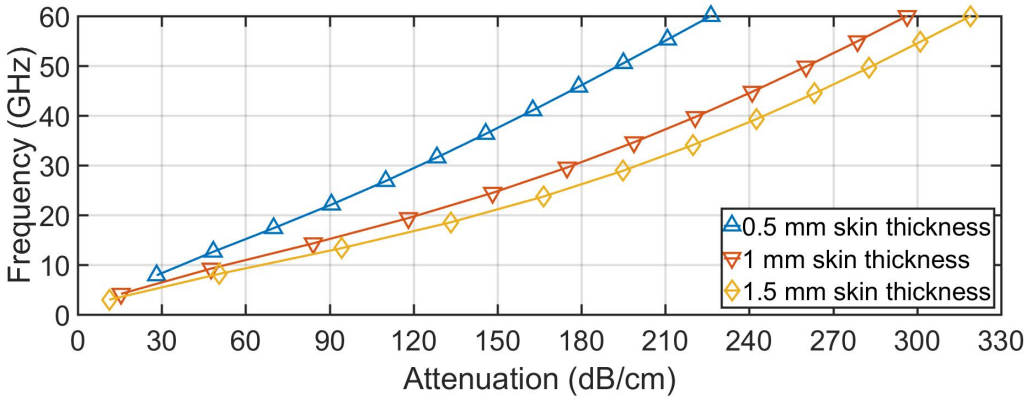

Figure 2.20: Transverse attenuation in the air layer of the TE fundamental mode for different skin thickness models (0.5 mm, 1 mm, 1.5 mm) up to 10 GHz (fat thickness is 13 mm)

2.10.3 Electromagnetic fields distribution

Once the wavenumbers γ in the propagation direction and k_{t_i} in the transverse direction are found in sections 2.10.1 and 2.10.2, the electromagnetic field distribution in the human body model can be then obtained by solving Maxwell's equations via the auxiliary vector potentials $\boldsymbol{A}$ (magnetic vector potential) and $\boldsymbol{F}$ (electric vector potential) with appropriate boundary conditions.

In [139], the time-harmonic electromagnetic fields $\boldsymbol{E}$ and $\boldsymbol{H}$ in a homogeneous medium are calculated by the vector potentials $\boldsymbol{A}$ and $\boldsymbol{F}$ as

$$\boldsymbol{E} = \boldsymbol{E_A} + \boldsymbol{E_F} \tag{2-67}$$

$$\boldsymbol{H} = \boldsymbol{H_A} + \boldsymbol{H_F} \tag{2-68}$$

where

$$\boldsymbol{E_A} = -j\omega\boldsymbol{A} - j\frac{1}{\omega\mu\varepsilon}\nabla(\nabla\cdot\boldsymbol{A}) \tag{2-69}$$

$$\boldsymbol{E_F} = -\frac{1}{\varepsilon}\nabla\times\boldsymbol{F} \tag{2-70}$$

$$\boldsymbol{H_A} = \frac{1}{\mu}\nabla\times\boldsymbol{A} \tag{2-71}$$

$$\boldsymbol{H_F} = -j\omega\boldsymbol{F} - j\frac{1}{\omega\mu\varepsilon}\nabla(\nabla\cdot\boldsymbol{F}) \tag{2-72}$$

It can be noted that $\boldsymbol{E}$ and $\boldsymbol{H}$ in (2-67) and (2-68) are both composed with two parts: one part due to the $\boldsymbol{A}$ potential and the other one due to the $\boldsymbol{F}$ potential. Obviously, once $\boldsymbol{A}$ and $\boldsymbol{F}$ are known, the $\boldsymbol{E}$ and $\boldsymbol{H}$ can then be easily deduced.

The vector potentials $\boldsymbol{A}$ and $\boldsymbol{F}$ in source-free condition and in lossy media should satisfy the vector wave equations

$$\nabla^2\boldsymbol{A} - k_i^2\boldsymbol{A} = 0 \tag{2-73}$$

$$\nabla^2\boldsymbol{F} - k_i^2\boldsymbol{F} = 0 \tag{2-74}$$

where $k_i^2 = (j\omega\sqrt{\mu\varepsilon})^2 = -\omega^2\mu\varepsilon$ is the square of the complex intrinsic wavenumber in the homogeneous lossy tissue "i" as defined in (2-8). In a rectangular coordinate system, the electric field $\boldsymbol{E}$ can then be expanded from (2-67), (2-69), and (2-70) as

$$\begin{aligned}
\boldsymbol{E} &= -j\omega\boldsymbol{A} - j\frac{1}{\omega\mu\varepsilon}\nabla(\nabla\cdot\boldsymbol{A}) - \frac{1}{\varepsilon}\nabla\times\boldsymbol{F} \\
&= \hat{a}_x\left[-j\omega A_x - j\frac{1}{\omega\mu\varepsilon}\left(\frac{\partial^2 A_x}{\partial x^2} + \frac{\partial^2 A_y}{\partial x\partial y} + \frac{\partial^2 A_z}{\partial x\partial z}\right) - \frac{1}{\varepsilon}\left(\frac{\partial F_z}{\partial y} - \frac{\partial F_y}{\partial z}\right)\right] \\
&\quad + \hat{a}_y\left[-j\omega A_y - j\frac{1}{\omega\mu\varepsilon}\left(\frac{\partial^2 A_x}{\partial x\partial y} + \frac{\partial^2 A_y}{\partial y^2} + \frac{\partial^2 A_z}{\partial y\partial z}\right) - \frac{1}{\varepsilon}\left(\frac{\partial F_x}{\partial z} - \frac{\partial F_z}{\partial x}\right)\right] \\
&\quad + \hat{a}_z\left[-j\omega A_z - j\frac{1}{\omega\mu\varepsilon}\left(\frac{\partial^2 A_x}{\partial x\partial z} + \frac{\partial^2 A_y}{\partial y\partial z} + \frac{\partial^2 A_z}{\partial z^2}\right) - \frac{1}{\varepsilon}\left(\frac{\partial F_y}{\partial x} - \frac{\partial F_x}{\partial y}\right)\right]
\end{aligned} \tag{2-75}$$

and the magnetic field $\boldsymbol{H}$ can be obtained from (2-68), (2-71), and (2-72) as

$$\begin{aligned}
\boldsymbol{H} &= \frac{1}{\mu}\nabla\times\boldsymbol{A} - j\omega\boldsymbol{F} - j\frac{1}{\omega\mu\varepsilon}\nabla(\nabla\cdot\boldsymbol{F}) \\
&= \hat{a}_x\left[-j\omega F_x - j\frac{1}{\omega\mu\varepsilon}\left(\frac{\partial^2 F_x}{\partial x^2} + \frac{\partial^2 F_y}{\partial x\partial y} + \frac{\partial^2 F_z}{\partial x\partial z}\right) + \frac{1}{\mu}\left(\frac{\partial A_z}{\partial y} - \frac{\partial A_y}{\partial z}\right)\right] \\
&\quad + \hat{a}_y\left[-j\omega F_y - j\frac{1}{\omega\mu\varepsilon}\left(\frac{\partial^2 F_x}{\partial x\partial y} + \frac{\partial^2 F_y}{\partial y^2} + \frac{\partial^2 F_z}{\partial y\partial z}\right) + \frac{1}{\mu}\left(\frac{\partial A_x}{\partial z} - \frac{\partial A_z}{\partial x}\right)\right] \\
&\quad + \hat{a}_z\left[-j\omega F_z - j\frac{1}{\omega\mu\varepsilon}\left(\frac{\partial^2 F_x}{\partial x\partial z} + \frac{\partial^2 F_y}{\partial y\partial z} + \frac{\partial^2 F_z}{\partial z^2}\right) + \frac{1}{\mu}\left(\frac{\partial A_y}{\partial x} - \frac{\partial A_x}{\partial y}\right)\right]
\end{aligned} \tag{2-76}$$

A TE/TM field decomposition can be obtained using the Hertz potential. In fact, it can be found from (2-75) and (2-76) that, if we suppose $\boldsymbol{A}$ is equal to zero and $\boldsymbol{F}$ has only a $\hat{a}_z$ component, which means

$$\boldsymbol{A} = 0 \tag{2-77}$$

$$\boldsymbol{F} = \hat{a}_z F_z(x, y, z) \tag{2-78}$$

we can get a TE propagation mode in the direction of z-axis. Since in our model, we suppose the dimension along y-axis is infinite and has no field variation ($\frac{\partial}{\partial y} = 0$), the x-, y-, z- components of $\boldsymbol{E}$ and $\boldsymbol{H}$ can thereby be deduced from (2-75) and (2-76)

$$\begin{aligned} E_x &= 0 & H_x &= -j\frac{1}{\omega\mu\varepsilon}\frac{\partial^2 F_z}{\partial x \partial z} \\ E_y &= \frac{1}{\varepsilon}\frac{\partial F_z}{\partial x} & H_y &= 0 \\ E_z &= 0 & H_z &= -j\frac{1}{\omega\mu\varepsilon}\left(\frac{\partial^2}{\partial z^2} + \beta^2\right) F_z \end{aligned} \tag{2-79}$$

Similarly, the TM mode in the direction of z-axis can be obtain by assuming $\boldsymbol{F}$ is equal to zero and $\boldsymbol{A}$ has only a $\hat{a}_z$ component

$$\boldsymbol{F} = 0 \tag{2-80}$$

$$\boldsymbol{A} = \hat{a}_z A_z(x, y, z) \tag{2-81}$$

and the corresponding x-, y-, z- components of $\boldsymbol{E}$ and $\boldsymbol{H}$ can be deduced from (2-75) and (2-76)

$$\begin{aligned} E_x &= -j\frac{1}{\omega\mu\varepsilon}\frac{\partial^2 A_z}{\partial x \partial z} & H_x &= 0 \\ E_y &= 0 & H_y &= -\frac{1}{\mu}\frac{\partial A_z}{\partial x} \\ E_z &= -j\frac{1}{\omega\mu\varepsilon}\left(\frac{\partial^2}{\partial z^2} + \beta^2\right) A_z & H_z &= 0 \end{aligned} \tag{2-82}$$

Therefore, if we have the solutions of $\boldsymbol{A}$ and $\boldsymbol{F}$, the time-harmonic instantaneous field of each component can then be deduced by the multiplication of the real part of each component in equations (2-79) and (2-82) with a time

variation $e^{j\omega t}$ (e.g., for the x- electric field E_x of TM mode in equation (2-82), the instantaneous field expression can be deduced as $\mathrm{Re}[E_x e^{j\omega t}]$).

Then, the next step is to appratiately define the scalar potential function $A_z(x,y,z)$ or $F_z(x,y,z)$ for the TM mode and the TE mode respectively in each layer of the human body model. We use here the separation of variables method [139], which implies that the x, y, z variations of $A_z(x,y,z)$ and $F_z(x,y,z)$ are separable.

In the case of separation of variables form for the $\mathrm{TE_Z}$ mode, only the $F_z(x,y,z)$ function need to be defined and $A_z(x,y,z)$ is equal to zero. As the variation in the y-axis is not considered, and the considered wave propagates toward the positive z-axis (figure 2.21), to satisfy the vector wave equation (2-74) by applying (2-9), the solution of F_z in the layer "i" can be expressed in form of a product of two scalar functions $f(x)$ and $g(z)$

$$\begin{aligned} F_z &= f(x)g(z) \\ &= \left(Me^{-k_{t\_i}x} + Ne^{+k_{t\_i}x}\right)e^{-\gamma z} \end{aligned} \tag{2-83}$$

where M and N are constant values which represent the field amplitude [139]. In addition, this form can be simplified for the air and muscle layers, considered infinite along the positive x-axis direction and the negative x-axis direction respectively. No reflection can occur in these two layers. Therefore, supposing the original zero reference of the x-axis is the skin/fat surface as shown in figure 2.21, we can get the F_z function in each layer for the TE mode

$$\begin{aligned} \text{Air}: \quad & F_{z\_air} = A^{+}e^{-k_{t\_air}(x-d_{skin})}e^{-\gamma z} && \text{for} \quad x \geq d_{skin} \\ \text{Skin}: \quad & F_{z\_skin} = \left(B^{+}e^{-k_{t\_skin}x} + B^{-}e^{+k_{t\_skin}x}\right)e^{-\gamma z} && \text{for} \quad 0 \leq x < d_{skin} \\ \text{Fat}: \quad & F_{z\_fat} = \left(C^{+}e^{-k_{t\_fat}x} + C^{-}e^{+k_{t\_fat}x}\right)e^{-\gamma z} && \text{for} \quad -d_{fat} \leq x < 0 \\ \text{Muscle}: \quad & F_{z\_muscle} = D^{-}e^{+k_{t\_muscle}\left(x+d_{fat}\right)}e^{-\gamma z} && \text{for} \quad x < -d_{fat} \end{aligned} \tag{2-84}$$

For the TM mode, the form of the A_z function is the same as the F_z described above. So A^{+}, B^{+}, B^{-}, C^{+}, C^{-}, D^{-} in (2-84) are unknown variables to be found.

The final step in the field distribution calculation is to apply the boundary conditions at the air/skin, skin/fat, and fat/muscle interfaces for all the components of the $\boldsymbol{E}$ and $\boldsymbol{H}$ fields. These components are either tangential (y- and z-components) or normal (x-component) to the surface. The

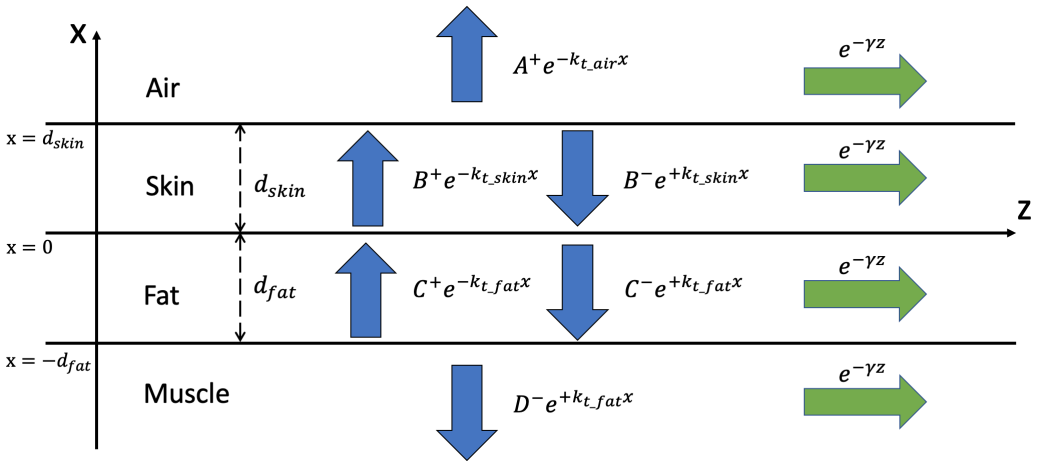

Figure 2.21: Electromagnetic field distribution calculation model for the on-body propagation

tangential components of electromagnetic field $\boldsymbol{E}$ and $\boldsymbol{H}$ across a boundary surface between two media are continuous while the normal components of the electromagnetic flux density $\boldsymbol{D} = \varepsilon \boldsymbol{E}$ and $\boldsymbol{B} = \mu \boldsymbol{H}$ are also continuous. That means for TE mode

$$\begin{aligned} \mu_{layer1} H_{x\_layer1} &= \mu_{layer2} H_{x\_layer2} \\ E_{y\_layer1} &= E_{y\_layer2} \\ H_{z\_layer1} &= H_{z\_layer2} \end{aligned} \tag{2-85}$$

and for TM mode

$$\begin{aligned} \varepsilon_{layer1} E_{x\_layer1} &= \varepsilon_{layer2} E_{x\_layer2} \\ H_{y\_layer1} &= H_{y\_layer2} \\ E_{z\_layer1} &= E_{z\_layer2} \end{aligned} \tag{2-86}$$

However, these boundary conditions are not all independent, thus an appropriate set of boundary configurations should be built up for the calculation.

Since we only study the propagation properties of the human body channel, without considering the source, we only need to find the field solution of the analyzed propagation mode on the x-axis (since no variation is considered in the y-axis) at a referred z position (e.g., $z = 0$) and with a subjective

power value set on the field amplitudes in (2-84). Therefore, with the field solution on the referred x-axis, we apply the z-axis variation $e^{-\gamma z}$ and the time variation $e^{j\omega t}$ to get the cross-sectional field distribution in the xz-plane of the human body model, i.e., the wave of the analyzed mode travels from the xy-plane at $z = 0$ toward the positive z-axis direction.

Firstly, let us analyze the field distribution without considering the dielectric loss in the tissues, which results in the use of only the real part of the complex permittivity for each corresponding tissue. The purpose of this configuration is to validate our numerical calculation code by comparing it with CST simulation results. In addition, as represented in section 2.10.1, the attenuation in the direction of propagation becomes considerably high as the frequency increases. Ignoring the dielectric loss in the tissues allows us to observe more easily the field distribution feature and the essential confinement behavior of the propagating wave.

To do so, for the previous 1 mm-thickness skin and 13 mm-thickness fat human body model (figure 2.15(b)), the electromagnetic field distributions of the fundamental TE mode and the TM(1) mode are calculated at 60 GHz in Matlab using equations (2-79) and (2-82), and the linearly plotted results are shown in figure 2.22 and figure 2.23, respectively. For comparison, the CST port mode calculations performed with the frequency solver (figure 2.13) for the respective modes are shown in the captions of figures 2.22 and 2.23. As can be observed, the field distributions deduced from our code have the same form as the CST port mode distribution. It can also be seen that the TE mode field is slightly better confined in the skin layer. For the TM mode, more penetration in fat and less penetration in air of the magnetic field can be observed (figure 2.23).

To analyze the attenuation along the direction of propagation, it is more convenient to consider the power distribution. Using the obtained field distribution, the instantaneous flowing power density ($\mathrm{W/m^2}$) can be calculated by the instantaneous Poynting vector

$$\boldsymbol{S_{inst}} = \mathrm{Re}(\boldsymbol{E}) \times \mathrm{Re}(\boldsymbol{H}) \tag{2-87}$$

and the time-average real power density by

$$\boldsymbol{S_{av}} = \frac{1}{2}\mathrm{Re}\left(\boldsymbol{E} \times \boldsymbol{H}^*\right) \tag{2-88}$$

The instantaneous power densities for the fundamental TE mode in the lossless case at 10 GHz and 60 GHz are shown in figure 2.24 in linear scale.

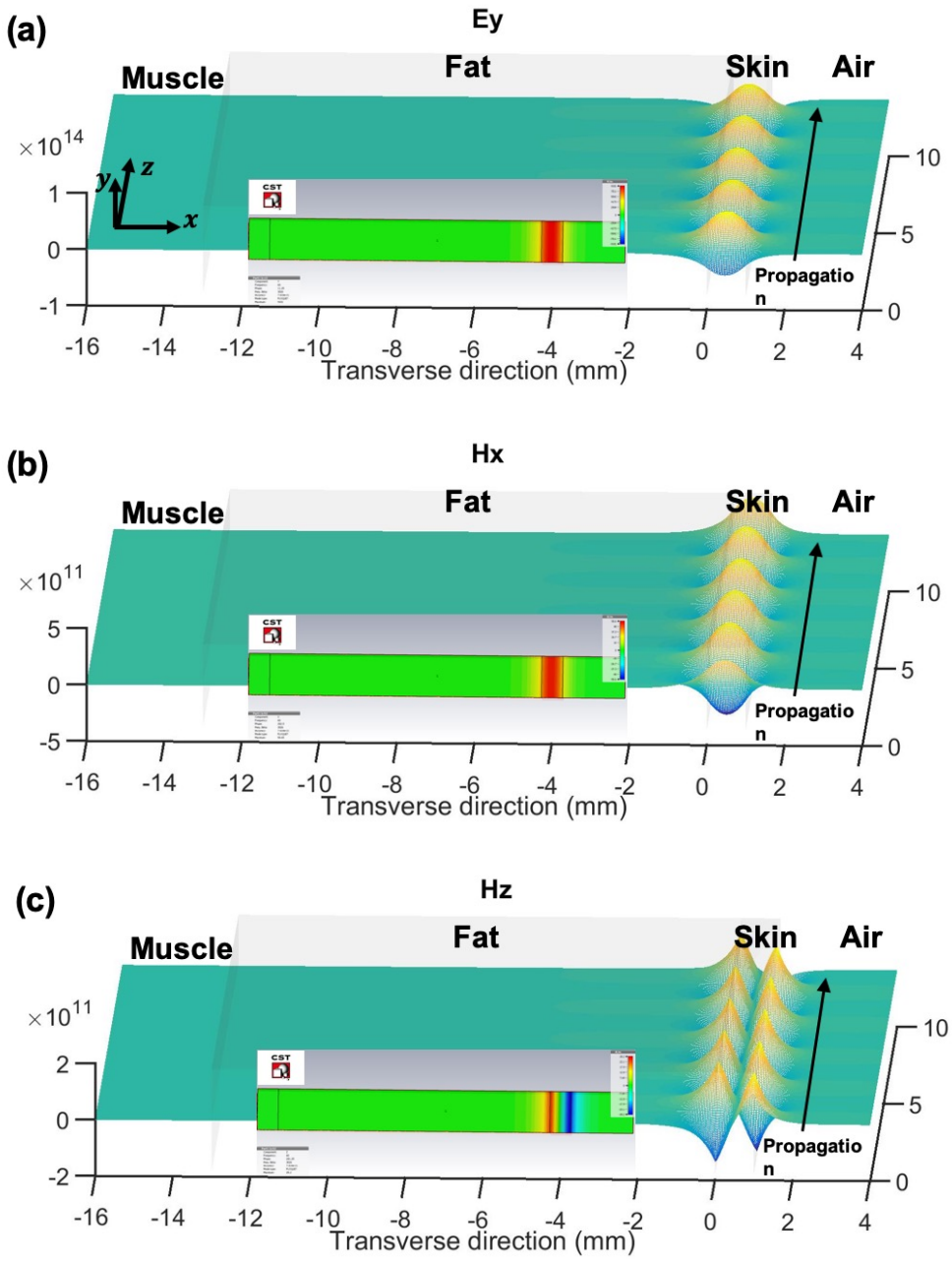

Figure 2.22: Field distributions of the fundamental TE mode of lossless body model at 60 GHz, skin thickness 1 mm and fat thickness 13 mm (a) E field in the y direction (b) H field in the x direction (c) H field in the z direction

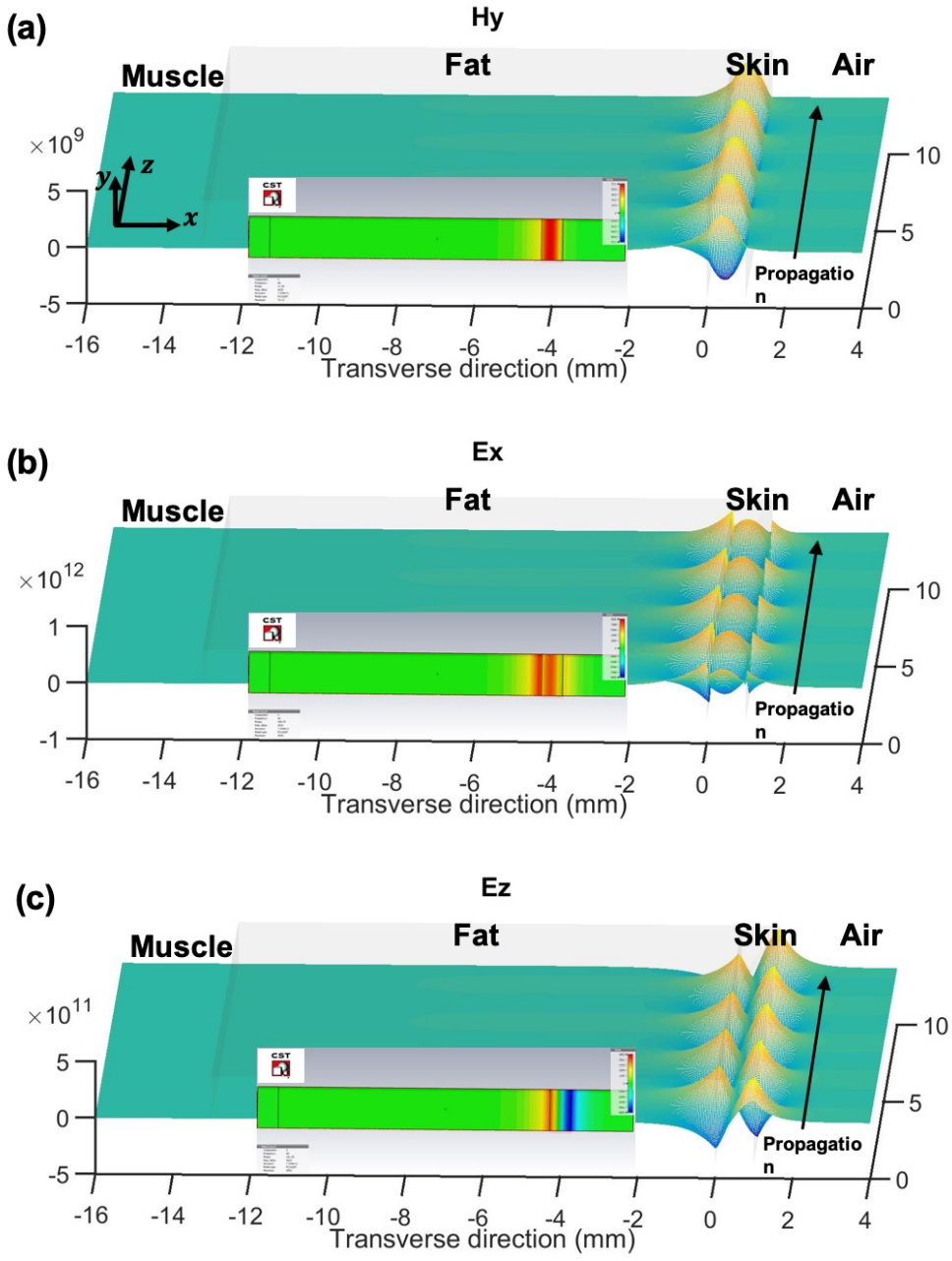

Figure 2.23: Field distributions of the TM(1) mode of lossless body model at 60 GHz, skin thickness 1 mm and fat thickness 13 mm (a) H field in the y direction (b) E field in the x direction (c) E field in the z direction

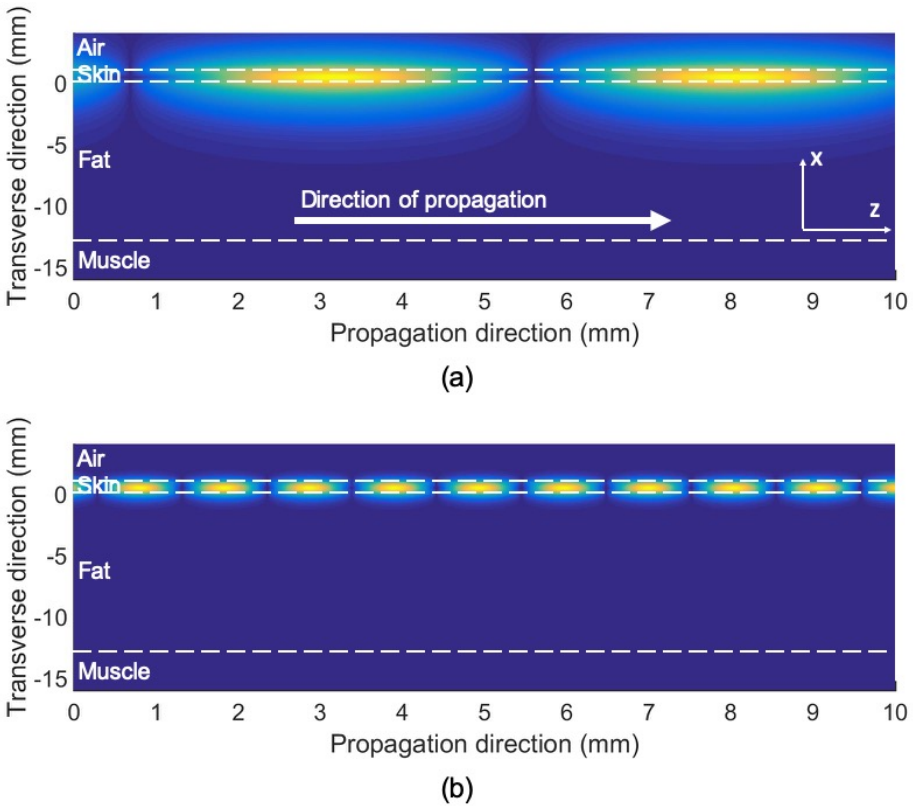

Figure 2.24: Instantaneous power density of the fundamental TE mode at (a) 10 GHz and (b) at 60 GHz for the lossless body model (skin thickness 1 mm and fat thickness 13 mm)

Again, it can be seen that the power is well confined inside the skin layer and the higher frequency leads to better confinement.

We now use the complex tissue permittivity in the TRM calculations to take into account the dielectric loss in the tissues. Figure 2.25 linearly exhibits the instantaneous power density of the fundamental TE mode at 4 GHz, 6 GHz, 8 GHz, and 10 GHz for the 1 mm-thick skin model. It can be clearly seen that the propagating wave at higher frequencies exhibits better skin-confinement property, but the attenuation in the direction of propagation is also greater. TE mode at 4 GHz has a 3.1 dB/cm attenuation in the direction of propagation, 15.2 dB/cm and 5.0 dB/cm in the transverse direction in the air layer and fat layer, respectively. The wave is better

confined at the skin/fat interface size. As for 10 GHz, the attenuations in the direction of propagation, the transverse direction of the air and fat are 17.7 dB/cm, 53.1 dB/cm, and 41.0 dB/cm, respectively. Therefore, the transmission frequency should be carefully chosen by considering the trade-off between the confinement and attenuation requirements, knowing that the confinement property is associated with the data security of the transmission and the attenuation in the direction of propagation involves the range and data rate of the wireless system.

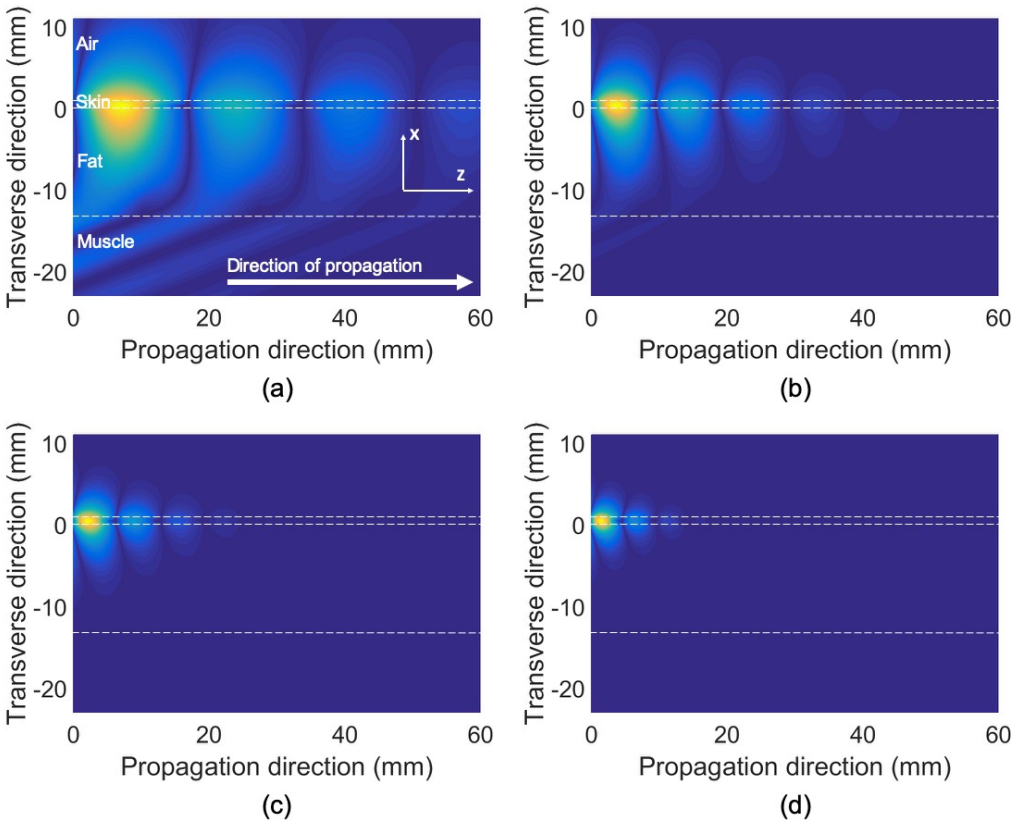

Figure 2.25: Instantaneous power density of the fundamental TE mode at (a) 4 GHz, (b) 6 GHz, (c) 8 GHz, and (d) 10 GHz) for the lossy 1 mm-thickness skin model

In addition, it can be observed that when dielectric loss is added to the tissues, the surface-waves in the air and fat layers have a propagation constant

vector that is no longer parallel to the skin/air and skin/fat surfaces but pointing inside the skin as discussed in the section 2.5 (figure 2.6).

To better illustrate the behavior of the two Zenneck surface-waves, the instantaneous power density of the "TM_Zenneck_Skin/Air" mode is shown in figure 2.26 for the 1 mm-thick skin model at 50 MHz (similar to the HBC band) and 1 GHz. It can be seen that at 50 MHz, even if this mode has ultra-low attenuation (0.02 dB/m) in the direction of propagation, the propagating wave is not bounded at all on the skin/air interface and exhibits approximately no transverse attenuation in the air (0.45 dB/m in the transverse direction). Therefore, the on-body propagation using this Zenneck mode at the HBC frequency is very easy to be intercepted. At 1 GHz, the attenuations in the direction of propagation, air transverse direction, and fat transverse direction are 0.1 dB/cm, 0.39 dB/cm, and 0.36 dB/cm, respectively. If the mode can be excited, this mode performs well enough for the on-body communication. However, as it is sensitive to the body surface impedance and has a upper cut-off frequency, the variation of the human body geometry in different persons (e.g., tissue thickness) may cancel this propagating mode at some higher frequencies.

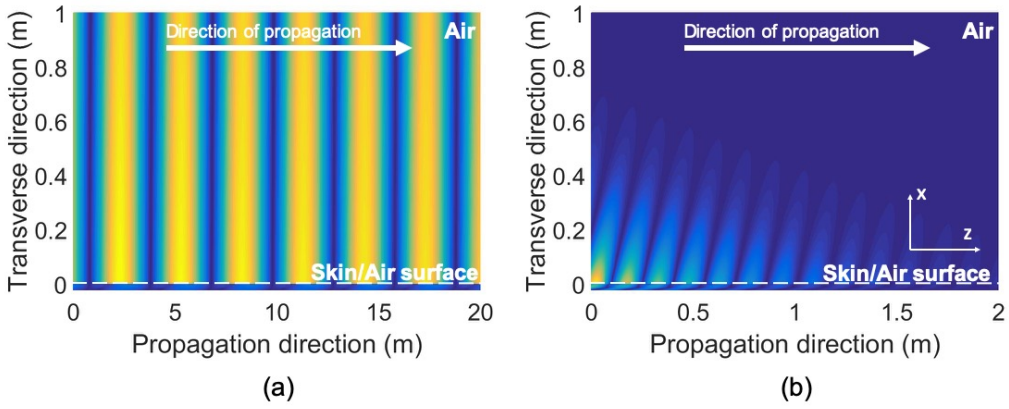

Figure 2.26: Instantaneous power density of the TM_Zenneck_Skin/Air mode at (a) 50 MHz and (b) 1 GHz for the 1 mm-thickness skin model

The "TM_Zenneck_Skin/Fat" mode propagating at the skin/fat interface is shown in figure 2.27 at 2 GHz and 6 GHz. This Zenneck mode has a lower transverse attenuation in the fat layer than the air layer (1.5 dB/cm,

4.9 dB/cm in fat and air at 2 GHz and 3.7 dB/cm, 20.7 dB/cm at 6 GHz, respectively). Most energy propagates in the fat layer, which may overheat the fat tissue [13]. In addition, since the muscle has a higher real part of permittivity than the skin, the propagation is attracted to the muscle/fat interface. Thus, it seems that this mode is more likely to be excited by a source located inside the human body.

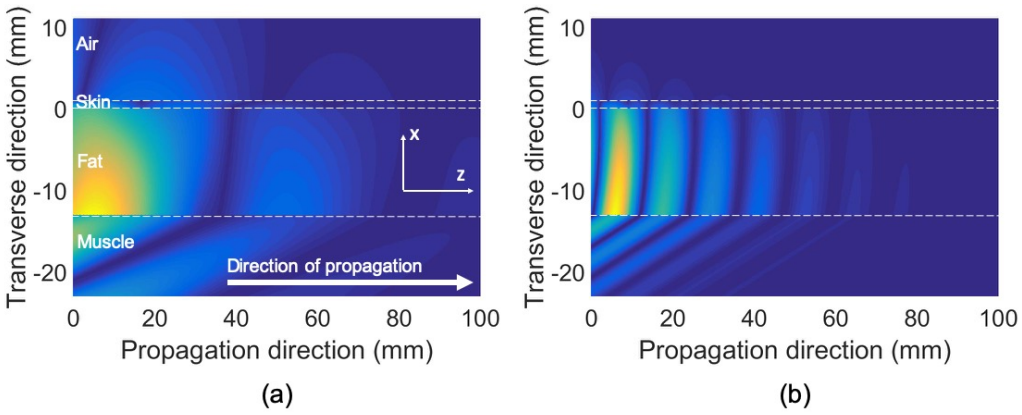

Figure 2.27: Instantaneous power density of the TM_Zenneck_Skin/Fat mode at (a) 2 GHz and (b) 6 GHz

Consequently, despite their low attenuation in the direction of propagation, these two modes do not exhibit any skin-confinement properties. More importantly, it is commonly accepted that these types of modes cannot be excited independently [151].

2.10.4 Fat thickness influence on the propagation

In order to study the influence of the muscle proximity to the skin on the fundamental TE mode, different thicknesses of fat ranging from 1 mm to 13 mm are studied, with the skin thickness fixed at 1 mm. The propagation and attenuation constants are given as a function of fat thickness in figure 2.28, with a frequency ranging from 4.5 GHz to 8 GHz (frequency range identified as a tradeoff between the skin-confinement and the attenuation along the direction of propagation). As shown in section 2.10.2, the propagation is less confined in skin at lower frequencies, which makes it more vulnerable to the

reflection from the fat/muscle interface. When the fat thickness decreases, larger attenuation and smaller propagation constant β are observed at a given frequency. The confined propagation is less sensitive to the change of fat thickness at higher frequency. Also, the cut-off frequency increases when the fat thickness decreases. No confined mode was found in the model with a fat thickness less than 10 mm at 4.5 GHz, 5 mm for 5 GHz, and 3 mm for 6 GHz. The thickness of fat layer noticed in medical articles varies from 1 mm to 50 mm [152], so the operating frequency should be used with respect to the expected location of sensors on the body, depending on the targeted application.

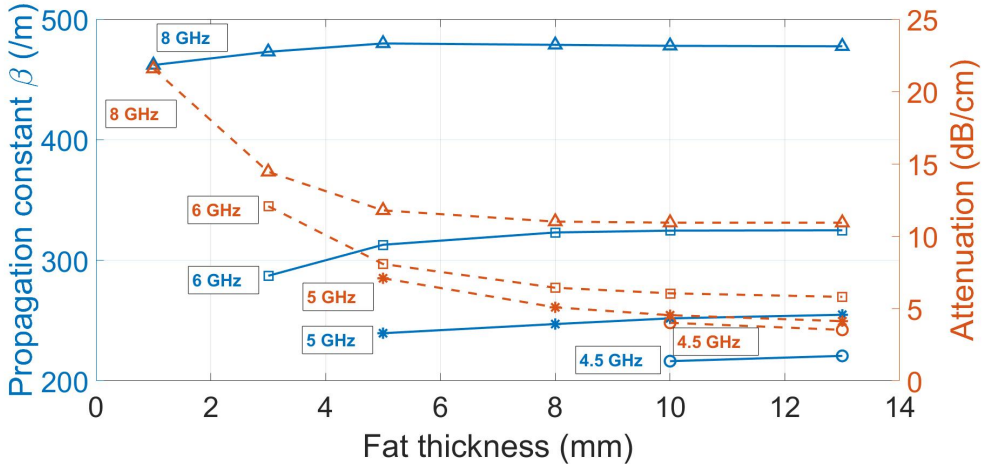

Figure 2.28: Propagation and attenuation constants in the direction of propagation in function of fat thickness (skin thickness is 1 mm)

2.10.5 Surface impedance

Surface impedance plays an important role in the propagation of surface-wave. In order to maximize the link performance, it is necessary to select a source that best fits the polarization of the propagating wave. In addtion, the surface impedance values should be considered when antennas are designed very close or in direct contact with the human body. The surface impedance of the multilayered human body model can be calculated using the transverse wavevector components obtained from the TRM calculations and the

transmission line technique. The deduced surface impedance values of the fundamental TE mode and the two Zenneck TM modes are shown in figures 2.29 and 2.30, respectively. According to [139, 153], the TM mode is supported by an inductive surface impedance, while the TE mode is supported by a capacitive surface impedance, which is verified in our analysis.

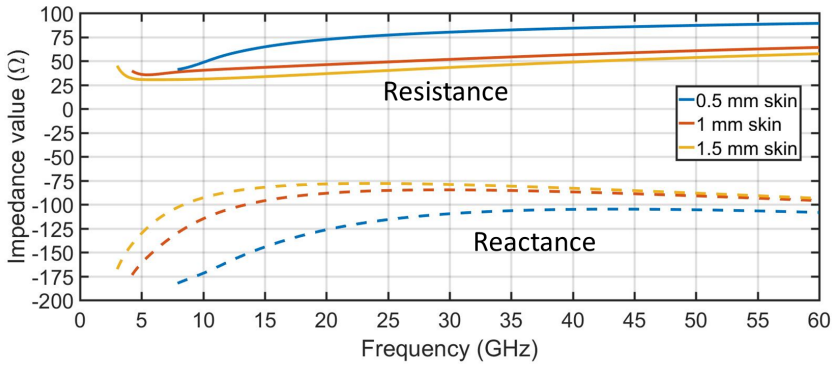

Figure 2.29: Fundamental TE mode surface impedance for different skin thickness models (0.5 mm, 1 mm, 1.5 mm) (fat thickness fixed at 13 mm)

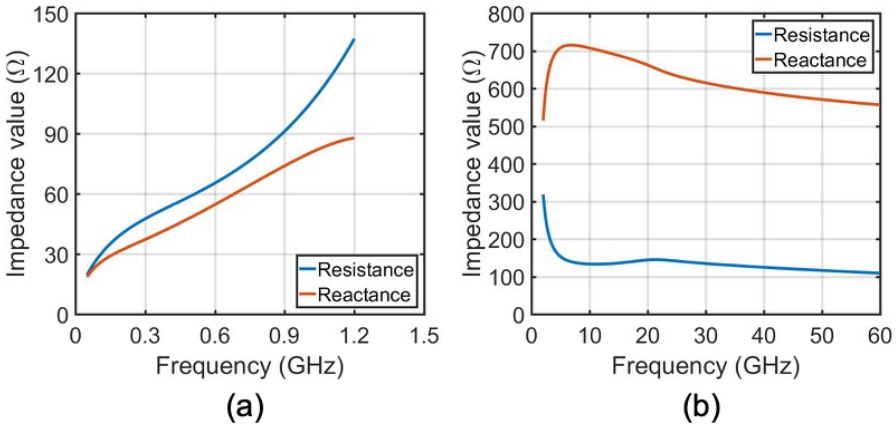

Figure 2.30: Zenneck TM modes surface impedances for the 1 mm-thickness skin model (a) TM_Zenneck_Skin/Air mode (b) TM_Zenneck_Skin/Fat mode

As can be seen from figure 2.29, the negative reactance of the fundamental

TE mode varies from -175j to -75j Ω, which represents a capacitive behavior. For the 1 mm-thickness and 1.5 mm-thickness skin models, the resistance is approximately 50 Ω, and for the thinner 0.5 mm-thickness skin model, the resistance is around 70 - 90 Ω. In contrast, the Zenneck TM modes possess a positive reactance value (inductance feature). It can be noted that the "TM_Zenneck_Skin/Fat" mode (figure 2.30(b)) exhibits very high surface impedance values in terms of resistance (500 - 700 Ω). However, this mode is more confined inside the human body and therefore has less impact on the on-body antennas.

2.11 Discussion for the Surface-Wave Excitation

In order to analyze the possibility of the skin-confined propagation mode excitation, a horizontally polarized $\lambda/2$ dipole antenna is simulated at 5 GHz with the multilayered human body model in CST (figure 2.31). The thicknesses of the air, skin, fat, muscle layers in the simulation are 30 mm, 1 mm, 13 mm, and 16 mm respectively. The dipole is located on the skin and is in direct contact with the skin. In order to increase the contact area of the dipole with the skin surface, the cross section of the dipole was chosen to be square form rather than cylindrical. As the dipole is horizontally polarized, this is similar to some extent to the galvanic coupling mechanism excitation

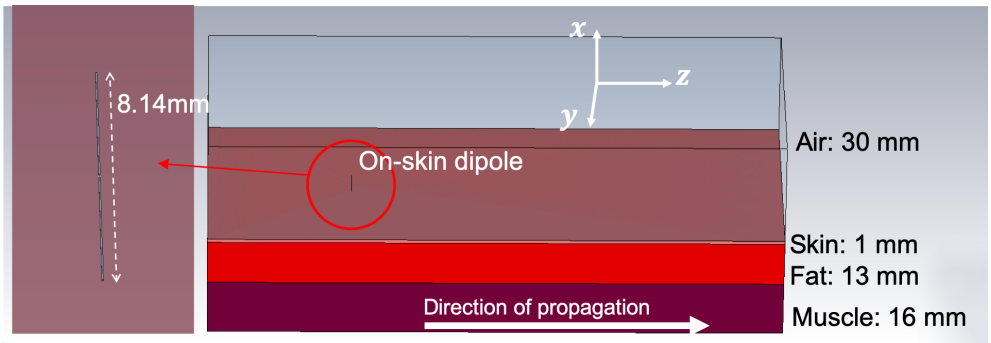

Figure 2.31: Horizontally polarized $\lambda/2$ on-skin dipole with the human body model

mentioned in section 1.10.1, thereby coupling with the fundamental TE skin-confined mode is expected is this simulation configuration.

Since the dipole is in contact with both air and skin, the characteristic wavelength used for the $\lambda/2$ dipole design should be between the intrinsic wavelength of air and skin, which at 5 GHz are 60 mm and 10 mm, respectively. The length of the dipole was finally optimized to 8.14 mm in the simulation. The S11 parameter is -9.4 dB at 5 GHz (figure 2.32), which signifies that 88% source energy was accepted by the dipole. In order to study the coupling ability between the dipole radiation and the skin-confined surface-wave, the dielectric loss was at first not taken into consideration.

The absolute electric field and the time-average power density is shown in figure 2.33. It can be seen that the power is confined in the skin and the electric field has the fundamental TE surface-wave mode as shown in figure 2.22. It should be noted that in our simulation the magnetic field intensity is very small compared to the electric field. From the electric filed distribution, the guided wavelength in the skin is spatially estimated as about 25 mm, which is an equivalent propagation constant β of about 250 rad/m. For the same model, the fundamental TE mode calculated with TRM has a propagation constant of 235 rad/m at 5 GHz, which fits with the simulation. In addition, it can be noted from the simulation that a certain amount of energy enters vertically the human body.

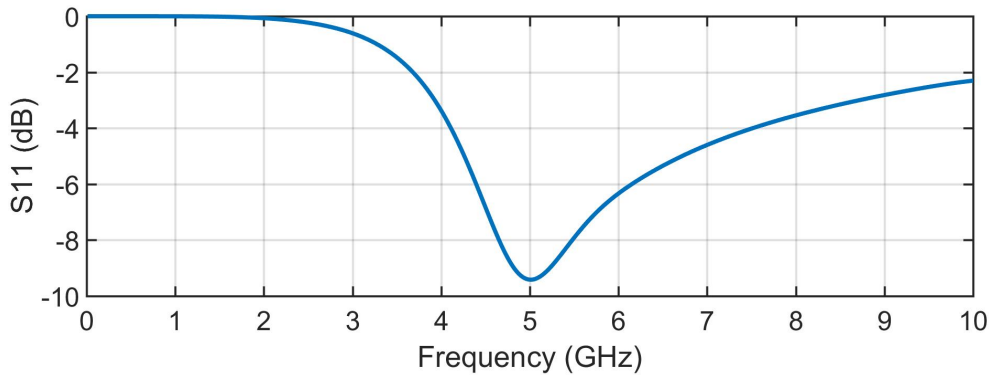

Figure 2.32: S11 parameters of the on-skin dipole at 5 GHz in lossless condition

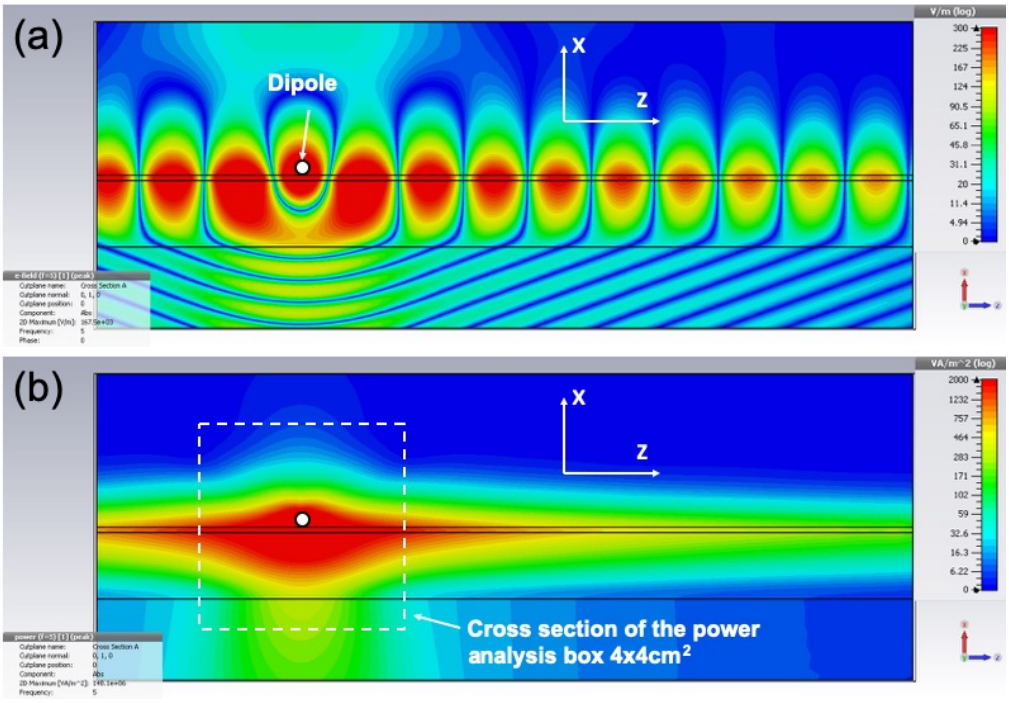

Figure 2.33: (a) Electric field distribution (dBV/m) and (b) time-average power density (dBW/m) of on-skin dipole in lossless case (skin thickness 1 mm, fat thickness 13 mm)

In order to obtain more insights regarding the power distribution in each layer, a closed square box of 4 x 4 x 4 cm^3 was placed around the dipole source as shown in figure 2.33(b), and the electromagnetic fields lying at each surface of the box were extracted from the simulation to calculate the outward power in all normal directions of the box. The box is divided into two parts, one lying in the air layer and the other one lying within the tissues (skin, fat, muscle). The purpose is to see how much energy is coupled to the human body. The calculation result is shown in figure 2.34, the unit for the values in the figure is mW.

As shown in figure 2.34, the average radiated power of the dipole (sum of all surfaces) is 451 mW. As mentioned at the beginning of this section, the S11 parameter showed that 88% energy is radiated from the excitation source of the dipole, and the excitation power in the simulation is 500 mW. Thus, theoretically, a total of 440 mW radiation power should be found form all the

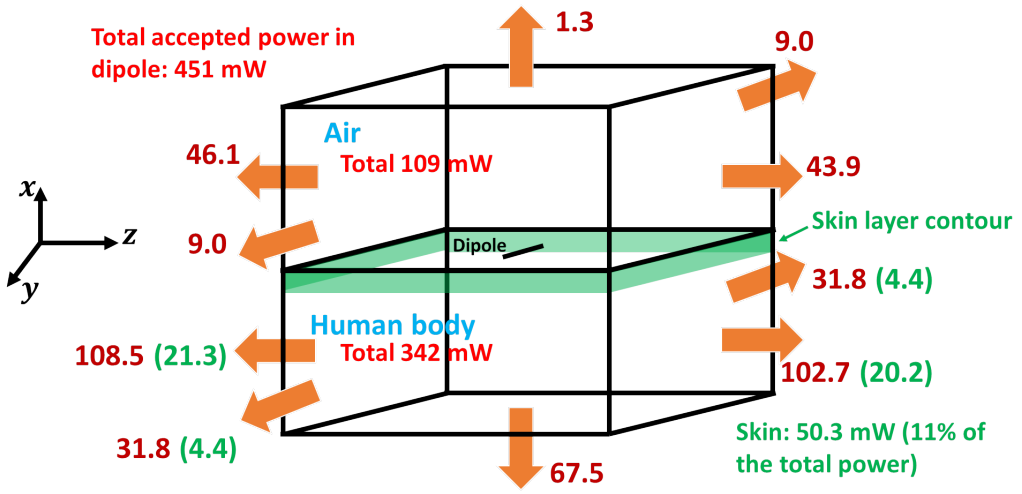

Figure 2.34: 4 x 4 x 4 cm^3 box for the outward power calculation (mW) of the on-skin dipole in lossless case (skin thickness 1 mm, fat thickness 13 mm)

surfaces of the closed box, which is in fair agreement with our calculations.

Figure 2.34 shows that 109 mW of power is radiated into the air and 342 mW of power is coupled to the human body (ratio 1:3). A 301 mW power (67% of the total power) follows the z-axis direction (the direction of the TE mode propagation) while a 67.5 mW power enters vertically the human body (15% of the total power). If we only observe the outward power from the skin layer along the z-axis and y-axis directions (shown with the green values in figure 2.34), we can observe that 11% of the total radiated power is completely confined inside the skin layer. However, as illustrated in section 2.10.2 as well as in figure 2.33, the surface-wave is less confined in the skin at low frequencies. These 11% of power are not the only useful power that can contribute to the link budget between the on-body transmitter and receiver, because even though the fundamental TE mode is confined to the skin, it also extends within air and fat layers. The coupling between the receiver sensor near-field and the TE mode determines the amount of power the receiver can collect. Therefore, the exact surface length along the x-axis that we should use to estimate the power that potentially contribute to the link budget is not trivial. For example, if the thickness of these surfaces exceeds the actual skin thickness (thereby, reaching the air and fat layers),

and becomes 3 mm instead of the previous 1 mm (i.e., extending 1 mm into air and fat), the calculated total skin-confined power is doubled from 50 mW to 93 mW, which is about 21% of the total radiated power.

To get even more insights, figure 2.35 shows separately the electric and magnetic energy distribution obtained by the simulation. It can be seen that the electric field exhibits stronger energy in the skin, witch confirms again the TE propagation mode coupling behavior from the horizontal dipole source.

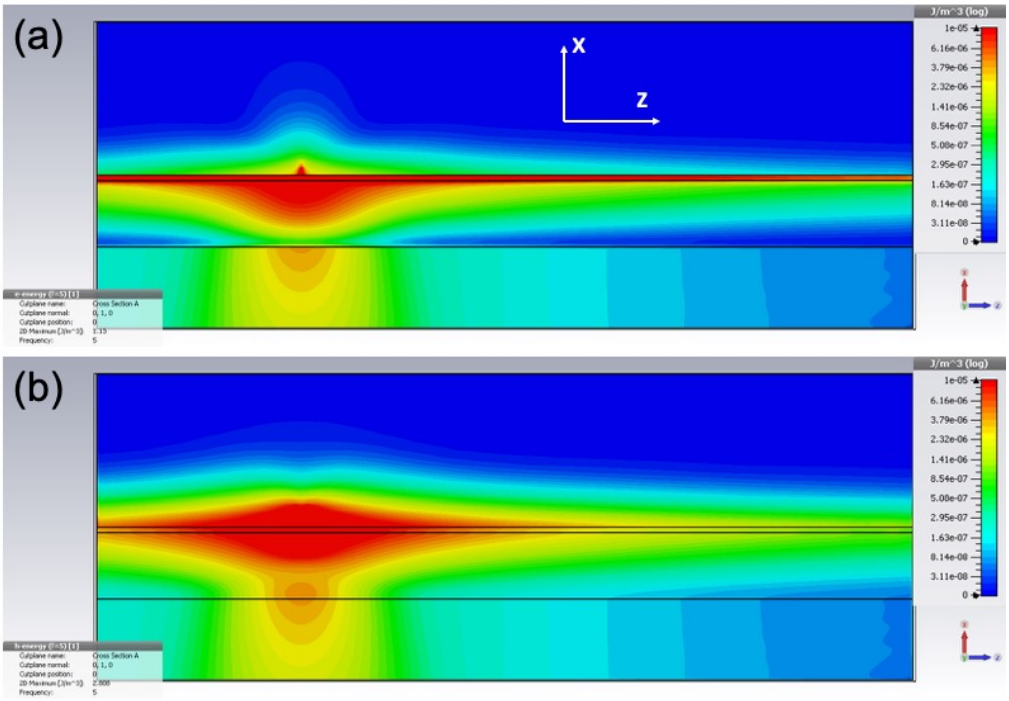

Figure 2.35: Average (a) electric and (b) magnetic energy density (dBJ/m^3) of on-skin dipole in lossless case (skin thickness 1 mm, fat thickness 13 mm)

Figures 2.36 and 2.37 show the S11 parameters and the absolute electric field distribution when dielectric losses are added into the simulation. The dipole impedance matching is slightly shifted to lower frequency (from 5 GHz to 4.8 GHz) and very high body power absorption is observed. The simulation showed that from a total of 497 mW accepted and radiated power from the dipole, 415 mW (84%) was absorbed by the skin, 6 mW and

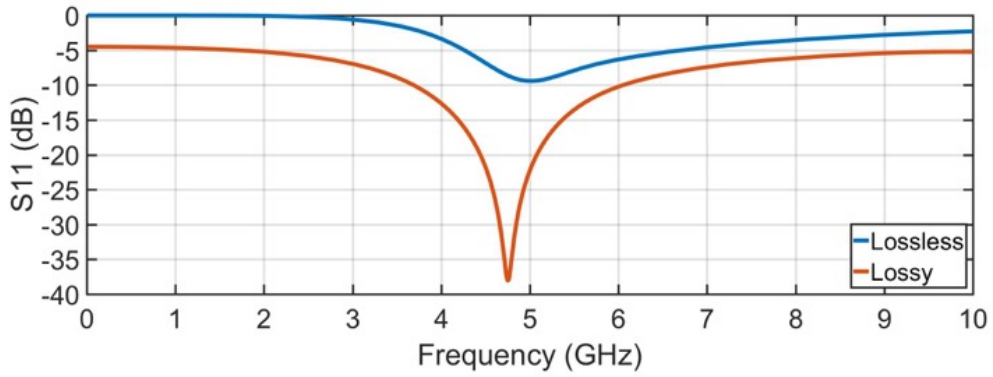

Figure 2.36: Comparison of S11 parameters of the on-skin dipole at 5 GHz between lossless and lossy conditions

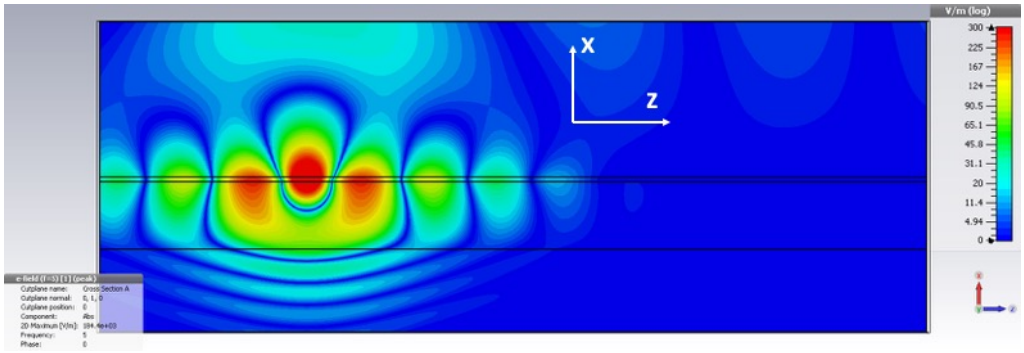

Figure 2.37: Electric field distribution (dBV/m) of the on-skin dipole in lossy case at 5 GHz

1 mW were absorbed by the fat and muscle tissues, respectively. This also indirectly shows that most power of the dipole is coupled to the skin-confined propagation wave.

Another situation was also simulated in which the horizontal dipole was inserted in the middle of the skin (in-body excitation). However, the observed phenomenon is very similar to the dipole on the skin. In this case, since the dipole is entire covered by the skin tissue, its length is reduced to 6.68 mm.

On the other hand, a more directive TE type antenna, such as an Yagi-Uda dipole array placed along the skin surface, is expected to be more efficient

for the excitation. Such directive antenna can avoid vertical excitation power towards the human body while coupling more energy into the skin layer in only one desired direction.

Nevertheless, it is clear that the fundamental skin-confined TE mode is possible to be excited by a horizontal dipole that sticks to the skin. It has also been observed that operating in the 3 - 8 GHz UWB frequency range could allow short-range propagation within the human skin. For instance, if we refer to the 15.7 dBm transmit power of the 500 MHz UWB bandwidth as mentioned in section 1.7 and a receiver detection level of -100 dBm, it can be deduced from table 2.5 that for the 1 mm-thickness skin and 13 mm-thickness fat human body model, the fundamental TE propagation mode can theoretically achieve a 37 cm communication range at 4 GHz and a 10 cm range at 8 GHz, respectively. While for the 0.5 mm-thickness skin and 13 mm-thickness fat model, the TE mode can realize a 20 cm communication range at 8 GHz.

As will be further explained in the following chapter 3, the leaky-wave antennas use traveling-waves as its radiation mechanism. This allows us to think of the possibility to use the human body channel (skin) as a transmission support for periodic leaky-wave antenna for off-body communication purposes. However, after our study, the attenuation of the on-body propagation is too large for leaky wave antenna designs, especially at high frequencies, knowing that high attenuation will result in large lobe form of the leaky-wave radiation. In addition, high attenuation in the direction of propagation will not allow the periodic leaky-wave antenna to have sufficient number of periods to efficiently radiate the traveling energy. Furthermore, even if the attenuation is relatively small at low frequencies, the size of leaky-wave antenna will be too large to be worn on the human body.

Nevertheless, the TRM dispersion analysis is still a very powerful approach for studying waveguides used in leaky-wave antenna designs, especially when the guiding structure becomes very complicated (e.g., adding a metasurface). Therefore, the TRM code developed in this chapter will be used in our next work to enhance the scanning range for leaky-wave antennas.

Chapter 3

Enhanced Scanning Range Leaky-Wave Antenna Design

As mentioned earlier, although remote monitoring using on-body sensors is becoming more and more attractive in the medical domain, they can still suffer from limited battery life and are not suitable for use in certain particular situations, such as burn patients. Moreover, placing on-body sensors on patients is an expensive and time-consuming work. Therefore, non-contact monitoring using Doppler radar has become a promising technique in medical monitoring, and leaky-wave antennas are very good candidates for Doppler radar because they have a very simple structure with high gain and frequency-scanning capabilities.

For such monitoring applications, fast scanning properties are typically desired to cover the entire surveillance area with a limited operating frequency bandwidth. Since leaky-wave antennas are based on guiding structures and their scanning capability is frequency dependent, our previously developed TRM dispersion analysis code will be very beneficial and powerful for analyzing the scanning capability of the leaky-wave antennas, especially when the guiding structure of the antenna becomes very complicated (e.g., multilayer structure, addition of metasurface, etc).

3.1 Introduction of leaky-wave antennas

A leaky-wave antenna is a traveling-wave guiding structure that uses some specific radiation mechanism to continueously leak energy along its length

to the surrounding area. This type of antenna is classified into a series of traveling-wave antennas that have been invented and used for more than 70 years [154]. A wide variety of applications and theoretical analysis have been developed. However, interest in such antennas at millimeter wavelength has only begun in recent decades [155].

The traveling wave in a leaky-wave antenna is typically characterized by a complex propagation constant

$$\gamma = \alpha + j\beta \tag{3-1}$$

where β is the phase constant of the waveguide, and α is the attenuation (leakage) constant due to the field leakage, which is defined by the leakage per unit length. The greater the leakage capability, the larger the value of α.

Since the leakage occurs over the length of the leaky-wave antenna, if the leakage rate is small and the length of the leaky-wave is finite, the propagation will reach the end of the antenna, so the entire length of the guiding structure will act as an effective aperture. In this case, since the radiation beamwidth depends on the effective aperture size, the beamwidth will depend on the antenna length, and the leakage constant α affects the radiation efficiency. In the other case where the leakage rate is large, all the guided fields leak away before reaching the end of the antenna, so the effective radiating aperture is smaller than the antenna length, thus the leakage constant α will in turn affect the beam width and a portion of the leaky-wave antenna is useless for the radiation. Therefore, the antenna length in this case should be carefully chosen to ensure the efficiency of the radiating structure. It is well known that a small effective aperture provides a large beam, so a small leakage constant α will result in a narrow beam with a sufficient length of guiding structure.

As indicated in figure 3.1, the direction angle θ of the main radiation beam of the leaky-wave antenna relative to the broadside direction (i.e., normal to the antenna surface) is calculated as

$$\theta = \sin^{-1}\left(\frac{\beta}{k_0}\right) \qquad \text{with } |\beta| < k_0 \tag{3-2}$$

where k_0 is the free space wavenumber, which can be deduced from the previous equation (2-2) in section 2.3. Obviously, the direction of radiation depends on the propagation constant β of the guiding structure. If the waveguide is dispersive, i.e., β changes with frequency, the direction of radiation can be controlled by varying the frequency of the waveguide excitation port.

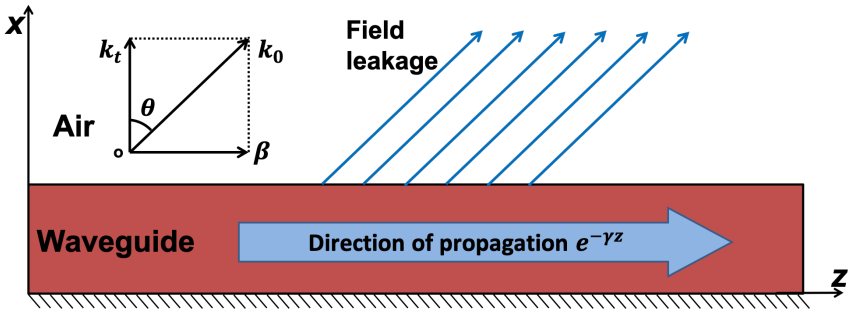

Figure 3.1: Radiation mechanism of leaky-wave antenna

Therefore, the leakage constant α and the phase constant β along the propagation direction of the waveguide characterize the radiation of leaky-wave antenna. The phase constant β controls the direction of the radiation and the leakage constant α controls the beamwidth and the radiation efficiency. Furthermore, large variations in the amplitude of the field distribution along the leaky-wave antenna may result in high sidelobe levels. For this reason, the leakage constant α should be well considered in the antenna design to ensure low sidelobes and high radiation directivity.

3.2 Advantages

Leaky-wave antennas have many advantageous properties. Typically, a leaky-wave antenna has a directive narrow beam with high gain [156, 157]. This is important to ensure reliable, efficient, and high data rate wireless communication. Moreover, the radiation beam has frequency-scanning characteristics that make the antenna suitable for use in radar detection systems [156, 158].

Compared to conventional antenna arrays, the beam scanning mechanism of a leaky-wave antenna does not require feeding network to feed the antenna, which makes it simpler and more cost-effective [157, 159, 160]. Leaky-wave antennas are basically planar or quasi-planar structures that have a low profile [161] and are compatible with other planar devices [162]. When produced in large quantities, periodic elements such as printed metal strips or dielectric grooves can be fabricated using a simple etching process, which greatly reduces manufacturing costs. Since the antenna is made of a guiding structure

and uses traveling-wave as the radiating mechanism, it could limit undesired and imperfect transitions between guiding media.

3.3 Fast-Wave and Slow-Wave

A fast wave is a propagating wave whose phase velocity ν_p is greater than the speed of light in free space

$$c = \frac{1}{\sqrt{\mu_0 \varepsilon_0}} \simeq 3 \times 10^8 \text{ m/s} \tag{3-3}$$

where μ_0 and ε_0 are the free space permeability and permittivity, respectively. At a given frequency, the relation between the phase velocity ν_p and the phase constant β of a wave propagating in a waveguide is

$$\nu_p = \frac{\omega}{\beta} \tag{3-4}$$

where ω is the angular frequency. The fast-wave definition then leads to

$$\nu_p > c \tag{3-5}$$

Consider that the convention of propagation is $e^{-j\beta z}$ as shown in figure 3.1, and the wave propagates in the positive direction ($\beta > 0$), equation (3-5) reduces to

$$\frac{\omega}{\beta} > \frac{1}{\sqrt{\mu_0 \varepsilon_0}} = \frac{\omega}{\omega\sqrt{\mu_0 \varepsilon_0}} = \frac{\omega}{k_0} \tag{3-6}$$

thus

$$0 < \beta < k_0 \tag{3-7}$$

This means that if the phase constant β of the propagating wave along the propagation direction is smaller than k_0, the wave is considered to be a fast-wave.

As described in section 2.3 and shown in figure 3.1, the free space wavenumber k_0 can be decomposed into a component k_t in the transverse direction (x-axis) and a component β in the direction of propagation (z-axis) by the following relation:

$$k_0^2 = \beta^2 + k_t^2 \tag{3-8}$$

Thereby, we can deduce the transverse wavenumber as

$$k_t = \sqrt{k_0^2 - \beta^2} \tag{3-9}$$

In the case of fast-wave $\beta < k_0$, the transverse component k_t is a positive real value, which means that the wave travels in the transverse direction away from the guide. This explains that the fast-wave leaks its energy from the guiding structure, which is the main mechanism of the leaky-wave antennas.

Conversely, for $\beta > k_0$, the phase velocity of the propagating wave is less than the speed of light in free space, thus the wave is referred to a slow-wave. In this case, the solution of the transverse component is an imaginary value, which is interpreted as the exponential decay of the wave away from the waveguide in the cross direction. Therefore, the slow-wave is bounded to the guiding structure and no radiation occurs. Moreover, there is no longer real-value solution to the direction of leakage θ. Instead, a surface-wave is formed at the interface between the guide and the air as introduced in section 2.5 of chapter 2. Surface-waves are characterized by propagating waves that decay exponentially away from the waveguide surface, with most of the energy contained in or near the guide. This the main mechanism of open waveguides such as dielectric slab. At higher frequencies, the propagation typically becomes more tightly bound to the guiding structure.

For the propagation opposite to the direction defined in the convention $e^{-j\beta z}$, i.e., $\beta < 0$, the definitions of fast-wave and slow-wave are similar. Figure 3.2 defines the fast- and slow-wave zones in the "frequency - propagation constant" plane.

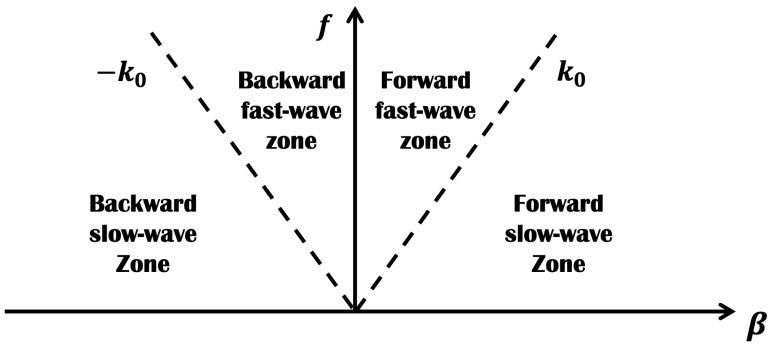

Figure 3.2: Fast-wave and slow-wave zones

As mentioned before, a leaky-wave antenna need to have a fast-wave component to radiate energy from the structure. If $0 < \beta < k_0$, the leakage

is in the forward direction, and conversely, if $-k_0 < \beta < 0$, the leakage occurs in the backward direction. In other slow-wave cases, waves are confined in the guide while leakage and radiation do not occur.

3.4 Different Types of Leaky-Wave Antenna

According to the geometry of the antenna along the direction of propagation, leaky-wave antennas can be classified into two categories : uniform antennas and periodic antennas. The uniform antennas have a uniform geometry along its length while the periodic antennas are periodically loaded or modulated.

3.4.1 Uniform leaky-wave antenna

The first leaky-wave antenna models were introduced in the 1940s based on closed guiding strucutres. One can be found in [154], which is a rectangular waveguide with a continuous slit cut in one of its guiding walls, as shown in figure 3.3. Since its geometry is uniform along the direction of propagation, this is a typical model of uniform leaky-wave antennas. In fact, all of these initial leaky-wave antennas in the 40-50s were based on uniform geometries. Since the rectanglar waveguide is filled with air, the propagation in the guide is a fast-wave [136]. The closed waveguide characteristic allows propagation to be confined inside the guide without energy leakage. However, if a long uniform slit is introduced over the length of the guide, the closed structure is opened at the slit as an aperture of magnetic current line, and the fast-wave will leak into the air, thereby achieving radiation.

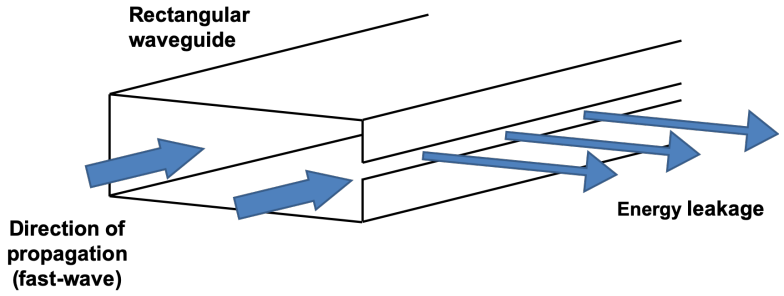

Figure 3.3: The first leaky-wave antenna model

Since the traveling-waves in the guiding strucutre propagate only in the forward direction, the energy leakage direction is thereby only in the forward quadrant, and the antenna can scan the beam with frequency from broadside to forward end fire. The antenna pattern is typically conical, and when radiation direction approaches to the broadside, the pattern form will change into a narrow donut-type shape [155]. However, the radiation beam cannot be too close to the broadside and the end fire direction. Assuming the antenna radiates in the broadside direction, according to equation (3-2), the phase constant β is then equal to zero and we are at the cutoff of the waveguide [139]. This is equivalent to a wave that does not travel in the guiding structure, and the traveling-wave antenna theory cannot be applied. On the other hand, if the antenna is supposed to radiate towards end-fire, this means that the phase constant β is equal to the free space wavenumber k_0. This is typically a TEM mode as described in section 2.3, which is not supported by a rectangular waveguide [139].

In recent years in the early 2000s, a new type of leaky-wave antenna, CRLH (Composite Right/Left Handed) antenna [163, 164], has attracted the attention of researchers. This type of antenna is commonly referred to as metamaterial leaky-wave antenna [165–167] or dominant mode leaky-wave antenna [168], which is typically a periodic structure whose unit cell size is very small with respect to the wavelength. The small size of the unit cells makes it possible to treat the CRLH strucutre as a homogeneous media, and so considering the CRLH strucutre as electrically uniform. The periodicity in such structures plays no direct role in radiation [161], and transmission line theory is typically used to analyze the behavior of such structures.

In theory, the CRLH structure consists of a right-handed (RH) section and a left-handed (LH) section, which can be modeled as an equivalent L_RC_R-C_LL_L circuit as shown in figure 3.4(a). Such structure can be realized by resonant cells as shown in figure 3.4(b) [165]. The characteristic of the RH section (L_RC_R circuit) can be referred to as a classical transmission line having a positive permittivity and permeability, while the LH section (C_LL_L circuit) has an atypical characteristic with a negative permittivity and permeability, which results in wave propagation having opposite phase velocity and group velocity. This nature allows the circuit to radiate at certain operating frequencies with beam scanning feature from the backward region to the forward region.

CRLH leaky-wave antenna can also eliminate the open stopband encountered in the traditional periodic leaky-wave antennas by adjusting the equiv-

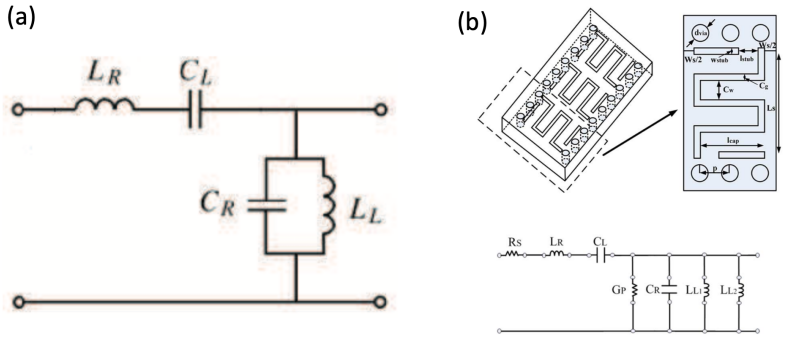

Figure 3.4: (a) CRLH unit cell equivalent circuit (b) example of CRLH resonant unit cell based on SIW transmission line [165]

alent unit cell circuit to a "balanced" condition $L_R C_L = C_R L_L$, so that the beam can scan through broadside from the backward region to the forward region without suffering from pattern degradation [161, 167], i.e., no radiation null at broadside. This is the main advantage of the CRLH leaky-wave antennas. However, it is not easy to maintain the balanced condition between different frequencies due to the high sensitivity of the dimensions of the CRLH strucutre [165]. In addition, the state of the art shows that it would take a very large number of cells to achieve an acceptable radiation efficiency. The structure at high frequencies is very complicated to design and fabricate, and exhibits low tolerance to fabrication and measurement inaccurancies [169]. Moreover, design optimization of such structure may take a large amount of time.

3.4.2 Periodic leaky-wave antenna

The other type of leaky-wave antenna is the periodic leaky-wave antenna, which is based on waveguides supporting slow-wave modes. The fundamental surface-wave mode is transformed into a leaky mode by periodically loading the structure along its length [161].

This type of antenna appeared decades after the emergence of the uniform leaky-wave antenna. One of the earliest periodic leaky-wave antenna models was introduced in [170], where an image dielectric line was used for the waveguide and an array of slots was cut into the ground plane on each

side of the narrow dielectric central line. The most commonly used slow-wave guiding strucutre in this class is the rectangular dielectric slab with or without ground plane. Since the waves propagating in the guide are slow-wave, even if the guide is open, they are bounded within the guide. However, surface perturbations, such as grating of grooves [171, 172] or grating of metal strips [173], can be added to the guiding structure to make it leaky, thereby achieving radiation. Figure 3.5 shows a classical periodic leaky-wave antenna model in which metal strips are periodically placed along the longitudinal direction of a grounded dielectric slab. In general, it is necessary to well select the dimensions (e.g., thickness) of the dielectric slab such that only the dominant mode propagates in the guide to ensure high radiation efficiency.

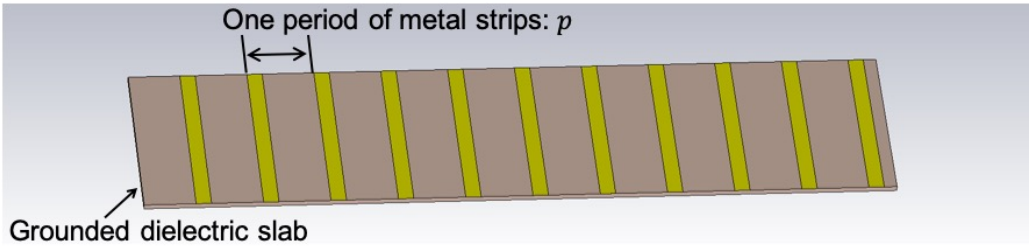

Figure 3.5: One classical periodic leaky-wave antenna based on a grounded dielectric slab covered with periodic metal strips

For slow-wave modes, leakage occurs only when discontinuities are presented on the waveguide. The added periodic arrays on the slow-wave guides can be effectively considered as discontinuities. According to [174], adding periodicity to the waveguide will create an infinite number of space harmonics (also called Floquet waves), and the propagation constant of the n-th space harmonic β_n is calculated as

$$\beta_n = \beta_0 \pm \frac{2\pi n}{p} \qquad (n = 0, \pm 1, \pm 2...) \tag{3-10}$$

where p is the spatial period of the grating and β_0 is the propagation constant of the fundamental space harmonic, which is often assumed to be equal to the phase constant β of the dominant slow-wave propagation mode of the guided wave without periodic perturbation. It should be noted that the addition of periodicity may modify the original dominant propagation mode of the

guide, i.e., $\beta_0 \neq \beta$. However, the added periodic grating is usually designed to not disturb too much the original propagation mode (e.g., narrow slots or strips).

When periodicity is added to the guiding structure, one or more space harmonics may fall into the fast-wave zone, as shown in figure 3.6, causing energy to leak from the waveguide, while other harmonics fall into the slow-wave zones bounded within the structure. However, since the space harmonics are all tied together and form the dominant propagation mode in the guiding structure, if one or more of the space harmonics becomes fast, the whole mode becomes leaky. Typically, only one radiation beam is desired in a leaky-wave antenna design, and the $n = -1$ space harmonic is the most used in the current literature, and the only one that falls into the leaky zone (i.e., $|\beta| < k_0$).

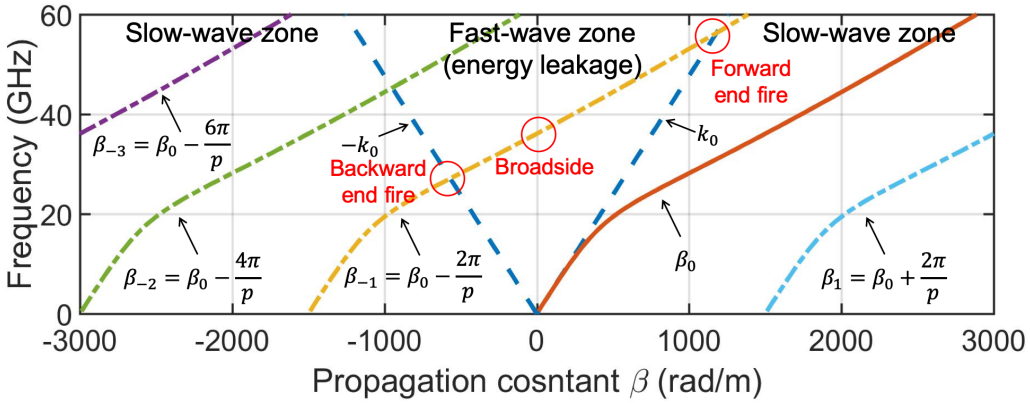

Figure 3.6: Space harmonics of periodic leaky-wave antenna

As can be seen from figure 3.6, at low frequencies, all space harmonics are slow and no radiation occurs. When the frequency reaches a critical value at which the $n = -1$ harmonic first becomes fast, the radiation beam emerges from the backward end-fire into the backward quadrant. As the frequency increases, the beam steers to the broadside and then to the forward quadrant. In contrast to the uniform antenna that can only radiate in the forward quadrant, the above mechanism allows the periodic antenna to scan from backward end-fire to forward end-fire. However, similarly to the uniform antenna, the radiation exhibits a narrow "open stopband" at the broadside radiation. In this stopband, the radiation is greatly reduced and

a high VSWR (Voltage Standing Wave Ratio) is encountered, which means that power is reflected back to the source instead of being radiated [175]. However, some methods may be used to eliminate this stopband, such as using a multilayer guiding structure [176] or periodically using a pair of perturbation arrays instead of a single one [177, 178].

3.5 Applications of Leaky-Wave Antenna

The numerous advantageous features of leaky-wave antennas, such as frequency beam scanning, low cost, highly directive beam pattern, and compatibility with other planar devices, make them attractive for radar systems, satellite communications, remote medical sensing, etc [162, 176]. Much effort has been made in the research community to design a leaky-wave antenna that maintains a fixed beam direction over a bandwidth as large as possible [179]. This is suitable when one wants to establish communication toward a specific area while benefiting from the interesting features of the leaky-wave antenna (e.g., high gain with low complexity). Comparatively, fewer works use the leaky-wave antenna's scanning capabilities that are interesting for radar-like applications. The benefit here is the opposite: maximizing the scanning range for a given frequency bandwidth. In the following sections, we introduce some applications where the leaky-wave antennas are used for their scanning properties.

3.5.1 Cooperative smart cars system

In [180], a CRLH Leaky-wave antenna is designed for the cooperative system of "smart cars". In recent years, more and more vehicles have been equipped with numerous electronic devices to enhance automotive safety. With these electronic devices, vehicles collect and interactively share traffic information (e.g., location of surrounding vehicles, real-time routing situations, pedestrian alerts, traffic signal timing, etc.) between them or with surrounding infrastructures (figure 3.7). This can detect the potential problems for drivers and help them avoid accidents. In addition, the system helps drivers save energy and time by selecting optimized navigation.

For communications of moving vehicle, V2X (Vehicle to Everything) wireless communication plays an important role and requires beam-scanning antennas to detect the position (distance, angle, etc.) of surrounding moving

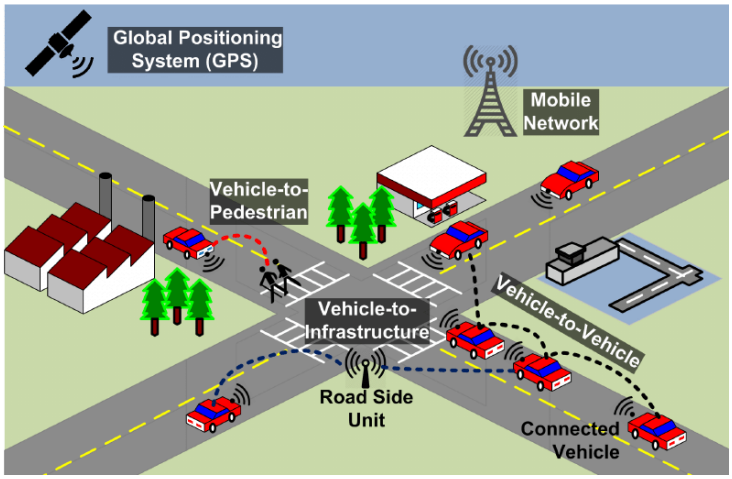

Figure 3.7: V2X (Vehicle to Everything) communication system [181]

vehicles, thereby continuing to establish an adaptive wireless link. Basically, this function can be implemented with a phased antenna array. However, the array antennas need relatively larger dimension to ensure high gain. Moreover, as the dimension of the array increases, the number of phase-shifters makes the antenna very expensive and complicated to manufacture. Leaky-wave antennas then become good candidates for such applications.

3.5.2 Real-time spectrum analyzer

In [182], using the frequency beam scanning characteristics of a leaky-wave antenna, a microwave analog real-time spectrum analyzer (RTSA) is implemented to analyze transient complex non-stationary signals (figure 3.8). In recent years, ultra-wideband (UWB) systems have rapidly emerged in the domains of radar, security and EMC (Electromagnetic compatibility). These systems typically use ultra-fast transient signals with rapid spectral variations in time. In order to characterize these transient signals, real-time time-frequency display is required to obtain simultaneously time and spectral information, where the signal energy distribution can be color-coded at each time-frequency point [183].

At microwaves, RTSAs are typically based on digital short-time Fourier transform (STFT) [182]. For UWB signals with ultra-fast transients, high

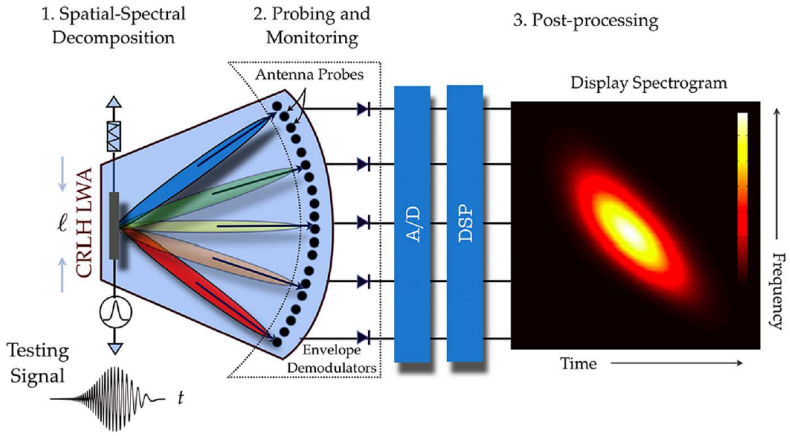

Figure 3.8: Real-time spectrum analyzer (RTSA) scheme using leaky-wave antenna [182]

time-resolution STFT requires small sampling durations, which results in long acquisition times. Therefore, the STFT process requires a large amount of computing and memory resources, which can severely affects the RTSA system functionalities and limits its performance to UWB systems.

The leaky-wave antenna based RTSA uses the spectral-spatial feature of the antenna. Since the leaky-wave antenna may have large bandwidth frequency-scanning characteristic, probes can be angular-separately mounted at different far field positions, as shown in figure 3.8, to easily measure the power variation of the corresponding frequency in real-time. The measurement results are then sent to the post-processing unity for data processing and display. Compared to digital RTSAs, the leaky-wave antenna based RTSA has the advantage of instantaneous acquisition, low computational cost, frequency scalability, and wideband operation.

3.5.3 5G signal direction of arrival estimation

The forthcoming fifth-generation (5G) mobile cellular communications technology is considered to be a "key technology" that connects everything in modern society. In the future, not only smartphones, but all electronic objects will be connected to the network and work together to make our society "intelligent" (e.g., smart cities, home automation, smart electric grids,

healthcare enhancement, etc.). In order to build such cooperation, 5G networks require high data rates, reduced latency, and large-scale device connectivity. With 5G connection, new emerging technologies such as virtual reality and augmented reality could be ensured to be available to everyone on the move. Applications and services that require high data rates, such as cloud computing, 4K streaming movies, and holographic technology, will also be delivered over wireless connections. Moreover, the reduced latency makes real-time control such as driverless cars possible.

In order to power-effectively realize high data rates, the signal is directed using narrow radio beam from the base station toward a specific direction where the user is located, rather than being emitted in all directions as in the conventional mobile cellular network. Therefore, beam scanning antennas are required. In such applications, DoA (Direction of Arrival) estimation plays an important role to find the nearby connected devices, get their locations and directions of movement, thus accurately estimate the direction of the arriving signal in order to assign the user an appropriate data transmission beam with a specific angle.

In [184], a SIW-based leaky-wave antenna is proposed for DoA estimation in the 5G candidate millimeter band (57 - 66 GHz). The angle of incidence is estimated by measuring the power through the leaky-wave antenna at different frequencies. With the frequency of the peak of the measured power, the corresponding signal arrival direction can be deduced since the leaky-wave antenna is a frequency depending beam scanning antenna. The proposed antenna has high efficiency at the broadside and has low return loss. However, the antenna has a scanning range of only 16° (from -8° to 8°) and the detection range is only within one meter.

3.5.4 Non-contact medical monitoring

As mentioned in section 1.4, non-sensor medical applications have numerous advantageous features, such as enhanced mobility, long-term operating time, etc. The leaky-wave antennas could be very beneficial for such applications.

In [185], CRLH leaky-wave antennas are applied to Doppler radar in the frequency range of 5.1 to 6.5 GHz for detecting human vital signs (breathing and heartbeat rates). In the proposed model (figure 3.9), two identical leaky-wave antennas are separately used for transmission and reception. The transmission signal is controlled by a voltage-controlled oscillator. At the operating frequency band, the effective scanning coverage of the antenna

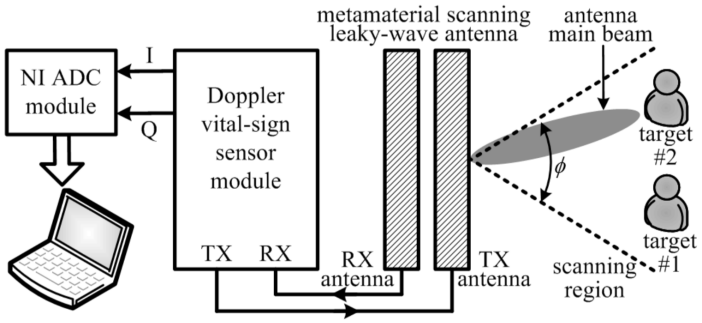

Figure 3.9: Leaky-wave antenna based non-contact medical monitoring [185]

is 59°. At the reception module, the Doppler frequency is derived by processing the transmitted and received signals in an in-phase/quadrature-phase (de)modulator, and finally a fast-Fourier transformation is applied to display the measured breath and heartbeat rates in the spectrogram. The measured heartbeat rate is compared to data measured simultaneously by a finger pulse sensor and good agreement is observed between the two results.

3.6 Scanning Range of Leaky-Wave Antennas in Current Literature

Table 3.1 shows some current leaky-wave antennas in the literature and their characteristics, including substrate relative permittivity ε_r, maximum gain, beam-scanning range, bandwidth, fractional bandwidth (FBW), and scanning-range/bandwidth ratio (SRBR). The FBW is calculated as

$$\text{FBW} = \frac{f_{max} - f_{min}}{f_c} \tag{3-11}$$

where f_{max} and f_{min} are the lower and upper frequencies of the operating band, respectively, and f_c is the center frequency, i.e., $(f_{max} + f_{min})/2$. FBW is commonly used to qualify how wide the bandwidth of an antenna, which typically varies up to 200%. The SRBR here is defined as the scanning range divided by the FBW and is a useful metric to determine how fast is the angular scanning, regardless the carrier frequency.

Ref.	Antenna type	Thickness [mm]	ε_r	Scan range [°]	Gain [dB]	Bandwidth [GHz] and fractional bandwidth	SRBR [°/%]
[186]	GDS periodic LWA	0.648	2.25	-24 to 0 (24)	17	140 to 175 (22%)	1.1
[187]	GDS periodic LWA	12.7	2.8	-70 to -5 (65)	17	4.5 to 6.5 (36%)	1.8
[176]	GDS periodic LWA	1.27	10.2	-15 to 10 (25)	16	22 to 25 (13%)	1.9
[162]	GDS periodic LWA	1.27	10.2	-5 to 14 (19)	23.5	20 to 22 (10%)	1.9
[188]	GDS periodic LWA	2.54	10.2	-65 to 25 (90)	16	12 to 17 (34%)	2.6
[158]	GDS periodic LWA	0.5	11.9	18 to 38 (20)	14.2	153 to 165 (8%)	2.5
[189]	GDS periodic LWA	0.4	11.9	-20 to 0 (20)	18	97 to 103 (6%)	3.3
[190]	SIW periodic LWA	0.8	3.55	-35 to 35 (70)	12.5	8 to 12 (40%)	1.8
[191]	SIW periodic LWA	1.524	3.66	-40 to 25 (65)	15	10 to 14 (33%)	2.0
[178]	SIW periodic LWA	1	10.2	-78 to 47 (125)	15	12.3 to 15.6 (24%)	5.2
[192]	Insert dielectric guide periodic LWA	2.393	2.9	-9 to 40 (49)	14.2	50 to 85 (52%)	0.9
[193]	Microstrip line periodic LWA	1.575	2.2	-3 to 3 (6)	16	9.7 to 10.3 (6%)	1
[194]	SIW CRLH LWA	0.76	2.17	-70 to 70 (140)	12	7.5 to 13.5 (57%)	2.5
[159]	SIW CRLH LWA	0.254	2.2	-28 to 15 (43)	20	50 to 70 (33%)	1.3
[166]	SIW CRLH LWA	0.508	2.2	-33 to 25 (58)	16	32 to 42 (27%)	2.1
[165]	SIW CRLH LWA	0.508	2.2	-17 to 13 (30)	15	24 to 27 (12%)	2.5
[167]	SIW CRLH LWA	0.508	2.2	-65 to 54 (119)	-	8.3 to 10.8 (26%)	4.6
[169]	Microstrip line CRLH LWA	0.25	6.15	-50 to 45 (95)	13	20 to 29 (37%)	2.6
[195]	Gain-Loss C-section Phasers LWA	0.787	2.2	(84)	-	4.9 to 5.1 (4%)	21

Table 3.1: Comparison of current leaky-wave antennas (LWAs) (SIW: substrate integrated waveguide, GDS: grounded dielectric slab, CRLH: Composite Right/Left Handed)

As can be seen from table 3.1, denser substrates typically result in a larger scanning range. In addition, the thicknesses of the substrates also plays an important role in the scanning range. For example, the antennas in [188] and [158] are the same type of periodic leaky-wave antennas based on grounded dielectric slab (GDS) waveguides. The antenna in [188] has a 2.54 mm substrate of $\varepsilon = 10.2$, while the antenna in [158] has a 0.5 mm substrate of $\varepsilon = 11.9$. Although the substrate used in the former has a smaller dielectric constant, it has a higher beam-scanning capability because the thickness of the waveguide is much thicker than the latter.

Since leaky-wave antennas scan their radiation beam with frequency, the scanning capability depends on the dispersion of the waveguide. The dispersion of a waveguide is greatly influenced by its structure, substrate (e.g., permittivity, thickness, etc.), and operating frequency.

On the other hand, the CRLH type leaky-wave antennas can achieve high scanning range properties because their equivalent unit cell circuit design is based on a resonant structure. If the pattern of the unit cells is very resonant, the phase constant of the CRLH transmission line can be very dispersive around the resonance frequency [167]. By enlarging L_R (or C_R) as indicated in figure 3.4, the sensitivity of propagation constant with respect to the frequency can be increased. At the same time, in order to maintain the balanced condition, C_L (or L_L) should be lowered simultaneously, which also helps to achieve higher sensitivity. To enlarge L_R, a transverse slot is adopted in the SIW-based CRLH unit cell design in [167] as an additional series inductor to increase the sensitivity of the propagation constant β to the frequency in the X-band of 8.3-10.8 GHz. However, as mentioned in section 3.4.1, the balanced condition becomes difficult to satisfy when the frequency gets high.

3.7 Method to Enhance the Scanning Range

In order to achieve fast beam scanning characteristics, a leaky wave antenna needs a highly dispersive waveguide to support its wave propagation. To improve the dispersion of conventional waveguides in printed technologies (e.g., the GDS waveguide), different strategies can be considered, such as using high permittivity substrates as mentioned in [169] or by acting on the substrate thickness as presented in the previous section 3.6. However, available low-loss planar substrates are limited in terms of dielectric constant

values, and increasing substrate thickness generates higher order propagation modes that are difficult to handle. Other approaches can be implemented to increase the scanning range such as the one in [195], where a high scanning sensitivity leaky-wave antenna is theoretically presented using Gain-Loss C-Section Phasers. Nevertheless, the antenna is difficult and expensive to be realized and consumes a large amount of power for high sensitivity solution.

Another method is to artificially make the substrate denser by using meta-surfaces. It is therefore possible to change the electromagnetic behavior of a waveguide in order to increase to some extent its frequency dispersion. In [196], a periodic leaky-wave antenna using sinusoidally modulated surface impedance composed of a grid of strips on a GDS is investigated but the scanning capability is not deeply discussed.

3.8 Classical GDS Periodic Leaky-Wave Antenna

GDS is a very simple and conventional waveguide that is commonly used in leaky-wave antenna designs. This waveguide only supports TM and TE propagation modes, and the fundamental propagation mode is TM_0 mode [139]. Such structure is easy to integrate with other planar circuits, such as microstrip and coplanar transmission lines. In addition, the GDS guide exhibits lower losses compared to other planar technologies [188].

3.8.1 GDS dispersion calculation for different substrates

Since the periodic leaky-wave antennas are based on guided modes that travel along the structure, the first step in analyzing and designing such antennas is to completely describe the dispersion properties of the guiding structure. Figure 3.10 shows the cross-sectional geometry of the GDS in the xz-plane, which consists of two layers: air and grounded dielectric. Since GDS is a multilayer planar structure, the dispersion analysis can be achieved by the TRM procedure, such as for the human body propagation analysis in section 2.6.

The dimensions of the GDS model along y-axis and z-axis are assumed to be infinite to simplify the dispersion calculation. The model is supposed lossless, thus from equation (2-2), the intrinsic wavenumber (i.e., the magnitude

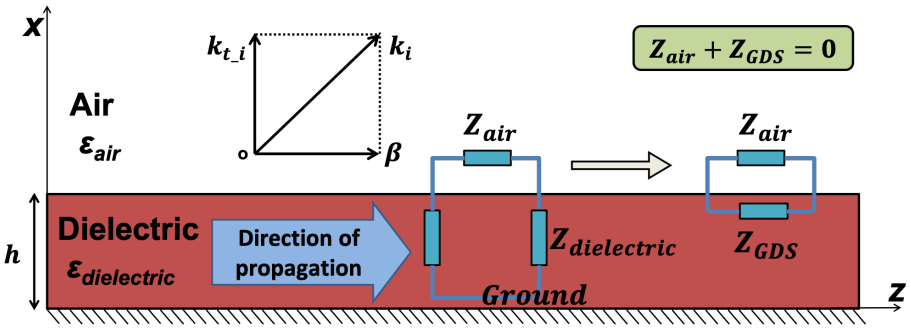

Figure 3.10: Grounded dielectric slab guide model and the TRM analysis

of the wavevector) of each layer is given by

$$k_i = \omega\sqrt{\varepsilon_i \mu_i} \tag{3-12}$$

where ω, ε_i, and μ_i represent the angular frequency, the permittivity and the permeability of the layer "i" respectively. The wavevector in each layer is decomposed into two components: k_{t_i} in the transverse direction (x-axis) and β in the direction of propagation (z-axis) using the following relation:

$$k_i^2 = \beta^2 + k_{t\_i}^2 \tag{3-13}$$

As introduced in section 2.6, β should be identical in the air layer and the substrate layer for a propagation mode to exist.

At the air/substrate interface, the transverse impedance seen looking into the bottom side can be calculated as

$$Z_{GDS} = jZ_{substrate} \tan\left(k_{t\_substrate} h\right) \tag{3-14}$$

where h is the thickness of the substrate and $Z_{substrate}$ is the characteristic impedance of the substrate in the transverse direction. The transverse impedance seen looking toward the upper side is the air transverse characteristic impedance Z_{air}. The above $Z_{substrate}$ and Z_{air} can be deduced from equations (2-58) and (2-59) for the TE and TM propagation modes, respectively. Thereby, the TRM condition at the air/substrate interface is

$$Z_{air} + Z_{GDS} = 0 \tag{3-15}$$

and the propagation constant β can be numerically found.

Using the TRM analysis procedure, dispersion of different GDS configurations can be easily plotted. Only the fundamental TM mode is considered in the analysis because it is this mode to be used to achieve the radiation of leaky-wave antenna. If higher order propagation modes exist, a part of the radiation energy will be taken away by these modes, thereby decreasing the efficiency of the antenna and creating additional beams in other directions if their harmonics fall into the fast-wave zone.

Figure 3.11 shows the GDS dispersion curves in the 57 GHz to 64 GHz license-free frequency range for different commercial substrate parameters of Rogers company: RT/duroid® 5880 ($\varepsilon_r = 2.2$), TMM® 4 ($\varepsilon_r = 4.5$), RT/duroid® 6006 ($\varepsilon_r = 6.15$), RT/duroid® 6010 ($\varepsilon_r = 10.2$). The thicknesses of the substrates are identically fixed at 0.5 mm and the dielectric loss is not

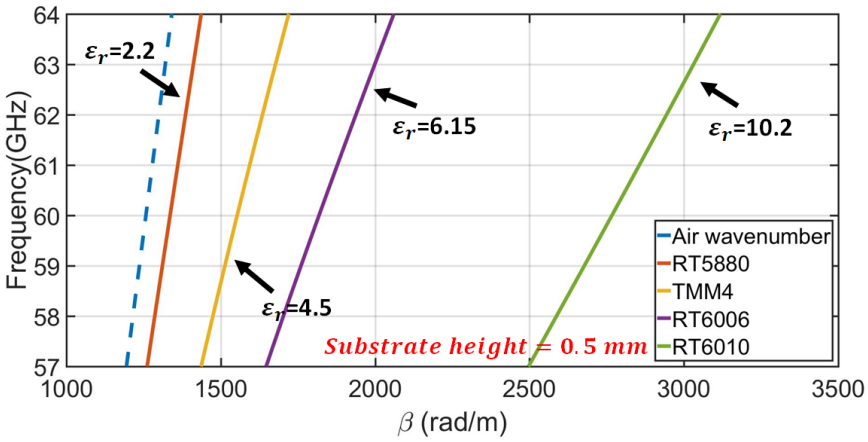

Figure 3.11: Dispersion of the fundamental TM mode for different Rogers substrates with thickness of 0.5 mm

considered in the analysis. As expected, substrates with higher permittivity are more dispersive.

Figure 3.12 shows the dispersion curves for substrate RT/duroid® 6010 ($\varepsilon_r = 10.2$) of different thicknesses. It can be observed that in the frequency range of 57 GHz to 64 GHz, the 0.508 mm-thickness substrate is the most dispersive among the five analyzed thicknesses because it exhibits the largest $\Delta\beta = 617$ in the operation band.

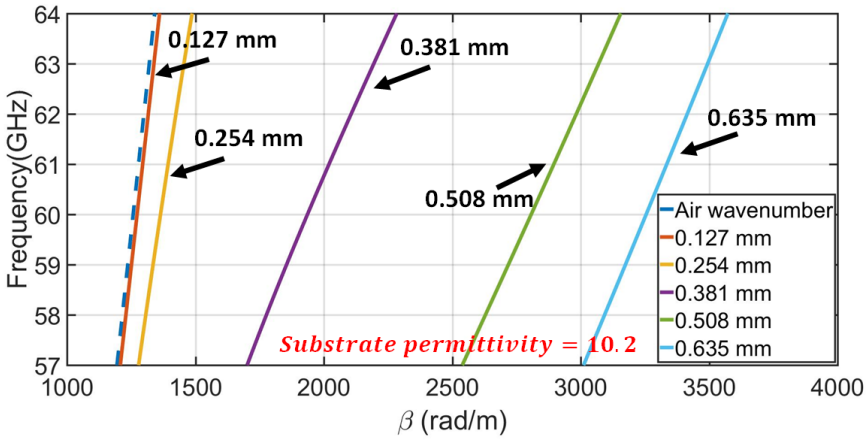

Figure 3.12: Dispersion of the fundamental TM mode for different thicknesses for the lossless substrate RT/duroid® 6010 (ε_r =10.2)

Consequently, by changing the permittivity and thickness of the substrate, the GDS waveguide can be made more dispersive. It should be noted that the permittivity and the thickness should be carefully chosen so that only the fundamental propagation mode exists in the operating frequency band. This mono-mode condition for GDS waveguide can be verified by

$$N < \frac{k_0 h}{\pi}\sqrt{\varepsilon_r - 1} \tag{3-16}$$

where k_0 is the intrinsic wavenumber in free space, and the largest integer of N is the total number of surface-wave modes supported by the GDS waveguide [197], thereby it is less than 1 for a mono-mode waveguide. Therefore, from equation (3-16), we can deduce that, for a given frequency f and substrate ε_r, the thickness of substrate should satisfy

$$h < \frac{c}{2f\sqrt{\varepsilon_r - 1}} \tag{3-17}$$

to exhibit only the dominant TM_0 propagation mode.

3.8.2 Scanning range of GDS periodic leaky-wave antennas with different substrates

Using the previously deduced dispersion curves of the GDS waveguides and the design period for the leaky-wave antenna, the radiation scanning range

can be theoretically calculated by the formulas (3-2) and (3-10) given in section 3.1.

Table 3.2 shows the theoretical scanning range of two GDS periodic leaky-wave antennas using different substrates ($\varepsilon_r = 10.2$ and $\varepsilon_r = 20$) in the 57 - 64 GHz frequency band. As can be calculated from equation (3-17), to ensure that only the dominant mode exists in the operation frequency band, the thickness of the $\varepsilon_r = 10.2$ substrate should be less than 0.77 mm, and the thickness of the $\varepsilon_r = 20$ substrate should be less than 0.54 mm. In our work, we chose the commercially available thickness $h = 0.254$ mm (0.01 inches) for both substrates, because when a metasurface is added at the air/substrate interface in the next sections, thicker substrate would support the first higher order mode. The periods p of the two leaky-wave antennas are separately calculated, using equations (3-2) and (3-10), to radiate toward the same backward direction $\theta = -13°$ at 64 GHz, i.e., $p = 3.5$ mm for the $\varepsilon_r = 10.2$ substrate, and $p = 2.5$ mm for the $\varepsilon_r = 20$ substrate, respectively. As expected, the scanning range of the denser substrate antenna is almost four times larger than the one with lower permittivity in the operating frequency band.

Frequency	$\varepsilon_r = 10.2$, $p = 3.5mm$		$\varepsilon_r = 20$, $p = 2.5mm$	
	β	Beam direction	β	Beam direction
57 GHz	1279 rad/m	-25.6°	1513 rad/m	-56.8°
60 GHz	1364 rad/m	-20.1°	1758 rad/m	-36.9°
62 GHz	1424 rad/m	-16.6°	1971 rad/m	-24.7°
64 GHz	1487 rad/m	-13.3°	2224 rad/m	-12.5°

Table 3.2: Theoretical scanning ranges of the two GDS-based periodic Leaky-wave antennas ($\varepsilon_r = 10.2 \Rightarrow \Delta\theta = 12.3°$, $\varepsilon_r = 20 \Rightarrow \Delta\theta = 44.3°$)

To verify the scanning range analysis, full-wave simulations are performed with CST time domain solver for both antennas. Different techniques can be used to add periodicity to the slow-wave guide to generate a leaky-wave antenna. One of the most classical methods is to periodically print metal strips on the guiding structure.

Figure 3.13 shows the antenna models in the simulation where the substrates are assumed to be lossless and the metal is a perfect electric conductor. Waveguide port is used to excite the appropriate propagation mode. The boundary conditions are set to PML, where an extra free space is added

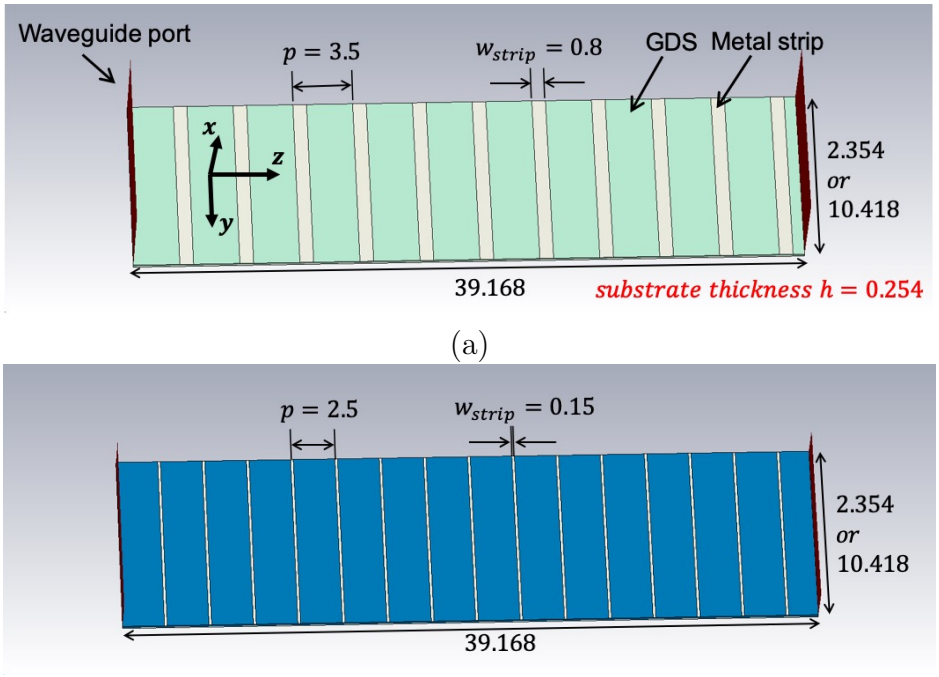

Figure 3.13: Simulation models of the GDS-based metal strips periodic leaky-wave antennas (dimensions in mm) with (a) lossless substrate RT/duroid® 6010 ($\varepsilon_r = 10.2$) and (b) lossless substrate of $\varepsilon_r = 20$

between the antenna structure and PML for farfield calculations. The two antennas have the same length of 39.168 mm, and each antenna design are simulated with two different antenna widths (2.354 mm and 10.418 mm as indicated in figure 3.13). With the given antenna length and the defined leaky-wave antennas periods, the antenna with substrate $\varepsilon_r = 10.2$ has approximately 11 periods while the antenna with substrate $\varepsilon_r = 20$ has about 15 periods. The width of the periodic metal strips w_{strip} should be well chosen to appropriately excite the propagating mode and control the leakage constant α [162,176]. Since the wavelength and the period of the leaky-wave antenna of the denser substrate are smaller, the strip width w_{strip} should be consequently narrower. In our models, in order to effectively radiate with a limited antenna length, while the metal strip does not affect too much the characteristics of the original GDS waveguide, w_{strip} is chosen to be 0.8 mm

for the leaky-wave antenna with substrate $\varepsilon_r = 10.2$, and 0.15 mm for the one with substrate $\varepsilon_r = 20$, respectively. It should be noted that at certain frequencies, the strip may be resonate and interfere with the propagation in the GDS waveguide. For example, as can be seen from figure 3.14, the S21 parameter of the 10.418 mm-width antenna with substrate $\varepsilon_r = 10.2$ drops at 61.4 GHz. If we refer to the yz-plane magnetic field distribution inside the antenna, as shown in figure 3.15, the strips exhibit resonance features at 61.4 GHz, which causes more losses in the propagation and reduces the radiation efficiency, thereby degrading the desired farfield pattern. With both permittivites, the antennas are well matched over the bandwidth of interest (S11 < -10 dB). It is to be noted that the leakage with $\varepsilon_r = 20$ is smaller than the one with $\varepsilon_r = 10.2$ as the transmission parameter S21 is higher, which means that less power has been radiated into the air.

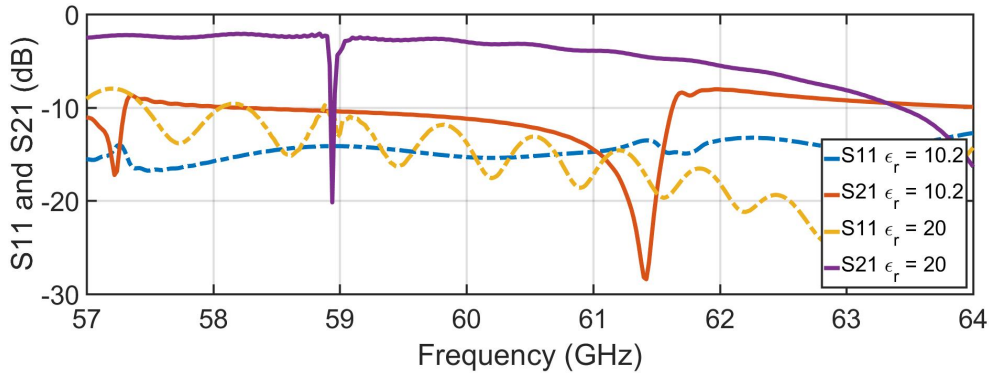

Figure 3.14: S11 and S21 parameters of the simulated classical GDS-based leaky-wave antennas

Figure 3.16 shows the farfield patterns of the 10.418 mm-width antennas in the xz-plane, with frequencies ranging from 57 GHz to 64 GHz. The detailed radiation direction and corresponding gain are represented in tables 3.3 and 3.4 for the antennas with substrate $\varepsilon_r = 10.2$ and $\varepsilon_r = 20$, respectively. At the operating frequencies, the antenna with substrate $\varepsilon_r = 10.2$ has a total scanning range of 12.3° in the backward quadrant from -28.3° to -16°, while the antenna with substrate $\varepsilon_r = 20$ has a four times scanning range of 47.1° from -52.1° to -5° in the backward quadrant. It can be seen that the larger width antenna can achieve higher radiation gain as expected.

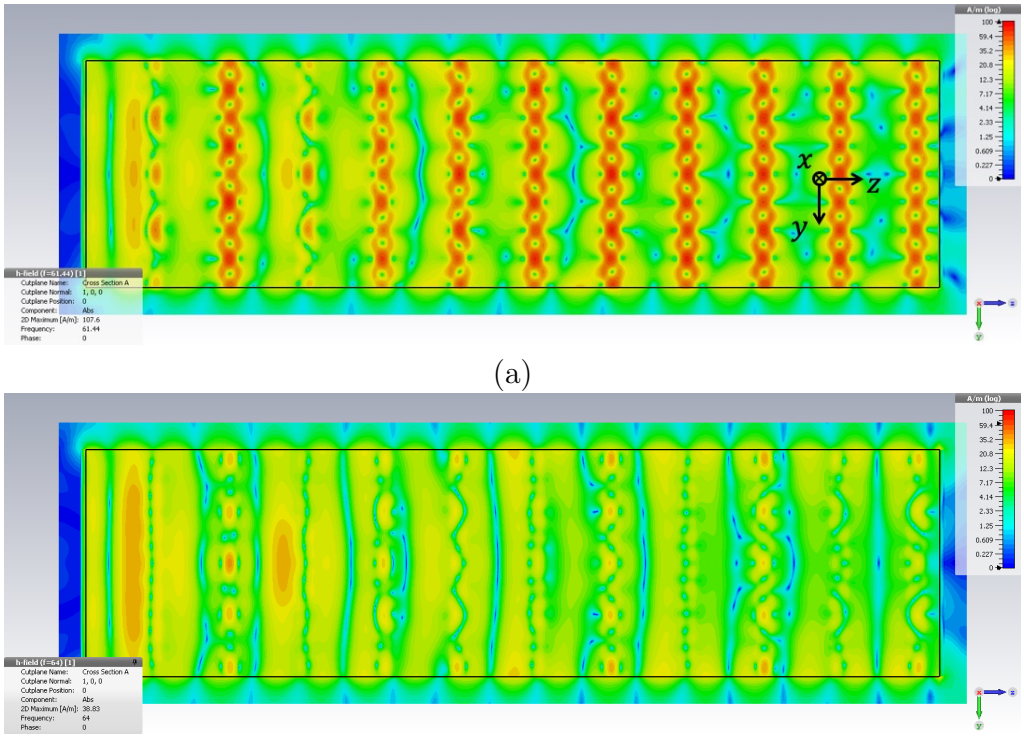

(a)

(b)

Figure 3.15: Magnetic field distribution in absolute value (dBA/m) in the GDS-based leaky-wave antenna ($\varepsilon_r = 10.2$) of the cross-sectional yz-plane (a) at 61.44 GHz (b) at 64 GHz

Compared to the theoretical scanning directions in table 3.2, the antenna models with larger antenna width (10.418 mm) have a slightly offset scanning coverage (about 3° for the substrate $\varepsilon_r = 10.2$ and 5° to 7° for the substrate $\varepsilon_r = 20$). However, as shown in tables 3.2, 3.3, and 3.4, when the antenna width is reduced to 2.35 mm, the simulated scanning ranges of these two antennas are much more consistent with the theoretical values.

Furthermore, we can observe from figure 3.16(a) that due to the metal strip resonance effect, the radiation gain at 57 GHz and 60 GHz is relatively lower for the antenna with substrate $\varepsilon_r = 10.2$. As for the antenna with substrate $\varepsilon_r = 20$ (figure 3.16(b)), when the radiation beam is close to

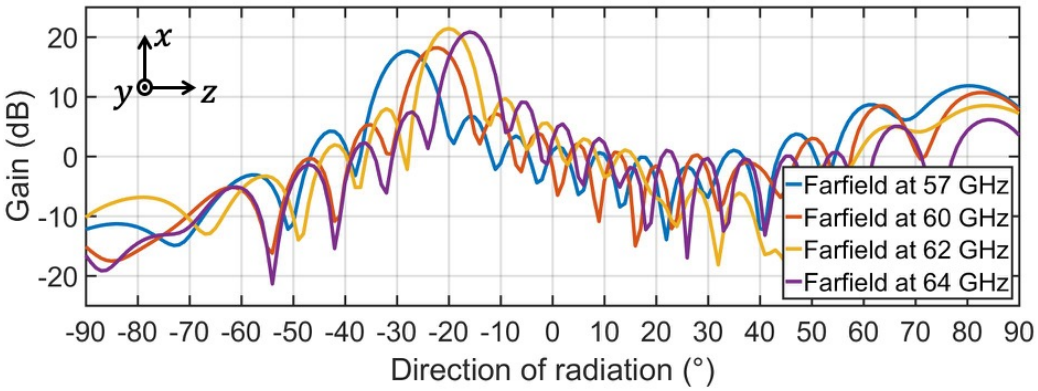

(a)

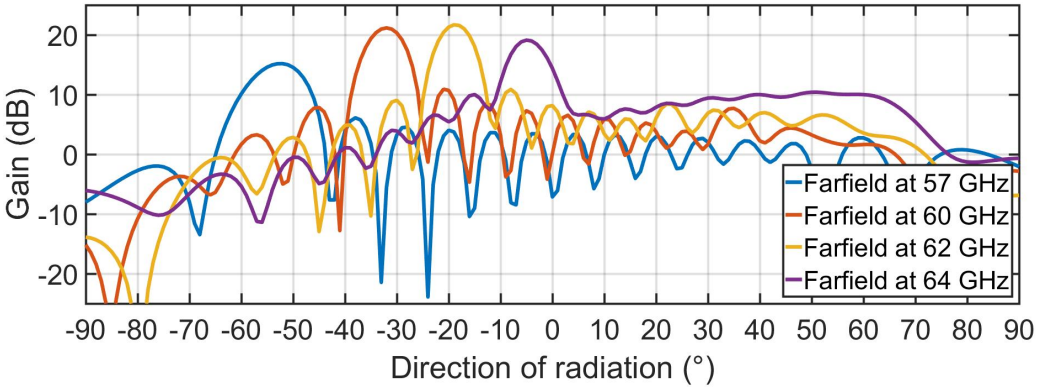

(b)

Figure 3.16: Farfield patterns in the xz-plane of the 10.418 mm-width GDS-based leaky-wave antennas (a) with lossless substrate RT/duroid® 6010 (ε_r = 10.2) (b) with lossless substrate (ε_r = 20)

$\varepsilon_r = 10.2$, $p = 3.5$ mm, $w_{strip} = 0.8$ mm				
Frequency	antenna width = 2.354 mm		antenna width = 10.418 mm	
	Direction	Gain	Direction	Gain
57 GHz	-27.0°	8.9 dB	-28.3°	17.6 dB
60 GHz	-21.0°	9.6 dB	-22.3°	18.2 dB
62 GHz	-17.3°	9.9 dB	-20.0°	21.4 dB
64 GHz	-13.4°	9.5 dB	-16.0°	20.8 dB

Table 3.3: Beam direction and gain of the GDS-based leaky-wave antenna with substrate ε_r = 10.2 in the frequency band of 57 - 64 GHz

$\varepsilon_r = 20$, $p = 2.5$ mm, $w_{strip} = 0.15$ mm				
Frequency	antenna width = 2.354 mm		antenna width = 10.418 mm	
	Direction	Gain	Direction	Gain
57 GHz	-56.4°	6.4 dB	-52.1°	15.2 dB
60 GHz	-38.8°	11.8 dB	32.0°	21.2 dB
62 GHz	-26.7°	14.0 dB	-18.5°	21.6 dB
64 GHz	-12.4°	14.8 dB	-5.0°	19.1 dB

Table 3.4: Beam direction and gain of the GDS-based leaky-wave antenna with substrate $\varepsilon_r = 20$ in the frequency band of 57 - 64 GHz

the backward end-fire, the radiation gain becomes degraded due to relatively worse S11 matching, and the beamwidth is larger. On the other hand, the gain decreases when the beam approaches to the broadside to encounter the open stopband, and a forward radiation between 30° and 60° arises consequently.

3.9 Metasurface-based Enhanced-Dispersion Waveguide

3.9.1 Design methodology

As introduced in section 3.7, to increase the scanning range of the leaky-wave antenna, highly dispersive waveguide is required. Section 3.8 shows that using higher permittivity materials can improve the dispersion of the GDS. However, high permittivity values are not easily available as planar low-loss substrates. Therefore, the method proposed here is to use metasurfaces to artificially make the substrate of the GDS denser, thereby increasing the dispersion of the waveguide that supports the propagation of the leaky-wave antenna. Metasurface can also be referred to the partially reflecting surface [160, 162, 176], which is a periodic structure with electrically small unit cells, i.e., the cell size is much smaller than the wavelength.

To assess the metasurface solution with respect to the GDS, we define three waveguides of identical thickness ($h = 0.254$ mm) as shown in figure 3.17:

1. GDSL – the original low dispersive GDS whose relative permittivity of substrate is ε_l (figure 3.17(a));

2. GDSH – the objective high dispersive GDS whose relative permittivity of substrate is $\varepsilon_h > \varepsilon_l$ (figure 3.17(b));

3. GDSM – the enhanced GDSL that includes a metasurface (figure 3.17(c)).

The goal is to design a GDSM that mimics the dispersive behavior of the GDSH around 60 GHz while using the same low permittivity substrate as the GDSL. To do so, dispersions of the GDSL and GDSH are firstly studied by the TRM introduced in section 3.8.1, and the analysis models are shown in figure 3.17 (a) and (b). Again, only the fundamental TM_0 mode is considered here as it is the one that will become leaky in this study. However, it has been verified in section 3.8.2 that no higher order modes exist within the frequency range of interest using an $h = 0.254$ mm thickness substrate. The substrates are considered lossless and the characteristics of the GDSL and GDSH at 60 GHz are calculated numerically by TRM and are given in table 3.5.

Models	β	$k_{substrate}$	$k_{t\_substrate}$	Z_{GDSx}
GDSL	1364 rad/m	4015 rad/m	3776 rad/m	158j Ω
GDSH	1758 rad/m	5622 rad/m	5340 rad/m	367j Ω
GDSM	1758 rad/m	4015 rad/m	3608 rad/m	138j Ω

Table 3.5: Characteristics of the TM_0 mode at 60 GHz for GDSL, GDSH, and GDSM (the subscript $_x$ in Z_{GDSx} is referred to L, H, or M)

The propagation constants β of GDSL and GDSH at 60 GHz are 1364 rad/m and 1758 rad/m respectively. Then, using equation (3-12), the intrinsic substrate wavenumbers $k_{substrate}$ are calculated for these two structures, which are 4015 rad/m and 5622 rad/m, respectively. The transverse components $k_{t\_substrate}$ of the intrinsic substrate wavenumbers are therefore deduced as 3776 rad/m and 5340 rad/m, respectively. Consequently, the brought surface impedance Z_{GDSL} and Z_{GDSH} from the ground to the air/substrate interface, as indicated in figure 3.17 and determined by the formulas (2-59) and (3-14), are 158j Ω and 367j Ω, respectively, which are inductive impedances. As mentioned in section 2.10.5, inductive surface impedance supports TM propagation mode, which agrees well with our calculations.

For the GDSM, we have an additional metasurface at the air/substrate interface of the GDSL (figure 3.17(c)), so the equivalent transverse impedance seen looking toward the bottom side from the air/substrate interface is

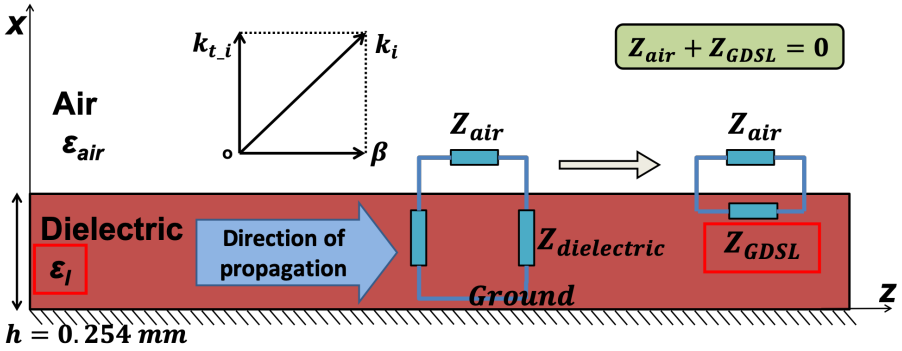

(a)

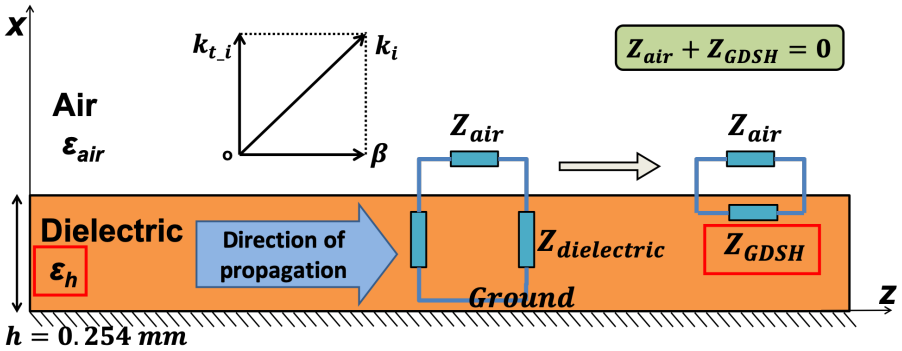

(b)

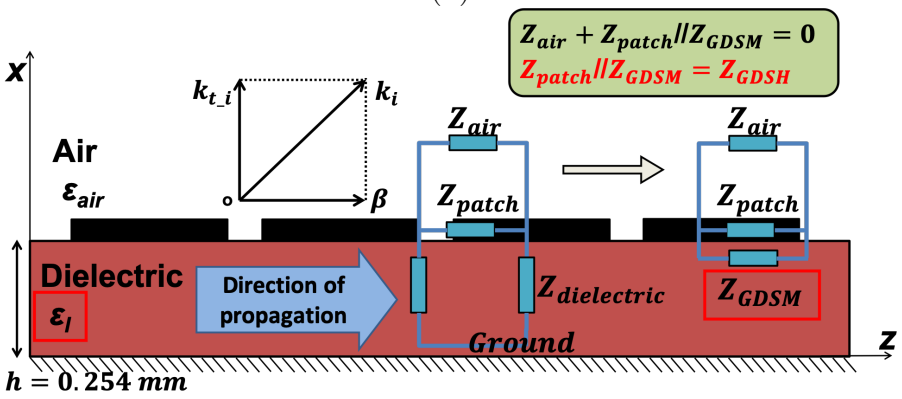

(c)

Figure 3.17: Enhanced dispersion waveguide design procedure

$Z_{meta}//Z_{GDSM}$, i.e., Z_{meta} in parallel with Z_{GDSM}, where Z_{GDSM} is the brought impedance from the ground of the GDSM structure. Thus the TRM condition becomes

$$Z_{air} + Z_{meta}//Z_{GDSM} = 0 \tag{3-18}$$

where Z_{meta} is the impedance of the metasurface. Since the GDSM mimics the GDSH at 60 GHz, the following conditions should also be satisfied

$$Z_{meta}//Z_{GDSM} = Z_{GDSH} \qquad \text{at } 60\ GHz \tag{3-19}$$

$$\beta_{GDSM} = \beta_{GDSH} \qquad \text{at } 60\ GHz \tag{3-20}$$

Therefore, the transverse component $k_{t\_substrate}$ used for the Z_{GDSM} calculation needs to be determined in (3-13) with the propagation constant of GDSH. Nevertheless, the substrate of GDSM is still the lower permittivity one $\varepsilon_r = 10.2$ of GDSL, thus the intrinsic substrate wavenumber $k_{substrate}$ used in (3-13) should be the one of GDSL. Finally, from equations (2-59) and (3-14), we can deduce the ground-brought air/substrate surface impedance for the fundamental TM mode as

$$Z_{GDSM} = j\frac{\sqrt{\omega_{60}^2\varepsilon_0\varepsilon_l\mu_0 - \beta_{GDSH}^2}}{\omega_{60}\varepsilon_0\varepsilon_l}\tan(\sqrt{\omega_0^2\varepsilon_0\varepsilon_l\mu_0 - \beta_{GDSH}^2}h) \tag{3-21}$$

where ω_{60} is the angular frequency of 60 GHz. Using the values of GDSM in table 3.5, we can easily deduce that $Z_{GDSM} = 138\text{j}\ \Omega$. Then, from (3-19), the metasurface impedance Z_{meta} required to convert the substrate from $\varepsilon_r = 10.2$ to $\varepsilon_r = 20$ at 60 GHz is -221j Ω, which is a pure reactance (or a capacitance of C=12 fF).

3.9.2 Metasurface calculations

As introduced in the previous section 3.9.1, the capacitive surface impedance needs to be added in parallel in the TRM calculation to convert the GDS waveguide to a higher permittivity structure. This can be achieved by a planar array type metasurface. Such metasurface is introduced and studied in [198], which gives a simple and accurate analytical grid impedance formulas based on the approximate Babinet principle for these metasurfaces. The actual topology of the architecture of the metasurface is a planar array of metal strips or patches as shown in figure 3.18.

Let us first consider the strip array structure in figure 3.18(a), which is a square grid of metal strips located on a dielectric substrate in the yz-plane.

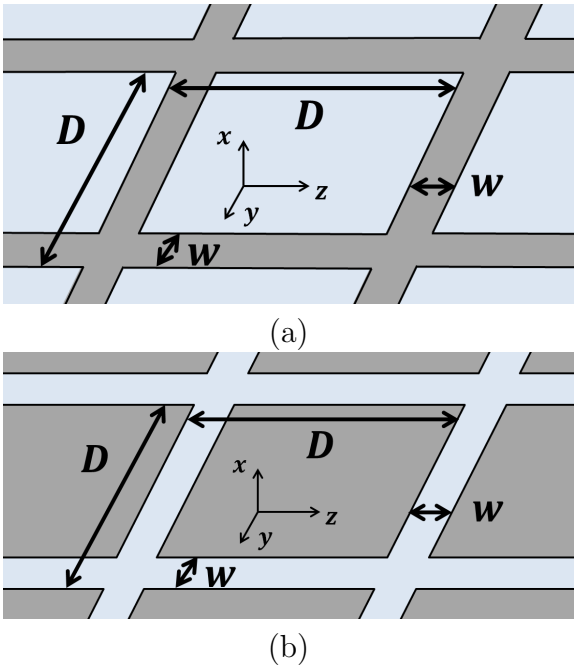

Figure 3.18: Metasurfaces (a) array of metal grids (b) array of metal patches

The width of metal strips is defined as w, and the grid period is defined as D which is electrically small. Assuming that $w \ll D$, then the strip could be seen as a conducting wire and the grid becomes a mesh of crossed metal wires. Considering that the plane of incidence is the xz-plane, when the incident wave has a non-zero y-axis or z-axis electric field component (i.e., parallel to the strips), the response of the grid surface is inductive. According to [198], this inductive grid impedance Z_s can be calculated as

$$Z_s = \frac{\boldsymbol{E}}{\boldsymbol{J}} \tag{3-22}$$

where $\boldsymbol{E}$ is the tangential component of the total electric field in the xz-plane and $\boldsymbol{J}$ the averaged surface current density induced by the incident wave flowing along the strips. The average is made over the grid period D.

For the case of TE-polarized incidence in the xz-plane, $\boldsymbol{E}$ has only a y-axis component $\boldsymbol{E_y}$ and its induced current $\boldsymbol{J_y}$ on the strips is also in the same direction. Otherwise, for the TM-polarized incidence, the electric field component and its induced current is only in the z-axis direction, thus $\boldsymbol{E_z}$

and $\boldsymbol{J_z}$ respectively.

The averaged boudary conditions for such mesh (derived by M.I Kontorovich in the 1950s) can be found in [199] for the TE-polarized and TM-polarized incident fields:

$$\boldsymbol{E_y^{TE}} = j\frac{\eta_{eff}}{2}\alpha \boldsymbol{J_y^{TE}} \tag{3-23}$$

$$\boldsymbol{E_z^{TM}} = j\frac{\eta_{eff}}{2}\alpha[\boldsymbol{J_z^{TM}} + \frac{1}{k_{eff}^2(1+\frac{b}{D})}\frac{b}{D}\frac{\partial^2}{\partial z^2}\boldsymbol{J_z^{TM}}] \tag{3-24}$$

where b and D are the periods of the grid structure along the z-axis and y-axis, respectively. In our case of a square grid, the periods in both directions are identical, i.e., $b = D$. So the formulas (3-23) and (3-24) are simplified as

$$\boldsymbol{E_y^{TE}} = j\frac{\eta_{eff}}{2}\alpha \boldsymbol{J_y^{TE}} \tag{3-25}$$

$$\boldsymbol{E_z^{TM}} = j\frac{\eta_{eff}}{2}\alpha[1 + \frac{1}{2k_{eff}^2}\frac{\partial^2}{\partial z^2}]\boldsymbol{J_z^{TM}} \tag{3-26}$$

In (3-25) and (3-26), η_{eff} is the effective wave impedance of the dielectric substrate with the metasurface placed on it, which is calculated with the relative permittivity ε_{eff}:

$$\eta_{eff} = \sqrt{\frac{\mu_0}{\varepsilon_0\varepsilon_{eff}}} \tag{3-27}$$

where μ_0 and ε_0 are the permeability and permittivity in free space, respectively. In our case of metal wire on a dielectric substrate, the relative effective permittivity is approximated as

$$\varepsilon_{eff} = \frac{\varepsilon_r + 1}{2} \tag{3-28}$$

where ε_r is the relative permittivity of the dielectric substrate. On the other hand, the parameter k_{eff} is the wavenumber propagating in the dielectric substrate with the effective permittivity ε_{eff}, which is calculated as

$$k_{eff} = k_0\sqrt{\varepsilon_{eff}} \tag{3-29}$$

where k_0 is the wavenumber in free space. Finally, α is the grid parameter introduced in [199]:

$$\alpha = \frac{k_{eff}D}{\pi}\ln(\frac{1}{\sin\frac{\pi w}{2D}}) \tag{3-30}$$

where D and w are the previously mentioned grid period and grid width, respectively.

It should be noted that the above formulas are used for electrically dense arrays. The ideal frequency condition is $D \ll \lambda$. At the frequency of $\lambda = D$, the calculation is still good enough. However, if we exceed this limit, the phase variation on the surface is too fast and the average calculation will fail.

For an oblique-incidence excitation with an angle of incidence θ relative to the normal of the surface, the wave vector k_0 can be decomposed into an x-axis component k_{0x} and a z-axis component k_{0z}, where $k_{0x} = k_0 \cos\theta$ and $k_{0z} = k_0 \sin\theta$. So the term $\partial/\partial z$ in equation (3-26) can be replaced by $-jk_{0z}$, i.e., $\partial/\partial z = -jk_0 \sin\theta$. From this relation and the equations (3-22), (3-25), and (3-26), the grid impedance Z_s of the TE-polarized and TM-polarized oblique excitation in the xz-plane can be derived as

$$Z_s^{TE} = j\frac{\eta_{eff}}{2}\alpha \tag{3-31}$$

$$Z_s^{TM} = j\frac{\eta_{eff}}{2}\alpha(1 - \frac{k_0^2 \sin^2\theta}{2k_{eff}^2}) \tag{3-32}$$

We can note that the grid impedance of the TE-polarized excitation is independent of the angle of incidence. However, for the TM-polarized excitation waves, the angle of incidence changes the grid impedance value of the metal strips array metasurface. The obtained impedance have an inductive form.

For the complementary structure in figure 3.18(b), an array of square metal patches on a dielectric substrate, the grid impedance Z_p can be deduced using the approximate Babinet principle [199]:

$$Z_s^{TE} Z_p^{TM} = \frac{\eta_{eff}^2}{4} \tag{3-33}$$

$$Z_s^{TM} Z_p^{TE} = \frac{\eta_{eff}^2}{4} \tag{3-34}$$

where Z_p^{TM} and Z_p^{TE} are the grid impedance of the complementary structure (array of metal patches) for the TM-polarized and TE-polarized excitation, respectively. As shown in the Babinet principle, if the plane of incidence for the strips array in figure 3.18(a) is the xz-plane, the plane of incidence

for the array of patches in figure 3.18(b) will be the xy-plane. However, our structure is assumed as square arrays of strips or patches, changing the plane of incidence will therefore not influence the grid impedance calculation.

The grid impedance of the array of patches can then be deduced as

$$Z_p^{TE} = -j\frac{\eta_{eff}}{2\alpha(1-\frac{k_0^2\sin^2\theta}{2k_{eff}^2})} \tag{3-35}$$

$$Z_p^{TM} = -j\frac{\eta_{eff}}{2\alpha} \tag{3-36}$$

It can be seen that, unlike the array of strips, the grid impedance of patches array is a capacitive one, and it is the TM-polarized mode now that is independent of the angle of incidence.

As mentioned in the beginning of this section, a capacitive metasurface is required to improve the dispersion of the classical GDS. Therefore, we will use the patch array type metasurface in our leaky-wave antenna design.

Basically, the patch and gap dimensions of the metasurface are desired to be as small as possible to increase the antenna performance as the unit size needs to be electrically small. Moreover, smaller unit size makes the choice of antenna size and the addition of periodicity more flexible. However, due to the fabrication tolerances, the patch unit of the metasurface and especially the gap between the patches cannot be too small. Thus, we consider the gap size w as 0.05 mm. As the leaky mode is the fundamental TM mode, from equations (3-27), (3-28), (3-30), and (3-36), in addition of the previously deduced metasurface impedance (-221j Ω) in the end of section 3.9.1, we can deduce the period of the patches array metasurface as $D = 0.288$ mm, so the square metal patch of the metasurface has a length of 0.238 mm.

3.9.3 Simulations of the metasurface-based GDS waveguide

To verify the TRM calculations for the metasurface-based GDS waveguide, simulations are performed using eigen mode solver in CST. In order to model an infinite extent of the structure, a cell of the metasurface-based GDS waveguide is implemented with periodic boundary conditions in the xy-planes and xz-planes as shown in figure 3.19. The upper and lower boundary conditions of the yz-planes are configured to be "magnetic" (i.e., the tangential magnetic field is equal to zero) and "electric" (i.e., the tangential electric

field is equal to zero), respectively, to appropriately excite the TM mode. The substrate is assumed to be lossless and the metal uses perfect electric conductor.

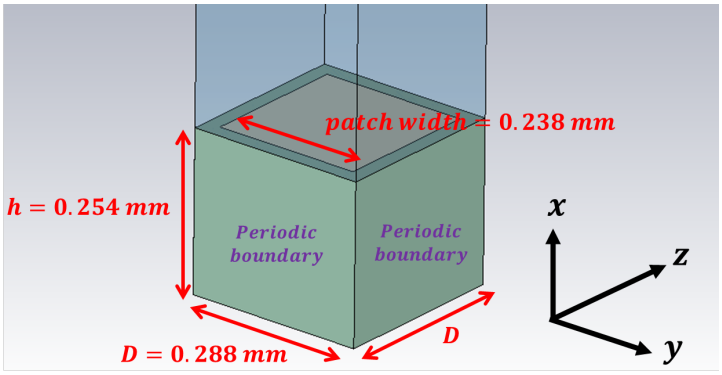

Figure 3.19: GDSM waveguide unit cell model in CST for eigen mode solver

CST eigen mode solver can provide the plot of "frequency versus spatial phase variation" between the two xy-boundary-planes. The propagation constant β can then be deduced with the phase variation from the relation

$$\beta = \frac{phase}{D} \tag{3-37}$$

where D is the unit length of 0.288 mm. Therefore, dispersion curve of the metasurface-based waveguide can be derived.

Figure 3.20 shows the dispersion curves deduced from the TRM of the three previous models GDSL, GDSH, and GDSM, as well as the dispersion curve of GDSM deduced from CST. It can be seen that the CST result is in good agreement with the TRM calculation for the GDSM model. From the TRM analysis, the GDSM has the same dispersion behavior as the GDSH at 60 GHz. However, the GDSM structure is slightly less dispersive than the GDSH in the operating frequency band of 57 - 64 GHz because to fully mimic the GDSH dispersion, the GDSM would need different metasurface impedances at different frequencies, thus different patch and gap sizes for the patches array, which is obviously not possible. As can be seen from figure 3.20, the GDSM propagation constant is identical to the GDSH one at 60 GHz, which is the frequency for which the metasurface has been designed to mimic the behavior of the substrate $\varepsilon_r = 20$.

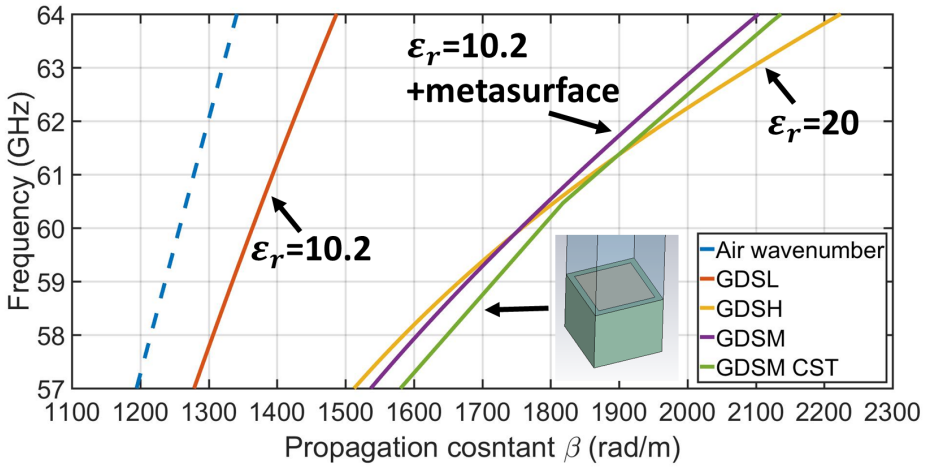

Figure 3.20: Comparison of dispersion curves for the GDSL, GDSH, and GDSM models between TRM and CST

Another full-wave simulation of the GDSM is additionally performed in CST using the time domain solver as shown in figure 3.21. The dimensions of the model are length × width = 39.168 mm × 10.418 mm. In addition, dielectric loss is considered in the RT/duroid® 6010 substrate ($\tan\delta = 0.0023$), and the metal parts (metasurface patches and the ground) use annealed copper ($\sigma = 5.8\times10^7$ S/m) as their material. The waveguide port is implemented to excite the propagation mode. However, it should be noted that the CST waveguide port is not able to properly excite the desired propagation mode. The port is placed on the border of the metasurface, which excites a quasi-TEM mode, which will then couple into the appropriate GDSM propagation mode. This results in a mismatch that will not exist (or largely reduced) when a tapered transition is added.

Figure 3.22 shows the electromagnetic field distribution of the absolute value at 60 GHz in the cross section of xz-plane. The field distribution has a form of TM propagation mode. From the magnetic field distribution in figure 3.22(b), the propagation wavelength λ_g can be approximately estimated to be about 3.5 mm. Therefore, the phase constant can be derived as $\beta = 2\pi/\lambda_g = 1795$ rad/m, which is in good agreement with the TRM-calculated 60 GHz phase constant of the GDSM shown in table 3.5 (i.e., $\beta = 1758$ rad/m).

As can be seen from figure 3.22, the simulated GDSM structure radiates

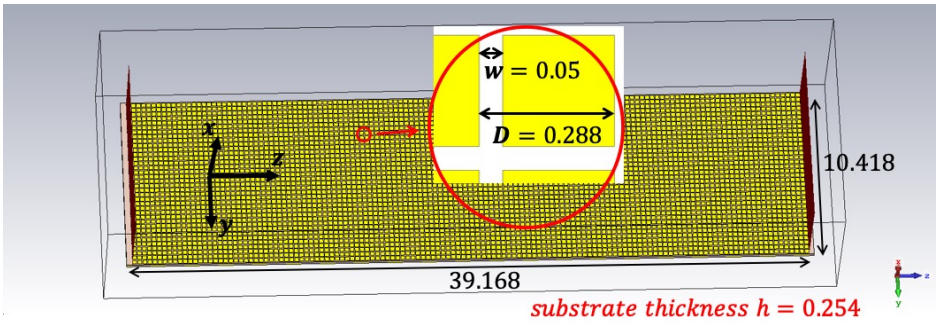

Figure 3.21: GDSM waveguide model in CST for time domain solver (dimensions in mm)

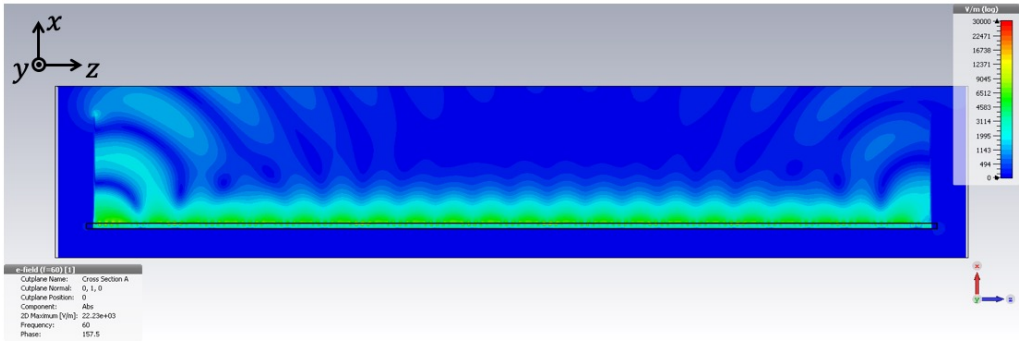

(a)

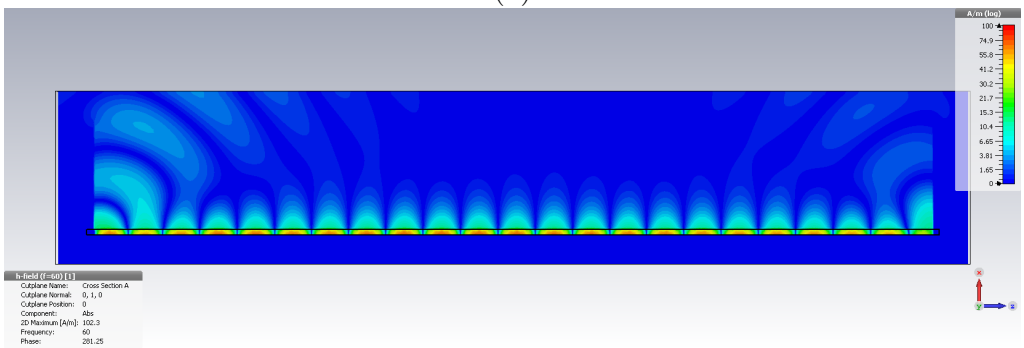

(b)

Figure 3.22: Field distribution in absolute value at 60 GHz in xz-plane of the GDSM waveguide (a) the electric field (b) magnetic field

at the beginning (left side) and the end (right side) of the metasurface. This is because, as mentioned earlier, the port mode calculated in the simulation is not the same as the GDSM propagation mode, therefore causing mismatch. Even though the GDSM mode is successfully coupled into the waveguide from the excitation port mode, the waves see discontinuities at the coupling section at the two ports, and thus the structure radiates at these ends. In addition, since the dielectric loss and metal conduction loss are considered in the simulation, the radiation on the end side of the waveguide is comparatively smaller.

Figure 3.23 shows the far field patterns of the waveguide in simulation. As anticipated, it can be seen that due to the discontinuities at the edges of the metasurface, the GDSM guide exhibits a 10 dB of radiation from about 20° to 40° in the forward quadrant as observed in figure 3.22. In further design optimization, this discontinuity at the starting border of the metasurface should be taken into consideration to avoid unwanted radiation. For example, the beginning of the metasurface can be gradually changed to have smoother transition between the GDS propagation mode and the GDSM propagation mode.

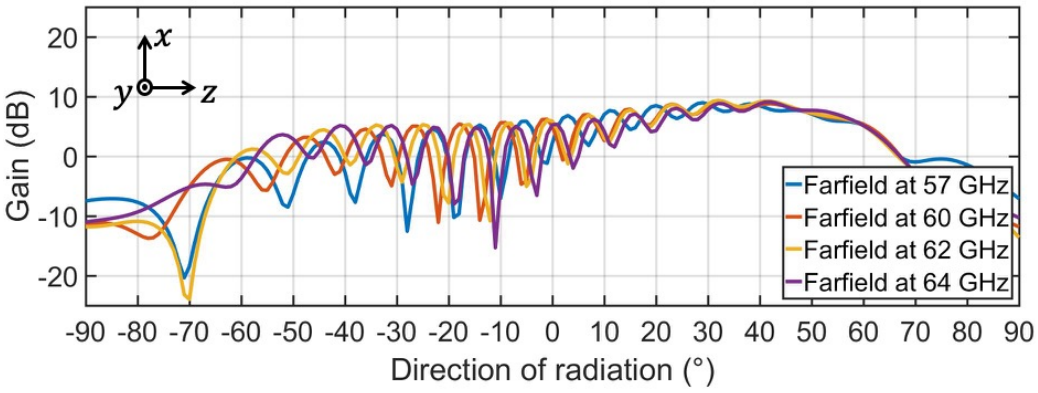

Figure 3.23: Farfield patterns of the GDSM waveguide in xz-plane

3.10 Leaky-Wave Antenna Based on New Designed Waveguide

With the previously designed dispersion-enhanced waveguide using the 0.254 mm-thickness Rogers substrate RT/duroid® 6010 ($\varepsilon_r = 10.2$, $\tan\delta = 0.0023$), a periodic leaky-wave antenna is realized by adding periodicity to the GDSM structure. The method used here is to etch a row of patches every 9 metasurface's patch periods D. Therefore, the period p of the designed leaky-wave antenna is $9 \times D = 2.592$ mm, and the etched leakage gap width between the two adjacent patches is 0.388 mm, as shown in figure 3.24(a). The total dimensions of the model designed in full-wave simulation are length $\times$ width = 39.168 mm $\times$ 10.418 mm, which consists in 15 leaky-wave antenna periods in the longitudinal z-axis direction.

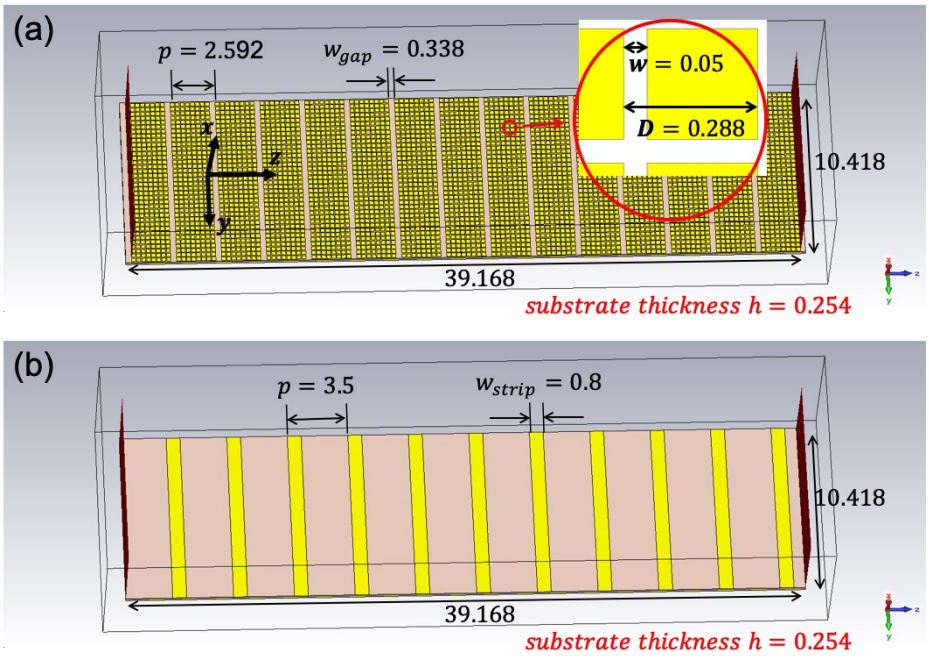

Figure 3.24: (a) GDSM-based leaky-wave antenna design (b) classical GDS-based leaky-wave antenna (dimensions in mm)

To assess the enhanced scanning capability of designed antenna, it is compared with a classical GDS-based leaky-wave antenna using the same

substrate of the same dimensions (but the period is changed to $p = 3.5$ mm in order to obtain the same radiation direction at 64 GHz), as shown in figure 3.24(b). The dielectric loss and the copper conduction loss ($\sigma = 5.8 \times 10^7$ S/m) are considered in both simulations.

Figure 3.25 shows the farfield patterns in the cross-sectional xz-plane of the simulated GDSM-based leaky-wave antenna and the classical GDS based leaky-wave antenna at 57 GHz, 60 GHz, 62 GHz, and 64 GHz. The beam direction and gain are represented in table 3.6 for the designed GDSM-based antenna, and in table 3.7 for the classical GDS-based antenna, respectively.

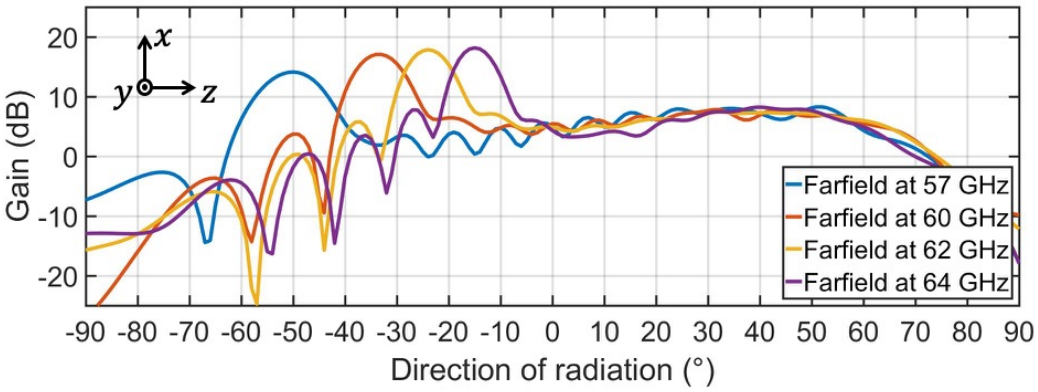

(a)

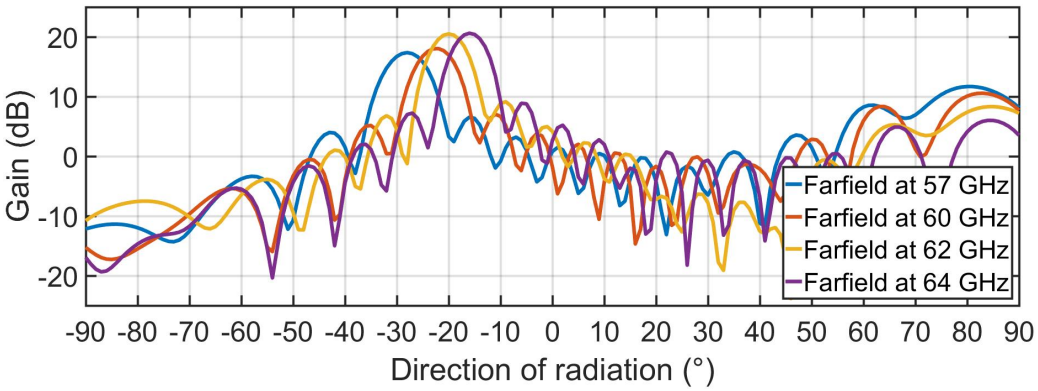

(b)

Figure 3.25: Farfield patterns in the xz-plane (a) designed GDSM-based leaky-wave antenna (b) classical GDS-based leaky-wave antenna

	57 GHz	60 GHz	62 GHz	64 GHz	Δ
Theoretical direction	-47.9°	-32.1°	-22.6°	-13.8°	$\Delta\theta = 34.1°$
Simulated direction	-50.6°	-34°	-24.3°	-15°	$\Delta\theta = 35.6°$
Simulated directivity	16.8 dB	18.9 dB	19.5 dB	20.2 dB	$\Delta D = 3.4$ dB
Simulated gain	14.1 dB	17 dB	17.8 dB	18.2 dB	$\Delta G = 4.1$ dB

Table 3.6: Comparison between theoretical scanning ranges and simulated scanning range of the GDSM-based periodic leaky-wave antenna

	57 GHz	60 GHz	62 GHz	64 GHz	Δ
Simulated direction	-28.1°	-22.5°	-20°	-16°	$\Delta\theta = 12.1°$
Simulated directivity	18 dB	18.7 dB	21.5 dB	21.4 dB	$\Delta D = 3.5$ dB
Simulated gain	17.3 dB	18 dB	20.5 dB	20.6 dB	$\Delta G = 3.3$ dB

Table 3.7: Simulated scanning range, directivity, and gain of the GDS-based periodic leaky-wave antenna

According to the dispersion of the GDSM waveguide derived from the TRM in section 3.9.3 and the leaky-wave antenna period p, the theoretical scanning range of the newly designed GDSM-based leaky-wave antenna antenna in the operating frequency band of 57 GHz to 64 GHz can be derived, as shown in table 3.6, with a total range of 34.1° in the backward quadrant from -47.9° to -13.8°.

As can be found in figure 3.25 and table 3.6, the designed GDSM-based antenna in simulation has a total scanning range of 35.6° from -50.6° to -15°, which is in good agreement with the theoretical scanning range. However, as can be seen from table 3.6, the simulated beam directions are slightly shifted by 1° to 2° compared to the theoretical values. This is because the periodically etched patches of the GDSM-based antenna remove a portion of the metasurface, which slightly affects the dispersion-enhanced propagation in the GDSM waveguide, thereby decreasing the propagation constant. The larger the etched gap (w_{gap} in figure 3.24), the smaller the percentage of the metasurface coverage, and thus the propagation constant decreases to approach the classical GDS waveguide. Furthermore, due to the discontinuity between the excitation mode and the GDSM propagation mode, the forward radiation observed from the GDSM waveguide in section 3.9.3 appears again here in the farfield patterns diagram. However, the gain of the main beam of the leaky-wave antenna is about 10 dB larger at 62 GHz and 64 GHz.

The total scanning range is increased from 12.1° to 35.6° from the classical leaky-wave antenna to the GDSM-based antenna. Therefore, an improvement of a 2.9 ratio is achieved as expected from the dispersion analysis. As the operating frequency band (57 - 64 GHz) has a 11.6% fractional bandwidth, the designed antenna has a SRBR value of 3.1, which is larger than the current GDS-based periodic leaky-wave antennas using the same substrate presented in table 3.1. It should be noted that the substrate target of GDSH during the waveguide dispersion enhancement design in section 3.9 was chosen to be $\varepsilon_r = 20$. This target permittivity can be augmented (e.g., $\varepsilon_r = 30$) to further increase the scanning range. On the other hand, the target permittivity should be careful verified to avoid the appearance of higher propagation modes at the operating frequencies. Compared to the classical

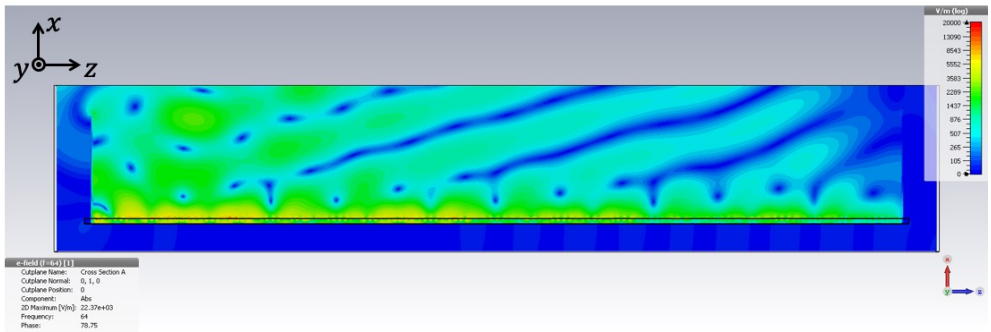

(a)

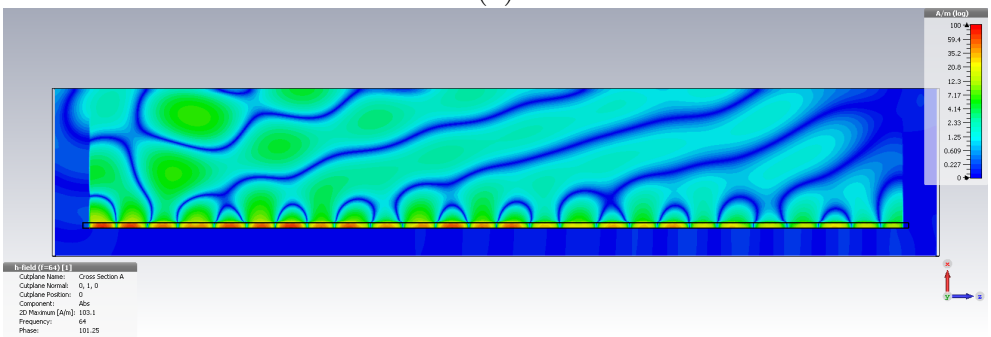

(b)

Figure 3.26: Field distribution in absolute value at 64 GHz of the GDSM-based leaky-wave antenna in the cross section of xz-plane (a) electric field (dBV/m) (b) magnetic field (dBA/m)

GDS-based antenna, the GDSM-based leaky-wave antenna has about 1 dB smaller directivity and larger beam width.

Figure 3.26 shows the electromagnetic field distribution in absolute value of the GDSM-based antenna at 64 GHz in the central xz-plane. The backward leakage wavefront can be well observed despite a disturbance at the feeding edge by the forward radiation of the discontinuity.

Several attempts have been made to remove the undesired forward radiation from the discontinuity at the starting edge of the metasurface. One uses a tapered transition at the beginning of the metasurface, as shown in figure 3.27. The tapered transition starts with two patches, and is then made to symmetrically add one patch per side in the y-axis direction every six patches along the z-axis direction.

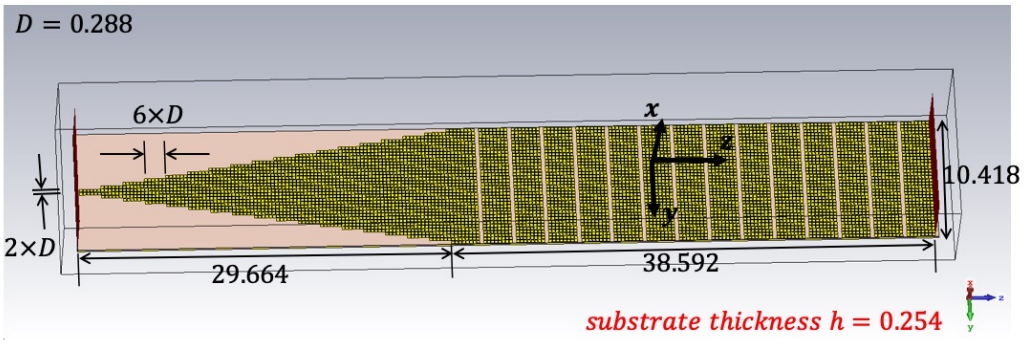

Figure 3.27: Designed leaky-wave antenna with a tapered starting edge of metasurface

The simulated farfield patterns are shown in figure 3.28, and the detailed parameters are shown in table 3.8. It can be observed that by making a smooth tapered transition between the excited GDS-based propagation mode and the metasurface-based propagation mode, the unwanted forward

	57 GHz	60 GHz	62 GHz	64 GHz	Δ
Simulated direction	-50.2°	-34.7°	-25°	-15.2°	$\Delta\theta = 35°$
Simulated directivity	17.6 dB	18.6 dB	18.2 dB	16.7 dB	$\Delta D = 1$ dB
Simulated gain	13.4 dB	15.9 dB	15.7 dB	14.9 dB	$\Delta G = 2.5$ dB

Table 3.8: Simulated scanning range, directivity, and gain of the designed leaky-wave antenna with a tapered starting edge

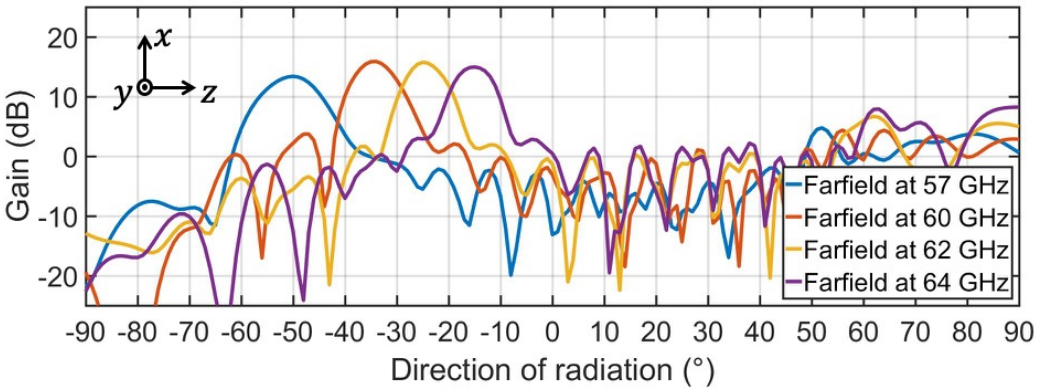

Figure 3.28: Farfield patterns of the designed leaky-wave antenna with a tapered starting edge of metasurface

radiation is significantly reduced. Since the dielectric and metal of the transition create additional losses, the gain of the main beam is smaller compared to the original design. However, the tapered transition model exhibits smaller variation in gain in the operating frequency range.

3.11 Launcher

3.11.1 Launcher design

In the previous simulation, the propagation mode was excited by a numerical waveguide port. However, the radiation properties of the antenna also depend on the performance of the feeder.

It should be noted that efficient surface-wave excitation can be difficult for wide-band operation at microwave and millimeter-wave frequencies. Rectangular waveguide and coaxial transmission line feeding systems [187] may be considered, but these conventional topologies may introduce parasitic losses, exhibit bandwidth limitation, and are generally not uniplanar with manufacturing costs increasing with frequency [200]. In contrast, planar slot configurations in the ground plane of a single-layer GDS have been recognized as an efficient mean of exciting TM mode surface-waves [200, 201].

In our work, we have designed a planar Yagi-Uda-type surface-wave launcher as mentioned in [162, 197, 202], which is a set of slots etched within

the ground plane of the GDS and fed by a coplanar transmission line. The input signal from the coplanar line is coupled into the dominant surface-wave mode of the GDS, with the half-wavelength slot in the antenna ground plane acting as a magnetic dipole source. Folded reflectors are used to counteract the backward radiation and enhance the forward beam of the main radiating element. Generally, the reflectors are slightly longer than the main radiating slot [197]. This type of launcher not only offers the benefits of a single-layer structure and an integrated coplanar waveguide feeding, but can also improves antenna performances (S11 reflection coefficient, gain) [200]. The launcher is typically directive and has small side lobes.

Therefore, a 50 Ω coplanar waveguide line was first designed. Then the launcher is designed using the configuration rules presented in [202] and numerically optimized with the help of the study results in [203]. Finally the input impedance is matched to 50 Ω with tuning stubs (short-circuited stubs for the coplanar waveguide line). Figure 3.29 shows the dimensions of the designed launcher.

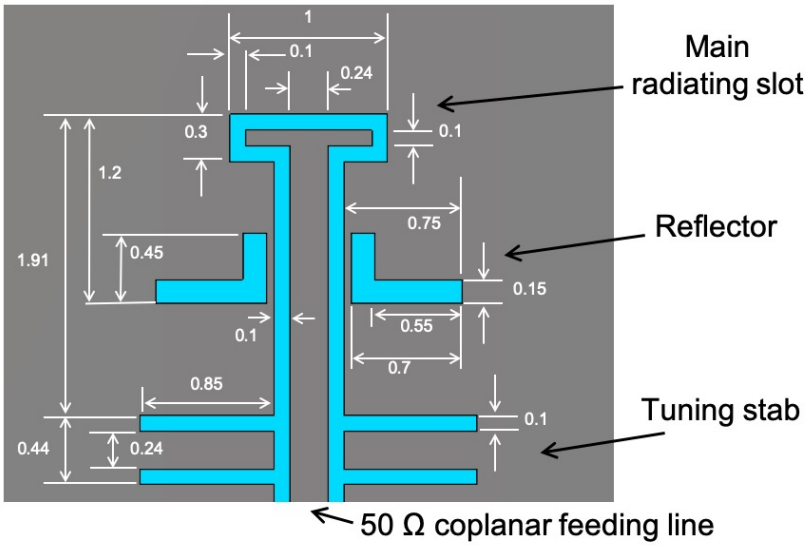

Figure 3.29: TM mode surface-wave launcher design

3.11.2 Simulations of launcher

The designed launcher is singly simulated in CST with the time domain solver, as shown in figure 3.30, where a waveguide port is implemented to excite the coplanar transmission line. The substrate is the same as the one used in the previous leaky-wave antenna design, i.e., the 0.254 mm-thickness RT/duroid® 6010 ($\varepsilon_r = 10.2$). Losses are not considered in the simulation. Therefore, since the launcher acts as a magnetic dipole, its farfield patterns can provide us with a first view of its capability to excite surface-waves to the substrate, i.e., the main radiation beam should point in the direction in which the wave propagates within the substrate. The surrounding xy- and xz-boundaries are set to PMLs. The input impedance of the feeding coplanar line is verified by the simulation, which is 50.23 Ω.

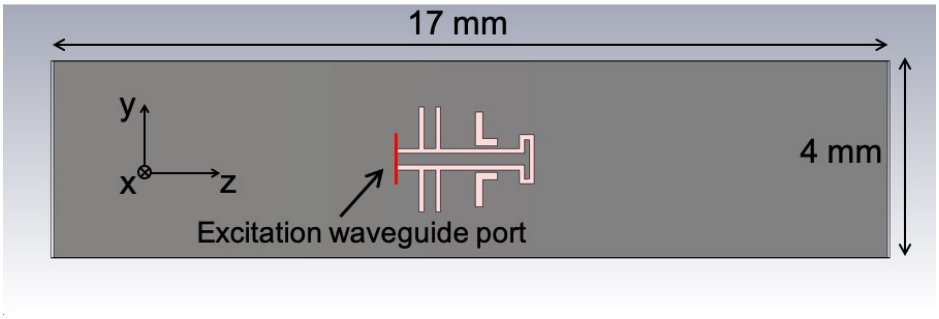

Figure 3.30: Simulation model of the designed TM mode launcher

The farfield patterns of the launcher in the yz-plane are shown in figure 3.31, and the ones in the xz-plane are shown in figure 3.32. It can be seen that the launcher has very directive radiation beam in the positive z-axis direction with maximum gain of 12.4 dB, 13.3 dB, 13.4 dB, and 12.8 dB at 57 GHz, 59 GHz, 61 GHz, and 63 GHz, respectively. At 63 GHz, the backward pattern is relatively larger (7.4 dB) than the other frequencies, but could still be acceptable since the forward main beam is 5.4 dB higher. As can be seen from the xz-plane radiation patterns in figure 3.32, very little energy leaks to the air and most of the energy is coupled to the substrate. The radiation efficiency of the simulated launcher is more than 93% at the four simulated frequencies in the operating band.

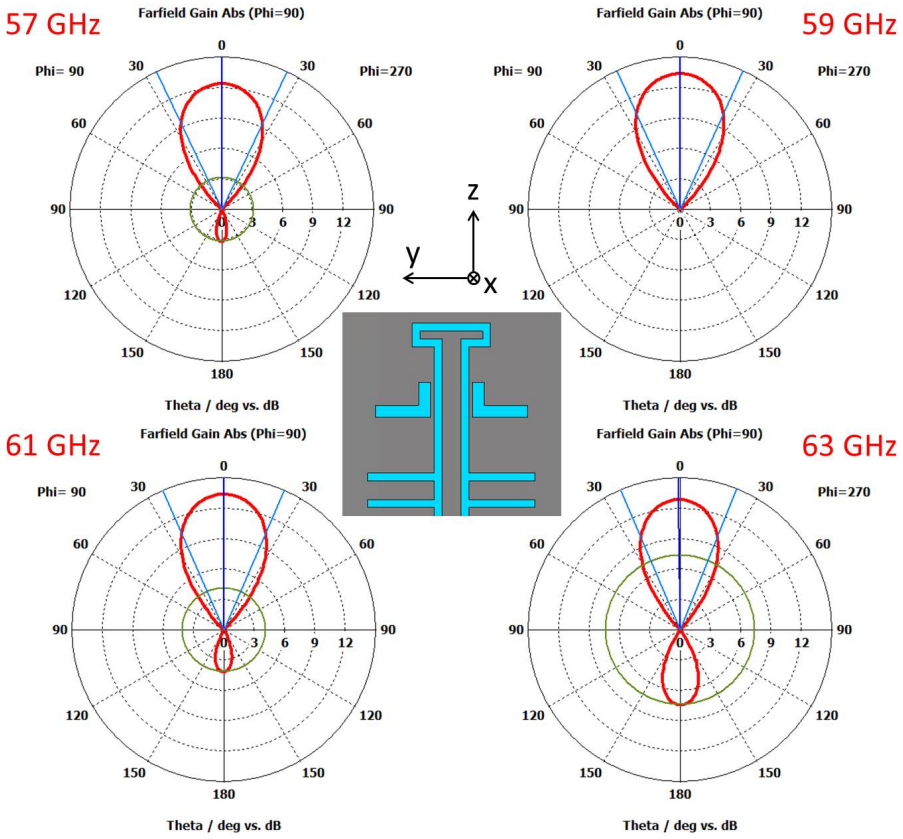

Figure 3.31: Farfield patterns of the launcher in yz-plane

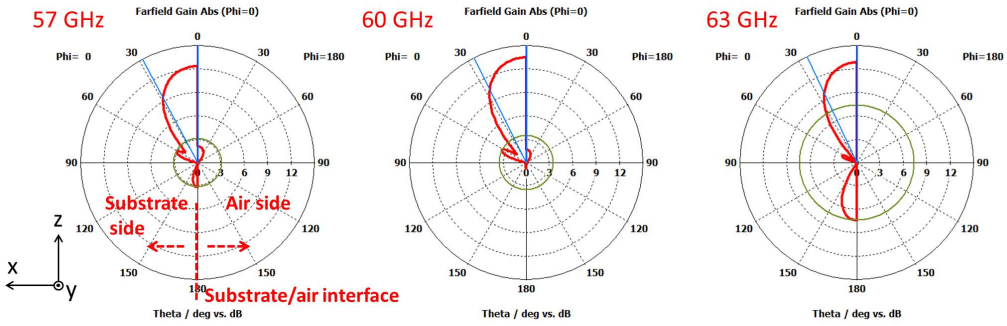

Figure 3.32: Farfield patterns of the launcher in xz-plane

Figure 3.33 shows the simulated S11 parameter of the launcher. We can observe that the launcher has a -10 dB frequency band of 6.7 GHz from 56.7 GHz to 63.4 GHz, which is very suitable for our operating frequency band (57 - 64 GHz).

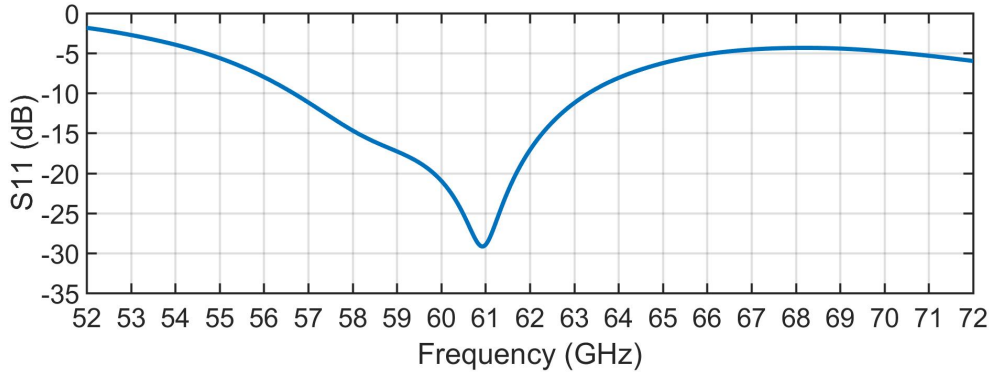

Figure 3.33: Simulated S11 parameter of the designed launcher

3.11.3 Simulations of leaky-wave antenna with launcher

In this section, we present the simulation results for the designed GDSM-based leaky-wave antenna that is fed by the launcher presented in the previous section. It should be noted that the launcher needs to be placed to a suitable distance from the metasurface to properly excite the propagating wave inside the GDSM-based waveguide [200, 204]. In our simulation, the launcher is placed at 0.388 mm from the edge of the metasurface, as shown in figure 3.34.

Figure 3.35 shows the S11 parameters of the simulated model. The -10 dB frequency bandwidth is 7.8 GHz from 56.4 GHz to 64.1 GHz, which is slightly larger than the launcher simulation in figure 3.33.

The simulated farfield pattern of the leaky-wave antenna in the xz-plane is shown in figure 3.36, where the main beam direction and gain are shown in table 3.9. The total scanning range is 36.6° from -52° to -15.4° at the operating frequency band of 57 GHz to 64 GHz, which is in good agreement with the simulation results in section 3.10. However, the leaky-wave antenna with launcher has smaller gain because there is an additional energy conversion step in the model – energy coupling from the coplanar line launcher to the

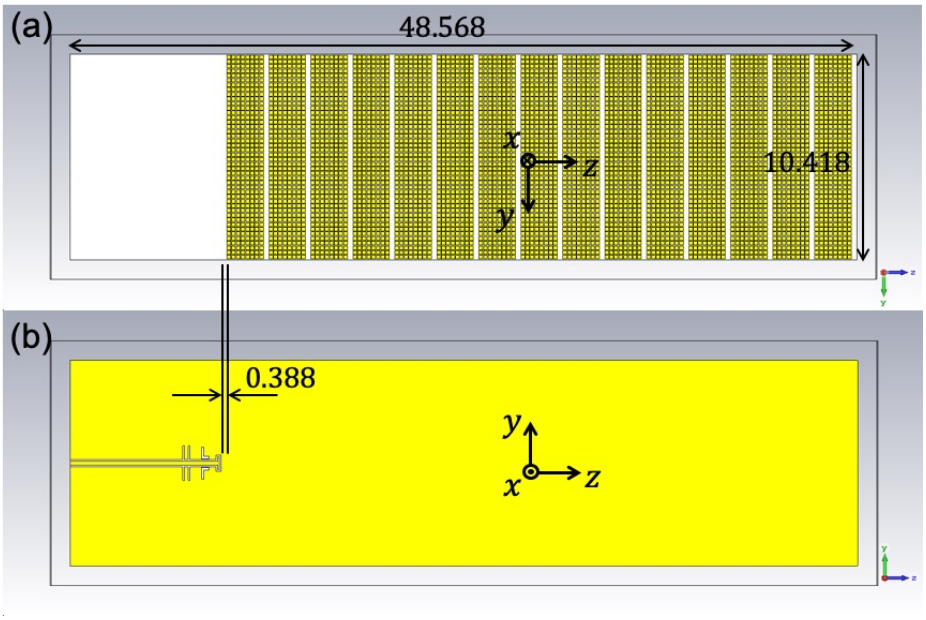

Figure 3.34: Designed GDSM-based leaky-wave antenna with launcher (dimensions in mm) (a) metasurface side (b) ground side

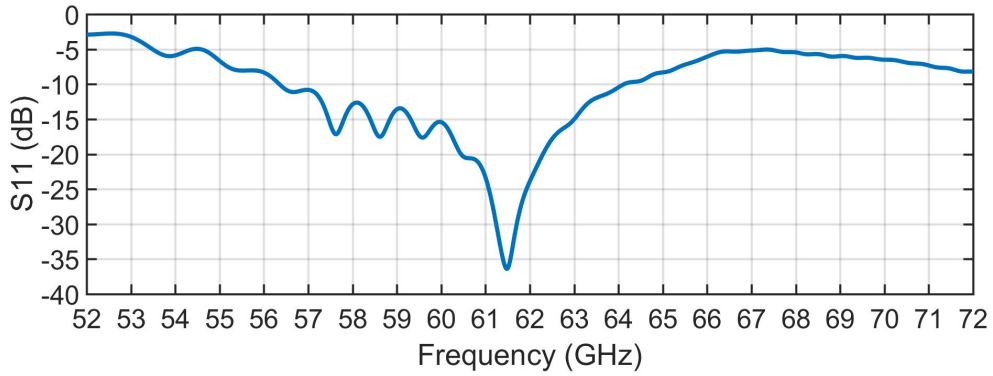

Figure 3.35: S11 parameter of the designed leaky-wave antenna with launcher

fundamental TM mode of the GDS waveguide. The energy is not fully converted to the TM mode by the launcher. It can be observed that the forward radiation from the discontinuity at the starting border of the metasurface is

smaller at 62 GHz and 64 GHz. The radiation beam at 57 GHz is slightly disturbed.

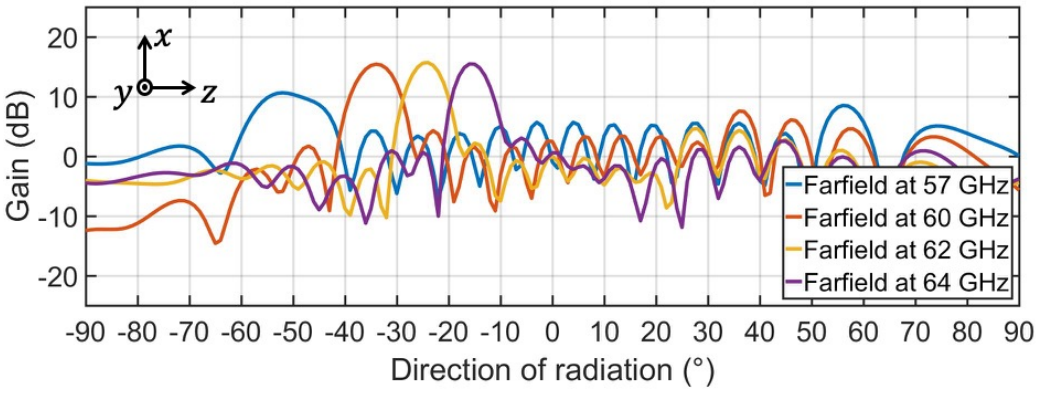

Figure 3.36: Farfield patterns of the designed leaky-wave antenna with launcher

	57 GHz	60 GHz	62 GHz	64 GHz
Simulated direction	-52°	-34°	-24.4°	-15.4°
Simulated gain	10.6 dB	15.4 dB	15.7 dB	15.4 dB
Radiation efficiency	75%	72%	74%	72%
Total efficiency	69%	70%	73%	65%

Table 3.9: Simulated scanning range and gain of the GDSM-based periodic Leaky-wave antenna with launcher

As shown in table 3.9, the radiation efficiency (relative to the accepted energy at the excitation port) at the operating frequencies of 57 - 64 GHz is more than 70%. Moreover, since the S11 reflection coefficient in this frequency band is less than -10 dB, the radiation efficiency can be approxiatively referred to as the total efficiency of the GDSM-based leaky-wave antenna fed with launcher. Therefore, approximately 20% to 25% of the energy is lost in the strucutre materials (copper and dielectric substrate). The radiation efficiency is relatively significant compared to the SIW-based periodic leaky-wave antenna presented in [158] using the same substrate, which has only a radiation efficiency of 37% to 43%. In addition, a periodic comb-line microstrip leaky-wave antenna in [193] has demonstrated a 55% radiation efficiency.

Figure 3.37 shows the magnetic field distribution in absolute value in the yz-plane of the substrate at 60 GHz. As can be seen, most of the energy is directed by the launcher to the forward direction to excite the antenna.

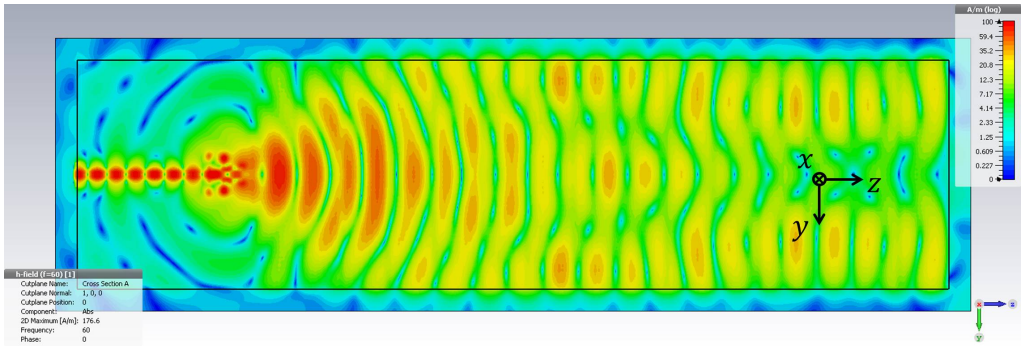

Figure 3.37: Magnetic field distribution in absolute value (dBA/m) in the substrate of the cross-sectional yz-plane at 60 GHz

3.11.4 Simulations of leaky-wave antenna with launcher and connector

In order to achieve experimental measurements, the designed antenna requires a connector to power the coplanar line of the launcher. A 1.85 mm jack end (female) launch connector (model reference number 1892-04A-5 [205]) manufactured by Southwest Microwave is added to the previous simulation to verify if it is suitable for experimental use.

The dimensions of the connector are shown in figure 3.38, and the simulated model is shown in figure 3.39. The connector is commonly used for the transition between coaxial cable and printed circuit boards (PCBs) operating at frequencies up to 67 GHz. A threaded clamping plate is implemented to fix the connected PCB as shown in figures 3.38 and 3.39.

Figure 3.40 shows the simulated S11 parameters, which has greatly changed compared to the simulation without connector. The -10 dB bandwidth has been reduced from 7.7 GHz to only 1.9 GHz (59.6 GHz to 61.5 GHz). This is due to the discontinuity between the coaxial access and the coplanr line as well as the launcher being designed with an ungrounded

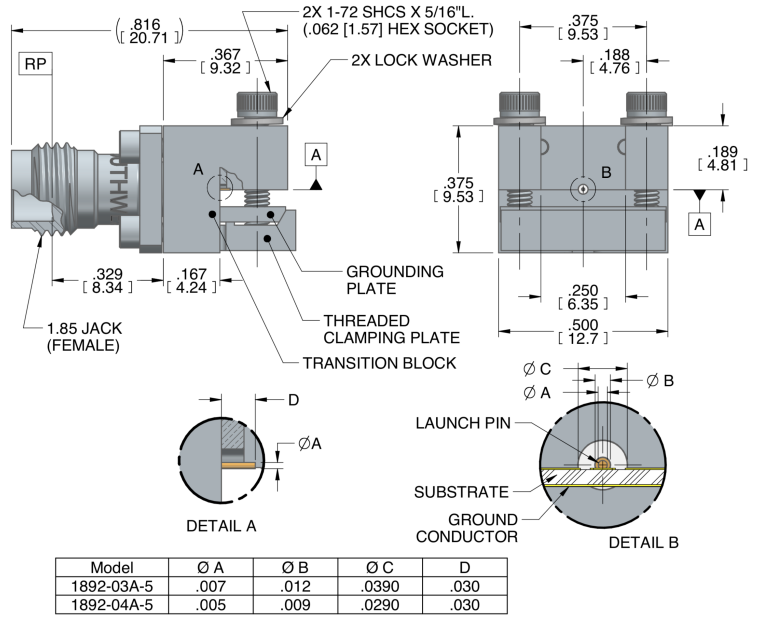

Model	Ø A	Ø B	Ø C	D
1892-03A-5	.007	.012	.0390	.030
1892-04A-5	.005	.009	.0290	.030

Figure 3.38: Dimensions of connector (dimensions in inch) [205]

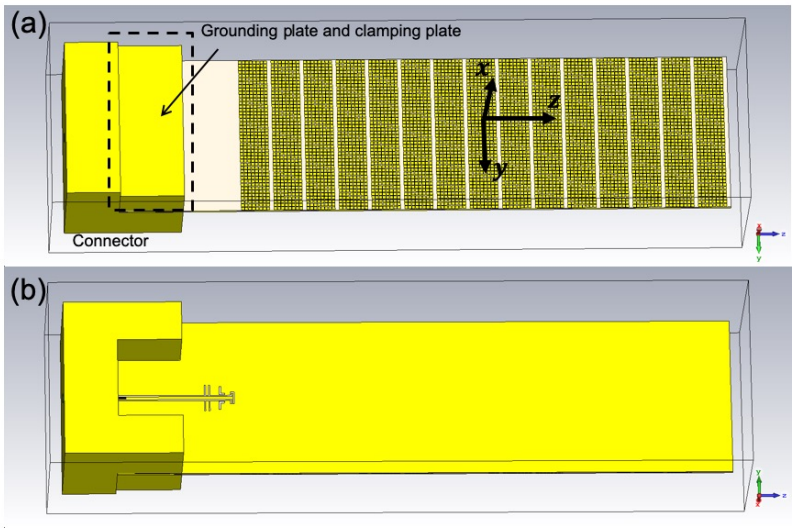

Figure 3.39: Designed leaky-wave antenna with launcher and connector

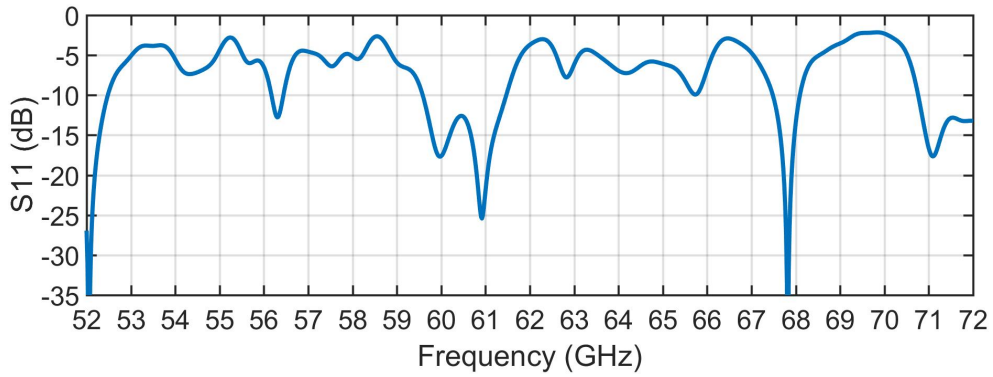

Figure 3.40: S11 parameters of the designed Leaky-wave antenna with launcher and connector

coplanar line. The grounding and clamping plates of the connector changed the geometry of the initial launcher design, which added a ground to the starting coplanar line of the launcher, as shown in figure 3.39. Therefore, the input impedance of the launcher is no longer matched to 50 Ω. For example, for the coplanar line configuration in figure 3.29, the ungrounded coplanar line calculator in [206] gives an input impedance of 50.67 Ω, while the grounded coplanar line calculator in [207] gives an input impedance of 41.55 Ω. Consequently, the transitions "coaxial cable to grounded coplanar line" and "grounded coplanar line to ungrounded coplanar line" at the launcher section degrades the performance of the energy transfer to the leaky-wave antenna.

The farfield patterns are shown in figure 3.41, and the detailed characteristics such as main beam direction, maximum gain, radiation efficiency, and total efficiency are shown in table 3.10. As expected from the S11

	57 GHz	60 GHz	62 GHz	64 GHz
Simulated direction	-52°	-35°	-26°	-17.9°
Simulated gain	9.2 dB	13.3 dB	12.1 dB	14.7 dB
Radiation efficiency	37%	60%	30%	37%
Total efficiency	24%	59%	17%	30%

Table 3.10: Characteristics of the GDSM-based periodic Leaky-wave antenna with launcher and connector

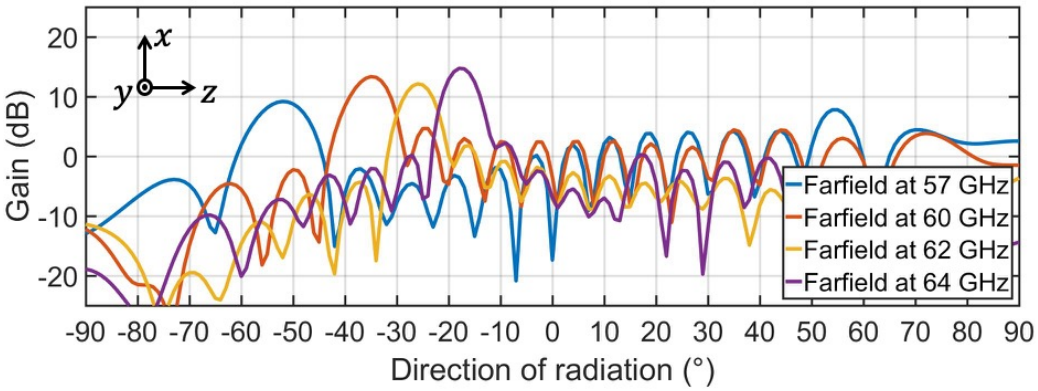

Figure 3.41: Farfield patterns of the designed Leaky-wave antenna with launcher and connector

parameters, the maximum gain of the main beams have been degraded by 1 dB to 2 dB, especially at 62 GHz (3 dB degradation). Furthermore, the radiation efficiency and the total efficiency of the antenna have drastically dropped. The total efficiency of the antenna with connector drops to less than 30% at 57 GHz, 62 GHz, and 64 GHz.

Figure 3.42 shows the magnetic field distribution in absolute value in the yz-plane of the substrate at 60 GHz and 62 GHz. It can be seen that due to the mismatch of the "coaxial cable to grounded coplanar line" and "grounded coplanar line to ungrounded coplanar line", a part of the energy is reflected and trapped in the grounded coplanar line board, which results in higher dielectric losses and lower antenna efficiency.

Consequently, the tested connector is not suitable to be directly used for experimental measurements. A transition from grounded coplanar line to ungrounded coplanar line should be further designed and added to the beginning of the launcher to eliminate the perturbation from the fixation ground plate of the connector. Moreover, the transition between the coaxial connector and the grounded coplanar line should be also optimized. We have conducted several attempts of optimizing smoother transition, but due to a lack of time, this work has not succeeded (e.g. the simulation of the metasurface-based antenna with launcher in figure 3.34 takes 36 hours, and the same simulation model with the additional connector, even if the calculation accuracy is reduced by a quarter, takes 32 hours).

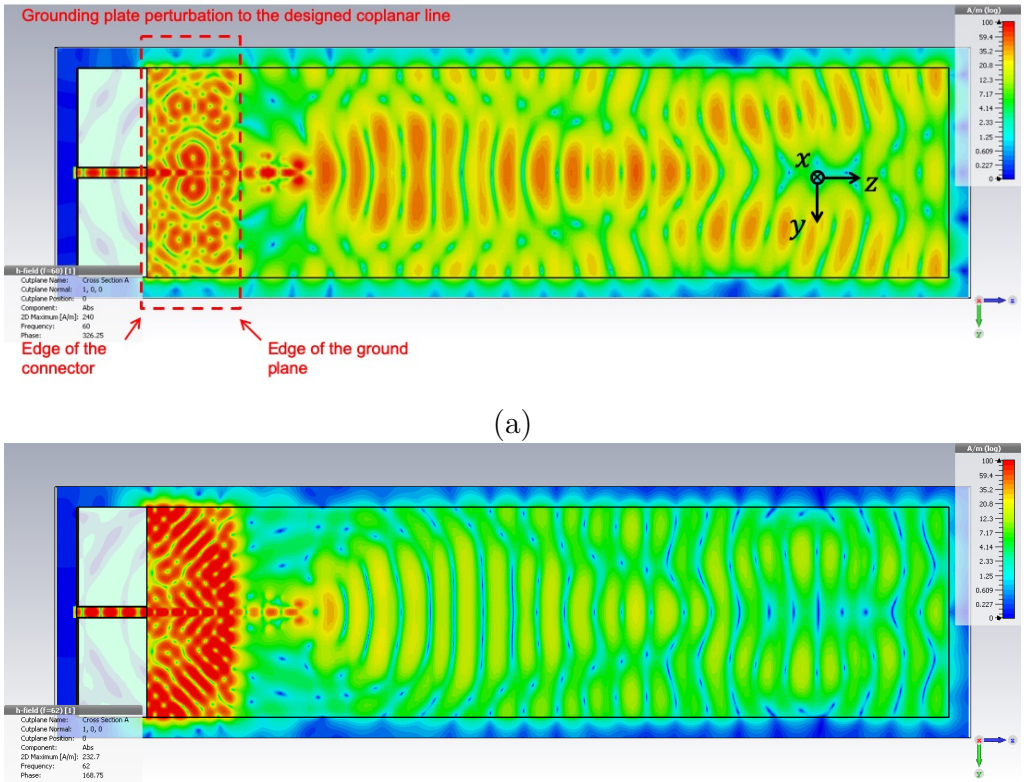

(a)

(b)

Figure 3.42: Magnetic field distribution in absolute value (dBA/m) in the substrate of the cross-sectional yz-plane (a) at 60 GHz (b) at 62 GHz

3.12 Test of Fabrication

Although the designed antenna is not suitable with the Southwest Microwave connector, the manufacturing process was tested in this work.

Due to the planar and patch-printing features of the antenna, a simple fabrication process can be achieved with a laser structuring machine. Laser processing is a maskless process with no chemical and low cost [158]. Compared to traditional etch printing technology, the laser-structured printing technology has numerous advantages, such as speed and accuracy.

The laser machine used in the fabrication test was the LPKF ProtoLaser S4 [208], which uses a 532 nm wavelength green laser to achieve minimum

of 75 µm line and 25 µm space. This machine is specifically designed for structuring of laminated printed boards, such as our patch array metasurface antenna. In order to obtain clean edges and smooth grooves, all parameters of the laser process have been optimized and precisely adjusted.

Figure 3.43 shows a manufacturing sample of the designed leaky-wave antenna. The fabrication accuracy of the sample was measured, which is within 10 µm. It could be noted that in order to reduce the accuracy error ratio of the production model, a larger patch and gap dimensions (D and w indicated in figure 3.18) of the metasurface may be considered in future works.

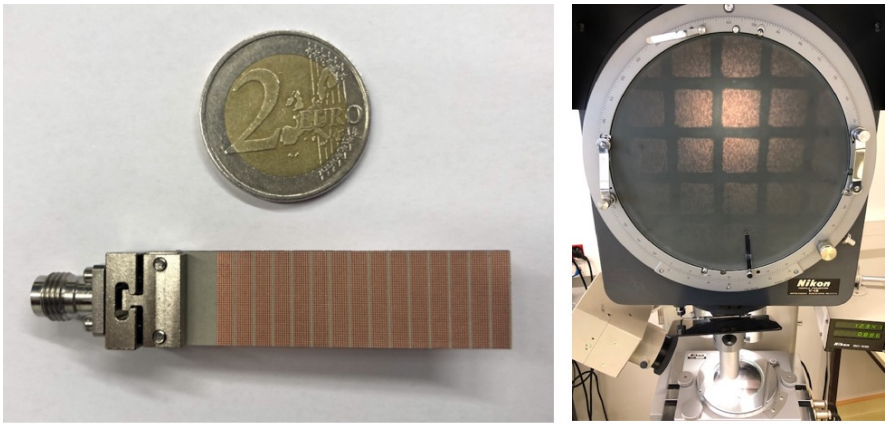

Figure 3.43: Leaky wave antenna fabrication test (a) prototype (b) microscope view of the metasurface

Several attempts of prototype radiation pattern measurements have been done. Unfortunately, the beams of the leaky radiation were observed with only one prototype (see figure 3.44). Although the beams exhibit a 10° shift toward the backward direction compared to the simulation result, the enhanced scanning range capability is very consistent with the simulation (i.e., $\Delta\theta = 37.5°$ in the measurement in the operating frequency range of 57 GHz to 64 GHz, and $\Delta\theta = 35.6°$ in the simulation). In addition, the launcher of this measured prototype is not the final optimized design, which exhibits high parasite side-lobes and affect greatly the desired leaky radiation. Several aspects need to be further investigated and therefore are open for perspectives

of this work:

- Connector: the connector requires screw to be attached to the substrate. The screwing strength and the placement exactness of the connector influences the matching.
- Substrate: the permittivity used in the simulations was the one given by the constructor. It would be beneficial to characterize the substrate because a few percents of error upon ε_r may completely cancel the leaky-wave mode.
- Etching accuracy: a deeper sensitivity analysis should be carried out in order to determine its effect on the radiation pattern.

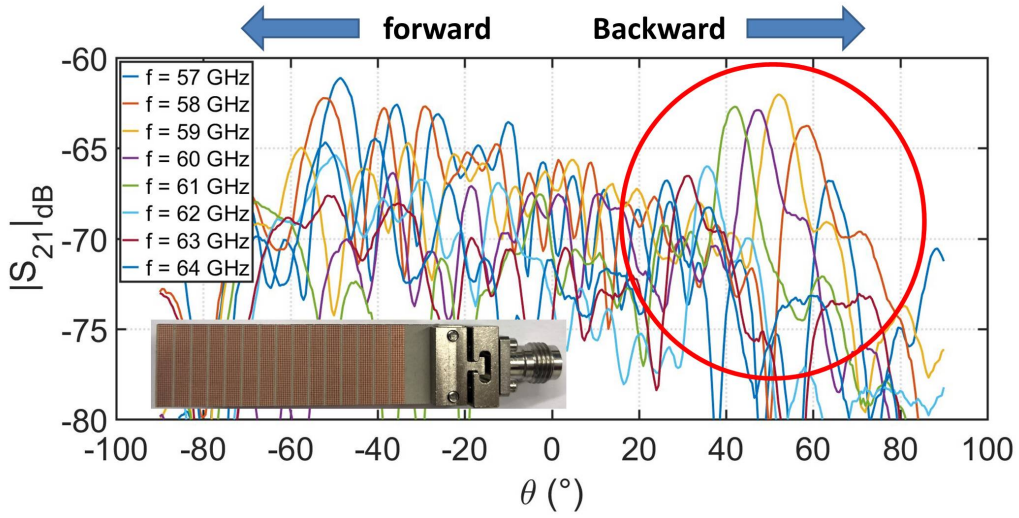

Figure 3.44: Antenna farfield measurement results

3.13 Discussions

In this chapter, the enhanced scanning range metasurface-based leaky-wave antenna design with launcher is validated in the full-wave simulations. The simple and accurate antenna design process is introduced. However, in order to perform experimental measurements, there is necessary to further design

a transition from grounded coplanar line to ungrounded coplanar line and add it to the launcher part to effectively feed the antenna, or consider using other types of connector to feed directly the ungrounded coplanar line of the designed launcher.

In addition, it is desirable for the starting edge of the metasurface to have a smoother form (e.g., taper form) to eliminate unwanted forward radiation from the abrupt discontinuities, which may results in increased gain and efficiency for the main leaky radiation beam. Moreover, since the width of the launcher is much smaller than the width of the antenna, a transition (e.g., planar lens [209]) between the launcher and the antenna may also be preferable to make the cylindrical excitation waves planar before reaching the antenna, thereby increasing the gain and the radiation performance.

Lastly, it would be beneficial to optimize the antenna length (number of periods), antenna width, and etched periodicity width w_{gap} to increase the radiation gain. The relation between the leakage constant and these dimension characteristics requires further investigation.

Conclusion and Perspective

Two contributions have been achieved in this thesis dissertation for medical applications: skin-confined on-body propagation analysis for secure communication between on-body sensors in BAN and enhanced scanning-range leaky-wave antenna for non-contact medical monitoring Doppler radar systems, respectively. The transverse resonance method has played an essential role in these analysis works.

Firstly, a dispersion analysis of the on-body propagation modes within human skin has been achieved using transverse resonance technique and a multilayer human body model, in order to better understand the body-antenna interaction as well as to assess whether the skin-confined transmission mechanism can be used to ensure secure communication between on-body sensors in BAN. It has been observed that when the propagating wave is TE polarized, operating in the frequency range of 3 GHz to 8 GHz could allow short distance (tens of centimeters) skin-confined propagation. This frequency band is also interesting as it is considered as UWB channel in the IEEE 802.15.6 standard dedicated to BAN. In this frequency range, the propagation is better confined to the human body, which naturally enables secure on-body communications and solves data privacy issues. In addition, compared to the HBC operation frequencies proposed in BAN standard, this frequency range improves the transmission bandwidth, thereby having the potential to achieve higher transmission data rates, and/or to use low-duty cycle communication schemes, such as On-Off-Keying modulations, to decrease energy consumption. Full-wave simulations have shown that the skin-confined TE propagation mode of interest can be excited by a horizontal dipole placed directly on human skin or inside the human skin. It can be expected that a more directive TE polarized antenna, such as Yagi-Uda dipole array, could be more efficient for the excitation. Thus some valuable future work can focused on this area of research to find more efficient launchers for the skin-confined

propagation.

For the enhanced scanning-range leaky-wave antenna design, a TRM-based dispersion analysis is also conducted to study different waveguide structures in order to design a periodic leaky-wave antenna that radiates backward. The antenna design procedure steps are introduced in detail, and the method is proved to be simple and accurate. A more conventional leaky-wave antenna is firstly designed using a grounded dielectric slab that is periodically loaded with thin metal strips, and is then compared to a more dispersive structure based on a metasurface of square patches. Simulations results are in good agreement with theoretical calculations and enhanced scanning capabilities are obtained thanks to the metasurface. Indeed, by using the same substrate and the same fractional bandwidth of 11.6% at 60 GHz, a scanning range from -50.6° to -15° is achieved with the metasurface compared to a -28.1° to -16° range of the classical leaky-wave antenna. An improvement of a 2.9 ratio is therefore achieved as expected from the dispersion analysis. It should be noted that a larger scanning range could be further achieved by choosing a denser substrate in the design procedure as long as it is verified that only one propagation mode exists in the operation band. Such scanning range enhancement method is very beneficial when the choice of substrate is limited and is easy to fabricate.

A surface-wave launcher has also been designed to excite the metasurface-based leaky-wave antenna with a total efficiency of 70% observed in the operation frequency band of 57 - 64 GHz in the full-wave simulation. However, discontinuities at the starting edge of the metasurface cause undesired radiation in the forward quadrant. In future work, a smoother transition between the excited propagation mode and the metasurface propagation mode need to be performed to feed the antenna more efficiently. In addition, even if the designed launcher is efficient for the metasurface-based leaky-wave antenna, the launcher is fed by an ungrounded coplanar transmission line, which is not suitable for the "coaxial cable to grounded coplanar line" connectors typically available. In order to perform experimental measurements to verify the antenna design, a transition between the coaxial connector and the ungrounded coplanar line should be further optimized in future works. Moreover, as the launcher width is much smaller than the antenna width, a transition (e.g., planar lens) between the launcher and the antenna may also be preferred to transfer the excited cylindrical waves into a plane wave before reaching the antenna, thereby increasing the gain value and the radiation performance.

Bibliography

[1] G.-Z. Yang, *Body Sensor Networks*. Springer, 2006.

[2] "IEEE standard for local and metropolitan area networks - part 15.6: Wireless body area networks," *IEEE Std 802.15.6-2012*.

[3] A. W. Astrin, H.-B. Li, and R. Kohno, "Standardization for body area networks," *IEICE Transactions*, vol. 92-B, pp. 366–372, Feb. 2009.

[4] N. R. Hooyman, K. Y. Kawamoto, and H. A. Kiyak, *Social Gerontology: A Multidisciplinary Perspective*. Pearson, 2017.

[5] "Global population profile: 2002," [Online], Available: https://www.census.gov/prod/2004pubs/wp-02.pdf, Accessed: Jun. 2019.

[6] M. Patel and J. Wang, "Applications, challenges, and prospective in emerging body area networking technologies," *IEEE Wireless Communications*, vol. 17, no. 1, pp. 80–88, Feb. 2010.

[7] S. Movassaghi, M. Abolhasan, J. Lipman, D. Smith, and A. Jamalipour, "Wireless body area networks: A survey," *IEEE Communications Surveys Tutorials*, vol. 16, no. 3, pp. 1658–1686, Jan. 2014.

[8] "Holter monitor," [Online], Available: https://www.mayoclinic.org/tests-procedures/holter-monitor/about/pac-20385039, Accessed: Jun. 2019.

[9] "Holter monitor," [Online], Available: http://https://www.hopkinsmedicine.org/health/treatment-tests-and-therapies/holter-monitor, Accessed: Jul. 2019.

[10] S. Ullah, H. Higgins, B. Braem, B. Latre, C. Blondia, I. Moerman, S. Saleem, Z. Rahman, and K. Kwak, "A comprehensive survey of wireless body area networks," *Journal of medical systems*, vol. 36, pp. 1065–94, Aug. 2010.

[11] S. L. Cotton, R. D'Errico, and C. Oestges, "A review of radio channel models for body centric communications," *Radio Science*, vol. 49, no. 6, pp. 371–388, Jun. 2014.

[12] D. M. Barakah and M. Ammad-uddin, "A survey of challenges and applications of wireless body area network (WBAN) and role of a virtual doctor server in existing architecture," in *2012 Third International Conference on Intelligent Systems Modelling and Simulation*, Feb. 2012, pp. 214–219.

[13] K. Y. Yazdandoost and K. Sayrafian-Pour, "Channel model for body area network (BAN)," [Online], Available: https://mentor.ieee.org/802.15/dcn/08/15-08-0780-12-0006-tg6-channel-model.pdf, Accessed: Jun. 2019.

[14] B. Zhen, M. Patel, S. Lee, and E. Won, "Body area network (BAN) technical requirements," [Online], Available: https://mentor.ieee.org/802.15/dcn/08/15-08-0037-03-0006-ieee-802-15-6-technical-requirements-document-v-4-0.doc, Accessed: Jun. 2019.

[15] R. Negra, I. Jemili, and A. Belghith, "Wireless body area networks: Applications and technologies," *Procedia Computer Science*, vol. 83, May 2016.

[16] K. J. Cash and H. A. Clark, "Nanosensors and nanomaterials for monitoring glucose in diabetes," *Trends in molecular medicine*, vol. 16, no. 12, pp. 584–593, Sep. 2010.

[17] K. S McKeating, A. Aube, and J.-F. Masson, "Biosensors and nanobiosensors for therapeutic drug and response monitoring," *The Analyst*, vol. 141, Dec. 2015.

[18] V. Kumar, N. Kapoor, S. Kumar, M. Juneja, and A. Khanuja, "Area efficient high performance word line segmented architecture in 7nm

finfet sram compiler," in *2019 32nd International Conference on VLSI Design and 2019 18th International Conference on Embedded Systems (VLSID)*, Jan. 2019, pp. 437–442.

[19] K. S. Kwak, S. Ullah, and N. Ullah, "An overview of IEEE 802.15.6 standard," in *2010 3rd International Symposium on Applied Sciences in Biomedical and Communication Technologies (ISABEL 2010)*, Nov. 2010, pp. 1–6.

[20] C. Otto, A. Milenkovic, C. Sanders, and E. Jovanov, "System architecture of a wireless body area sensor network for ubiquitous health monitoring," *Journal of Mobile Multimedia*, vol. 1, pp. 307–326, Jan. 2006.

[21] K. Van Laerhoven, B. Lo, J. WP Ng, S. Thiemjarus, R. King, S. Kwan, H. Gellersen, M. Sloman, O. Wells, P. Needham, N. Peters, A. Darzi, C. Toumazou, and G.-Z. Yang, "Medical healthcare monitoring with wearable and implantable sensors," Jan. 2004.

[22] L. Wolf and S. Saadaoui, "Architecture concept of a wireless body area sensor network for health monitoring of elderly people," in *2007 4th IEEE Consumer Communications and Networking Conference*, Jan. 2007, pp. 722–726.

[23] H. Tannous, D. Istrate, A. Benlarbi-Delai, J. Sarrazin, D. Gamet, M.-C. Ho Ba Tho, and T. T. Dao, "A new multi-sensor fusion scheme to improve the accuracy of knee flexion kinematics for functional rehabilitation movements," *Sensors*, vol. 16, no. 11, p. 1914, Nov. 2016.

[24] N. Oliver and F. Flores-Mangas, "Healthgear: a real-time wearable system for monitoring and analyzing physiological signals," in *International Workshop on Wearable and Implantable Body Sensor Networks (BSN'06)*, Apr. 2006, pp. 4 pp.–64.

[25] M. Welsh, S. Moulton, T. Fulford-Jones, and D. Malan, "CodeBlue: An ad hoc sensor network infrastructure for emergency medical care," *MobiSys 2004 Workshop on Applications of Mobile Embedded Systems (WAMES 2004)*, Jan. 2004.

[26] V. Shnayder, B.-r. Chen, K. Lorincz, T. Fulford-Jones, and M. Welsh, "Sensor networks for medical care," Jan. 2005, p. 314.

[27] K. Lorincz, D. J. Malan, T. R. F. Fulford-Jones, A. Nawoj, A. Clavel, V. Shnayder, G. Mainland, M. Welsh, and S. Moulton, "Sensor networks for emergency response: challenges and opportunities," *IEEE Pervasive Computing*, vol. 3, no. 4, pp. 16–23, Oct. 2004.

[28] D. Curtis, E. Shih, J. Waterman, J. Guttag, J. M. Bailey, T. Stair, R. Greenes, and L. Ohno-Machado, "Physiological signal monitoring in the waiting areas of an emergency room," *BODYNETS 2008 - 3rd International ICST Conference on Body Area Networks*, p. 5, Jan. 2008.

[29] K. Wac, R. Bults, B. van Beijnum, I. Widya, V. Jones, D. Konstantas, M. Vollenbroek-Hutten, and H. Hermens, "Mobile patient monitoring: The mobihealth system," in *2009 Annual International Conference of the IEEE Engineering in Medicine and Biology Society*, Sep. 2009, pp. 1238–1241.

[30] D. Lewis, "802.15.6 call for applications - response summary," [Online], Available: https://mentor.ieee.org/802.15/file/08/15-08-0407-00-0006-tg6-applications-summary.doc, Accessed: Jun. 2019.

[31] B. Latré, B. Braem, I. Moerman, C. Blondia, and P. Demeester, "A survey on wireless body area networks," *Wireless Networks*, vol. 17, no. 1, pp. 1–18, Jan. 2011.

[32] C. A. Chin, G. V. Crosby, T. Ghosh, and R. Murimi, "Advances and challenges of wireless body area networks for healthcare applications," in *2012 International Conference on Computing, Networking and Communications (ICNC)*, Jan. 2012, pp. 99–103.

[33] M. T. Arefin, M. Hanif, and A. F. Haque, "Wireless body area network: An overview and various applications," *Journal of Computer and Communications*, vol. 5, pp. 53–64, May 2017.

[34] A. Rangarajan, "Emerging trends in healthcare adoption of wireless body area networks," *Biomedical Instrumentation and Technology*, vol. 50, pp. 264–276, Jan. 2016.

[35] P. Kumar and H.-J. Lee, "Security issues in healthcare applications using wireless medical sensor networks: A survey," *Sensors (Basel, Switzerland)*, vol. 12, pp. 55–91, Jan. 2012.

[36] J. Khan and M. R. Yuce, *Wireless Body Area Network (WBAN) for Medical Applications*, Jan. 2010.

[37] S. Xu, Y. Zhang, L. Jia, K. Mathewson, K. Jang, J. Kim, H. Fu, X. Huang, P. Chava, R. Wang, S. Bhole, L. Wang, Y. Na, Y. Guan, M. Flavin, Z. Han, Y. Huang, and J. Rogers, "Soft microfluidic assemblies of sensors, circuits, and radios for the skin," *Science*, vol. 344, no. 6179, pp. 70–74, Jan. 2014.

[38] "Imagine living a healthier life with GlucoWise™," [Online], Available: http://www.gluco-wise.com/, Accessed: Jun. 2019.

[39] Y. Fan and C. Wen, "A virtual reality soldier simulator with body area networks for team training," *Sensors (Basel, Switzerland)*, vol. 19, no. 3, p. 451, Jan. 2019.

[40] T. D. Than, G. Alici, H. Zhou, and W. Li, "A review of localization systems for robotic endoscopic capsules," *IEEE Transactions on Biomedical Engineering*, vol. 59, no. 9, pp. 2387–2399, Sep. 2012.

[41] "Endoscopy: Meaning, cost, and types," [Online], Available: practo.com/health-wiki/endoscopymeaning-cost-types/176/article, Accessed: Jul. 2019.

[42] "Pillcam - small bowel capsule endoscopy," [Online], Available: http://www.hemorrhoidtreatmentnyc.com/services-small-bowel-capsule-endoscopy.html, Accessed: Jul. 2019.

[43] "Pill endoscopy test," [Online], Available: https://sosyalforum.org/pill-endoscopy-test, Accessed: Jul. 2019.

[44] G. Ciuti, A. Menciassi, and P. Dario, "Capsule endoscopy: From current achievements to open challenges," *IEEE Reviews in Biomedical Engineering*, vol. 4, pp. 59–72, Oct. 2011.

[45] "Qardiocore," [Online], Available: https://www.getqardio.com/fr/qardiocore-wearable-ecg-ekg-monitor-iphone/, Accessed: Aug. 2019.

[46] M. W. Alam, T. Sultana, and S. Alam, "A heartbeat and temperature measuring system for remote health monitoring using wireless body area network," *International Journal of Bio-Science and Bio-Technology*, vol. 8, pp. 171–190, Feb. 2016.

[47] D. Martins and H. Guyennet, "Wireless sensor network attacks and security mechanisms: A short survey," in *2010 13th International Conference on Network-Based Information Systems*, Sep. 2010, pp. 313–320.

[48] T. Hall, D. Y. C. Lie, T. Q. Nguyen, J. C. Mayeda, P. E. Lie, J. Lopez, and R. E. Banister, "Non-contact sensor for long-term continuous vital signs monitoring: A review on intelligent phased-array Doppler sensor design," *Sensors*, vol. 17, no. 11, p. 2632, Nov. 2017.

[49] T. Hall, C. Stout, N. Brewer, G. Dominguez, J. Tsay, A. Boothby, V. Das, J. Lopez, T. Nguyen, R. E. Banister, and D. Y. C. Lie, "Extending the range of phased array non-contact vital signs monitoring in an office cubicle setting," in *Texas Symposium on Wireless and Microwave Circuits and Systems*, Apr. 2014, pp. 1–4.

[50] M. Amin, *Radar for Indoor Monitoring: Detection, Classification, and Assessment*. CRC Press, 2017.

[51] D. Obeid, G. Zaharia, S. Sadek, and G. Zein, "Microwave Doppler radar for heartbeat detection vs electrocardiogram," *Microwave and Optical Technology Letters*, vol. 54, Nov. 2012.

[52] C. G. Caro and J. A. Bloice, "Contactless apnoea detector based on radar," *The Lancet*, vol. 298, no. 7731, pp. 959–961, Oct. 1971.

[53] M. Bimpas, N. Paraskevopoulos, K. Nikellis, D. Economou, and N. Uzunoglu, "Development of a three band radar system for detecting trapped alive humans under building ruins," *Progress in Electromagnetics Research-pier - PROG ELECTROMAGN RES*, vol. 49, pp. 161–188, Jan. 2004.

[54] C. I. Franks, B. H. Brown, and D. M. Johnston, "Contactless respiration monitoring of infants," *Medical and biological engineering*, vol. 14, no. 3, pp. 306–312, May 1976.

[55] D. Obeid, S. Sadek, G. Zaharia, and G. E. Zein, "Doppler radar for heartbeat rate and heart rate variability extraction," in *2011 E-Health and Bioengineering Conference (EHB)*, Nov. 2011, pp. 1–4.

[56] T. Zhang, J. Sarrazin, G. Valerio, and D. Istrate, "Estimation of human body vital signs based on 60 GHz Doppler radar using a

bound-constrained optimization algorithm," *Sensors (Basel, Switzerland)*, vol. 18, no. 7, p. 2254, Jul. 2018.

[57] [Online], Available: https://atap.google.com/soli/, Accessed: Jun. 2019.

[58] B. Johny and A. Anpalagan, "Body area sensor networks: Requirements, operations, and challenges," *IEEE Potentials*, vol. 33, no. 2, pp. 21–25, Mar. 2014.

[59] S. J. Marinkovic, E. M. Popovici, C. Spagnol, S. Faul, and W. P. Marnane, "Energy-efficient low duty cycle mac protocol for wireless body area networks," *IEEE Transactions on Information Technology in Biomedicine*, vol. 13, no. 6, pp. 915–925, Nov. 2009.

[60] L. F. W. van Hoesel, T. Nieberg, H. J. Kip, and P. J. M. Havinga, "Advantages of a tdma based, energy-efficient, self-organizing mac protocol for wsns," in *2004 IEEE 59th Vehicular Technology Conference. VTC 2004-Spring (IEEE Cat. No.04CH37514)*, vol. 3, May 2004, pp. 1598–1602 Vol.3.

[61] R. Ali Khan and A.-S. Khan Pathan, "The state-of-the-art wireless body area sensor networks: A survey," *International Journal of Distributed Sensor Networks*, vol. 14, p. 155014771876899, Apr. 2018.

[62] L. van den Bosch, E. Segers, and L. Verhoeven, "Incidence of cardiac arrests and unexpected deaths in surgical patients before and after implementation of a rapid response system," [Online], Available: http://www.annalsofintensivecare.com/content/2/1/20, Accessed: Jul. 2019.

[63] "Proposed changes in the commission's rules regarding human exposure to radiofrequency electromagnetic fields," [Online], Available: https://www.fcc.gov/document/proposed-changes-commissions-rules-regarding-human-exposure, Accessed: Jun. 2019.

[64] "ICNIRP guidelines for limiting exposure to time-varying electric, magnetic and electromagnetic fields (up to 300 GHz)," [Online], Available: https://www.icnirp.org/cms/upload/publications/ICNIRPemfgdl.pdf, Accessed: Jun. 2019.

[65] J. J. Kang and S. Adibi, "A review of security protocols in mhealth wireless body area networks (wban)," vol. 523, Jun. 2015, pp. 61–83.

[66] H. Li, J. Schwoerer, Y. Yoon, J. Farserotu, W. Yang, K. Sayrafian, D. Miniutti, D. Lewis, and A. Gowans, "IEEE 802.15.6 regulation subcommittee report," [Online], Available: https://mentor.ieee.org/802.15/dcn/08/15-08-0034-08-0006-ieee-802-15-6-regulation-subcommittee-report.doc, Accessed: Jun. 2019.

[67] I. Frigyes, J. Bito, and P. Bakki, *Advances in Mobile and Wireless Communications – Views of the 16th IST Mobile and Wireless Communication Summit*. Springer Science & Business Media, 2008.

[68] "Medical device radiocommunications service (MedRadio)," [Online], Available: https://www.fcc.gov/medical-device-radiocommunications-service-medradio, Accessed: Jun. 2019.

[69] C. Park and T. S. Rappaport, "Short-range wireless communications for next-generation networks: UWB, 60 GHz Millimeter-Wave WPAN, And ZigBee," *IEEE Wireless Communications*, vol. 14, no. 4, pp. 70–78, Aug. 2007.

[70] J. Feng Zhao, X. Mei Chen, B. Dong Liang, and Q. Xia Chen, "A review on human body communication: Signal propagation model, communication performance, and experimental issues," *Wireless Communications and Mobile Computing*, vol. 2017, pp. 1–15, Oct. 2017.

[71] S. L. Cotton, W. G. Scanlon, and B. K. Madahar, "Millimeter-wave soldier-to-soldier communications for covert battlefield operations," *IEEE Communications Magazine*, vol. 47, no. 10, pp. 72–81, Oct. 2009.

[72] "ETSI TR 101 994-1, Electromagnetic compatibility and Radio spectrum Matters (ERM); Short Range Devices (SRD); Technical characteristics for SRD equipment using Ultra Wide Band technology (UWB) Part 1: Communications applications," [Online], Available: https://www.etsi.org/deliver/etsi_tr/101900_101999/10199401/01.01.01_60/tr_10199401v010101p.pdf, Accessed: Sep. 2019.

[73] S. Adibi, *Mobile Health : A Technology Road Map*. Springer, 2015.

[74] J. S. Min and H. Samueli, "Analysis and design of a frequency-hopped spread-spectrum transceiver for wireless personal communications," *IEEE Transactions on Vehicular Technology*, vol. 49, no. 5, pp. 1719–1731, Sep. 2000.

[75] M. Honkanen, A. Lappetelainen, and K. Kivekas, "Low end extension for bluetooth," in *Proceedings. 2004 IEEE Radio and Wireless Conference (IEEE Cat. No.04TH8746)*, Sep. 2004, pp. 199–202.

[76] D. I. Shin, S. J. Huh, and P. J. Pak, "Patient monitoring system using sensor network based on the ZigBee radio," in *2007 6th International Special Topic Conference on Information Technology Applications in Biomedicine*, Nov. 2007, pp. 313–315.

[77] J. Lee, Y. Su, and C. Shen, "A comparative study of wireless protocols: Bluetooth, UWB, ZigBee, and Wi-Fi," in *IECON 2007 - 33rd Annual Conference of the IEEE Industrial Electronics Society*, Nov. 2007, pp. 46–51.

[78] K. Y. Yazdanboost and R. Kohno, "Ultra wideband L-loop antenna," in *2005 IEEE International Conference on Ultra-Wideband*, Sep. 2005, pp. 201–205.

[79] Kamya Yekeh Yazdandoost and Ryuji Kohno, "UWB antenna for wireless body area network," in *2006 Asia-Pacific Microwave Conference*, Dec. 2006, pp. 1647–1652.

[80] S. Shahid, M. Ali Babar Abbasi, M. Rizwan, and M. Tarar, "Bend profiling of textile antenna for body centric wireless communication," Apr. 2014.

[81] G. A. Conway and W. G. Scanlon, "Antennas for over-body-surface communication at 2.45 GHz," *IEEE Transactions on Antennas and Propagation*, vol. 57, no. 4, pp. 844–855, Apr. 2009.

[82] T. Alves, B. Poussot, J. Laheurte, H. Terchoune, M. Wong, and V. F. Hanna, "Analytical propagation modelling of BAN channels based on the creeping wave theory," in *Proceedings of the Fourth European Conference on Antennas and Propagation*, Apr. 2010, pp. 1–5.

[83] R. Chandra and A. J. Johansson, "Miniaturized antennas for link between binaural hearing aids," in *2010 Annual International Conference of the IEEE Engineering in Medicine and Biology*, Aug. 2010, pp. 688–691.

[84] X. Y. Wu, L. Akhoondzadeh-Asl, Z. P. Wang, and P. S. Hall, "Novel Yagi-Uda antennas for on-body communication at 60GHz," in *2010 Loughborough Antennas Propagation Conference*, Nov. 2010, pp. 153–156.

[85] N. Chahat, M. Zhadobov, S. A. Muhammad, L. Le Coq, and R. Sauleau, "60-GHz textile antenna array for body-centric communications," *IEEE Transactions on Antennas and Propagation*, vol. 61, no. 4, pp. 1816–1824, Apr. 2013.

[86] S. Shahid, M. Rizwan, M. A. B. Abbasi, H. Zahra, S. M. Abbas, and M. A. Tarar, "Textile antenna for body centric WiMAX and WLAN applications," in *2012 International Conference on Emerging Technologies*, Oct. 2012, pp. 1–5.

[87] C. Hertleer, A. Tronquo, H. Rogier, L. Vallozzi, and L. Van Langenhove, "Aperture-coupled patch antenna for integration into wearable textile systems," *IEEE Antennas and Wireless Propagation Letters*, vol. 6, pp. 392–395, 2007.

[88] C. Hertleer, H. Rogier, L. Vallozzi, and L. Van Langenhove, "A textile antenna for off-body communication integrated into protective clothing for firefighters," *IEEE Transactions on Antennas and Propagation*, vol. 57, no. 4, pp. 919–925, Apr. 2009.

[89] T. Tuovinen, K. Y. Yazdandoost, and J. Iinatti, "Monopole ultra wideband antenna for on-body communication in wireless body area network," in *2011 Loughborough Antennas Propagation Conference*, Nov. 2011, pp. 1–4.

[90] Y. Sun, W. Cheung, and T. Yuk, "Planar monopole ultra-wideband antennas with different radiator shapes for body-centric wireless networks," pp. 839–843, Jan. 2012.

[91] S. Zhu and R. Langley, "Dual-band wearable textile antenna on an EBG substrate," *IEEE Transactions on Antennas and Propagation*, vol. 57, no. 4, pp. 926–935, Apr. 2009.

[92] N. Chahat, M. Zhadobov, L. Le Coq, and R. Sauleau, "Wearable end-fire textile antenna for on-body communications at 60 GHz," *IEEE Antennas and Wireless Propagation Letters*, vol. 11, pp. 799–802, Jul. 2012.

[93] M. Okoniewski and M. A. Stuchly, "A study of the handset antenna and human body interaction," *IEEE Transactions on Microwave Theory and Techniques*, vol. 44, no. 10, pp. 1855–1864, Oct. 1996.

[94] K.-L. Wong and C.-I. Lin, "Characteristics of a 2.4-GHz compact shorted patch antenna in close proximity to a lossy medium," *Microwave and Optical Technology Letters*, vol. 45, no. 6, pp. 480–483, Apr. 2005.

[95] S. Razafimahatratra, J. Sarrazin, G. Valerio, F. Sarrazin, M. Casaletti, P. Doncker, and A. Benlarbi-Delai, "Input impedance of an aperture over a lossy half-space: Application to on-body antenna performance at 60GHz," *Progress In Electromagnetics Research C*, vol. 83, pp. 161–178, Apr. 2018.

[96] E. Reusens, W. Joseph, G. Vermeeren, and L. Martens, "On-body measurements and characterization of wireless communication channel for arm and torso of human," Jan. 2007, pp. 264–269.

[97] "Dielectric properties of body tissues in the frequency range 10 Hz - 100 GHz," [Online], Available: http://niremf.ifac.cnr.it/tissprop/, Accessed: Feb. 2016.

[98] T. G. Zimmerman, "Personal area networks: Near-field intrabody communication," *IBM Systems Journal*, vol. 35, no. 3.4, pp. 609–617, 1996.

[99] T. Handa, S. Shoji, S. Ike, S. Takeda, and T. Sekiguchi, "A very low-power consumption wireless ecg monitoring system using body as a signal transmission medium," in *Proceedings of International Solid State Sensors and Actuators Conference (Transducers '97)*, vol. 2, Jun. 1997, pp. 1003–1006 vol.2.

[100] M. Wegmueller, N. Felber, W. Fichtner, A. Lehner, O. Hess, J. Froehlich, N. Kuster, R. Reutemann, and M. Oberle, "Measurement system for the characterization of the human body as a communication channel at low frequency," in *2005 IEEE Engineering in Medicine and Biology 27th Annual Conference*, Jan. 2005, pp. 3502–3505.

[101] T. Handa, S. Shoji, S. Ike, S. Takeda, and T. Sekiguchi, "A very low-power consumption wireless ECG monitoring system using body as a signal transmission medium," in *Proceedings of International Solid State Sensors and Actuators Conference (Transducers '97)*, vol. 2, Jun. 1997, pp. 1003–1006 vol.2.

[102] B. M. Kibret, "The human body antenna: Characteristics and its application," Ph.D. dissertation, Victoria University, 2016.

[103] A. Lea, P. Hui, J. Ollikainen, and R. G. Vaughan, "Propagation between on-body antennas," *IEEE Transactions on Antennas and Propagation*, vol. 57, no. 11, pp. 3619–3627, Nov. 2009.

[104] N. Chahat, G. Valerio, M. Zhadobov, and R. Sauleau, "On-body propagation at 60 ghz," *IEEE Transactions on Antennas and Propagation*, vol. 61, no. 4, pp. 1876–1888, Apr. 2013.

[105] T. Alves, B. Poussot, and J. Laheurte, "Analytical propagation modeling of BAN channels based on the creeping-wave theory," *IEEE Transactions on Antennas and Propagation*, vol. 59, no. 4, pp. 1269–1274, Apr. 2011.

[106] L. Petrillo, T. Mavridis, J. Sarrazin, D. Lautru, A. Benlarbi-Delaï, and P. De Doncker, "Analytical creeping wave model and measurements for 60 ghz body area networks," *IEEE Transactions on Antennas and Propagation*, vol. 62, no. 8, pp. 4352–4356, Aug. 2014.

[107] A. Lea, P. Hui, J. Ollikainen, and R. G. Vaughan, "Propagation between on-body antennas," *IEEE Transactions on Antennas and Propagation*, vol. 57, no. 11, pp. 3619–3627, Nov. 2009.

[108] "Murata's contactless bed sensors," [Online], Available: https://www.murata.com/en-us/products/sensor/accel/sca10h_11h, Accessed: Jun. 2019.

[109] M. Kumar, A. Veeraraghavan, and A. Sabharwal, "Distanceppg: Robust non-contact vital signs monitoring using a camera," *Biomedical optics express*, vol. 6 5, pp. 1565–88, Apr. 2015.

[110] L. Chioukh, H. Boutayeb, L. Li, L. Yahia, and K. Wu, "Integrated radar systems for precision monitoring of heartbeat and respiratory status," in *2009 Asia Pacific Microwave Conference*, Dec. 2009, pp. 405–408.

[111] H. Chuang, H. Kuo, F. Lin, T. Huang, C. Kuo, and Y. Ou, "60-GHz millimeter-wave life detection system (MLDS) for noncontact human vital-signal monitoring," *IEEE Sensors Journal*, vol. 12, no. 3, pp. 602–609, Mar. 2012.

[112] N. Chahat, M. Zhadobov, L. Le Coq, S. I. Alekseev, and R. Sauleau, "Characterization of the interactions between a 60-GHz antenna and the human body in an off-body scenario," *IEEE Transactions on Antennas and Propagation*, vol. 60, pp. 5958–5965, Dec. 2012.

[113] S. L. Cotton, W. G. Scanlon, and P. S. Hall, "A simulated study of co-channel inter-ban interference at 2.45 GHz and 60 GHz," in *The 3rd European Wireless Technology Conference*, Sep. 2010, pp. 61–64.

[114] O. P. Gandhi and A. Riazi, "Absorption of millimeter waves by human beings and its biological implications," *IEEE Transactions on Microwave Theory and Techniques*, vol. 34, no. 2, pp. 228–235, Feb. 1986.

[115] N. Chahat, M. Zhadobov, and R. Sauleau, "Broadband tissue-equivalent phantom for ban applications at millimeter waves," *IEEE Transactions on Microwave Theory and Techniques*, vol. 60, no. 7, pp. 2259–2266, Jul. 2012.

[116] T. Baykas, C. Sum, Z. Lan, J. Wang, M. A. Rahman, H. Harada, and S. Kato, "IEEE 802.15.3c: the first IEEE wireless standard for data rates over 1 Gb/s," *IEEE Communications Magazine*, vol. 49, no. 7, pp. 114–121, Jul. 2011.

[117] C. Li and J. Lin, "Optimal carrier frequency of non-contact vital sign detectors," in *2007 IEEE Radio and Wireless Symposium*, Jan. 2007, pp. 281–284.

[118] T. Mavridis, L. Petrillo, J. Sarrazin, A. Benlarbi-Delaï, and P. De Doncker, "V-Band velocity estimation of creeping waves around the human body," *IEEE Antennas and Wireless Propagation Letters*, vol. 14, pp. 313–316, Feb. 2015.

[119] H. Liu, J. Sarrazin, F. Deshours, T. Mavridis, L. Petrillo, Z. Liu, P. De Doncker, and A. Benlarbi-Delaï, "Performance assessment of IR-UWB body area network (BAN) based on IEEE 802.15.6 standard," *IEEE Antennas and Wireless Propagation Letters*, vol. 15, pp. 1645–1648, Jan. 2016.

[120] A. Fort, J. Ryckaert, C. Desset, P. De Doncker, P. Wambacq, and L. Van Biesen, "Ultra-wideband channel model for communication around the human body," *IEEE Journal on Selected Areas in Communications*, vol. 24, no. 4, pp. 927–933, Apr. 2006.

[121] H. Ghannoum, C. Roblin, and X. Begaud, "Investigation and modeling of the uwb on-body propagation channel," *Wireless Personal Communications*, vol. 52, pp. 17–28, Jan. 2010.

[122] L. Petrillo, T. Mavridis, J. Sarrazin, A. Benlarbi-Delaï, and P. De Doncker, "Statistical on-body measurement results at 60 GHz," *IEEE Transactions on Antennas and Propagation*, vol. 63, no. 1, pp. 400–403, Jan. 2015.

[123] A. R. Guraliuc, M. Zhadobov, O. De Sagazan, and R. Sauleau, "Solid phantom for body-centric propagation measurements at 60 ghz," *IEEE Transactions on Microwave Theory and Techniques*, vol. 62, no. 6, pp. 1373–1380, Jun. 2014.

[124] T. Mavridis, C. Leduc, L. Petrillo, J. Sarrazin, M. Zhadobov, R. Sauleau, A. Benlarbi-Delaï, and P. D. Doncker, "Millington effect and propagation enhancement in 60-GHz body area networks," *IEEE Transactions on Antennas and Propagation*, vol. 64, no. 2, pp. 776–781, Feb. 2016.

[125] G. A. Conway and W. G. Scanlon, "Antennas for over-body-surface communication at 2.45 GHz," *IEEE Transactions on Antennas and Propagation*, vol. 57, no. 4, pp. 844–855, Apr. 2009.

[126] S. Razafimahatratra, J. Sarrazin, A. Benlarbi-Delaï, T. Mavridis, L. Petrillo, P. De Doncker, C. Leduc, M. Zhadobov, and R. Sauleau, "On-body propagation characterization with an H-plane substrate integrated waveguide (SIW) horn antenna at 60 GHz," in *2015 European Microwave Conference (EuMC)*, Sep. 2015, pp. 211–214.

[127] S. L. Cotton, G. A. Conway, and W. G. Scanlon, "A time-domain approach to the analysis and modeling of on-body propagation characteristics using synchronized measurements at 2.45 ghz," *IEEE Transactions on Antennas and Propagation*, vol. 57, no. 4, pp. 943–955, Apr. 2009.

[128] Y. Zhao, A. Sani, Y. Hao, S. Lee, and G. Yang, "A subject-specific radio propagation study in wireless body area networks," in *2009 Loughborough Antennas Propagation Conference*, Nov. 2009, pp. 80–83.

[129] P. S. Hall, Y. Hao, Y. I. Nechayev, A. Alomainy, C. C. Constantinou, C. Parini, M. R. Kamarudin, T. Z. Salim, D. T. M. Hee, R. Dubrovka, A. S. Owadally, W. Song, A. Serra, P. Nepa, M. Gallo, and M. Bozzetti, "Antennas and propagation for on-body communication systems," *IEEE Antennas and Propagation Magazine*, vol. 49, no. 3, pp. 41–58, Jun. 2007.

[130] J. Ryckaert, P. De Doncker, R. Meys, A. de Le Hoye, and S. Donnay, "Channel model for wireless communication around human body," *Electronics Letters*, vol. 40, no. 9, pp. 543–544, Apr. 2004.

[131] A. Lea, P. Hui, J. Ollikainen, and R. G. Vaughan, "Propagation between on-body antennas," *IEEE Transactions on Antennas and Propagation*, vol. 57, no. 11, pp. 3619–3627, Nov. 2009.

[132] M. Grimm and D. Manteuffel, "On-body antenna parameters," *IEEE Transactions on Antennas and Propagation*, vol. 63, no. 12, pp. 5812–5821, Dec. 2015.

[133] A. Gupta and T. D. Abhayapala, "Body area networks: Radio channel modelling and propagation characteristics," in *2008 Australian Communications Theory Workshop*, Jan. 2008, pp. 58–63.

[134] D. Ma and W. X. Zhang, "Analytic propagation model for wireless body-area networks," *IEEE Transactions on Antennas and Propagation*, vol. 59, no. 12, pp. 4749–4756, Dec. 2011.

[135] A. Fort, F. Keshmiri, G. R. Crusats, C. Craeye, and C. Oestges, "A body area propagation model derived from fundamental principles: Analytical analysis and comparison with measurements," *IEEE Transactions on Antennas and Propagation*, vol. 58, no. 2, pp. 503–514, Feb. 2010.

[136] D. M. Pozar, *Microwave Engineering*. John Wiley & Sons, 2004.

[137] H. F. Cook, "The dielectric behaviour of some types of human tissues at microwave frequencies," *British Journal of Applied Physics*, vol. 2, no. 10, pp. 295–300, Oct. 1951.

[138] A. W. Guy, J. F. Lehmann, and J. B. Stonebridge, "Therapeutic applications of electromagnetic power," *Proceedings of the IEEE*, vol. 62, no. 1, pp. 55–75, Jan. 1974.

[139] C. A. Balanis, *Advanced Engineering Electromagnetics*. Wiley, 1989.

[140] M. Balda, "cxroot - complex root of complex function," [Online], Available: https://fr.mathworks.com/matlabcentral/fileexchange/22661-cxroot-complex-root-of-complex-function, Accessed: Mar. 2016.

[141] "La peau humaine normale," [Online], Available: https://biologiedelapeau.fr/spip.php?article9, Accessed: Sep. 2016.

[142] "An overview of the skin," [Online], Available: https://www.webmd.com/beauty/cosmetic-procedures-overview-skin#1, Accessed: Sep. 2019.

[143] M. M. Black, "A modified radiographic method for measuring skin thickness," *British Journal of Dermatology*, vol. 81, no. 9, pp. 661–666, Sep. 1969.

[144] "Harpenden skinfold caliper," [Online], Available: http://www.harpenden-skinfold.com/measurements.html, Accessed: Oct. 2016.

[145] H. Alexander and D. L. Miller, "Determining skin thickness with pulsed ultra sound," *Journal of Investigative Dermatology*, vol. 72, no. 1, pp. 17 – 19, Jan. 1979.

[146] C. H. Daly and J. B. Wheeler, "The use of ultra-sonic thickness measurement in the clinical evaluation of the oral soft tissues," *Int Dent J.*, vol. 21, no. 4, pp. 418–429, Dec. 1971.

[147] R. Marks, P. J. Dykes, and E. Roberts, "The measurement of corticosteroid induced dermal atrophy by a radiological method," *Archives of Dermatological Research*, vol. 253, no. 2, pp. 93–96, Jan. 1975.

[148] P. Dykes and R. Marks, "Measurement of skin thickness: A comparison of two in vivo techniques with a conventional histometric method," *Journal of Investigative Dermatology*, vol. 69, no. 3, pp. 275 – 278, Sep. 1977.

[149] C. Then, J. Menger, G. Benderoth, M. Alizadeh, T. Vogl, F. Hübner, and G. Silber, "A method for a mechanical characterisation of human gluteal tissue," *Technology and health care : official journal of the European Society for Engineering and Medicine*, vol. 15, pp. 385–98, Feb. 2007.

[150] D. A. Hill and J. R. Wait, "Excitation of the zenneck surface wave by a vertical aperture," *Radio Science*, vol. 13, no. 6, pp. 969–977, Nov. 1978.

[151] K. A. Michalski and J. R. Mosig, "The sommerfeld halfspace problem redux: Alternative field representations, role of zenneck and surface plasmon waves," *IEEE Transactions on Antennas and Propagation*, vol. 63, no. 12, pp. 5777–5790, Dec. 2015.

[152] H. Zahouani, C. Pailler-Mattei, B. Sohm, R. Vargiolu, V. Cenizo, and R. Debret, "Characterization of the mechanical properties of a dermal equivalent compared with human skin in vivo by indentation and static friction tests," *Skin research and technology : official journal of International Society for Bioengineering and the Skin (ISBS) [and] International Society for Digital Imaging of Skin (ISDIS) [and] International Society for Skin Imaging (ISSI)*, vol. 15, pp. 68–76, Mar. 2009.

[153] R. E. Collin, *Field Theory of Guided Waves*. Wiley-Blackwell, 1991.

[154] W. W. Hansen, "Radiating electromagnetic wave guide," U.S. Patent 2 402 622, 25, 1946.

[155] J. du Preez and S. Sinha, *Millimeter-Wave Antennas: Configurations and Applications*. Springer International Publishing, 2016.

[156] R. Shaw, A. A. Khan, D. Samantaray, and M. K. Mandal, "A comparative study on substrate integrated waveguide periodic leaky wave antennas with differently shaped periodic slots," in *2015 IEEE Applied Electromagnetics Conference (AEMC)*, Dec. 2015, pp. 1–2.

[157] F. M. Monavar, S. Shamsinejad, R. Mirzavand, J. Melzer, and P. Mousavi, "Beam-steering SIW leaky-wave subarray with flat-topped footprint for 5G applications," *IEEE Transactions on Antennas and Propagation*, vol. 65, no. 3, pp. 1108–1120, Mar. 2017.

[158] A. Taeb, A. S. Abdellatif, G. Z. Rafi, S. Gigoyan, S. Safavi-Neini, and M. Basha, "A low-cost silicon-based beam-steering grating antenna for g-band applications," in *2014 IEEE Antennas and Propagation Society International Symposium (APSURSI)*, Jul. 2014, pp. 1282–1283.

[159] M. Steeg, B. Khani, V. Rymanov, and A. Stöhr, "Novel 50-70 GHz compact PCB leaky-wave antenna with high broadside efficiency and low return loss," in *2016 41st International Conference on Infrared, Millimeter, and Terahertz waves (IRMMW-THz)*, Sep. 2016, pp. 1–2.

[160] M. S. Rabbani, J. Churm, and A. Feresidis, "Millimetre-wave beam steerable leaky-wave antenna for 5G systems," in *12th European Conference on Antennas and Propagation (EuCAP 2018)*, Apr. 2018, pp. 1–4.

[161] D. R. Jackson, C. Caloz, and T. Itoh, "Leaky-wave antennas," *Proceedings of the IEEE*, vol. 100, no. 7, pp. 2194–2206, Jul. 2012.

[162] S. K. Podilchak, A. P. Freundorfer, and Y. M. M. Antar, "Planar leaky-wave antenna designs offering conical-sector beam scanning and broadside radiation using surface-wave launchers," *IEEE Antennas and Wireless Propagation Letters*, vol. 7, pp. 155–158, Feb. 2008.

[163] A. A. Oliner, "A planar negative-refractive-index medium without resonant elements," in *IEEE MTT-S International Microwave Symposium Digest, 2003*, vol. 1, Jun. 2003, pp. 191–194 vol.1.

[164] C. Caloz and T. Itoh, "Transmission line approach of left-handed (lh) materials and microstrip implementation of an artificial lh transmission line," *IEEE Transactions on Antennas and Propagation*, vol. 52, no. 5, pp. 1159–1166, May 2004.

[165] W. Cao, Z. N. Chen, W. Hong, B. Zhang, and A. Liu, "A beam scanning leaky-wave slot antenna with enhanced scanning angle range and flat gain characteristic using composite phase-shifting transmission line," *IEEE Transactions on Antennas and Propagation*, vol. 62, no. 11, pp. 5871–5875, Nov. 2014.

[166] N. Kumar, R. Agrawal, and S. C. Gupta, "Step by step designing of composite right left handed leaky wave antenna on substrate integrated waveguide using s slots," in *2016 International Conference on Computing, Communication and Automation (ICCCA)*, Apr. 2016, pp. 1414–1417.

[167] Q. Yang, Y. Zhang, and X. Zhang, "X-band composite right/left-handed leaky wave antenna with large beam scanning-range/bandwidth ratio," *Electronics Letters*, vol. 48, no. 13, pp. 746–747, Jun. 2012.

[168] Lei Liu, C. Caloz, and T. Itoh, "Dominant mode leaky-wave antenna with backfire-to-endfire scanning capability," *Electronics Letters*, vol. 38, no. 23, pp. 1414–1416, Nov. 2002.

[169] M. H. Rahmani and D. Deslandes, "Backward to forward scanning periodic leaky-wave antenna with wide scanning range," *IEEE Transactions on Antennas and Propagation*, vol. 65, no. 7, pp. 3326–3335, Jul. 2017.

[170] H. Cooper, M. Hoffman, and S. Isaacson, "Image line surface wave antenna," in *1958 IRE International Convention Record*, vol. 6, Mar. 1958, pp. 230–239.

[171] F. K. Schwering and S.-T. Peng, "Design of dielectric grating antennas for millimeter-wave applications," *IEEE Transactions on Microwave Theory and Techniques*, vol. 31, no. 2, pp. 199–209, Feb. 1983.

[172] A. Taeb, A. S. Abdellatif, G. Z. Rafi, S. Gigoyan, S. Safavi-Neini, and M. Basha, "A low-cost silicon-based beam-steering grating antenna for G-band applications," in *2014 IEEE Antennas and Propagation Society International Symposium (APSURSI)*, Jul. 2014, pp. 1282–1283.

[173] T. N. Trinh, R. Mittra, and R. J. Paleta, "Horn image guide leaky-wave antenna," in *1981 IEEE MTT-S International Microwave Symposium Digest*, Jun. 1981, pp. 20–22.

[174] R. E. Collin and F. J. Zucker, *Antenna theory*. McGraw-Hill, 1969.

[175] J. L. Volakis, *Antenna Engineering Handbook*. McGraw-Hill Education, 2007.

[176] D. Comite, S. K. Podilchak, P. Baccarelli, P. Burghignoli, A. Galli, A. P. Freundorfer, and Y. M. M. Antar, "A dual-layer planar leaky-wave antenna designed for linear scanning through broadside," *IEEE Antennas and Wireless Propagation Letters*, vol. 16, pp. 1106–1110, Dec. 2016.

[177] K. Solbach and B. Adelseck, "Dielectric image line leaky wave antenna for broadside radiation," *Electronics Letters*, vol. 19, no. 16, pp. 640–641, Aug. 1983.

[178] J. Liu, W. Zhou, and Y. Long, "A simple technique for open-stopband suppression in periodic leaky-wave antennas using two nonidentical elements per unit cell," *IEEE Transactions on Antennas and Propagation*, vol. 66, no. 6, pp. 2741–2751, Jun. 2018.

[179] S. Bruni, A. Neto, and F. Marliani, "The ultrawideband leaky lens antenna," *IEEE Transactions on Antennas and Propagation*, vol. 55, no. 10, pp. 2642–2653, Oct. 2007.

[180] M. K. Khattak and S. Kahng, "Enhanced gain metamaterial-based leaky-wave beam-forming antenna for the V2X communication," in *2015 International Conference on Emerging Technologies (ICET)*, Dec. 2015, pp. 1–2.

[181] E. ben Hamida, H. Noura, and W. Znaidi, "Security of cooperative intelligent transport systems: Standards, threats analysis and cryptographic countermeasures," *Electronics*, vol. 4, Jul. 2015.

[182] S. Gupta, S. Abielmona, and C. Caloz, "Microwave analog real-time spectrum analyzer (RTSA) based on the spectral–spatial decomposition property of leaky-wave structures," *IEEE Transactions on Microwave Theory and Techniques*, vol. 57, no. 12, pp. 2989–2999, Dec. 2009.

[183] L. Cohen, "Time-frequency distributions - a review," *Proceedings of the IEEE*, vol. 77, no. 7, pp. 941–981, Jul. 1989.

[184] B. Husain, M. Steeg, and A. Stöhr, "Estimating direction-of-arrival in a 5G hot-spot scenario using a 60 GHz leaky-wave antenna," in *2017 IEEE International Conference on Microwaves, Antennas, Communications and Electronic Systems (COMCAS)*, Nov. 2017, pp. 1–4.

[185] Chao-Hsiung Tseng and Chia-Hung Chao, "Noncontact vital-sign radar sensor using metamaterial-based scanning leaky-wave antenna," in *2016 IEEE MTT-S International Microwave Symposium (IMS)*, May 2016, pp. 1–3.

[186] M. Geiger, M. Hitzler, and C. Waldschmidt, "A flexible dielectric leaky-wave antenna at 160 GHz," in *2017 47th European Microwave Conference (EuMC)*, Oct. 2017, pp. 240–243.

[187] Z. Hu, Z. Shen, and W. Wu, "Reconfigurable leaky-wave antenna based on periodic water grating," *IEEE Antennas and Wireless Propagation Letters*, vol. 13, pp. 134–137, Jan. 2014.

[188] C. S. Prasad and A. Biswas, "Dielectric image line-based leaky-wave antenna for wide range of beam scanning through broadside," *IEEE Transactions on Antennas and Propagation*, vol. 65, no. 8, pp. 4311–4315, Aug. 2017.

[189] A. Zandieh, A. S. Abdellatif, A. Taeb, and S. Safavi-Naeini, "Low-cost and high-efficiency antenna for millimeter-wave frequency-scanning applications," *IEEE Antennas and Wireless Propagation Letters*, vol. 12, no. Jan., pp. 116–119, 2013.

[190] A. Mallahzadeh and S. Mohammad-Ali-Nezhad, "Periodic collinear-slotted leaky wave antenna with open stopband elimination," *IEEE Transactions on Antennas and Propagation*, vol. 63, no. 12, pp. 5512–5521, Dec. 2015.

[191] Y. Lyu, F. Meng, G. Yang, D. Erni, Q. Wu, and K. Wu, "Periodic SIW leaky-wave antenna with large circularly polarized beam scanning range," *IEEE Antennas and Wireless Propagation Letters*, vol. 16, pp. 2493–2496, Jul. 2017.

[192] X. Bai, S. Qu, K. Ng, and C. H. Chan, "Sinusoidally modulated leaky-wave antenna for millimeter-wave application," *IEEE Transactions on Antennas and Propagation*, vol. 64, no. 3, pp. 849–855, Mar. 2016.

[193] J. T. Williams, P. Baccarelli, S. Paulotto, and D. R. Jackson, "1-D combline leaky-wave antenna with the open-stopband suppressed: Design considerations and comparisons with measurements," *IEEE Transactions on Antennas and Propagation*, vol. 61, no. 9, pp. 4484–4492, Sep. 2013.

[194] A. P. Saghati, M. M. Mirsalehi, and M. H. Neshati, "A HMSIW circularly polarized leaky-wave antenna with backward, broadside, and forward radiation," *IEEE Antennas and Wireless Propagation Letters*, vol. 13, pp. 451–454, Mar. 2014.

[195] N. Nguyen Trong, L. Zou, C. Fumeaux, and C. Caloz, "Ultra-high and tunable sensitivity leaky-wave scanning using gain-loss C-section phasers," *Applied Physics*, Jun. 2017.

[196] A. M. Patel and A. Grbic, "A printed leaky-wave antenna based on a sinusoidally-modulated reactance surface," *IEEE Transactions on Antennas and Propagation*, vol. 59, no. 6, pp. 2087–2096, Jun. 2011.

[197] H. F. Hammad, Y. M. M. Antar, A. P. Freundorfer, and S. F. Mahmoud, "Uni-planar CPW-fed slot launchers for efficient TM0 surface-wave excitation," *IEEE Transactions on Microwave Theory and Techniques*, vol. 51, no. 4, pp. 1234–1240, Apr. 2003.

[198] O. Luukkonen, C. Simovski, G. Granet, G. Goussetis, D. Lioubtchenko, A. V. Raisanen, and S. A. Tretyakov, "Simple and accurate analytical

model of planar grids and high-impedance surfaces comprising metal strips or patches," *IEEE Transactions on Antennas and Propagation*, vol. 56, no. 6, pp. 1624–1632, Jun. 2008.

[199] S. Tretyakov, *Analytical Modeling in Applied Electromagnetics*. Artech House, 2003.

[200] S. K. Podilchak, P. Baccarelli, P. Burghignoli, A. P. Freundorfer, and Y. M. M. Antar, "Analysis and design of annular microstrip-based planar periodic leaky-wave antennas," *IEEE Transactions on Antennas and Propagation*, vol. 62, no. 6, pp. 2978–2991, Jun. 2014.

[201] S. F. Mahmoud, Y. M. M. Antar, H. F. Hammad, and A. P. Freundorfer, "Theoretical considerations in the optimization of surface waves on a planar structure," *IEEE Transactions on Antennas and Propagation*, vol. 52, no. 8, pp. 2057–2063, Aug. 2004.

[202] H. F. Hammad, Y. M. M. Antar, and A. P. Freundorfer, "Uni-planar slot antenna for TM slab mode excitation," *Electronics Letters*, vol. 37, no. 25, pp. 1500–1501, Dec. 2001.

[203] S. Sierra-Garcia and J. . Laurin, "Study of a CPW inductively coupled slot antenna," *IEEE Transactions on Antennas and Propagation*, vol. 47, no. 1, pp. 58–64, Jan. 1999.

[204] S. K. Podilchak, P. Baccarelli, P. Burghignoli, A. P. Freundorfer, and Y. M. M. Antar, "Optimization of a planar "bull-eye" leaky-wave antenna fed by a printed surface-wave source," *IEEE Antennas and Wireless Propagation Letters*, vol. 12, pp. 665–669, May 2013.

[205] "1.85mm jack (female) end launch connector," [Online], Available: https://www.centricrf.com/content/pdf/1892-04A-5.pdf, Accessed: Aug. 2019.

[206] "Coplanar waveguide calculator," [Online], Available: https://www.microwaves101.com/calculators/864-coplanar-waveguide-calculator, Accessed: Sep. 2019.

[207] "Coplanar waveguide with ground characteristic impedance calculator," [Online], Available: https://chemandy.com/calculators/coplanar-waveguide-with-ground-calculator.htm, Accessed: Sep. 2019.

[208] "LPKF ProtoLaser S4," [Online], Available: https://www.lpkf.com/en/industries-technologies/research-in-house-pcb-prototyping/produkte/lpkf-protolaser-s4/, Accessed: Aug. 2019.

[209] S. K. Podilchak, A. P. Freundorfer, and Y. M. M. Antar, "New leaky-wave antennas using surface-wave launchers and planar metallic grating lenses," in *2009 International Conference on Electromagnetics in Advanced Applications*, Sep. 2009, pp. 365–368.